

9-6-2019 10:30 AM

MRI Investigations of Metabolic and Structural Brain Changes in Alzheimer's Disease and Vitamin D Deprivation

Dickson Wong, *The University of Western Ontario*

Supervisor: Bartha, Robert, *The University of Western Ontario*

A thesis submitted in partial fulfillment of the requirements for the Doctor of Philosophy degree in Medical Biophysics

© Dickson Wong 2019

Follow this and additional works at: <https://ir.lib.uwo.ca/etd>



Part of the [Medical Biophysics Commons](#)

Recommended Citation

Wong, Dickson, "MRI Investigations of Metabolic and Structural Brain Changes in Alzheimer's Disease and Vitamin D Deprivation" (2019). *Electronic Thesis and Dissertation Repository*. 6611.
<https://ir.lib.uwo.ca/etd/6611>

This Dissertation/Thesis is brought to you for free and open access by Scholarship@Western. It has been accepted for inclusion in Electronic Thesis and Dissertation Repository by an authorized administrator of Scholarship@Western. For more information, please contact wlsadmin@uwo.ca.

Abstract

Alzheimer's disease (AD) is a neurodegenerative disorder of the brain that presents as progressive impairment across several cognitive domains. The biological mechanisms underlying the development of AD remain unclear, with amyloid-beta plaques, neurofibrillary tangles, calcium dysregulation, and oxidative stress all contributing to neurodegeneration in AD. Vitamin D (VitD) deficiency, a common condition in the elderly, may modulate these mechanisms and complicate the AD process. Due to this complicated pathogenesis, the diagnosis of AD requires subjective clinical judgement, staging of AD is challenging, and it remains difficult to predict when and who will progress to AD. The purpose of this thesis was to study the metabolic and structural changes of specific brain regions as a consequence of AD alone and under conditions of AD and VitD deprivation. Identification of biological changes underlying the early symptoms of AD will help to identify and stage individuals prior to symptom onset.

In one study, proton magnetic resonance spectroscopy (^1H -MRS), diffusion tensor imaging (DTI), and neuropsychological testing was used to measure the metabolic and microstructural processes associated with episodic memory impairment. Individuals with AD, mild cognitive impairment (MCI), and normal elderly controls (NEC) were studied. Left hippocampal glutamate and posterior cingulate *N*-acetyl aspartate concentrations were reduced in MCI and AD compared to NEC. Differences in DTI metrics indicated volume and white matter loss along the cingulum in AD compared to NEC. Metabolic and microstructural changes were also associated with episodic memory performance assessed using *Craft Story 21 Recall* and *Benson Complex Figure Copy*. The results of this study suggested that metabolite concentrations may provide insight into the underlying biological processes of AD and increase the confidence of a clinical diagnosis of MCI or AD.

To improve glutamate measurement in future studies, the echo time (T_E) for ^1H -MRS

measurement of glutamate at 7 T was optimized for signal strength and measurement precision in a second study. Time-domain simulations were performed and verified against *in vivo* and *in vitro* measurements. The results of this study indicated that $T_E = 105$ ms was optimal for *in vivo* glutamate measurement at 7 T with the semi-LASER (localization by adiabatic selective refocusing) sequence as this echo time produced the greatest glutamate signal while also producing the lowest measurement coefficient of variation. Use of a long T_E will also decrease power deposition and minimize macromolecule contributions to the spectrum.

In a third study, the role of VitD deficiency in AD was comprehensively evaluated in the APP_{Swe}/PS1 Δ E9 mouse model of mild AD using ¹H-MRS, high-resolution MRI, and spatial memory tasks. VitD deficiency did not change ventricle volume, an MRI marker of neuronal loss, but did result in changes in metabolite concentrations consistent with astrogliosis and gliosis. Overall, VitD deficient mice also performed better or improved on measures of spatial memory than mice on a nutritionally sufficient control diet. The results of this study suggested that VitD deficiency may improve memory by upregulating beneficial reactive astrogliosis in the prodromal stages of AD.

Keywords: Alzheimer's disease, high magnetic field, magnetic resonance spectroscopy, diffusion tensor imaging, N-acetyl aspartate, glutamate, Vitamin D

Lay Summary

Alzheimer's disease (AD) is a brain disorder that causes a progressive decline in memory and thinking. No one knows what gives rise to AD, but it includes abnormal deposits of different proteins, irregular calcium levels, and changes in antioxidant defences. Vitamin D (VitD) deficiency, a common condition in the elderly, could also play a role. Uncertainty of the root cause makes it hard for physicians to diagnose and predict the progress of AD. The purpose of this thesis was to study brain changes due to AD and VitD deficiency.

In one study, brain chemistry and structure in individuals with AD were studied using magnetic resonance imaging (MRI) techniques. Compared to elderly individuals without AD, individuals with AD had lower amounts of glutamate (the chemical responsible for cell communication), which was associated with volume loss and deterioration of structural connections. Changes occurred in the brain circuit responsible for episodic memory, the type of memory affected early in AD. As expected, changes were associated with performance on tests of episodic memory. Therefore, measuring brain chemicals could provide insight into biological processes underlying AD symptoms and increase a physician's confidence in their diagnosis.

In a second study, computer simulations were used to determine the best settings for glutamate measurement. The simulation results were verified against measurements made in a model with a known amount of glutamate and in the human brain. The optimal settings provided the greatest amount of glutamate signal, while also providing the best measurement precision.

In a third study, the role of VitD deficiency was evaluated in mice genetically engineered to reproduce aspects of the early stages of human AD. MRI was also used to measure brain chemistry. Over time, VitD deficiency resulted in brain chemical changes indicative of increased numbers of astrocytes, special cells that support and protect nerve cells in the brain. VitD deficient mice also performed better on tests of memory than mice that

were not VitD deficient. The results of this study suggested that VitD deficiency may actually improve memory in the early stages of AD through a beneficial increase in astrocyte numbers.

Acknowledgements

To my supervisor, Rob Bartha: Thank you for your kindness and your patience. Thank you for your unrelenting positivity whenever things seem to go awry and for your willingness to entertain any ideas I may have had, however outrageous. Our discussions and your teaching have made me a better researcher.

To the members of my advisory committee: Thank you Manuel Montero-Odasso and Michael Borrie for the invaluable scientific discussions, for your clinical perspective, and for your continued advice. Thank you to Ravi Menon for your technical and scientific expertise.

To the staff of the Centre for Functional and Metabolic Mapping (CFMM) at Robarts Research Institute: Thank you to Miranda Bellyou for the care you took in looking after my mice. I could not have done much of my research without you. Thank you to Alex Li and Trevor Szekeres for the numerous MRI scans that you ran for my studies. Thank you to Sue Bedford for your kindness in welcoming the study participants, for your help with expenses and logistics, and for the many wonderful baked goods you have brought in.

To my fellow Bartha Lab members: thank you for letting me bounce my ideas off you, thank you for making Robarts a fun place to work, and most importantly thank you for your friendships. I have learned a lot from all of you.

To my friends in the MD/PhD program: Thank you to all of my peers, who uniquely understand the challenge of the program and who are always there for support. Thank you to Jim Lewis for your guidance and Stacey Bastien for always being a kind and reliable go-to person for help with navigating the program.

To the friends that I have made during my time in London, thank you for all the fun on the soccer field, the volleyball court, and on stage. To my oldest and best friends, Andy Xiao, Kitty Chan, and Michelle Chan, thanks for staying in touch and for your constant

support even though visits became fewer and farther in between as the research work piled up.

To my partner, Lisa Hur: You have helped me through ups and downs, bringing positivity and joy during the lows, and injecting excitement during the highs. You see in me what I don't see in myself and make me want to be a better person each day. Thank you for your love and understanding, and for always being there by my side through the unavoidable late nights and long hours. Let us grow as we go.

To our puppies, Luna and 별이: Thank you for the much needed puppy therapy sessions at the end of the day. Both of you are a bundle of joy.

Finally, to my family: To my brother, Jason, thank you for doing what brothers do best and for being a good uncle to Luna. Mom and Dad, thank you for teaching me the value of hard work, for always pushing me to do my best and to give my all. Thank you for supporting me in all of my endeavours. As immigrants, the two of you had to work hard and sacrifice a lot for yourselves in order to give my brother and I what we needed to achieve our hopes and dreams. For that I am truly grateful.

*"Whoever you are, no matter how lonely,
the world offers itself to your imagination,
calls to you like the wild geese, harsh and exciting
over and over announcing your place
in the family of things. "*

Mary Oliver

Dedicated to my late grandfather (公公) and my late grandmother (婆婆), who loved me for who I was and were proud of what I wanted to be.

Contents

Abstract	ii
Lay Summary	iv
Acknowledgements	vi
Contents	x
List of Figures	xix
List of Tables	xxiv
List of Abbreviations	xxv
1 Introduction	1
1.1 Overview of Thesis	1
1.2 Alzheimer’s Disease	2
1.2.1 Overview	2
1.2.2 Pathogenesis and Neuropathology of Alzheimer’s Disease	3
1.2.2.1 Familial and Sporadic Alzheimer’s Disease	3
1.2.2.2 Amyloid and Tau Proteinopathies	4
1.2.2.3 Calcium Dysregulation, Oxidative Stress, and Synaptic Dysfunction	5

1.2.3	Clinical Diagnosis	7
1.2.4	Treatment of Alzheimer's Disease	8
1.2.5	Neuroimaging of Alzheimer's Disease	9
1.2.5.1	Magnetic Resonance Imaging	10
1.2.5.2	Positron Emission Tomography	11
1.2.5.3	Magnetic Resonance Spectroscopy	12
1.2.6	Neuropsychological Testing in Alzheimer's Disease	17
1.2.7	Transgenic Mouse Models of Alzheimer's Disease	19
1.3	Principles of Magnetic Resonance	21
1.3.1	Excitation and Adiabatic Pulses	21
1.3.2	Relaxation	23
1.3.3	Spatial Encoding	25
1.4	Proton Magnetic Resonance Spectroscopy	26
1.4.1	Chemical Shift and J-Coupling	26
1.4.2	Water Suppression	31
1.4.3	Localization	32
1.4.4	Post-Acquisition Signal Processing	34
1.4.5	Spectral Fitting	35
1.4.6	Metabolite Simulations for Prior Knowledge	36
1.4.7	Metabolite Quantification	37
1.4.8	Sources of Variability	38
1.4.8.1	Spectroscopy Voxel Placement and Participant Movement	38
1.4.8.2	Field Inhomogeneity	39
1.4.8.3	Chemical Shift Displacement Error	39
1.4.8.4	Signal Bleed	39
1.4.8.5	Macromolecule Signals	40

1.4.8.6	Signal-to-Noise Ratio, Linewidth, and the Cramér-Rao Lower Bound	40
1.4.8.7	Intrinsic Variation of Metabolite Levels	41
1.5	Diffusion Tensor Imaging	42
1.5.1	Water Diffusion in Tissue	42
1.5.2	Diffusion Weighting of the MRI Signal	43
1.5.3	The Diffusion Tensor	44
1.5.3.1	Mean Diffusivity	48
1.5.3.2	Fractional Anisotropy	48
1.5.3.3	Combinations of Eigenvalues	49
1.5.4	Tractography	49
1.6	References	50

2	Reduced hippocampal glutamate and posterior cingulate NAA in MCI and AD is associated with episodic memory performance and white matter integrity in the cingulum	73
2.1	Introduction	74
2.2	Materials and Methods	76
2.2.1	Subjects	76
2.2.2	Data Acquisition	77
2.2.2.1	Magnetic Resonance Imaging	77
2.2.2.2	Magnetic Resonance Spectroscopy	78
2.2.2.3	Diffusion Weighted Imaging	78
2.2.2.4	Cognitive Testing	80
2.2.3	Data Processing	80
2.2.3.1	Post-Processing of Acquired Images	80
2.2.3.2	Quantification of Metabolite Concentrations	81

2.2.3.3	Tractography and Diffusion Metrics in the Cingulum	86
2.2.4	Statistical Analyses	89
2.3	Results	92
2.3.1	Magnetic Resonance Spectroscopy	92
2.3.2	Diffusion in the Cingulum	92
2.3.3	Tests of Episodic Memory	93
2.3.4	Correlations	96
2.4	Discussion	98
2.4.1	Posterior Cingulate Cortex	99
2.4.2	Hippocampus	100
2.4.3	Study Limitations	102
2.5	Conclusion	104
2.6	Acknowledgements	105
2.7	References	105
2.8	Supplementary Figures	118
2.9	Supplementary Tables	120
2.10	Co-Authorship Statement	120
3	Optimized in vivo glutamate measurement using long-echo-time semi-LASER at	
	7 T	122
3.1	Introduction	123
3.2	Methods	124
3.2.1	Time-domain simulations	124
3.2.2	¹ H-MRS acquisition	126
3.2.2.1	Hardware and shimming	126
3.2.2.2	Pulse sequence	126
3.2.3	In vivo data	127

3.2.3.1	Acquisition	127
3.2.3.2	Post-processing	127
3.2.3.3	Prior knowledge	128
3.2.3.4	Spectral fitting	129
3.2.3.5	Glutamate-to-creatine ratio (Glu/Cr)	132
3.2.3.6	Effect of macromolecule contribution	133
3.2.3.7	Sample size calculations	133
3.2.4	In vitro data	134
3.2.4.1	Acquisition	134
3.2.4.2	Post-processing, prior knowledge, and spectral fitting . . .	134
3.3	Results	135
3.3.1	Spectral quality	135
3.3.2	Echo-time dependence of glutamate signal energy	135
3.3.3	In vivo spectral fitting quality	137
3.3.4	Sample size calculations	139
3.3.5	T_2 relaxation times	139
3.4	Discussion	142
3.5	Conclusions	147
3.6	Acknowledgement	148
3.7	References	148
3.8	Supplementary Figures	155
3.9	Co-Authorship Statement	155
4	Chronic Vitamin D deficiency in adult APP/PS1 mice: Effect on memory performance and brain metabolite levels	157
4.1	Introduction	158
4.2	Methods	159

4.2.1	Subjects	159
4.2.2	Diets and Vitamin D Status	160
4.2.3	Behavioural Studies	162
4.2.3.1	Morris Water Maze	162
4.2.3.2	Barnes Maze	165
4.2.3.3	Confounding Variables of Spatial Learning and Memory	167
4.2.4	Magnetic Resonance Imaging and Ventricle Volume	168
4.2.5	Magnetic Resonance Spectroscopy	169
4.2.5.1	Acquisition	169
4.2.5.2	Post-Processing	172
4.2.5.3	Metabolite Quantification	173
4.2.6	Statistical Analyses	174
4.2.6.1	Analysis of Longitudinal Data	174
4.2.6.2	Analysis of Spatial Maps of Mouse Activity	176
4.3	Results	176
4.3.1	Vitamin D Status	176
4.3.2	Morris Water Maze	178
4.3.2.1	Training Phase	178
4.3.2.2	Probe Trial	179
4.3.3	Barnes Maze	181
4.3.3.1	Training Phase	181
4.3.3.2	Probe Trial	183
4.3.4	Confounding Variables of Spatial Learning and Memory	185
4.3.4.1	Weight and Wire Hang Time	185
4.3.4.2	Open Arm Time in the EPM	185
4.3.5	Ventricle Volume	186
4.3.6	Magnetic Resonance Spectroscopy	186

4.4	Discussion	187
4.5	Conclusion	193
4.6	Acknowledgements	194
4.7	References	194
4.8	Co-Authorship Statement	204
5	Summary and Future Work	205
5.1	Summary	205
5.1.1	Reduced hippocampal glutamate and posterior cingulate NAA in MCI and AD is associated with episodic memory performance and white matter integrity in the cingulum	205
5.1.2	Optimized in vivo glutamate measurement using long-echo-time semi-LASER at 7 T	206
5.1.3	Chronic Vitamin D deficiency in adult APP/PS1 mice: Effect on memory performance and brain metabolite levels	207
5.2	Conclusions	208
5.3	Future Work	210
5.3.1	The Clinical Utility of Brain Metabolite Concentrations	210
5.3.2	Optimized Acquisition of Brain Metabolite Signals	211
5.3.3	The Role of Vitamin D in Alzheimer's Disease	211
A	Physics of Magnetization and The Equilibrium Magnetization	213
A.1	Magnetization	213
A.2	Measuring Magnetization	216
B	Quantum Mechanical Calculations for the Simulation of Metabolite Spin Systems	218
B.1	Overview	218

B.2	Describing the State of a System	218
B.3	Describing Measurable Quantities	220
B.4	Time Evolution of a System State	221
B.5	Describing a Statistical Ensemble of Quantum Mechanical Systems	221
B.6	Time Evolution of a Statistical Ensemble of Quantum Mechanical Systems	222
B.7	General Procedure for Metabolite Spin-System Simulations	223
C	Absolute Metabolite Quantification Using an Internal Water Reference	225
C.1	Corrections for T_1 and T_2 Relaxation	226
C.1.1	T_1 and T_2 Correction for the Measured Water Signal (S_W)	228
C.1.2	T_1 and T_2 Correction for the Measured Metabolite Signal (S_m)	229
C.2	Corrections for Number of Averages (N_{avg}), Number of MRS-visible ^1H Nuclei (ρ), and Gain/Scaling Factors (G)	229
C.3	Summary of Corrections for the Measured Water Signal	230
C.4	Summary of Corrections for the Measured Metabolite Signal	230
C.5	Metabolite Quantification Equations	230
C.5.1	Voxel Concentration	230
C.5.2	Tissue Concentration	231
D	Metabolite Simulation Code	233
D.1	Spin System Definitions	247
D.2	RF Pulse Definitions	248
D.2.1	90-degree Excitation Pulse	248
D.2.2	Adiabatic Full Passage Pulse	252
E	Research Ethics Approvals	262
F	Licenses	265

List of Figures

1.1	Excitation in the rotating frame ($\hat{x}', \hat{y}', \hat{z}'$).	22
1.2	Peak splitting behaviour of the lactate spin system.	29
1.3	A diffusion-weighted spin-echo sequence.	45
1.4	The diffusion tensor for isotropic and anisotropic diffusion.	47
2.1	Examples of spectroscopy voxel placement and the representative spectra in the left hippocampus and PCC.	79
2.2	Three dimensional transparent whole brain (grey) of a single subject in two different orientations showing the position of the spectroscopy (green shaded regions) in relation to the left cingulum fibre tracts reconstructed using diffusion-based probabilistic tractography.	88
2.3	Diffusion-based tractography of the left cingulum.	90
2.4	Diffusion metrics plotted as a function of the position along the hippocampal portion of the cingulum.	94
2.5	Diffusion metrics (FA and RD) as a function of the position along the cingulate gyrus portion of the cingulum.	95

2.6	Significant correlations between the left hippocampal glutamate concentration and the average RD and AxD in the first 25% of the hippocampal portion of the cingulum are shown. Significant correlations the NAA concentration in the PCC and the average RD, and the average FA in the last 60-90% of the cingulate gyrus portion of the cingulum are also shown.	97
2.7	Significant correlations between left hippocampal glutamate concentration and the delayed Craft Story 21 Recall paraphrase score and the delayed Benson Complex Figure copy score are shown. Significant correlations between posterior cingulate NAA concentration and the delayed CSR paraphrase score and the delayed BCFC score are also shown.	98
2.S1	Significant correlations between NAA levels in the PCC and the average RD and AxD in the first 25% of the hippocampal portion of the cingulum are shown.	118
2.S2	Left hippocampal glutamate levels were positively correlated with the delayed CSR verbatim z-score.	118
2.S3	NAA concentration in the PCC was correlated with the immediate CSR verbatim score, the immediate CSR paraphrase score, and the delayed CSR verbatim z-score.	119
3.1	The macromolecule model included in the prior knowledge template. . . .	130
3.2	The calculated signal energies of glutamate from simulated data and average in vivo data are plotted from $T_E = 45$ ms to $T_E = 215$ ms. Examples of in vivo ^1H -MRS spectra collected from a $2 \times 2 \times 2$ cm ³ voxel in the left sensorimotor cortex at $T_E = 45$ ms and $T_E = 105$ ms respectively using the semi-LASER sequence are also shown. The voxel position and the in vivo glutamate spectral pattern as a function of echo time are also shown.	136

3.3	The calculated signal energies of glutamate, glutamine, and GABA from in vitro data obtained using a mixed-metabolite phantom from $T_E = 45$ ms to $T_E = 215$ ms; the differences in signal energy between the glutamate signal and the glutamine and GABA signals from $T_E = 45$ ms to $T_E = 215$ ms; and examples of in vitro ^1H -MRS spectra collected from a $2.5 \times 2.5 \times 2.5$ cm ³ voxel in the centre of the phantom at $T_E = 45$ ms and $T_E = 105$ ms respectively.	138
3.4	CRLBs for the glutamate fit are plotted as a function of echo time with standard errors; inter-subject coefficients of variance of Glu/Cr are plotted against echo time; the energy of the glutamate signal fitted to in vivo data acquired at $T_E = 45$ ms from Subject V1 as a function of the lm5 and lm6 macromolecule amplitude; and the variation of the macromolecule model by changing the lm5 and lm6 macromolecule lineshapes from 20% of its original value to 220% of its original value.	140
3.5	Estimated number of participants per group required to detect a 10% change in Glu/Cr between two groups at a 95% confidence level are plotted across echo time.	141
3.S1	The calculated signal energies of NAA, creatine, choline, <i>myo</i> -inositol, and glutathione from average in vivo data are plotted from $TE = 45$ ms to $TE = 215$ ms.	155
4.1	A summary of the study design and the 2-week assessment schedule at each time point.	161
4.2	Examples of the mouse tracking in the Morris water maze, Barnes maze, and the elevated plus maze are shown. Examples of spatial maps of maze activity are also shown.	164

4.3	Method of brain extraction, ventricle segmentation, and ventricle volume measurement from high resolution ($150 \times 150 \times 150 \mu\text{m}^3$) TrueFISP images. Ventricle volume is also plotted with respect to age.	170
4.4	Spectroscopy voxel position encompassing both hippocampi of the mouse brain are shown with an example of the post-processed ^1H -MRS spectra acquired from the voxel. Longitudinal measurements of NAA, creatine, lactate, and taurine concentrations are also plotted.	171
4.5	Serum 25(OH)D levels as measured by radioimmunoassay.	177
4.6	The performance of APP _{Swe} /PS1 Δ E9 mice in the Morris water maze (MWM) is shown in blue for mice on the control diet and in red for mice on the Vitamin D deficient (VitD-) diet.	180
4.7	The performance of APP _{Swe} /PS1 Δ E9 mice in the Barnes maze (BM) is shown in blue for mice on the control diet and in red for mice on the Vitamin D deficient (VitD-) diet.	182
4.8	Average maps of probe trial activity in the Barnes maze (BM) are shown for APP _{Swe} /PS1 Δ E9 mice on the control diet at 6 months, 9 months, 12 months, and 15 months of age. Comparisons of activity maps using permutation testing are also shown.	184
4.9	The correlation between NAA concentration in the hippocampus of 12 month old APP _{Swe} /PS1 Δ E9 mice as measured by ^1H -MRS and average proximity to the target platform location in the MWM probe trial is shown in (a). Creatine concentration in the hippocampus of 12 month old mice were also associated with lower average proximity in the MWM probe trial, as shown in (b). The 12 to 15 month change in primary latency in the BM probe trial of APP _{Swe} /PS1 Δ E9 mice on the Vitamin D deficient (VitD-) diet is plotted against the 12 to 15 month change in hippocampal lactate (Lac) concentration as measured by ^1H -MRS in (c).	188

A.1	Protons and neutrons are each made of three quarks. (a) A proton has two up quarks and one down quarks, a net charge of $+e$, and a net spin of $1/2$. (b) A neutron has two down quarks and one up quark, with a net charge of 0 and a net spin of $1/2$	214
A.2	Torque, $\vec{\tau}$, exerted by the magnetic field, \vec{B}_0 , on the magnetization, \vec{M}_0 , changes the angular momentum, \vec{J} , in the direction of $\vec{\tau}$. Since $\vec{M}_0 \parallel \vec{J}$, the \vec{M}_0 also changes in the direction of $\vec{\tau}$, resulting in clockwise precession about \vec{B}_0 . . .	217

List of Tables

2.1	A summary of relationships between metabolite parameters in the prior knowledge template.	83
2.2	A summary of the metabolite-specific T_1 and T_2 values used for relaxation correction of the fitted metabolite signals.	87
2.S1	The group means, standard deviations (SD), and standard errors (SE) of the Craft Story 21 Recall and Benson Complex Figure Copy z-scores are shown in this table.	120
3.1	A summary of relationships between metabolite parameters in the prior knowledge template.	131
3.2	T_2 values (mean \pm SD) of various metabolites of interest measured from a voxel in the sensorimotor cortex of Subjects V1, V2, V3, and V4.	141
4.1	A summary of relationships between metabolite parameters in the prior knowledge template.	173
4.2	A summary of the metabolite-specific T_1 and T_2 values used for relaxation correction of the fitted metabolite signals.	175

List of Abbreviations

^1H	proton
2xFAD	double transgenic familial Alzheimer's disease mice
A β	amyloid-beta
AAT	aspartate aminotransferase
AceCS-1	acetyl CoA synthetase-1
acetyl CoA	acetyl-coenzyme A
AD	Alzheimer's disease
ADC	apparent diffusion coefficient
AFP	adiabatic full passage
AHP	adiabatic half passage
Ala	alanine
ANOVA	analysis of variance
ApoE	apolipoprotein E
APP	amyloid-beta precursor protein
ASPA-II	aspartoacylase II
Asp-NAT	<i>L</i> -aspartate <i>N</i> -acetyltransferase
AxD	axial diffusivity
BCFC	Benson Complex Figure Copy
BM	Barnes maze
CDR	Clinical Dementia Rating Scale

ChEI	cholinesterase inhibitor
Cho	choline
Cr	creatine
CRLB	Cramér-Rao lower bound
CSF	cerebrospinal fluid
CSR	Craft Story 21 Recall
CV	coefficient of variation
DLB	Lewy body dementia
DOF	degree-of-freedom
DTI	diffusion tensor imaging
EAAT1/2	excitatory amino acid transporter 1/2
ECC	eddy current correction
EPM	elevated plus maze
FA	fractional anisotropy
FDG	fluorodeoxyglucose
FID	free-induction decay
FISP	fast imaging with steady state precession
fMRI	functional magnetic resonance imaging
FOV	field of view
FSE	fast spin echo
FTD	frontotemporal dementia
FWER	familywise error rate
GABA	γ -aminobutyric acid
GDS	Geriatric Depression Score
GFAP	glial fibrillary acidic protein
Glc	glucose
Gln	glutamine

Glu	glutamate
Glu/Cr	glutamate-to-creatine ratio
Gly	glycine
GM	grey matter
GroPCho	glycerophosphorylcholine
GSH	glutathione
HSVD	Hankel singular value decomposition
InsP ₃	inositol triphosphate
Lac	lactate
LASER	localization by adiabatic selective refocusing
LVGCC	<i>L</i> -type voltage gated calcium channels
MAPT	microtubule associated protein tau
MCI	mild cognitive impairment
MD	mean diffusivity
mGluRs	metabotropic glutamate receptors
MMSE	Mini-Mental State Examination
MoCA	Montreal Cognitive Assessment
MRI	magnetic resonance imaging
MRS	magnetic resonance spectroscopy
MRSI	magnetic resonance spectroscopic imaging
MWM	Morris water maze
Myo	<i>myo</i> -inositol
NAA	<i>N</i> -acetylaspartate
NAAG	<i>N</i> -acetylaspartyl glutamate
NAT8L	<i>N</i> -acetyltransferase-8 like protein
NEC	normal elderly control
NFT	neurofibrillary tangle

NMDAR	<i>N</i> -methyl- <i>D</i> -aspartate receptor
Nrf2	nuclear factor-erythroid-2-related factor 2
OVS	outer-volume suppression
PC	phosphorylcholine
PCC	posterior cingulate cortex
PCNN	pulse-coupled neural network
PET	positron emission tomography
PEth	phosphorylethanolamine
PiB	Pittsburgh Compound B
PRESS	point resolved spectroscopy
PrP ^C	prion protein
PS1	presenilin 1
PS2	presenilin 2
QUALITY	quantification improvement by converting lineshapes to the Lorentzian type
QUECC	combined QUALITY deconvolution and eddy current correction
RD	radial diffusivity
RF	radiofrequency
ROI	region of interest
ROS	reactive oxygen species
Scyllo	<i>scyllo</i> -inositol
SD	standard deviation
SNR	signal-to-noise ratio
STEAM	stimulated acquisition mode
Tau	taurine
TCA	tricarboxylic acid
TE or T_E	echo time

Tg	transgenic
TR	repetition time
TSP	3-trimethylsilyl proprionate
VaD	vascular dementia
VAPOR	variable power RF pulses with optimized relaxation delays
VGLUT1/2	vesicular glutamate transporter 1/2
VitD	Vitamin D
WM	white matter

1

Introduction

1.1 Overview of Thesis

The purpose of this thesis was to study the metabolic and structural changes of specific brain regions as a consequence of Alzheimer's disease (AD) and under conditions of Vitamin D deprivation. The studies presented in this thesis applied techniques such as magnetic resonance spectroscopy, diffusion tensor imaging, and neuropsychological and behavioural testing to study the chemistry, structure, and function of the brain in both human participants with AD and a pre-clinical mouse model of AD.

Sections 1.2.1 – 1.2.4 of this chapter provide a brief summary of the current understanding of Alzheimer's disease. Commonly used neuroimaging techniques, neuropsychological testing, and pre-clinical mouse models of AD are summarized in Sections 1.2.1 – 1.2.4. The remaining section (Section 1.3) briefly describes the physics of nuclear magnetic resonance. These physical principles are the basis of the two main techniques used in this thesis to study brain metabolism and structure: magnetic resonance spectroscopy and diffusion tensor imaging.

The following three chapters of the thesis describe the scientific investigations that were completed. The first study (Chapter 2) investigated the association between white matter

structure in the cingulum and metabolism in the hippocampus and posterior cingulate cortex, as such measurements could provide valuable information to support a clinical diagnosis of mild cognitive impairment or probable Alzheimer's disease. It was hypothesized that glutamate and *N*-acetyl aspartate concentrations as measured by magnetic resonance spectroscopy would be lower in the posterior cingulate cortex and hippocampus of individuals with Alzheimer's disease as compared to normal elderly controls and significantly correlated with both measures of microstructural integrity in the cingulum and measures of episodic memory. In line with this hypothesis, a relative reduction in hippocampal glutamate was found in individuals with Alzheimer's disease and was associated with decreased microstructural integrity and episodic memory performance.

With glutamate as a metabolite of interest, a second study was performed (Chapter 3) to find the spectroscopy acquisition parameters that optimized future measurements of glutamate concentration using proton magnetic resonance spectroscopy at a field strength of 7 Tesla.

Finally, magnetic resonance spectroscopy was applied in the third study (Chapter 4) to examine changes in brain metabolism in a pre-clinical mouse model of Alzheimer's disease after Vitamin D deficiency. It was hypothesized that Vitamin D deficiency would decrease *N*-acetyl aspartate concentrations and worsen spatial memory performance, but the results of this study did not support this hypothesis.

The last chapter (Chapter 5) summarizes the main scientific contributions of the thesis and describes opportunities for future investigations.

1.2 Alzheimer's Disease

1.2.1 Overview

Dementia, a decline in memory and thinking that interferes with activities of daily life, affects over 47 million people worldwide of which over 550,000 are Canadians [1]. In Canada,

dementia is already a major burden on the healthcare system, with the cost of care for patients with dementia being \$10.4 billion in 2016 and expected to rise to \$16.6 billion by 2031 [2]. The most common form of dementia is Alzheimer's disease (AD), accounting for 60-80% of dementia cases [3].

AD is a neurodegenerative disorder of the brain that not only results in progressive memory impairments, but also progressive language, visual, and executive function problems [4]. Patients with AD can also develop neuropsychiatric symptoms such as apathy, depression, anxiety, and aggression [5] that can impact the quality of life of both patient and caregiver [6]. The biological mechanisms of AD are complex and heterogeneous, without a clear cause [4] or a clear chain of events that lead to symptoms and impairments [3]. This has resulted in a wide range of treatments that target different aspects of AD. There are many different research tools developed to probe these different aspects, including a variety of neuroimaging techniques, neuropsychiatric tests, and mouse models of AD.

1.2.2 Pathogenesis and Neuropathology of Alzheimer's Disease

1.2.2.1 Familial and Sporadic Alzheimer's Disease

There are two forms of Alzheimer's disease: a rare form called familial AD that accounts for about 5% of AD cases, and a more common form called sporadic AD [7]. The pathogenesis of familial AD is better understood than the pathogenesis of sporadic AD.

Familial AD results from either a mutation in the presenilin 1 (PS1) gene on chromosome 14 [8], the presenilin 2 (PS2) gene on chromosome 1 [9, 10], or the amyloid- β precursor protein (APP) gene on chromosome 21 [11]. APP codes for the protein from which amyloid- β ($A\beta$) is cleaved, while PS1 and PS2 code for the catalytic core of the γ -secretase enzyme that cleaves APP [12, 13, 14]. Mutations in these genes cause abnormal $A\beta$ production, processing, and aggregation, which is thought to ultimately result in AD. Repetitions of the APP located on chromosome 21 can also result in abnormal amyloid processing and

AD, as is the case in trisomy 21 (Down syndrome). Although all mutations can occur, PS1 mutations are the most common, accounting for the majority of familial AD cases [7, 15]. Familial AD typically occurs in individuals aged 30-60 years of age.

In contrast, sporadic AD typically presents in individuals over 60 years of age. As in familial AD, the same proteinopathies ($A\beta$ and tau tangles, discussed below) are exhibited in sporadic AD, but without APP, PS1, or PS2 mutations. Though no single gene has been identified to cause sporadic AD, polymorphisms of the apolipoprotein E (ApoE) gene have been identified to confer risk for sporadic AD [16]. Individuals who have inherited two alleles of the ApoE- ϵ 4 polymorphism increases the risk of developing AD by 15 times [17].

1.2.2.2 Amyloid and Tau Proteinopathies

The neuropathology of AD is characterized by the occurrence of two main molecular lesions: the aggregation of amyloid plaques and the formation of intraneuronal neurofibrillary tangles [3]. As the disease progresses, amyloid first deposits in the isocortex, followed by the allocortex (i.e. the entorhinal cortex, hippocampal formation, amygdala, insular cortex, and cingular cortex), and finally the subcortical nuclei [18]. Neurofibrillary tangles (NFTs) begin forming in the entorhinal cortex and hippocampus, followed by the limbic structures, and finally the isocortex, with the association areas being affected earlier and more severely than the primary sensory, motor, and visual areas [19]. Importantly, deposition of amyloid plaques and NFTs and the subsequent loss of neurons in the nucleus basalis of Meynert is thought to be responsible for the widespread deficiency of cortical acetylcholine observed in AD [20, 21].

Amyloid plaques are mainly composed of $A\beta$ protein. $A\beta$ peptides of either 40 or 42 amino acids long are formed from the sequential cleavage of APP by the β - and γ -secretases [22, 23]. The peptides can then aggregate into different forms, such as the insoluble fibrils of amyloid plaques. $A\beta$ can also aggregate into soluble oligomers of 2 to 6 peptides [24], the

concentration of which correlates better with synapse loss in AD than the concentration of A β plaques in the brain [25].

Neurofibrillary tangles result from the misfolding and hyperphosphorylation of the microtubule-associated tau protein. This abnormal form of tau is insoluble, aggregating as a helical fibrils in the neuron [3]. The loss of normal tau and aggregation of abnormal tau renders microtubules unstable, and is thought to cause the breakdown of dendrites and axons of the neuron [23].

There is evidence that A β deposition precedes and drives NFT formation [26, 27], which is in line with the current prevailing theory of AD pathogenesis: the “amyloid cascade” hypothesis. This theory postulates that amyloid dyshomeostasis, either as a result of increased relative A β production throughout life (as in familial AD) or a failure of A β clearance mechanisms (as in sporadic AD), results in A β fibril and oligomer formation, which in turn leads to NFT formation and neuronal death, ultimately causing dementia [28].

1.2.2.3 Calcium Dysregulation, Oxidative Stress, and Synaptic Dysfunction

NFT formation is only one of many downstream events that can occur as a result of A β peptide formation and deposition. Another important result of A β peptide formation is neuronal calcium dysregulation. A β peptides contribute to this directly by inserting into the plasma membrane of the neuron, creating voltage-insensitive calcium pores, and increasing the intracellular concentration of calcium [29].

A β peptides can also indirectly increase the intracellular concentration of calcium by modulating the glutamatergic system. A β renders neurons vulnerable to excitotoxicity mediated by the ionotropic *N*-methyl-*D*-aspartate receptors (NMDARs) [30], glutamate-activated calcium channels, by direct association with the receptor subunits [31, 32] and by inhibiting glutamate reuptake from the synapse [33]. A β can also affect metabotropic glutamate receptors (mGluRs). Specifically, A β binds prion protein (PrP^C), activating the metabotropic G-protein coupled glutamate receptor, inducing inositol triphosphate (InsP₃)

formation and InsP_3 receptor activation, resulting in calcium release from the endoplasmic reticulum [34]. Interestingly, PS1 and PS2 mutations responsible for familial AD can also induce endoplasmic reticulum release via modulation of InsP_3 receptor gating and other cellular pathways, while ApoE- $\epsilon 4$ expression has been functionally linked to increased intracellular calcium levels [35]. Observed reductions in the AD brain of both vesicular glutamate transporters 1/2 (VGLUT1/2), proteins of the pre-synaptic neuron that maintain the storage of glutamate in vesicles, as well as excitatory amino acid transporters 1/2 (EAAT1/2), proteins of the astrocyte that clear glutamate from the synapse, also contribute to increased glutamate in the synapse, resulting in overactivation of NMDARs and increased calcium flux into the cell [36].

Increased intracellular calcium due to $A\beta$ has consequences for the neuron. First, positive feedback loops can be activated to increase intracellular calcium levels further. Due to calcium's positive charge, membrane depolarization will result in the activation of L-type voltage gated calcium channels (LVGCC) [31], which have increased activity and expression due to $A\beta$ [37, 38, 39, 40]. Increased intracellular calcium can also stimulate the cleavage of APP and the formation of more $A\beta$ peptides [41], perpetuating the calcium dysregulation. Second, cell metabolism is affected. Excessive intracellular calcium is taken up by the mitochondria via the mitochondrial calcium uniporter, which results in increased reactive oxygen species production, reduced energy metabolism, and mitochondrial dysfunction [32, 42]. Finally, increased intracellular calcium can activate pathways that induce synaptic depression. Specifically, prolonged NMDAR activation can eventually result in desensitization and internalization of the receptors. Coupled with the activation of extrasynaptic NMDARs and mGluRs due to the presence of glutamate outside of the synapse as a result of impaired glutamate uptake, long-term synaptic depression is induced [43]. Long-term synaptic depression with high levels of $A\beta$ ultimately leads to dendritic spine shrinkage, reduced glutamatergic transmission, and synaptic loss [44]. In fact, it is not neuronal loss, but rather synaptic loss that is the best correlate to cognitive impairment in AD [45].

These mechanisms offer many potential avenues for therapy. For example, increased reactive oxygen species production could potentially be counteracted by Vitamin D, since Vitamin D acts to increase the expression of nuclear factor-erythroid-2-related factor 2 (Nrf2), a transcription factor that activates genes to enhance expression of antioxidants and detoxifying enzymes [46]. Vitamin D can also lower LVGCC expression and reduce *L*-type currents in neurons [47, 48]. In addition, activation of extrasynaptic NMDARs that lead to long-term synaptic depression and synapse loss can be blocked by memantine [49], a drug currently approved for treatment of moderate-to-severe AD.

1.2.3 Clinical Diagnosis

Clinically, AD progression occurs along a continuum, beginning with an asymptomatic predementia phase called mild cognitive impairment (MCI) due to AD, followed by a symptomatic dementia phase called probable AD. Probable AD is diagnosed when the following diagnostic criteria are met [50]:

1. Progressive functional decline and cognitive impairment as assessed via history-taking, information from a knowledgeable informant (e.g. spouse, partner, or close friend), mental status examination, and neuropsychological testing
2. Neuropsychiatric symptoms that interfere with activities of daily life
3. Insidious onset over months to years
4. In addition to cognitive dysfunction in one other domain, the initial and most prominent cognitive deficits are:
 - (a) In learning and recall of recently learned information (amnestic presentation)
 - (b) In language processing, visuospatial cognition, and/or executive function (non-amnestic presentation)

5. Other forms of dementias have been ruled out and comorbidities or medications that could have a substantial effect on cognition are not present

The clinical distinction between MCI and probable AD is drawn by whether or not neuropsychological changes are significantly impairing activities of daily life. Those with MCI generally maintain independent function, even with impairment of cognitive function [51]. However, it remains difficult to identify where an individual lies along the disease continuum. Use of measurements of biomarkers of AD pathology, as well as volumetric, structural, functional, and metabolic measurements of the brain using various neuroimaging modalities may provide complementary information that can aid in staging the disease.

1.2.4 Treatment of Alzheimer's Disease

Treatment options for AD are limited, and only five drug therapies have been approved for the treatment of AD. Four of these therapies are cholinesterase inhibitors (ChEIs) designed to enhance cholinergic activity by preventing the breakdown of acetylcholine in the synapse, countering the effect of the widespread deficiency of cortical acetylcholine observed in AD. Of these ChEIs, tacrine is rarely used due to liver toxicity. The other three ChEIs, donepezil, galantamine, and rivastigmine, are regularly used for treating AD. A six month treatment with these therapies can modestly improve cognitive function, activities of daily living, and behaviour for those with mild, moderate, or severe dementia due to AD [52]. However, since acetylcholine is the major neurotransmitter of the parasympathetic nervous system, ChEIs can have unpleasant multi-system side-effects, such as nausea, gastrointestinal upset, diarrhoea, and bradycardia [53].

The fifth approved drug therapy is memantine, a non-competitive NMDAR antagonist [54]. Memantine is designed to reduce glutamatergic neuroactivity, countering the effects of glutamate excitotoxicity and calcium dysregulation observed in AD. A six to seven month

treatment with memantine is well tolerated and has been shown to provide a small improvement in cognition, activities of daily living, and behaviour for those with moderate to severe dementia due to AD but not for those with mild AD [55].

Memantine, donepezil, galantamine, and rivastigmine are considered symptomatic treatments for AD, as they do not modify the underlying disease processes. The development of disease-modifying therapies is an active area of research. To date, the majority of these agents are based on the “amyloid cascade” hypothesis of AD and are either molecules that target the activity of the secretase enzymes that cleave APP or immunotherapies that target the A β fibrils and oligomers directly [56]. Unfortunately, Phase III trials of both anti-secretase agents such as segmagacestat [57] and anti-A β agents such as bapineuzumab [58, 59] or solanezumab [60] failed to show improvement in cognition or functioning in AD patients, despite observed changes in plasma, cerebrospinal fluid, and neuroimaging biomarkers of A β load. As such, the development of interventions are shifting towards targeting tau and the NFTs [61]. Since A β load plateaus early while NFT load continues throughout the disease course [62, 63], therapies that target tau may have more potential for altering the disease course.

1.2.5 Neuroimaging of Alzheimer's Disease

In the context of AD, the current clinical use of neuroimaging is to rule out non-AD reasons for cognitive decline, such as space-occupying lesions and cerebrovascular disease [64, 65]. However, with neuroimaging becoming more accessible to the clinical community, its utility is extending beyond simply excluding surgically treatable causes of cognitive impairment to supporting a physician's diagnosis of AD. Various neuroimaging modalities could provide information about the underlying pathology that can help place an individual along the disease continuum. Neuroimaging is also a powerful research tool, helping us to better understand the pathology of AD *in vivo* with the aim of identifying biomarkers of disease progression and establishing their prognostic value. Importantly, identifying

structural, functional, and metabolic measurements of the brain that have utility in both the early detection of AD and in the prediction of which individuals with MCI will progress to AD will be needed to determine who will benefit from disease-modifying treatments once they become available.

1.2.5.1 Magnetic Resonance Imaging

Magnetic resonance imaging (MRI) is an imaging modality that excites protons using radiofrequency (RF) energy and measures the RF signal emitted by the protons as they return to their equilibrium energy state. Much of this signal comes from the protons of water due to the high water content in brain tissue. Differences in tissue characteristics manifest as changes in the RF signal allowing MRI to be sensitive to both volumetric and microstructural changes. Various structural imaging sequences such as MP2RAGE [66] can be used to acquire high resolution ($< 1 \text{ mm}^3$) anatomical images to assess volumetric changes, while diffusion tensor imaging (DTI) can be used to measure microstructural changes.

Spatial and temporal patterns of volumetric changes as measured by MRI match the progression of NFT deposition described in Section 1.2.2.2 [67, 68]. Other volumetric changes such as ventricular expansion have also been observed over the course of the disease [69]. These patterns of cerebral atrophy and ventricular expansion are strongly correlated with cognitive decline in AD [70]. Microstructural changes of the white matter as measured by diffusion tensor imaging also occur as a function of cognitive impairment in AD [71, 72]. Together, these observations suggest that structural MRI measurements have prognostic and diagnostic value. Indeed, studies have shown that structural MRI measurements are useful in identifying individuals with MCI that are likely to progress to AD [73, 74, 75] and in differentiating AD from other dementias [76].

However, the specificity of structural MRI measures in AD are limited by the fact that similar patterns of change are observed in other diseases and some individuals with AD may exhibit atypical patterns [77]. Further, structural changes seen on MRI occur after $A\beta$

load has plateaued [78], suggesting that structural MRI is limited in the early detection of AD.

1.2.5.2 Positron Emission Tomography

Insight in the early stages of AD may instead be gained by measuring brain metabolism, since metabolic changes may precede changes in cellular microstructure, neuronal density, and neuronal loss [79, 78, 80]. One common technique used to measure brain metabolism is positron emission tomography (PET). PET imaging involves the injection of a biologically active radiotracer. The radiotracer emits a positron that interacts with an electron to emit a pair of 511 keV γ -rays in opposite directions. Coincident detection of the γ -rays enables the reconstruction of the location and concentration of the radiotracer.

One of these radiotracers is the glucose analog, fluorodeoxyglucose (FDG). Since the brain uses glucose as a major energy source, FDG uptake in the brain correlates with brain metabolism. FDG-PET studies have shown progressive hypometabolism in the AD brain, beginning with parietotemporal association cortices, posterior cingulate, and precuneus regions and progressing to the frontal association cortices [81]. These patterns of FDG uptake have also proven useful in discriminating those with AD from those with other dementias and those who are healthy [82, 83]. FDG-PET is also useful in predicting the conversion from MCI to AD, performing slightly better than structural MRI measurements [84].

Other PET tracers can target the neuropathology of AD directly. Approved agents that target fibrillar $A\beta$ plaques include Pittsburgh Compound B (PiB), florbetapir, flutemetamol, and florbetaben. Studies using these agents have shown extensive $A\beta$ deposition in Alzheimer's disease [85, 86, 87, 88] with good correspondence between patterns of tracer uptake and $A\beta$ load evaluated post-mortem [89, 90, 87, 91]. Patterns of $A\beta$ uptake appear to change and then plateau before the appearance of clinical symptoms [78]. This suggests that $A\beta$ -PET may have utility in the early detection of AD, but not in tracking disease progression. Indeed, $A\beta$ -tracer uptake is not well correlated with the severity of AD [86,

92, 62]. A β -PET may be further limited as an estimated 20-30% of cognitively normal elderly have significant A β load as measured by PET [93, 77]. To address this drawback, PET tracers that target NFTs have been developed. Patterns of tracer uptake using quinolone derived PET tracers such as [^{18}F]THK-5105 have been shown to be associated with AD severity and brain atrophy [94].

1.2.5.3 Magnetic Resonance Spectroscopy

A less expensive, more accessible, and non-invasive method to measure *in vivo* brain metabolism in AD is proton magnetic resonance spectroscopy (^1H -MRS) [95]. Like structural MRI, ^1H -MRS is a technique that excites protons using RF energy and measures the emitted RF signal as the excited protons return to equilibrium. However, ^1H -MRS is capable of detecting not just the protons of water, but also the protons of biologically active metabolites. This allows ^1H -MRS to simultaneously measure levels of several metabolites relevant to neuronal function in specific brain regions. Metabolites visible to ^1H -MRS and most relevant to AD include *N*-acetylaspartate (NAA), glutamate (Glu), and *myo*-inositol (Myo).

1.2.5.3.1 *N*-acetyl Aspartate (NAA)

NAA is a free amino acid present in the brain at *in vivo* concentrations of between 7.5–17 mM, and appearing as a prominent resonance at 2.01 ppm on a ^1H -MRS spectrum [96]. It is synthesized in neurons by *N*-acetyltransferase-8 like protein (NAT8L) from acetyl-coenzyme A (acetyl CoA) and aspartate [97, 98]. NAA synthesis occurs mostly in the cytoplasm and requires acetyl CoA levels in excess of neuronal metabolic requirements [98]. NAA synthesis also occurs in the mitochondria [98, 99], and NAA levels can be lowered by inhibition of mitochondrial respiration [100]. Together, this suggests that low NAA levels may reflect neuronal loss, mitochondrial dysfunction and low neuronal energy reserves.

Since cerebral atrophy (see Section 1.2.5.1), mitochondrial dysfunction (see Section 1.2.2.3) and hypometabolism (see Section 1.2.5.2) have been reported in AD, it is unsurprising that NAA concentrations are decreased in MCI and AD compared to cognitively normal elderly controls [101, 102, 103, 104]. NAA levels appear to decline as the disease progresses [105] and are correlated with performance on cognitive tests in AD [106], suggesting that NAA levels could be a biomarker of AD progression.

NAA levels could also be markers of treatment response, as they have been reported to improve after treatment with rivastigmine [107] and donepezil [108], which are acetylcholinesterase inhibitors. Acetylcholinesterase inhibitors prevent the breakdown of acetylcholine in the synapse, which may reduce the rate of acetylcholine production by cholinergic neurons. Since acetylcholine is also derived from acetyl CoA [109], reduced acetylcholine production would result in more acetyl CoA available for both neuronal metabolism and NAA production. In this way, successful treatment with acetylcholinesterase inhibitors could result in increased NAA levels.

Other functions of NAA include its involvement in myelination. NAA is catabolized in oligodendrocytes by the sequential action of aspartoacylase II (ASPA-II) and acetyl CoA synthetase-1 (AceCS-1) into acetyl CoA, which is then used by the oligodendrocytes for the synthesis of myelin-associated lipids [110]. Thus, decreased NAA levels could negatively affect myelination processes. This is supported by the finding of decreased NAA in the demyelinated plaques of multiple sclerosis [111]. NAA is also a known osmolyte, with the redistribution of NAA from the intracellular to extracellular compartment being a mechanism by which neurons protect themselves against hypo-osmotic stress [112].

1.2.5.3.2 Glutamate

Glutamate is the primary excitatory neurotransmitter in the brain [113, 114], including in the hippocampus, a region of the brain that is highly dependent on glutamate signalling

[115]. It is present in the healthy brain in concentrations ranging from 6.0–12.5 mM and appears on a ^1H -MRS spectrum as two multiplets in the range of 2.0–2.5 ppm and a doublet of doublets at 3.74 ppm [96]. Detection of glutamate using ^1H -MRS is complicated by the fact that its resonances overlap with those of glutamine and macromolecules, but is possible with the appropriate selection of acquisition parameters such as echo time [116, 117, 118].

Measurement of glutamate using ^1H -MRS is of interest in AD, as dysfunction of the glutamatergic system is a large part of the neuropathology of AD (see Section 1.2.2.3). Briefly, impaired glutamate reuptake from the synapse and chronic activation of NMDARs and mGluRs lead to calcium dysregulation and eventual long-term synaptic depression, reduced glutamatergic transmission, and synaptic loss in AD. This process is reflected by decreases in glutamate concentration in AD as measured by ^1H -MRS [101, 118], since ^1H -MRS measures of glutamate reflect glutamatergic activity [119]. Decreased glutamate could also reflect neuronal hypometabolism and energy deficit in AD. The reason for this is two-fold: (1) glutamatergic neuronal activity is intimately coupled with neuronal metabolism [120] and (2) glutamate can be used as a substrate for energy production in a truncated tricarboxylic acid (TCA) cycle during energy depleted states [121, 122]. Additionally, glutamate levels could be related to reductions in synaptic density as well as the balance between excitatory and inhibitory synaptic activity [123].

The intimate involvement of glutamate with neuropathological mechanisms in AD suggests that changes in glutamate level could reflect responses to interventions that affect these mechanisms. Indeed, changes in glutamate concentrations as measured by ^1H -MRS have been reported in response to galantamine treatment and were correlated to cognitive performance [124].

1.2.5.3.3 *myo*-Inositol

myo-Inositol is a cyclic sugar alcohol present in the brain at concentrations of 4.0-9.0 mM and is visible on an ^1H -MRS spectrum as multiplets centred around 3.5 ppm [96]. The main role of *myo*-inositol is its involvement in the intracellular secondary messenger signalling system. It is the precursor to the membrane phospholipid phosphatidylinositol which is converted to InsP_3 by phospholipase C when receptors such as mGluRs are activated [125, 126]. InsP_3 then goes on to facilitate intracellular calcium release from the endoplasmic reticulum, before being metabolised back into *myo*-inositol [125].

Since increased InsP_3 signalling may be a contributor to calcium dysregulation in AD (see Section 1.2.2.3), metabolism of InsP_3 may also be increased, suggesting that there may be increased intracellular concentrations of *myo*-inositol in AD. Indeed, ^1H -MRS studies have shown increases in *myo*-inositol concentration in the AD brain [127, 128, 129]. Though neurons maintain a high intracellular concentration of *myo*-inositol [130], increased *myo*-inositol levels have also been associated with glial proliferation [111] and may also reflect neuroinflammatory processes in AD.

1.2.5.3.4 Choline

The strong resonance at 3.2 ppm on a ^1H -MRS spectrum comes from free choline and the choline containing compounds glycerophosphorylcholine (GroPCho), and phosphorylcholine (PCho) even though the total brain concentration of choline is quite low (1-2 mM) [96]. GroPCho and PCho are the metabolic products of phosphatidylcholine, a membrane phospholipid, that can be metabolised into free choline by various phospholipases into free choline, which is further converted to acetylcholine [131]. Thus, GroPCho and PCho are in equilibrium with both phosphatidylcholine and acetylcholine. As a result, the choline resonance measured on ^1H -MRS is correlated with acetylcholine levels in the brain [132], but may be altered by changes in membrane phospholipid turnover.

In AD, increases in choline levels as measured by ^1H -MRS have been reported [133, 134, 135]. This may seem counter-intuitive as there is a deficiency of acetylcholine in AD (see Section 1.2.2.2 and 1.2.4). Furthermore, AD-associated hypometabolism may also impair brain synthesis of choline [136]. To understand this apparent inconsistency, it is important to remember that the choline resonance in ^1H -MRS has contributions from GroPCho and PCho. Acetylcholine deficiency and impaired choline synthesis could shift the choline equilibrium, upregulating phosphatidylcholine breakdown into GroPCho and PCho, thereby promoting their metabolism into free choline. This compensatory mechanism would result in an increased ^1H -MRS choline signal. Indeed, membrane breakdown is known to occur in chronic neurodegeneration [137] and has been proposed as a way for the AD brain to compensate for declining acetylcholine [138].

1.2.5.3.5 The Metabolic Profile of AD

If ^1H -MRS is to be used to aid in diagnosis and staging of AD, changes in metabolite levels observed in AD should be specific to AD. However, decreased NAA, increased Myo, and increased Cho have also been reported in other dementias such as vascular dementia (VaD), Lewy body dementia (DLB), or frontotemporal dementia (FTD). Differentiating AD from these other dementias requires consideration of both the degree of the metabolic changes and the spatial pattern of the metabolic changes. For example, increased Myo levels and decreased NAA levels are also observed in FTD, but individuals with FTD have greater Myo increases and NAA decreases in the frontal lobe as compared to individuals with AD [139]. In VaD, NAA levels are also decreased, but NAA levels of those with VaD are greater than those with AD in the occipital lobe [140]. Comparisons of AD with VaD also show greater posterior cingulate cortex Myo levels in AD than in VaD [133]. Similarly, although NAA levels in DLB are also decreased in regions like the hippocampus and the parasagittal cortex [141, 142], NAA levels are preserved in the posterior cingulate cortex in DLB, while in AD they are not.

1.2.6 Neuropsychological Testing in Alzheimer's Disease

Assessing memory and cognition with neuropsychological testing is a crucial part of AD assessment in both the clinical and research domains. Though the neuropsychological profile of AD includes deficits in language and semantic memory, executive function, working memory, and visuospatial processing [143], episodic memory impairment is among the earliest and most severe cognitive changes in AD [144] and is considered the most clinically relevant for assessing AD patients [145].

The episodic memory system is responsible for the encoding and retrieval of personal experiences [146], and is associated with autonoetic awareness where a memory is framed in a personal context and is retrieved via mental re-enactment [147, 148]. Brain structures underlying this system include the hippocampus, entorhinal and perirhinal cortices, the retrosplenial and posterior cingulate cortex, and other structures of the Papez circuit [149, 146, 150]. Over the course of AD, NFTs spread along these structures (see Section 1.2.2.2), causing progressive episodic memory dysfunction.

Dysfunction of the episodic memory system results in decreases in the ability to learn new information and to recall recently learned information [146]. Thus, common assessments of episodic memory involve testing how well an individual learns new information and recalls it after a delay. Such assessments include the logical memory subtest of the Wechsler Memory Scale [151] and the Rey-Osterrieth complex figure copy test [152, 153]. In the logical memory test, participants are read a short story and are asked to recall the story immediately, and after a short delay. In the complex figure copy test, participants are shown a specially-designed figure that resembles no existing object and are asked to reproduce the figure. Then, after a short delay participants are asked to reproduce the figure from memory. The delay used in these tests are typically 15-20 minutes. Variations of these tests, such as the Craft Story 21 Recall [154] and the Benson Complex Figure Copy [155], are included in standardized neuropsychological batteries used for AD research. One such

battery is the National Alzheimer's Coordinating Centre Neuropsychological Battery [156].

Episodic memory function in an AD patient may also be assessed by asking a collateral source (i.e. a family member or close friend of the patient's) about the details of a recent salient personal experience, such as a vacation or wedding. Once the details of the experience are obtained, the patient is then asked to recall the experience. The accuracy of the recall gives a physician or researcher insight into the patient's episodic memory function. This type of assessment may be done formally as part of the Clinical Dementia Rating Scale (CDR) [157], a tool often used clinically to stage Alzheimer's disease, or informally as part of a collateral history taken by the physician. The CDR also includes tests of memory and problem solving, as well as questions about orientation to time and place and activities of daily living. This provides valuable information to the clinician about deficits of other cognitive domains beyond episodic memory, and the severity of AD.

Other tools used clinically to assess memory and cognition include the Mini-Mental State Examination (MMSE) [158] and the Montreal Cognitive Assessment (MoCA) [159]. The MMSE is a brief assessment of general cognitive function, while the MoCA is more comprehensive. The MoCA includes specific tasks that assess memory recall, visuospatial abilities, attention, concentration, working memory, and language. Attention and problem solving may be further assessed using the Trail Making Test [160]. In the first part of this test, participants are asked to connect 25 numbered circles distributed over a sheet of letter paper as quickly as possible in ascending numerical order. In the second part of this test, the circles contain either numbers or letters, and the participant must connect the circles as quickly as possible while alternating between numbers and letters.

Finally, it is important to assess whether an AD patient has any associated psychiatric symptoms, such as depression. This can be done by the clinician via a detailed social and medical history, and with the help of tools such as the Geriatric Depression Scale [161].

1.2.7 Transgenic Mouse Models of Alzheimer's Disease

In order to examine the temporal progression of AD and to evaluate therapies in a highly controlled manner, researchers have developed a plethora of genetically engineered mouse models of AD. Though the range of neuropathology and behavioural phenotypes expressed in AD mouse models are highly variable, every credible mouse model of AD exhibits progressive neuropathology of at least one neuropathological hallmark of AD, as well as robust cognitive changes that are evident in different behavioural testing paradigms targeting memory systems that involve brain structures affected in AD, such as the hippocampus [162]. These mouse models may be categorized by the AD neuropathology they aim to replicate: models that have amyloid pathology, models that have tau pathology, and models that express both.

Transgenic mouse models with amyloid pathology are based on our current understanding of the genetics of Alzheimer's disease, namely the APP, PS1, and PS2 mutations that are implicated in familial AD (see Section 1.2.2.1). Engineering mice that overexpress mutant APP results in mice that develop A β plaques and cognitive impairment [163]. Progressive synapse loss, gliosis, and neurochemical changes that model aspects of AD observed in humans have also been reported [164]. A commonly used APP mutation is the Swedish double mutation (K670N/M671L) usually referred to as APP_{Swe}, first used by Hsiao *et al* [165] to generate the Tg2576 transgenic mouse model. In the Tg2576 model, deficits of spatial memory as measured by the Morris water maze [166] were evident by 9–10 months, accompanied by elevated levels A β oligomers. Plaques were seen by 12 months of age. Although the original study did not demonstrate neuronal loss, subsequent studies have shown both impaired synaptic plasticity [167] and synaptic loss [168].

PS1 and PS2 mutations have also been used to generate AD mouse models with less success. This is because mice that overexpress PS1 and PS2 mutations elevate levels of A β oligomers but don't result in plaque formation [169]. However, when presenilin transgenic

mice are crossed with transgenic APP mice, extensive plaque formation is exhibited [170, 171]. These double transgenic mice produced using familial AD mutations (2xFAD) are widely used in the study of AD. The 2xFAD mice used for investigations in this thesis are APP_{Swe}/PS1 Δ E9 mice that contain both the APP_{Swe} mutation and the PS1 gene without exon 9. A β plaque deposition and concomitant astrocytosis begins as early as 4 months in the APP_{Swe}/PS1 Δ E9 model and plateaus at 12 months [172]. When compared to wild-type mice, spatial memory deficits are not apparent at 7 months of age [173], but appear at 11-12 months of age [174, 175]. The temporal pattern of A β deposition plateauing before the appearance of cognitive deficit mirrors the progression of AD in humans.

A major aspect of AD in humans that the APP_{Swe}/PS1 Δ E9 model – or APP transgenic mice in general – are unable to replicate is the presence of NFTs in the brain [163]. Development of AD mouse models that exhibit tau pathology has been hampered by the fact that the microtubule associated protein tau (MAPT) gene, implicated in other dementias with tauopathies, does not appear to be causally related to AD [176]. Nevertheless, MAPT mutations on chromosome 17 responsible for familial multiple system tauopathy with pre-senile dementia [177] have been used to create mouse models such as JNPL3 that develop NFTs as a function of age [178]. However, JNPL3 and other tau transgenic mice do not exhibit A β plaques [163].

To enable the study of interactions between A β and tau, transgenic mice with APP, pre-senilin, and tau mutations have been created [179]. These 3xFAD mice develop A β plaques, NFTs, synaptic alterations, and cognitive deficits as a function of age [179, 180].

Though transgenic mouse models of AD have been useful for the study of AD, they have some limitations. First, transgenic mouse models are based on genetic mutations implicated in familial AD. Since individuals with sporadic AD do not possess APP, PS1, PS2, or MAPT mutations, it is unclear whether or not these mice are accurately modelling all aspects of sporadic AD. Furthermore, there is a discrepancy in the temporal progression of the disease, with 2xFAD mice developing pathology over the course of a year, whereas

humans develop pathology over the course of decades. As such, ageing effects on the progression of AD may not be properly represented by mouse models. Finally, human brains appear to be more susceptible to AD pathology than mouse brains. For example, APP levels have to be 8 times normal for $A\beta$ plaques to develop in mice, whereas humans only need a 2-fold increase [181]. These differences between modelled AD pathology and actual AD pathology are important to consider when translating and applying knowledge gained from the study of transgenic mice to humans.

1.3 Principles of Magnetic Resonance

The physical phenomenon of nuclear magnetic resonance arises from the quantum mechanical properties of the protons and neutrons that make up atomic nuclei. In proton magnetic resonance imaging and spectroscopy, the nucleus of interest is ^1H , and the main magnetic field of the MR scanner, \vec{B}_0 , is oriented along the z -axis. The probability that a ^1H nucleus is in an energy state where the longitudinal component of its magnetic moment (μ_z) is aligned with \vec{B}_0 determines the net magnetic moment of an ensemble of ^1H nuclei, \vec{M}_0 , also called the equilibrium magnetization. For more details, see Appendix A.

1.3.1 Excitation and Adiabatic Pulses

The manipulation of \vec{M}_0 is called excitation and involves the application of another magnetic field, \vec{B}_1 , that lies in the \hat{x}, \hat{y} -plane with frequency ω . In other words, \vec{B}_1 is perpendicular to \hat{z} and rotates about \hat{z} with frequency ω . Since \vec{B}_1 is rotating about \hat{z} at ω , the motion of \vec{M}_0 in the presence of \vec{B}_1 may be more simply described in a frame of reference $(\hat{x}', \hat{y}', \hat{z}')$ that also rotates about \hat{z} at ω . The motion of \vec{M}_0 is described by the Bloch equation, which is

$$\frac{\delta \vec{M}}{\delta t} = \gamma \vec{M}_0 \times \left(\frac{\omega_0 - \omega}{\gamma} \hat{z}' + B_1 \hat{x}' \right) = \gamma \vec{M}_0 \times \vec{B}_{\text{eff}} \quad (1.1)$$

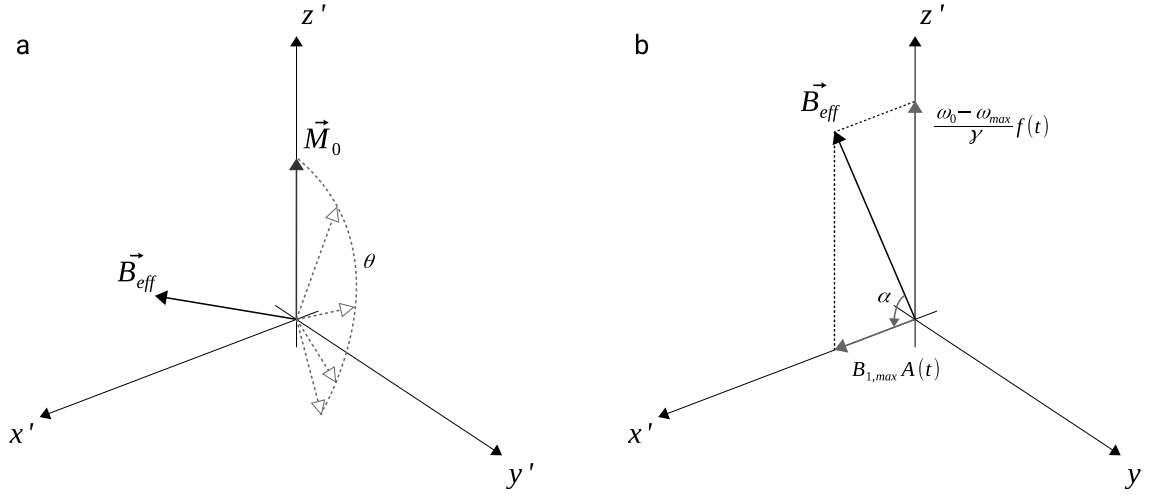


FIGURE 1.1: Excitation in the rotating frame $(\hat{x}', \hat{y}', \hat{z}')$ (a) The effective field, \vec{B}_{eff} created by the applied \vec{B}_1 field exerts a torque on \vec{M}_0 resulting in the rotation of \vec{M}_0 about \vec{B}_{eff} . (b) If the adiabatic condition, $\left| \frac{d\alpha}{dt} \right| \ll \gamma \left| \vec{B}_{\text{eff}}(t) \right|$, is met, \vec{M}_0 remains parallel with \vec{B}_{eff} . Then, \vec{M}_0 may be manipulated by manipulating \vec{B}_{eff} via frequency modulation ($f(t)$) and amplitude modulation ($A(t)$) of applied \vec{B}_1 pulse.

in the rotating frame. \vec{B}_{eff} is the effective field in the rotating frame created by the applied \vec{B}_1 . This effective field exerts a torque on \vec{M}_0 , resulting in the rotation of \vec{M}_0 about \vec{B}_{eff} (Figure 1.1a). The angle through which \vec{M}_0 rotates is the flip angle, θ :

$$\theta = \gamma \int_0^T B_{\text{eff}}(t) dt \quad (1.2)$$

where T is the duration of application of \vec{B}_1 .

Since conventional human and animal MRI scanners use magnetic fields on the order of several Tesla, the precession frequency of \vec{M}_0 lies in the radio-frequency (RF) range (Equation (A.9)). As a result, RF pulses are used to generate the \vec{B}_1 fields needed for excitation. The amplitude of the RF pulse is equal to B_1 , the amplitude of the \vec{B}_1 field, while the frequency of the RF pulse is equal to ω , the frequency of the \vec{B}_1 field. Both the amplitude and frequency components of the RF pulse may be modulated, but conventional RF pulses only use amplitude modulation, with the frequency held constant. Typically, on-resonance

1.3. Principles of Magnetic Resonance

excitation is desired, and ω is set equal to ω_0 .

Adiabatic RF pulses, which are often used in high-field magnetic resonance spectroscopy, use both amplitude and frequency modulation, resulting in the following components for \vec{B}_{eff} :

$$\vec{B}_{\text{eff}} = \frac{\omega_0 - \omega_{\text{max}}}{\gamma} f(t) \hat{z}' + B_{1, \text{max}} A(t) \hat{x}' \quad (1.3)$$

where $f(t)$ and $A(t)$ are the normalized frequency and amplitude modulation functions, respectively. At the beginning of an adiabatic pulse, the frequency modulation is large, the amplitude modulation is small and \vec{B}_{eff} is aligned with \hat{z}' . As time passes, the frequency modulation decreases, the amplitude modulation increases, and \vec{B}_{eff} rotates towards the \hat{x}', \hat{y}' -plane (Figure 1.1b). Once \vec{B}_{eff} has rotated through an angle $\alpha = 90^\circ$, a half passage is complete. Then, the frequency modulation increases again, the amplitude modulation decreases, and \vec{B}_{eff} rotates towards $-\hat{z}'$. Once \vec{B}_{eff} is aligned with $-\hat{z}'$ and $\alpha = 180^\circ$, a full passage is complete. In this scheme, \vec{M}_0 begins parallel with \vec{B}_{eff} . If the adiabatic condition, $\left| \frac{d\alpha}{dt} \right| \ll \gamma \left| \vec{B}_{\text{eff}}(t) \right|$, is satisfied throughout the pulse and the pulse length is short relative to T_1 and T_2 relaxation (see Section 1.3.2), \vec{M}_0 remains parallel with \vec{B}_{eff} throughout the pulse. In this way, \vec{M}_0 may be manipulated by an adiabatic RF pulse.

1.3.2 Relaxation

After excitation, \vec{M}_0 undergoes relaxation, which occurs due to energy transfer. Energy may transfer from the hydrogen nuclei (the 'spins') to the surrounding environment (the 'lattice') resulting in spin-lattice relaxation, also called T_1 relaxation. This energy transfer depends mainly on the motion of the neighbouring molecules and is most efficient when the average rate of motion is at ω_0 . \vec{M}_0 will return to its original equilibrium state via T_1 relaxation.

Relaxation may also occur due to dynamic interactions between the hydrogen nuclei without energy transfer to the lattice. This type of relaxation is called spin-spin relaxation or T_2 relaxation and causes the loss of phase coherence between nuclei. Loss of phase coherence between nuclei can also be a result of spatial variation in \vec{B}_0 (i.e. static field inhomogeneity). This type of relaxation is called T_2' relaxation. The combined effect of T_2 and T_2' relaxation is called T_2^* relaxation.

The motion of \vec{M}_0 during relaxation is best described by the Bloch equation in the rotating frame (Equation (1.1)). When written in terms of the components of \vec{M} , Equation (1.1) becomes:

$$\frac{dM_{x'}}{dt} = (\omega_0 - \omega)M_{y'} - \frac{M_{x'}}{T_2^*} \quad (1.4)$$

$$\frac{dM_{y'}}{dt} = -(\omega_0 - \omega)M_{x'} - \frac{M_{y'}}{T_2^*} \quad (1.5)$$

$$\frac{dM_{z'}}{dt} = \frac{M_0 - M_{z'}}{T_1} \quad (1.6)$$

with solutions:

$$M_{x'}(t) = e^{-t/T_2^*} (M_{x'}(0) \cos((\omega_0 - \omega)t) + M_{y'}(0) \sin((\omega_0 - \omega)t)) \quad (1.7)$$

$$M_{y'}(t) = e^{-t/T_2^*} (M_{y'}(0) \cos((\omega_0 - \omega)t) - M_{x'}(0) \sin((\omega_0 - \omega)t)) \quad (1.8)$$

$$M_{z'}(t) = M_{z'}(0)e^{-t/T_1} + M_0(1 - e^{-t/T_1}) \quad (1.9)$$

where M_0 is the magnitude of the magnetization in its original equilibrium state; M_x , M_y , M_z are the components of the magnetization after excitation; $t = 0$ is the instant in time immediately after excitation; T_1 is the spin-lattice relaxation time constant; and T_2^* is the time constant due to combined effects from spin-spin interaction (T_2) and excitation field

inhomogeneity (T_2'). T_2^* is defined by the following relation:

$$\frac{1}{T_2^*} = \frac{1}{T_2} + \frac{1}{T_2'} \quad (1.10)$$

Relaxation processes are important to consider because the relaxation time constants of water and metabolites affect the choice of various parameters during imaging and spectroscopy. Specifically, T_1 affects the choice of repetition time (TR) and T_2 affects the choice of echo time (TE). TR should be long enough to avoid signal saturation due to incomplete T_1 relaxation, while TE should be short enough to avoid T_2 related signal loss.

Assuming on-resonance excitation ($\omega_0 - \omega = 0$), Equations (1.7) and (1.8) can be simplified and combined to describe the evolution of the magnetization in the transverse plane (the \hat{x}', \hat{y}' -plane):

$$M_{x'y'}(t) = M_{x'y'}(0)e^{-t/T_2^*} \quad (1.11)$$

Since coils used for MR imaging are typically designed such that the sensitivity profile is optimized to detect magnetization in the transverse plane, $M_{x'y'}$ is the source of the detected MR signal. This detected signal is called the free induction decay (FID) signal.

1.3.3 Spatial Encoding

In order to form an image of an object with an MRI, spatial information is encoded in the measured FID signals by adding linear gradients to the main magnetic field, \vec{B}_0 :

$$\vec{G}(t) = \frac{d\vec{B}_z(t)}{d\vec{r}} \quad (1.12)$$

where $\vec{B}_z(t) = \vec{B}_0 + \vec{G}(t) \cdot \vec{r}$, and \vec{r} is the direction of \vec{B}_z variation. At each instant in time, the linear gradients impose a spatially dependent phase pattern on the spins:

$$\phi(\vec{r}, t) = -\gamma \int_0^t \vec{G}(\tau) d\tau \cdot \vec{r} \quad (1.13)$$

$$= -2\pi \vec{k}(t) \cdot \vec{r} \quad (1.14)$$

The resulting effect is that all components in the object with the spatial frequency corresponding to the phase pattern are now in phase and the recorded signal is sensitized to that particular spatial frequency. This spatial frequency is described by the parameter, \vec{k} , which is defined as follows:

$$\vec{k}(t) = \frac{\gamma}{2\pi} \int_0^t \vec{G}(\tau) d\tau \quad (1.15)$$

Each point in the space of \vec{k} corresponds to a different spatial frequency. When linear gradients are present, k -space is traversed, different spatial frequencies are sampled, and a frequency domain representation of the object is acquired. An image of the object can be obtained by performing an inverse Fourier transform of the acquired data.

1.4 Proton Magnetic Resonance Spectroscopy

In the studies presented in this thesis, single-voxel proton magnetic resonance spectroscopy (^1H -MRS) is used to non-invasively measure the levels of metabolites *in vivo* from a particular brain region. The details of this technique are briefly described in the present section.

1.4.1 Chemical Shift and J-Coupling

In MR imaging, the signal from the hydrogen nuclei of water is measured. In contrast, ^1H -MRS detects the signals from hydrogen nuclei present in metabolites. Since metabolites

have a different chemical structure than water, the hydrogen nuclei in these molecules experience a different local chemical environment.

Specifically, the chemical structure of a metabolite determines the electron distribution around a hydrogen nucleus. In an external magnetic field, \vec{B}_0 , electrons are in motion. Since electrons have charge, their motion produces an induced magnetic field, \vec{B}_{ind} . This induced magnetic field determines the local effective magnetic field at the nucleus, \vec{B}_{loc} :

$$\vec{B}_{\text{loc}} = \vec{B}_0 - \vec{B}_{\text{ind}} = \vec{B}_0(1 - \sigma) \quad (1.16)$$

where σ is a constant that depends on the chemical environment of the nucleus. This effect is called electron shielding. As a result, these nuclei resonate at a different frequency than that of the hydrogen nuclei in water. This frequency offset is called the chemical shift, which has dimensionless units of ppm and is defined as:

$$\delta = \frac{\nu - \nu_{\text{ref}}}{\nu_{\text{ref}}} \times 10^6 \quad (1.17)$$

Although the reference frequency, ν_{ref} , can be set to the frequency of water, a 3-trimethylsilyl propionate (TSP) is more typically used as the reference compound in ^1H -MRS. The reference compound is assigned $\delta = 0$ ppm.

Since hydrogen nuclei have different chemical shifts, plotting their signals with respect to chemical shift allows us to visualise a pattern of peaks along a ppm axis, or more simply, a spectral pattern. Since the chemical shifts of the hydrogen nuclei are determined by the chemical structure of the metabolite, each metabolite has a characteristic spectral pattern.

This spectral pattern can be complicated by spin-spin interactions between hydrogen nuclei in a molecule called J-coupling. J-coupling is a phenomena where the electron shielding of a nucleus is indirectly affected by the magnetic moment of neighbouring nuclei through chemical bonds, resulting in changes in the local field at the nucleus (Equation (1.16)). This depends on the spin orientations of the neighbouring nuclei. Thus, different

combinations of electron shielding effects can manifest locally at the nucleus. This can result in a single peak at δ being split into multiple sub-peaks with slightly different frequency shifts (Equation (1.16)). A coupling constant, J , simply defined as the frequency shift difference between these sub-peaks, can be used to quantify the coupling effect.

Peak splitting behaviour is predictable if spins are weakly coupled (i.e. $\frac{J}{|\nu_A - \nu_X|} \gg 1$ for nuclei A and X). An example of a weakly coupled spin system is lactate (Figure 1.2a). What would have been a single peak at 1.3 ppm from the methyl ($^3\text{CH}_3$) hydrogens and a single peak at 4.2 ppm from the methine (^2CH) hydrogen without J-coupling splits into a doublet and a quadruplet, when J-coupling is present (Figure 1.2b).

Consider the doublet methyl signal at $\nu_a = 1.3$ ppm. The hydrogens of the methyl group, H_a are weakly coupled to the neighbouring hydrogen of the methine group H_b with a coupling constant $^3J_{H_aH_b}$. The electron shielding experienced at H_a depends on the nuclear spin orientation of H_b . H_b may be in a spin-up state (parallel with \vec{B}_0 or in a spin-down state (anti-parallel with \vec{B}_0). Via Fermi contact and the Pauli exclusion principle, the spin-up state of H_b results in less electron shielding and a greater local field at H_a , leading to a peak at a slightly higher frequency, $\nu_a + \frac{^3J_{H_aH_b}}{2}$ (Figure 1.2c). Similarly, the spin-down state of H_b results in more electron shielding and a lower local field at H_a , leading to a peak at a slightly lower frequency $\nu_a - \frac{^3J_{H_aH_b}}{2}$. These two peaks comprise the methyl doublet observed at $\nu_a = 1.3$ ppm and have an amplitude ratio of 1:1. The fact that an aligned, spin-up state at the coupled nucleus leads to less electron shielding locally, and that an anti-aligned, spin-down state at the coupled nucleus leads to more electron shielding locally, can be extended to explain the observation of methine quadruplet observed at $\nu_b = 4.2$ ppm (Figure 1.2d). This quadruplet has an amplitude ratio of 1:3:3:1. In general, if the weak coupling condition, $\frac{J}{|\nu_A - \nu_X|} \gg 1$, is satisfied, a nucleus coupled to n neighbouring peaks will appear as a multiplet with $n + 1$ peaks in an amplitude ratio defined by Pascal's triangle (1:1, 1:2:1, 1:3:3:1, etc.).

For a strongly coupled spin system, where $\frac{J}{|\nu_A - \nu_X|} \approx 1$, the splitting behaviour is not

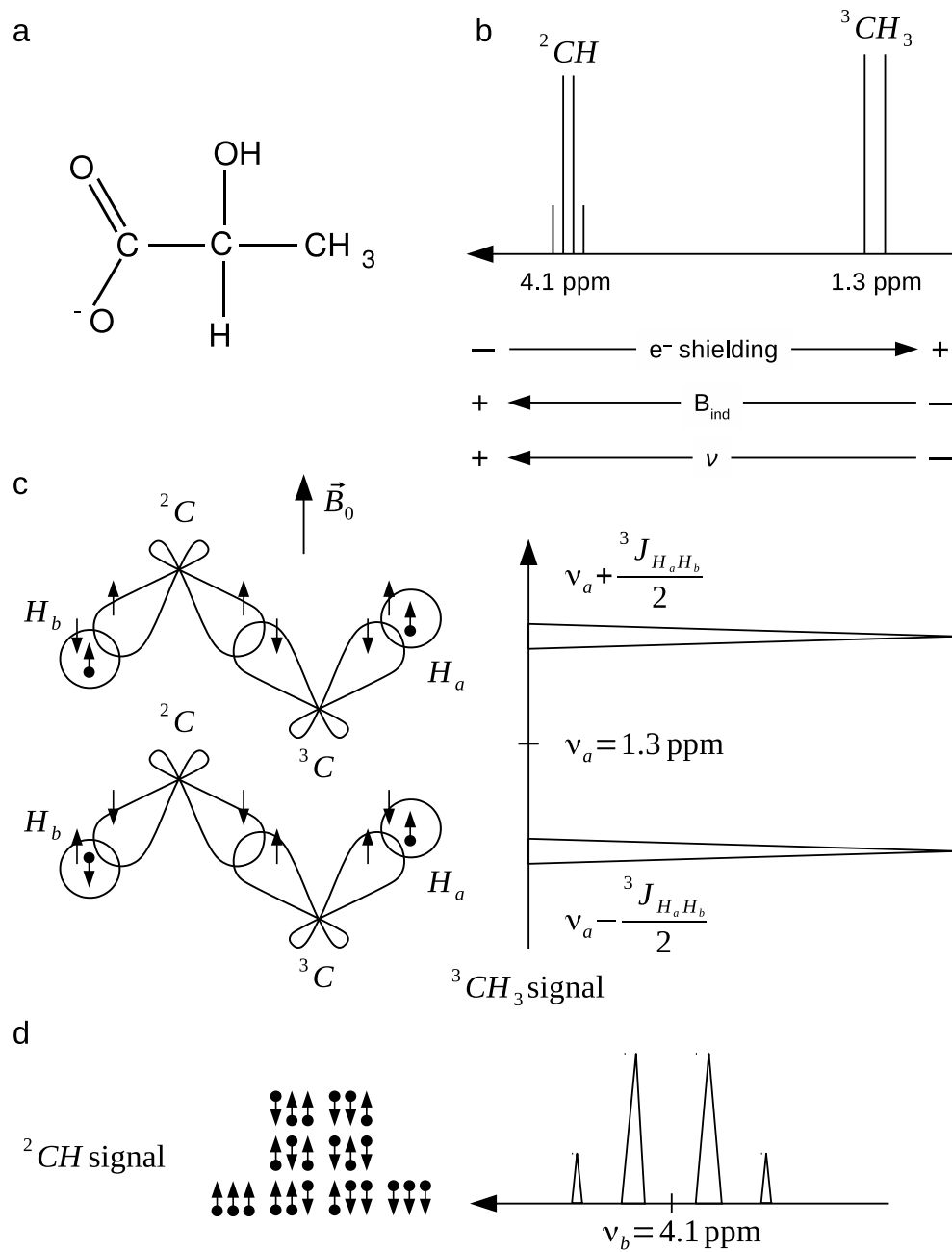


FIGURE 1.2: (a) The lactate molecule consists of an acetyl group at 1C , a methine group at 2C , and a methyl group at 3C . (b) The characteristic 1H -MRS spectrum of lactate consists of a doublet at 1.3 ppm from the methyl group and a quadruplet at 4.2 ppm from the methine group.

FIGURE 1.2: (c) Consider the doublet at $\nu_a = 1.3$ ppm. The hydrogens, H_a , from the methyl group are coupled to the hydrogen, H_b , from the methine group with coupling constant $^3J_{H_aH_b}$. The nuclear spin orientation of H_b may be aligned with \vec{B}_0 (spin-up) or anti-aligned (spin-down). Via Fermi contact, a spin-up nuclear spin orientation leads to an energetically favoured spin-down orientation for H_b 's electron spin. This electron spin orientation sets the orientations of the electron spins in the downstream chemical bonds via Pauli's exclusion principle, resulting in a spin-up electron spin orientation at H_a . Since this electron spin orientation is aligned with \vec{B}_0 , there is less electron shielding, a greater local field, and a peak at a higher frequency of $\nu_a + \frac{^3J_{H_aH_b}}{2}$. In the same way, a spin-down nuclear orientation of H_b leads to a spin-down electron spin orientation at H_a , resulting in more electron shielding, a lower local field, and a peak at a lower frequency of $\nu_a + \frac{^3J_{H_aH_b}}{3}$. These two peaks comprise the doublet and are in a 1:1 amplitude ratio. (d) Consider the quadruplet at $\nu_b = 1.4$ ppm, where the methine hydrogen is coupled to 3 methyl hydrogens. Using the same explanation as in (c), an aligned, spin-up state at a methyl hydrogen leads to less electron shielding at the methine hydrogen, and an anti-aligned, spin-down state at a methyl hydrogen leads to more electron shielding at the methine hydrogens. There are four magnetically distinct nuclear spin configurations for the 3 methyl hydrogens, resulting in four levels of electron shielding at the methine hydrogens, and a quadruplet of peaks in a 1:3:3:1 amplitude ratio.

intuitive, does not follow Pascal's triangle, and requires more complicated mathematics to describe (see Appendix B). However, whether or not J-coupling is strong or weak, it results in a few undesirable effects:

1. If there is a time-dependence to the J-coupling (e.g. chemical exchange), then J-coupling results in time-dependent fluctuations in the local magnetic field environment of nuclei and can therefore be a source of spin-spin relaxation.
2. J-coupling manifests as a frequency shift along the ppm axis, which leads to overlapping of peaks from different metabolites *in vivo*, complicating the process used to determine the concentration of metabolites from the spectrum.
3. J-coupling results in peak splitting, which effectively reduces the amplitudes of the peaks and decreases the SNR.

1.4.2 Water Suppression

In high quality ^1H -MRS data, the amplitudes of the peaks that comprise the spectrum of a metabolite reflect the metabolite's concentration. In the brain, the concentration of metabolites are on the order of $\sim 1\text{-}15\text{ M}$, and appears as low amplitude peaks on an acquired ^1H -MRS spectrum. In contrast, the concentration of water is much greater – $\sim 45.2\text{ M}$ in grey matter (GM), $\sim 40.3\text{ M}$ in white matter (WM), and $\sim 54\text{ M}$ in cerebrospinal fluid (CSF) – and appears as a large resonance at 4.7 ppm. Artefacts present on such large resonances, such as gradient coil vibration signal modulation [182], can overlap with metabolite peaks, complicating their measurement. Thus, to consistently and reliably detect metabolite signals, water suppression is commonly used.

There are different methods used to suppress the water signal. The method used for the studies presented in this thesis combines frequency selective excitation and gradient dephasing. A series of narrow bandwidth RF pulses ($\sim \pm 0.5\text{ ppm}$) centred on the frequency of the water resonance are used excite the water magnetization. Each excitation pulse is followed by a strong crusher gradient that dephases the water magnetization. The result of this RF pulse train is the destruction of the water signal. The acquisition of the metabolite signals immediately follows the water suppression scheme.

The exact order, timing, and amplitude of the frequency-selective RF pulses determines the effectiveness of the water suppression scheme. The specific water suppression scheme used in the studies presented in this thesis consists of seven variable power RF pulses with optimized relaxation delays (VAPOR) [183] between the pulses. The RF pulse powers required for optimal water suppression is set by calibrating the nominal flip angle of the first RF pulse. VAPOR is insensitive to RF pulse power, and provides excellent water suppression for nominal flip angles between 65° and 125° .

1.4.3 Localization

In single-voxel ^1H -MRS of the brain, metabolite signals are localized to a specific voxel placed in a region of the brain by using successive selective excitation. Selective excitation involves the use of RF pulses in conjunction with linear gradients. As discussed in Section 1.3.3, linear gradients add to \vec{B}_0 and change the magnetic field that nuclear spins experience. By the Larmor equation (Equation (A.9)), nuclear spins that reside at different spatial positions will precess at different resonant frequencies. Thus, RF pulses paired with gradients may be used to excite nuclear spins at specific spatial locations by carefully setting the carrier frequency and bandwidth of the RF pulse.

It follows that the precision of spatially selective excitation depends on both the sharpness of the RF pulse frequency profile as well as the spatial homogeneity of both \vec{B}_0 and the applied RF field, \vec{B}_1 . At high-field, such as 4T and above, achieving \vec{B}_0 and \vec{B}_1 homogeneity becomes more challenging, but use of adiabatic RF pulses for localization can help to overcome this problem. With adiabatic pulses, as long as the adiabatic condition is well-fulfilled, nuclear spins will behave as expected even in the presence of magnetic field inhomogeneity. In other words, adiabatic pulses are insensitive to \vec{B}_0 and \vec{B}_1 inhomogeneity. Compared to traditional RF pulses, adiabatic pulses also have sharper frequency profiles and bandwidths independent of RF amplitude. Therefore, adiabatic RF pulses can achieve selective excitation with greater precision in high-field applications and are preferred for localization in high-field ^1H -MRS.

The most common localization method in high-field ^1H -MRS that utilizes adiabatic RF pulses is the localization by selective refocusing (LASER) method [184]. The LASER pulse sequence begins with a non-selective adiabatic half passage (AHP) pulse that excites all of the spins into the transverse plane regardless of spatial position. This is followed by three pairs of adiabatic full passage (AFP) pulses that invert the spins 180° . Inversion reverses the phase of the spins; spins with high phase at the time of inversion lose phase, while spins

with low phase at the time of inversion gain phase. This causes the loss of phase coherence due to T_2' relaxation (see Section 1.3.2) to be reversed. Spins regain phase coherence at the echo time (TE) and generate a maximal signal that can be measured. The three pairs of AFP pulses in the LASER pulse sequence inverts spins localised to three orthogonal spatial slices. The intersection of these slices defines the three-dimensional voxel from which the measured signal originates.

Compared to non-adiabatic localization methods such as point resolved spectroscopy (PRESS) [185] and stimulated acquisition mode (STEAM) [186], the LASER pulse sequence requires the use of a longer TE. The reason for this is two-fold. First, AFP pulses are applied in pairs because the first AFP pulse introduces a non-linear phase dispersion across the excited slice which is refocussed by the second. Second, because adiabatic pulses deposit more RF power than traditional pulses, they must be made longer in order to stay within power deposition limits at high field. Power deposition is defined as the rate at which tissue absorbs energy when exposed to an RF field, also called the specific absorption rate (SAR). Limits on SAR are set by the U.S. Food and Drug Administration (FDA) and the International Electrotechnical Commission (IEC). FDA and IEC guidelines limit whole body SAR to <4 W/kg for any 15 minute average and whole head SAR to <3.2 W/kg for any 10 minute average. SAR over any 10 second period is also limited to less than two times the stated values. The MRI scanner estimates SAR in real-time and if these limits are exceeded, the scan will be automatically aborted.

These limitations may be partially addressed by replacing the non-selective AHP pulse with a traditional selective 90° excitation pulse. Since the excitation pulse is selective, one pair of AFP pulses becomes unnecessary. With two AFP pulses removed, and the AHP pulse replaced by a traditional pulse, less RF power is deposited, and shorter TEs can be achieved. This sequence is called the semi-LASER pulse sequence [187].

1.4.4 Post-Acquisition Signal Processing

After acquisition, ^1H -MRS signals are post-processed to correct lineshape distortions and to ensure that metabolite lineshapes are Lorentzian. There are two major sources of lineshape distortions.

The first source of lineshape distortions is \vec{B}_0 inhomogeneity in the voxel of interest. Though \vec{B}_0 shimming is typically applied prior to acquisition to ensure that the magnetic field experienced by the spins of interest is as homogeneous as possible, there may still be some remaining \vec{B}_0 inhomogeneity in the spectroscopy voxel, resulting in a Gaussian distribution of precession frequencies (Equation (A.9)) for the spins in the voxel. As a result, the acquired metabolite lineshapes will be more Gaussian than Lorentzian. This type of lineshape distortion may be corrected using a reference signal from a sample that has experienced the same magnetic inhomogeneities. Assuming that the reference and data signals have the same phase, the contribution of \vec{B}_0 can be deconvoluted from the acquired metabolite data signal by simply dividing the signals in the time domain [188]. This correction method is called QUALITY (QUAntification improvement by converting LIneshapes to the lorentzian TYpe).

For *in vivo* experiments, the only available reference signal is the water signal collected during the same scanning session from the same spectroscopy voxel used to collect the metabolite data signal. This complicates the application of QUALITY to the data because the T_2 of water in the brain is shorter than the T_2 of most metabolites of interest. In fact, at 7T, the T_2 of water in the brain is roughly half that of metabolites [189]. Thus, at the end of the time-domain signal, the water signal values are small, and dividing the metabolite data signal by the water signal will result in signal spikes. These can be avoided by simply restricting QUALITY to the beginning of the acquired metabolite data signal [190].

The second source of lineshape distortions are the rapidly switching magnetic field gradients used during the localization of the ^1H -MRS signal. Due to Faraday's Law, the

switching gradients induce eddy currents in conductive structures including the main magnet, the shim coil, and the gradient coils themselves, resulting in shifts in \vec{B}_0 and time-dependent variations in the gradient fields. Eddy current effects manifest as time-dependent phase changes in the acquired metabolite data signal, leading to lineshape distortions in the frequency domain, and may be corrected by subtracting the phase of a reference signal, such as the water signal, from the phase of the acquired data [191]. Unlike QUALITY, eddy current correction (ECC) can be applied to the whole data signal without introducing artefacts.

1.4.5 Spectral Fitting

Acquired *in vivo* ^1H -MRS data is comprised of signals from all metabolites, lipids, and macromolecules present in the voxel of interest. The amplitude of a metabolite signal in the time-domain is equivalent to the area under the metabolite spectrum in the frequency domain [96], and is proportional to the metabolite's concentration. Thus, to quantify the concentration of each metabolite, the acquired data must be decomposed into its constituent metabolite signals. This can be achieved by fitting signal models of metabolites of interest, such as the model of glutamate (Equation (3.1)), to the data.

The sum of all signal models to be fitted produces the prior knowledge template:

$$FID[n] = \sum_m^M \left(A_m e^{-(t[n]+TE)/T_{2,m}} \sum_k^K c_k e^{j(\omega_k(t[n]+t[0])+\phi_k)} e^{-\pi\alpha_k|t[n]+t[0]|} \right) \quad (1.18)$$

The prior knowledge template contains M metabolite models. Each metabolite model is the sum of K frequency components, or peaks, and has an associated scaling factor (A_m) and T_2 value ($T_{2,m}$). For each peak, an amplitude parameter (c_k), a frequency shift parameter (ω_k), a phase parameter (ϕ_k), and a Lorentzian linewidth parameter (α_k) are defined.

The prior knowledge template defined in Equation (1.18) is a discretized function of time ($t[n]$). Alternatively, the template can be defined in the frequency domain. However,

since the data is acquired in the time domain, spectral fitting is also often done in the time domain. Moreover, since the data acquisition time is finite, truncation of the time-domain data will occur, which introduces frequency-domain artefacts that complicate frequency-domain fitting.

Although time-domain fitting avoids truncation-related frequency-domain artefacts, it is affected by residual water signal not destroyed by water suppression. In the time-domain, residual water signal is spread throughout the entire acquired FID. Removal of the residual water signal is necessary, as it will affect the fitting process and subsequent metabolite quantification. This can be done by identifying frequency components of the FID that are close to that of water (4.7 ppm) using a Hankel singular value decomposition (HSVD) algorithm [192] and subtracting those components from the FID.

1.4.6 Metabolite Simulations for Prior Knowledge

Fitting performance can be improved by reducing the number of independent parameters in the prior knowledge template. To do this, parameters within metabolites and/or between metabolites can be constrained by defining relationships between the parameters. These parameter relationships can be defined either empirically or by using numerical simulation.

The empirical approach requires the acquisition of high quality ^1H -MRS data from a solution of each metabolite included in the prior knowledge template with the same acquisition sequence and magnetic field strength used to acquire *in vivo* data. This approach is both time and resource intensive, especially if different RF pulse shapes, pulse sequence parameters, pulse sequences, or field strengths are used in an experimental protocol.

A more efficient way to obtain and constrain a prior knowledge template is to use the results from numerical simulations. Numerical simulations implement a quantum mechanical representation of ensembles of metabolite spin-systems. The J-coupling interactions between spins and the interactions of spins with RF pulse shapes can be fully described using

quantum mechanical equations (see Appendix B). The different RF pulse shapes from the MRI scanner can be exactly replicated and the exact pulse sequence reproduced, allowing the simulations to generate the expectation values of metabolite amplitude, phase, and shift parameters that result from the application of the pulse sequence. Multiple simulations can also be run simultaneously for all metabolites included in the prior knowledge template. In this way, the values needed to define parameter relationships can be quickly obtained.

1.4.7 Metabolite Quantification

After fitting the prior knowledge template to the data, the fitted amplitude values (c_k in Equation (1.18)) of the metabolites are compared to the signal amplitude of a reference compound with known concentration in order to determine the absolute metabolite concentrations. For *in vivo* spectroscopy, the reference signal is typically a water-unsuppressed spectrum collected from the same spectroscopy voxel as the water-suppressed metabolite spectrum. The water-unsuppressed spectrum is simply the water signal – the same signal used for QUALITY and ECC (Section 1.4.4). A water signal is used as the internal reference rather than the signal of another metabolite such as creatine because water concentration in the brain is uniformly distributed and varies over only a small range in pathological states [193].

Using an internal water reference, the tissue metabolite concentration, $[M]$, may be calculated as follows:

$$[M] = \frac{\hat{S}_m}{\hat{S}_W} \times 55.14 \text{ M} \quad (1.19)$$

where 55.14 M is the concentration of pure water [96], \hat{S}_m is the corrected metabolite amplitude value, and \hat{S}_W is the corrected water amplitude value. Corrections applied to the spectra include:

- A correction for the number of averages used during data acquisition.
- A correction for any gain and scaling factors applied to the data during acquisition and post-processing.
- A correction for the T_1 and T_2 relaxation rates of metabolites and water in the gray matter (GM), white matter (WM), and cerebrospinal fluid (CSF) compartments.
- A correction for the relative proton density of water in GM, WM, and CSF as compared to that of pure water.

A more detailed explanation of the applied corrections is given in Appendix C.

1.4.8 Sources of Variability

Measurements of metabolite concentrations made using single-voxel ^1H -MRS may be affected by several sources of variability. Some of these are discussed below.

1.4.8.1 Spectroscopy Voxel Placement and Participant Movement

As discussed in Section 1.4.3, metabolite signals are localized to a specific voxel placed in a region of the brain. The location of this voxel is often prescribed manually by the operator of the MRI scanner using anatomical landmarks from a separately acquired anatomical image of the participant. Because of this, intra- and inter-operator variability, as well as participant movement between the acquisition of the anatomical image and the acquisition of the ^1H -MRS data are sources of variability. Participant motion during the acquisition can also result in frequency and phase drifts that introduce artefacts into the spectrum. Fortunately, some of these artefacts can be corrected post-acquisition using methods such as spectral registration [194]. However, spectral quality may still be reduced (e.g. increased linewidth and lower SNR).

1.4.8.2 Field Inhomogeneity

Spatially-dependent variations in \vec{B}_0 and \vec{B}_1 as well as time-dependent variations in \vec{B}_0 and the gradient fields are other sources of variability. Spatially-dependent variations can affect the localization of the ^1H -MRS signal, while time-dependent variations can result in lineshape distortions. These may be mitigated by using adiabatic RF pulses (see Section 1.4.3) and by using QUALITY correction, ECC correction, or combined QUALITY and ECC correction (see Section 1.4.4).

1.4.8.3 Chemical Shift Displacement Error

The location of the spectroscopy voxel defined using successive selective excitation assumes on-resonance excitation. As discussed in Section 1.4.1, hydrogen nuclei of metabolites resonate at a different frequency than that of the hydrogen nuclei in water (i.e. off-resonance) resulting in metabolite signals that are measured from locations slightly shifted from that of the defined spectroscopy voxel. Such chemical shift displacement errors (CSDEs) are a source of variability and must be considered, especially at high field, as CSDE increases linearly with field strength. Minimizing the CSDE requires the use of gradients with high amplitude and RF pulses with large bandwidths.

1.4.8.4 Signal Bleed

Another source of variability is the unintended measurement of signal that originates from outside of the defined spectroscopy voxel. This phenomenon, also known as outer volume signal bleed, occurs because RF pulses implemented on an MRI scanner do not have perfect excitation profiles and spins outside of the defined spectroscopy voxel will be excited. Outer volume signal bleed needs to be considered, especially for spectroscopy voxels prescribed in brain regions near other tissues such as skin, because strong outer volume signals

(e.g. from lipids) can overlap with and obscure metabolite signals. Fortunately, outer volume signal bleed can be minimized by saturating spins outside the defined spectroscopy sequence using an outer volume suppression scheme that immediately precedes the localization sequence such as in [187].

1.4.8.5 Macromolecule Signals

It is not only outer volume signals that overlap with metabolite signals. Macromolecule signals from within the voxel of interest can also overlap with metabolite signals, which complicates the metabolite fitting and quantification process. Macromolecule contributions can be estimated and accounted for using several approaches including spline fitting [195], direct measurement of the macromolecule signal with inversion recovery techniques [196], and by using a model of the macromolecule lineshapes in the prior knowledge template [117]. The choice of approach can significantly impact the quantification of metabolites and contribute to the variability in their measurements.

1.4.8.6 Signal-to-Noise Ratio, Linewidth, and the Cramér-Rao Lower Bound

The variability in the calculated metabolite concentrations can also be impacted by factors such as the signal-to-noise ratio (SNR) of the acquired data and the linewidth of the metabolite peaks [197].

SNR of the acquired data depends on the concentration of metabolite in the voxel of interest (which determines the amount of available metabolite signal), the size of the voxel of interest, and the number of averages. It is typically calculated by dividing the height of the largest metabolite peak by the standard deviation of the noise. Low SNR spectra affects spectral fitting by increasing the uncertainty in the estimated model parameters used to calculate metabolite concentrations. This, in turn, increases the variability of the measurement.

The lowest expected variation of an estimated model parameter is quantified using a value called the Cramér-Rao Lower Bound (CRLB). Put another way, the CRLB is the minimum expected error associated with modelling the data. CRLBs decrease in proportion with the level of noise, meaning that better SNR results in more precise estimates of model parameters and a lower variability of calculated metabolite concentrations. Increasing the spectroscopy voxel size and the number of averages will increase SNR and decrease measurement variability.

CRLBs are also affected by the linewidth of the metabolite peaks. Increased linewidths causes increased overlap of adjacent peaks of different metabolites (e.g. peaks of glutamate and glutamine) that results in greater uncertainty of estimated model parameters and increased variability in calculated metabolite concentrations. Since linewidths are driven by the quality of the shim, a high quality shim can ensure narrow linewidths and reduce metabolite measurement variability.

1.4.8.7 Intrinsic Variation of Metabolite Levels

Another source of variability that should be considered is related not to the measurement of the signal, but rather to human physiology. Metabolite levels in the brain can fluctuate with circadian rhythm, diet, medication, exercise, and sleep. For example, diurnal variations can be detected using magnetic resonance spectroscopy [198]. Thus, making the measurement at different times of day can introduce variability in the calculated metabolite concentrations between participants. Variations in the mediators of circadian rhythm, such as brain temperature, hydration, and osmotic regulation may also contribute to measurement variability.

1.5 Diffusion Tensor Imaging

In the study presented in Chapter 2, metrics derived from diffusion tensor imaging were used to indirectly measure the white matter structure in the brain and were related to ^1H -MRS measurements made in the hippocampus and posterior cingulate cortex. This imaging technique is briefly detailed in this section.

1.5.1 Water Diffusion in Tissue

As discussed in Section A.1, MRI is sensitive to the magnetization of an ensemble of ^1H nuclei. Though some of these ^1H nuclei are part of more complicated molecules such as metabolites and lipids, the overwhelming majority of the ^1H nuclei in tissue are part of water molecules. Whether the tissue is live or fixed, water molecules experience translational motion as a result of random thermal fluctuations. This random thermal motion is called Brownian motion.

In free fluids, Brownian motion results in isotropic diffusion governed by Einstein's equation:

$$r^2 = 6Dt \tag{1.20}$$

where r is the distance of diffusion, D is the diffusion coefficient, and t is the diffusion time. Thus, free water molecules travel a distance that is proportional to $\sqrt{6Dt}$.

However, water in tissue diffuses within, around, and through anatomical structures that hinder the diffusion of water. Thus, by measuring the apparent diffusion of water in tissue, the underlying anatomical microstructure can be probed.

1.5.2 Diffusion Weighting of the MRI Signal

The MRI signal can be sensitized to the diffusion of water by utilizing the magnetic field gradients. As discussed in Sections 1.3.3 and 1.4.3, magnetic field gradients add a linear spatial variation to the main magnetic field causing nuclear spins at different spatial positions to experience a different local magnetic field. As water molecules diffuse and move through space in the presence of a gradient, the proton nuclear spins experience different local magnetic fields and acquire random phase changes. The more diffusion that a water molecule experiences, the more phase is accrued by its spins. After the gradient is turned off, any diffusion also results in incomplete rephasing when a second gradient is applied. The result is an attenuation of the MRI signal that depends on the diffusion of water. Thus, both the length of the diffusion gradient and the time between gradients can be used to encode information about the diffusion of water in the MRI signal, resulting in a diffusion weighted image.

Mathematically, the signal attenuation observed in each voxel of a diffusion weighted image is described by the following equation:

$$S = S_0 e^{-bD} \quad (1.21)$$

where S is the signal after diffusion induced attenuation, S_0 is the measured signal without the use of diffusion gradients, D is the apparent diffusion coefficient (ADC), and b is a diffusion sensitivity parameter determined by the magnitude and duration of the diffusion gradients, as well as the timing of the RF pulse sequence used.

A common pulse sequence used for diffusion imaging is the diffusion-weighted spin-echo sequence (Figure 1.3). The spin-echo sequence begins with a 90° excitation pulse which excites water spins into the transverse plane. This is followed by a 180° refocusing pulse at time $TE/2$, which inverts the spins 180° . As described in Section 1.4.3, inversion allows spins to regain phase coherence at TE , generating a maximal signal that can be

measured.

Diffusion gradients spaced Δ apart with amplitude G and duration δ are placed between the RF pulses. The b -value is determined by these parameters. In the example shown in Figure 1.3a, where imaging gradients are not shown or considered, $b = \gamma^2 \delta^2 G^2 (\Delta - \frac{\delta}{3})$. This solution for the b -value is also called the Stejskal-Tanner equation. Practically, because imaging gradients are applied before the diffusion gradients, some interaction between the imaging gradients and the diffusion gradients occur. Due to this interaction, the actual analytical equation for b is a complicated function of both the imaging and diffusion gradient parameters.

Manipulating the gradient parameters allows diffusion weighted images with different b -values to be collected. At least two b -values are needed in order to determine the diffusion coefficient D at each image voxel using Equation (1.21):

$$D = \frac{1}{(b_m - b_n)} \ln \left(\frac{S(b_n)}{S(b_m)} \right) \quad (1.22)$$

Typically, b_m is 0 s/mm² in order to obtain S_0 at each voxel. The S_0 image is needed to correct image distortions caused by the imaging gradients. On the other hand, b_n is usually on the order of 1000 s/mm². More than two b -values can be used to more accurately estimate D (Figure 1.3b).

1.5.3 The Diffusion Tensor

The value of D estimated with Equation (1.22) is the value of the diffusion coefficient in the direction of the gradients. For example, if the two gradients in Figure 1.3 are in the x and y directions, D_{xy} would be estimated. Multiple gradients can be used to define a non-orthogonal direction and estimate D in the direction of any arbitrary vector.

Usually, D along many different directions are estimated in order to fully describe the anisotropic diffusion of water in the brain. Water diffusion in the brain is mainly hindered

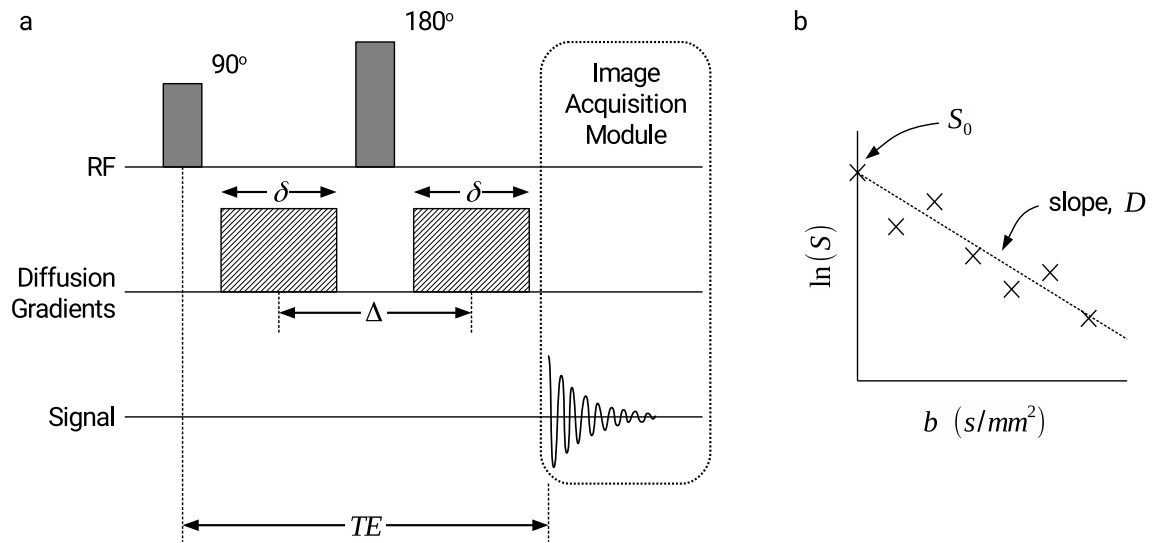


FIGURE 1.3: (a) A diffusion-weighted spin-echo sequence with echo time TE is depicted. The RF pulses, the diffusion gradients, and the generated MRI signal are shown. Imaging gradients are not shown. The diffusion gradients have amplitude G and duration δ . The time between gradients is Δ . (b) The b -value of the acquisition is determined by these gradient parameters. Multiple acquisitions with different gradient parameters allows diffusion weighted images at different b -values to be obtained and the diffusion coefficient D to be estimated at each image voxel.

by axonal bundles. Water tends to move more easily along axonal bundles rather than through or around them resulting in the anisotropic diffusion rather than isotropic diffusion. Thus, the ability to accurately measure anisotropic diffusion is needed in order to probe the anatomical structures of the brain.

The simplest way to model the anisotropic diffusion in each image voxel is by using a rank 2 diffusion tensor:

$$\mathbf{D} = \begin{bmatrix} D_{xx} & D_{xy} & D_{xz} \\ D_{yx} & D_{yy} & D_{yz} \\ D_{zx} & D_{zy} & D_{zz} \end{bmatrix} \quad (1.23)$$

By applying different gradients G_k and acquiring the corresponding signals S_k along K directions, a system of equations can be set up to determine the elements of the diffusion tensor:

$$\vec{A}\bar{\mathbf{D}} = \vec{B}$$

$$\begin{bmatrix} \bar{G}_1^T \\ \bar{G}_2^T \\ \vdots \\ \bar{G}_K^T \end{bmatrix} \bar{\mathbf{D}} = \begin{bmatrix} \ln \frac{S_1/S_0}{b_1} \\ \ln \frac{S_2/S_0}{b_2} \\ \vdots \\ \ln \frac{S_K/S_0}{b_K} \end{bmatrix} \quad k = 1 \cdots K, \quad K \geq 6 \quad (1.24)$$

where $\bar{G}_k = [G_x^2 \ G_y^2 \ G_z^2 \ 2G_xG_y \ 2G_xG_z \ 2G_yG_z]^T$, and $\bar{\mathbf{D}} = [D_{xx} \ D_{yy} \ D_{zz} \ D_{xy} \ D_{xz} \ D_{yz}]^T$. If $K = 6$, this system of equations can be solved with one unique solution. However, in practice, many different directions are acquired (i.e. $K \gg 6$) in order to improve SNR. With $K > 6$, the system of equations becomes overdetermined and there is no unique solution. In this case, $\bar{\mathbf{D}}$ may be solved by employing the pseudoinverse of \vec{A} and by using singular value decomposition approaches.

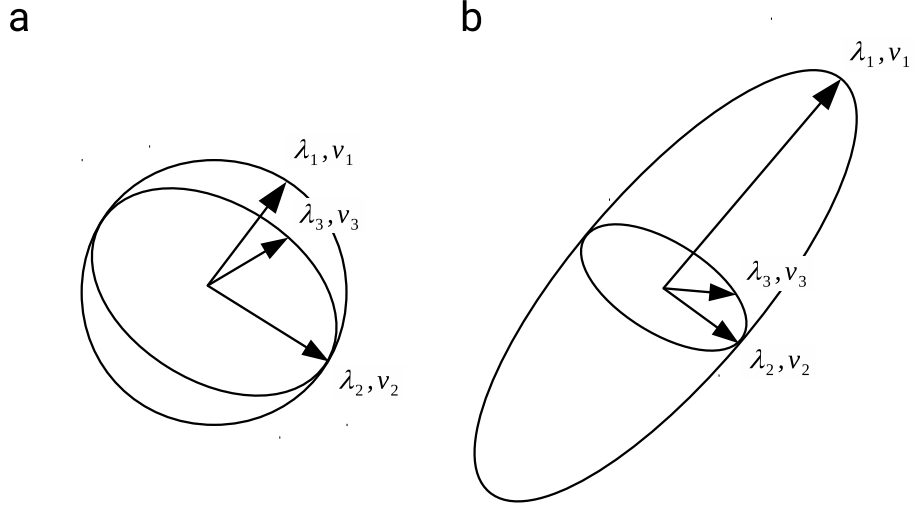


FIGURE 1.4: The diffusion tensor \mathbf{D} is depicted for isotropic diffusion in (a) and for anisotropic diffusion in (b). λ_1 , λ_2 , and λ_3 are the eigenvalues of \mathbf{D} and v_1 , v_2 , and v_3 are the eigenvectors of \mathbf{D} . The eigenvalues and eigenvectors of \mathbf{D} enables the calculation of metrics such as fractional anisotropy (FA). In the isotropic condition, $\lambda_1 \approx \lambda_2 \approx \lambda_3$ and FA is low. In the anisotropic condition, $\lambda_1 \gg \lambda_2 \approx \lambda_3$ and FA is high.

After \mathbf{D} is estimated, it is diagonalized to obtain \mathbf{D}' :

$$\mathbf{D}' = \begin{bmatrix} \lambda_1 & 0 & 0 \\ 0 & \lambda_2 & 0 \\ 0 & 0 & \lambda_3 \end{bmatrix} \begin{bmatrix} v_1 \\ v_2 \\ v_3 \end{bmatrix} \quad (1.25)$$

where λ_1 , λ_2 , and λ_3 are the eigenvalues of \mathbf{D} and v_1 , v_2 , and v_3 are the eigenvectors of \mathbf{D} . The eigenvalues and eigenvectors of \mathbf{D} characterizes diffusion at each voxel (Figure 1.4) and enables the voxelwise calculation of metrics such as mean diffusivity (MD), axial diffusivity (AxD), radial diffusivity (RD), and fractional anisotropy (FA). These metrics are used to infer information about the underlying anatomical brain structures.

1.5.3.1 Mean Diffusivity

The mean diffusivity metric is the directionally averaged diffusivity of water within a voxel:

$$MD = \frac{\lambda_1 + \lambda_2 + \lambda_3}{3} \quad (1.26)$$

MD describes the magnitude of the overall amount of water diffusion in each voxel and has units of $\mu\text{m}^2/\text{ms}$. Changes in the amount of water diffusion can be due to changes in the tissue. Increasing structure within cells can impede water diffusion, lowering MD [199]. Processes such as demyelination, inflammation, and oedema can increase water diffusion, in turn increasing MD [200]. Thus, MD is a sensitive but non-specific measure of underlying structural changes.

1.5.3.2 Fractional Anisotropy

Fractional anisotropy is calculated using MD and the eigenvalues of the diffusion tensor:

$$FA = \sqrt{\frac{(\lambda_1 - MD)^2 + (\lambda_2 - MD)^2 + (\lambda_3 - MD)^2}{2(\lambda_1^2 + \lambda_2^2 + \lambda_3^2)}} \quad (1.27)$$

FA is bounded between 0 and 1, and describes the degree to which diffusion is anisotropic. FA is considered a measure of axonal density, with dense packing resulting in more restricted, anisotropic water diffusion and higher FA [199]. Both demyelination and axonal degeneration cause axons to be less tightly packed together and lowers FA. Thus, FA is a sensitive but non-specific measure of microstructural changes in axonal fibre tracts of the brain.

However, the interpretation of FA is complicated by different confounding factors such as physiological and thermal image noise, image artefacts due to eddy currents or head motion, partial volume averaging between tissues, as well as crossing fibres within voxels

[200]. Various post-processing methods can compensate for the first three confounds, but the last confound is unavoidable. Crossing fibres cause the diffusion tensor to appear more similar to the tensor depicted in Figure 1.4a, thus decreasing the calculated FA. The amount of decrease is modulated by the angle and relative volume fractions of crossing fibres.

1.5.3.3 Combinations of Eigenvalues

Other combinations of eigenvalues can be calculated in order to demonstrate more specific microstructural changes in white matter fibre tracts of the brain. Two such combinations are the axial diffusivity (AxD) and the radial diffusivity (RD):

$$AxD = \lambda_1 \tag{1.28}$$

$$RD = \frac{\lambda_2 + \lambda_3}{2} \tag{1.29}$$

Changes in AxD are more specific to axonal degeneration, while changes in RD are more specific to myelin changes [201].

1.5.4 Tractography

The interpretation of MD, FA, RD, and AxD metrics are simplified if the analysis is restricted to particular fibre tracts in specific anatomical regions. For example, within a fibre tract that is homogeneous in direction, with few crossing fibres, changes in FA are much more likely to reflect real microstructural changes.

Identifying fibre tracts is the domain of tractography. In general, tractography identifies fibre tracts in a step-wise manner [200]:

1. Tractography begins by starting at a particular location called the seed point.
2. The next direction of travel is then estimated using the diffusion tensor at each voxel.
3. Finally, a small step is taken in that direction.

By repeating this process, an axonal tract may be followed voxel-by-voxel and identified [202]. Typically, constraints on this process are defined to refine the tracts that are identified. Examples of constraints include defining a maximum deflection angle that the next direction can have or the use of an FA threshold to terminate the process.

There are a plethora of methods to accomplish tractography, but they all fall into either the categories of deterministic tractography or probabilistic tractography. Typically, deterministic tractography uses the primary eigenvector of each voxel to define the trajectory of the fibre tract [199, 202]. On the other hand, probabilistic tractography uses the distribution of the diffusion tensors to estimate a distribution of probable fiber orientations at each voxel [203, 204]. Effectively, uncertainty about the orientation of axonal fibres is taken into account when identifying fibre tracts, making probabilistic methods better at identifying tracts in regions of crossing fibres than deterministic methods [199].

Once a fibre tract of interest is identified using tractography, the diffusion metrics can be mapped onto the tract, allowing the analysis along the fibre tract and the comparison of metric values of the same fibre tract across individuals.

1.6 References

- [1] M. Prince et al. “World Alzheimer Report 2016 Improving healthcare for people living with dementia. Coverage, Quality and costs now and in the future”. In: *Alzheimer’s Disease International (ADI)* (2016), pp. 1–140.
- [2] Public Health Agency of Canada. *A Dementia Strategy for Canada: Together We Aspire*. Tech. rep. Ottawa: Public Health Agency of Canada, 2019, p. 110.
- [3] H. W. Querfurth and F. M. LaFerla. “Alzheimer’s Disease”. In: *New England Journal of Medicine* 362.4 (Jan. 2010), pp. 329–344.
- [4] P. Scheltens et al. “Alzheimer’s disease”. In: *The Lancet* 388.10043 (July 2016), pp. 505–517.

1.6. References

- [5] C. Echávarri et al. "Neuropsychiatric symptoms in Alzheimer's disease and vascular dementia". In: *Journal of Alzheimer's Disease* 33.3 (2013), pp. 715–721.
- [6] C. L. Masters et al. "Alzheimer's disease". In: *Nature Reviews Disease Primers* 1 (Oct. 2015), p. 15056.
- [7] L. Bertram and R. E. Tanzi. "The genetic epidemiology of neurodegenerative disease". In: *Journal of Clinical Investigation* 115.6 (June 2005), pp. 1449–1457.
- [8] R. Sherrington et al. "Cloning of a gene bearing missense mutations in early-onset familial Alzheimer's disease". In: *Nature* 375.6534 (June 1995), pp. 754–760.
- [9] E. Levy-Lahad et al. "Candidate gene for the chromosome 1 familial Alzheimer's disease locus". In: *Science* 269.5226 (Aug. 1995), pp. 973–977.
- [10] E. I. Rogaev et al. "Familial Alzheimer's disease in kindreds with missense mutations in a gene on chromosome 1 related to the Alzheimer's disease type 3 gene". In: *Nature* 376.6543 (Aug. 1995), pp. 775–778.
- [11] A. Goate et al. "Segregation of a missense mutation in the amyloid precursor protein gene with familial Alzheimer's disease". In: *Nature* 349.6311 (Feb. 1991), pp. 704–706.
- [12] B. De Strooper et al. "Deficiency of presenilin-1 inhibits the normal cleavage of amyloid precursor protein". In: *Nature* 391.6665 (Jan. 1998), pp. 387–390.
- [13] Y. M. Li et al. "Photoactivated γ -secretase inhibitors directed to the active site covalently label presenilin 1". In: *Nature* 405.6787 (June 2000), pp. 689–694.
- [14] W. P. Esler. "A Portrait of Alzheimer Secretases—New Features and Familiar Faces". In: *Science* 293.5534 (Aug. 2001), pp. 1449–1454.
- [15] R. E. Tanzi. "A genetic dichotomy model for the inheritance of Alzheimer's disease and common age-related disorders". In: *Journal of Clinical Investigation* 104.9 (Nov. 1999), pp. 1175–1179.

- [16] E. H. Corder et al. "Gene dose of apolipoprotein E type 4 allele and the risk of Alzheimer's disease in late onset families". In: *Science* 261.5123 (Aug. 1993), pp. 921–923.
- [17] L. A. Farrer. "Effects of Age, Sex, and Ethnicity on the Association Between Apolipoprotein E Genotype and Alzheimer Disease". In: *JAMA* 278.16 (Oct. 1997), p. 1349.
- [18] D. R. Thal et al. "Phases of A β -deposition in the human brain and its relevance for the development of AD". In: *Neurology* 58.12 (June 2002), pp. 1791–1800.
- [19] H. Braak and E. Braak. "Neuropathological staging of Alzheimer-related changes." In: *Acta neuropathologica* 82.4 (Sept. 1991), pp. 239–59.
- [20] A. K. L. Liu et al. "Nucleus basalis of Meynert revisited: anatomy, history and differential involvement in Alzheimer's and Parkinson's disease". In: *Acta Neuropathologica* 129.4 (Apr. 2015), pp. 527–540.
- [21] T. Arendt et al. "Loss of neurons in the nucleus basalis of Meynert in Alzheimer's disease, paralysis agitans and Korsakoff's Disease." In: *Acta neuropathologica* 61.2 (1983), pp. 101–8.
- [22] V. Wilquet and B. De Strooper. "Amyloid-beta precursor protein processing in neurodegeneration." In: *Current opinion in neurobiology* 14.5 (Oct. 2004), pp. 582–8.
- [23] A. Serrano-Pozo et al. "Neuropathological alterations in Alzheimer disease". In: *Cold Spring Harbor Perspectives in Medicine* 1.1 (2011).
- [24] W. L. Klein, G. A. Krafft, and C. E. Finch. "Targeting small A β oligomers: the solution to an Alzheimer's disease conundrum?" In: *Trends in Neurosciences* 24.4 (Apr. 2001), pp. 219–224.

1.6. References

- [25] L. F. Lue et al. "Soluble amyloid β peptide concentration as a predictor of synaptic change in Alzheimer's disease". In: *American Journal of Pathology* 155.3 (Sept. 1999), pp. 853–862.
- [26] J. Lewis et al. "Enhanced neurofibrillary degeneration in transgenic mice expressing mutant tau and APP". In: *Science* 293.5534 (Aug. 2001), pp. 1487–1491.
- [27] J. Götz et al. "Formation of neurofibrillary tangles in P301L tau transgenic mice induced by A β 42 fibrils". In: *Science* 293.5534 (Aug. 2001), pp. 1491–1495.
- [28] D. J. Selkoe and J. Hardy. "The amyloid hypothesis of Alzheimer's disease at 25 years". In: *EMBO Molecular Medicine* 8.6 (June 2016), pp. 595–608.
- [29] H. Lin, R. Bhatia, and R. Lal. "Amyloid β protein forms ion channels: implications for Alzheimer's disease pathophysiology". In: *The FASEB Journal* 15.13 (Nov. 2002), pp. 2433–2444.
- [30] M. Mattson et al. "beta-Amyloid peptides destabilize calcium homeostasis and render human cortical neurons vulnerable to excitotoxicity". In: *The Journal of Neuroscience* 12.2 (Feb. 1992), pp. 376–389.
- [31] I. Bezprozvanny and M. P. Mattson. "Neuronal calcium mishandling and the pathogenesis of Alzheimer's disease". In: *Trends in Neurosciences* 31.9 (Sept. 2008), pp. 454–463.
- [32] E. Alberdi et al. "Amyloid β oligomers induce Ca²⁺ dysregulation and neuronal death through activation of ionotropic glutamate receptors". In: *Cell Calcium* 47.3 (Mar. 2010), pp. 264–272.
- [33] S. Li et al. "Soluble Oligomers of Amyloid β Protein Facilitate Hippocampal Long-Term Depression by Disrupting Neuronal Glutamate Uptake". In: *Neuron* 62.6 (June 2009), pp. 788–801.

- [34] J. W. Um et al. "Metabotropic Glutamate Receptor 5 Is a Coreceptor for Alzheimer A β Oligomer Bound to Cellular Prion Protein". In: *Neuron* 79.5 (Sept. 2013), pp. 887–902.
- [35] E. Popugaeva, C. Supnet, and I. Bezprozvanny. "Presenilins, Deranged Calcium Homeostasis, Synaptic Loss and Dysfunction in Alzheimer's Disease". In: *Messenger* 1.1 (2012), pp. 53–62.
- [36] T. J. Revett et al. "Glutamate system, amyloid β peptides and tau protein: functional interrelationships and relevance to Alzheimer disease pathology." In: *Journal of Psychiatry & Neuroscience* 38.1 (Jan. 2013), pp. 6–23.
- [37] S. Kim and H. Rhim. "Effects of amyloid- β peptides on voltage-gated L-type CaV1.2 and CaV1.3 Ca²⁺ channels". In: *Molecules and Cells* 32.3 (Sept. 2011), pp. 289–294.
- [38] N. Daschil et al. "CaV1.2 calcium channel expression in reactive astrocytes is associated with the formation of amyloid- β plaques in an Alzheimer's disease mouse model." In: *Journal of Alzheimer's Disease* 37.2 (Jan. 2013), pp. 439–51.
- [39] A. MacManus. "Enhancement of ⁴⁵Ca²⁺ Influx and Voltage-dependent Ca²⁺ Channel Activity by β -Amyloid-(1–40) in Rat Cortical Synaptosomes and Cultured Cortical Neurons. Modulation By The Proinflammatory Cytokine Interleukin-1 β ." In: *Journal of Biological Chemistry* 275.7 (Feb. 2000), pp. 4713–4718.
- [40] K. Ueda et al. "Amyloid beta protein potentiates Ca²⁺ influx through L-type voltage-sensitive Ca²⁺ channels: a possible involvement of free radicals". In: *Journal of neurochemistry* 68.1 (Jan. 1997), pp. 265–71.
- [41] H. W. Querfurth and D. J. Selkoe. "Calcium Ionophore Increases Amyloid β Peptide Production by Cultured Cells". In: *Biochemistry* 33.15 (Apr. 1994), pp. 4550–4561.
- [42] C. Supnet and I. Bezprozvanny. "The dysregulation of intracellular calcium in Alzheimer disease". In: *Cell Calcium* 47.2 (Feb. 2010), pp. 183–189.

1.6. References

- [43] L. Mucke and D. J. Selkoe. "Neurotoxicity of amyloid β -protein: Synaptic and network dysfunction". In: *Cold Spring Harbor Perspectives in Medicine* 2.7 (July 2012), a006338.
- [44] J. J. Palop and L. Mucke. "Amyloid- β -induced neuronal dysfunction in Alzheimer's disease: From synapses toward neural networks". In: *Nature Neuroscience* 13.7 (July 2010), pp. 812–818.
- [45] R. D. Terry et al. "Physical basis of cognitive alterations in alzheimer's disease: Synapse loss is the major correlate of cognitive impairment". In: *Annals of Neurology* 30.4 (Oct. 1991), pp. 572–580.
- [46] M. J. Berridge. "Vitamin D cell signalling in health and disease". In: *Biochemical and Biophysical Research Communications* 460.1 (2015), pp. 53–71.
- [47] L. D. Brewer et al. "Vitamin D Hormone Confers Neuroprotection in Parallel with Downregulation of L-Type Calcium Channel Expression in Hippocampal Neurons". In: *The Journal of Neuroscience* 21.1 (Jan. 2001), pp. 98–108.
- [48] L. D. Brewer et al. "Chronic 1 α ,25-(OH) $_2$ vitamin D3 treatment reduces Ca $^{2+}$ -mediated hippocampal biomarkers of aging." In: *Cell calcium* 40.3 (Sept. 2006), pp. 277–86.
- [49] P. Xia et al. "Memantine Preferentially Blocks Extrasynaptic over Synaptic NMDA Receptor Currents in Hippocampal Autapses". In: *Journal of Neuroscience* 30.33 (Aug. 2010), pp. 11246–11250.
- [50] G. M. McKhann et al. "The diagnosis of dementia due to Alzheimer's disease: Recommendations from the National Institute on Aging-Alzheimer's Association workgroups on diagnostic guidelines for Alzheimer's disease". In: *Alzheimer's and Dementia* 7.3 (May 2011), pp. 263–269. arXiv: NIHMS150003.

- [51] M. S. Albert et al. "The diagnosis of mild cognitive impairment due to Alzheimer's disease: Recommendations from the National Institute on Aging-Alzheimer's Association workgroups on diagnostic guidelines for Alzheimer's disease". In: *Alzheimer's and Dementia* 7.3 (May 2011), pp. 270–279. arXiv: NIHMS150003.
- [52] J. S. Birks. "Cholinesterase inhibitors for Alzheimer's disease". In: *Cochrane Database of Systematic Reviews* 1 (Jan. 2006). Ed. by J. S. Birks.
- [53] D. A. Casey, D. Antimisiaris, and J. O'Brien. "Drugs for Alzheimer's disease: are they effective?" In: *P & T : a peer-reviewed journal for formulary management* 35.4 (Apr. 2010), pp. 208–11.
- [54] J. W. Johnson and S. E. Kotermanski. "Mechanism of action of memantine." In: *Current opinion in pharmacology* 6.1 (Feb. 2006), pp. 61–7.
- [55] R. McShane et al. "Memantine for dementia". In: *Cochrane Database of Systematic Reviews* 3 (Mar. 2019).
- [56] J. Cummings et al. "Alzheimer's disease drug development pipeline: 2018". In: *Alzheimer's and Dementia: Translational Research and Clinical Interventions* 4 (2018), pp. 195–214.
- [57] R. S. Doody et al. "A Phase 3 Trial of Semagacestat for Treatment of Alzheimer's Disease". In: *New England Journal of Medicine* 369.4 (July 2013), pp. 341–350.
- [58] S. Salloway et al. "Two Phase 3 Trials of Bapineuzumab in Mild-to-Moderate Alzheimer's Disease". In: *New England Journal of Medicine* 370.4 (Jan. 2014), pp. 322–333.
- [59] A. I. Abushouk et al. "Bapineuzumab for mild to moderate Alzheimer's disease: A meta-analysis of randomized controlled trials". In: *BMC Neurology* 17.1 (Dec. 2017), p. 66.

1.6. References

- [60] R. S. Doody et al. "Phase 3 Trials of Solanezumab for Mild-to-Moderate Alzheimer's Disease". In: *New England Journal of Medicine* 370.4 (Jan. 2014), pp. 311–321.
- [61] E. E. Congdon and E. M. Sigurdsson. "Tau-targeting therapies for Alzheimer disease". In: *Nature Reviews Neurology* 14.7 (July 2018), pp. 399–415.
- [62] H. Engler et al. "Two-year follow-up of amyloid deposition in patients with Alzheimer's disease". In: *Brain* 129.11 (Sept. 2006), pp. 2856–2866.
- [63] M. Ingelsson et al. "Early A β accumulation and progressive synaptic loss, gliosis, and tangle formation in AD brain". In: *Neurology* 62.6 (Mar. 2004), pp. 925–931.
- [64] G. W. Small et al. "Current and future uses of neuroimaging for cognitively impaired patients". In: *The Lancet Neurology* 7.2 (Feb. 2008), pp. 161–172.
- [65] L. K. Ferreira and G. F. Busatto. "Neuroimaging in Alzheimer's disease: current role in clinical practice and potential future applications". In: *Clinics* 66.Suppl 1 (2012), pp. 19–24.
- [66] J. P. Marques et al. "MP2RAGE, a self bias-field corrected sequence for improved segmentation and T1-mapping at high field". In: *NeuroImage* 49.2 (Jan. 2010), pp. 1271–1281.
- [67] J. L. Whitwell et al. "MRI correlates of neurofibrillary tangle pathology at autopsy: A voxel-based morphometry study". In: *Neurology* 71.10 (Sept. 2008), pp. 743–749.
- [68] C. R. Jack et al. "Antemortem MRI findings correlate with hippocampal neuropathology in typical aging and dementia." In: *Neurology* 58.5 (Mar. 2002), pp. 750–7.
- [69] S. M. Nestor et al. "Ventricular enlargement as a possible measure of Alzheimer's disease progression validated using the Alzheimer's disease neuroimaging initiative database". In: *Brain* 131.9 (Sept. 2008), pp. 2443–2454.

- [70] B. H. Ridha et al. "Volumetric MRI and cognitive measures in Alzheimer disease: Comparison of markers of progression". In: *Journal of Neurology* 255.4 (Apr. 2008), pp. 567–574.
- [71] J. Acosta-Cabronero and P. J. Nestor. "Diffusion tensor imaging in Alzheimer's disease: Insights into the limbic-diencephalic network and methodological considerations". In: *Frontiers in Aging Neuroscience* 6.SEP (2014), p. 266.
- [72] J. Acosta-Cabronero et al. "Diffusion tensor metrics as biomarkers in Alzheimer's disease". In: *PLoS One* 7.11 (Nov. 2012). Ed. by W. Zhan, e49072.
- [73] C. DeCarli et al. "Qualitative estimates of medial temporal atrophy as a predictor of progression from mild cognitive impairment to dementia". In: *Archives of Neurology* 64.1 (Jan. 2007), pp. 108–115.
- [74] C. R. Jack et al. "Prediction of AD with MRI-based hippocampal volume in mild cognitive impairment." In: *Neurology* 52.7 (Apr. 1999), pp. 1397–403.
- [75] M. Grundman et al. "Brain MRI hippocampal volume and prediction of clinical status in a mild cognitive impairment trial". In: *Journal of Molecular Neuroscience* 19.1-2 (Aug. 2007), pp. 23–27.
- [76] E. J. Burton et al. "Medial temporal lobe atrophy on MRI differentiates Alzheimer's disease from dementia with Lewy bodies and vascular cognitive impairment: A prospective study with pathological verification of diagnosis". In: *Brain* 132.1 (Jan. 2009), pp. 195–203.
- [77] K. A. Johnson et al. "Brain imaging in Alzheimer disease". In: *Cold Spring Harbor Perspectives in Medicine* 2.4 (Apr. 2012), a006213.
- [78] C. R. Jack et al. "Hypothetical model of dynamic biomarkers of the Alzheimer's pathological cascade". In: *The Lancet Neurology* 9.1 (Jan. 2010), pp. 119–128. arXiv: NIHMS150003.

1.6. References

- [79] S. De Santi et al. "Hippocampal formation glucose metabolism and volume losses in MCI and AD". In: *Neurobiology of Aging* 22.4 (July 2001), pp. 529–539.
- [80] E. M. Reiman et al. "Hippocampal volumes in cognitively normal persons at genetic risk for Alzheimer's disease". In: *Annals of Neurology* 44.2 (Aug. 1998), pp. 288–291.
- [81] K. Ishii. "PET Approaches for Diagnosis of Dementia". In: *American Journal of Neuroradiology* 35.11 (Nov. 2014), pp. 2030–2038.
- [82] L. Mosconi et al. "Multicenter Standardized 18F-FDG PET Diagnosis of Mild Cognitive Impairment, Alzheimer's Disease, and Other Dementias". In: *Journal of Nuclear Medicine* 49.3 (Mar. 2008), pp. 390–398. arXiv: NIHMS150003.
- [83] L. M. Bloudek et al. "Review and meta-analysis of biomarkers and diagnostic imaging in Alzheimer's disease". In: *Journal of Alzheimer's Disease* 26.4 (Oct. 2011), pp. 627–645.
- [84] Y. Yuan, Z. X. Gu, and W. S. Wei. "Fluorodeoxyglucose-positron-emission tomography, single-photon emission tomography, and structural MR imaging for prediction of rapid conversion to alzheimer disease in patients with mild cognitive impairment: A meta-analysis". In: *American Journal of Neuroradiology* 30.2 (Feb. 2009), pp. 404–410.
- [85] W. E. Klunk et al. "Imaging Brain Amyloid in Alzheimer's Disease with Pittsburgh Compound-B". In: *Annals of Neurology* 55.3 (Mar. 2004), pp. 306–319.
- [86] C. C. Rowe et al. "Imaging β -amyloid burden in aging and dementia". In: *Neurology* 68.20 (May 2007), pp. 1718–1725.
- [87] C. M. Clark et al. "Use of florbetapir-PET for imaging β -amyloid pathology". In: *JAMA - Journal of the American Medical Association* 305.3 (Jan. 2011), pp. 275–283.

- [88] D. F. Wong et al. "In Vivo Imaging of Amyloid Deposition in Alzheimer Disease Using the Radioligand 18F-AV-45 (Flobetapir F 18)". In: *Journal of Nuclear Medicine* 51.6 (June 2010), pp. 913–920.
- [89] M. D. Ikonomovic et al. "Post-mortem correlates of in vivo PiB-PET amyloid imaging in a typical case of Alzheimer's disease". In: *Brain* 131.6 (June 2008), pp. 1630–1645.
- [90] B. J. Bacskai et al. "Molecular imaging with Pittsburgh compound B confirmed at autopsy: A case report". In: *Archives of Neurology* 64.3 (Mar. 2007), pp. 431–434.
- [91] C. M. Clark et al. "Cerebral PET with florbetapir compared with neuropathology at autopsy for detection of neuritic amyloid- β plaques: A prospective cohort study". In: *The Lancet Neurology* 11.8 (Aug. 2012), pp. 669–678.
- [92] A. Kadir et al. "Dynamic changes in PET amyloid and FDG imaging at different stages of Alzheimer's disease". In: *Neurobiology of Aging* 33.1 (Jan. 2012), 198.e1–198.e14.
- [93] C. Marcus, E. Mena, and R. R. M. Subramaniam. "Brain PET in the diagnosis of Alzheimer's disease". In: *Clinical nuclear medicine* 39.10 (Oct. 2014), e413–e426. arXiv: NIHMS150003.
- [94] N. Okamura et al. "Non-invasive assessment of Alzheimer's disease neurofibrillary pathology using 18F-THK5105 PET". In: *Brain* 137.6 (June 2014), pp. 1762–1771.
- [95] G. Öz et al. "Clinical Proton MR Spectroscopy in Central Nervous System Disorders". In: *Radiology* 270.3 (Mar. 2014), pp. 658–679.
- [96] R. A. de Graaf. *In Vivo NMR Spectroscopy*. 2nd ed. Chichester, UK: John Wiley & Sons, Ltd, Oct. 2007.

1.6. References

- [97] E. Wiame et al. "Molecular identification of aspartate N-acetyltransferase and its mutation in hypoacetylaspartia". In: *Biochemical Journal* 425.1 (Jan. 2010), pp. 127–139.
- [98] P. S. Ariyannur et al. "Methamphetamine-induced neuronal protein NAT8L is the NAA biosynthetic enzyme: Implications for specialized acetyl coenzyme A metabolism in the CNS". In: *Brain Research* 1335 (June 2010), pp. 1–13.
- [99] T. B. Patel and J. B. Clark. "Synthesis of N -acetyl-l-aspartate by rat brain mitochondria and its involvement in mitochondrial/cytosolic carbon transport". In: *Biochemical Journal* 184.3 (Dec. 1979), pp. 539–546.
- [100] T. E. Bates et al. "Inhibition of N-acetylaspartate production". In: *NeuroReport* 7.8 (May 1996), pp. 1397–1400.
- [101] N. Fayed et al. "Brain Glutamate Levels Are Decreased in Alzheimer's Disease". In: *American Journal of Alzheimer's Disease & Other Dementias* 26.6 (Sept. 2011), pp. 450–456.
- [102] T. Watanabe, A. Shiino, and I. Akiguchi. "Hippocampal metabolites and memory performances in patients with amnesic mild cognitive impairment and Alzheimer's disease". In: *Neurobiology of Learning and Memory* 97.3 (Mar. 2012), pp. 289–293.
- [103] T. Watanabe, A. Shiino, and I. Akiguchi. "Absolute quantification in proton magnetic resonance spectroscopy is useful to differentiate amnesic mild cognitive impairment from Alzheimer's disease and healthy aging." In: *Dement Geriatr Cognitive Disorders* 30.1 (2010), pp. 71–7.
- [104] R. M. R. Dixon et al. "Longitudinal quantitative proton magnetic resonance spectroscopy of the hippocampus in Alzheimer's disease". In: *Brain* 125.10 (Oct. 2002), pp. 2332–2341.

- [105] E. Adalsteinsson et al. "Longitudinal decline of the neuronal marker N-acetyl aspartate in Alzheimer's disease". In: *Lancet* 355.9216 (May 2000), pp. 1696–1697.
- [106] F. Jessen et al. "Decrease of N-acetylaspartate in the MTL correlates with cognitive decline of AD patients". In: *Neurology* 57.5 (Sept. 2001), pp. 930–932.
- [107] P. J. Modrego et al. "Changes in metabolite ratios after treatment with rivastigmine in Alzheimer's disease: A nonrandomised controlled trial with magnetic resonance spectroscopy". In: *CNS Drugs* 20.10 (2006), pp. 867–877.
- [108] K. R. R. Krishnan et al. "Randomized, placebo-controlled trial of the effects of donepezil on neuronal markers and hippocampal volumes in Alzheimer's disease". In: *American Journal of Psychiatry* 160.11 (Nov. 2003), pp. 2003–2011.
- [109] M. Zyśk et al. "Phenotype-Dependent Interactions between N -acetyl-L-Aspartate and Acetyl-CoA in Septal SN56 Cholinergic Cells Exposed to an Excess of Zinc". In: *Journal of Alzheimer's Disease* 56.3 (Feb. 2017). Ed. by M. Kleinschmidt, pp. 1145–1158.
- [110] J. R. Moffett et al. "N-Acetylaspartate in the CNS: From neurodiagnostics to neurobiology". In: *Progress in Neurobiology* 81.2 (Feb. 2007), pp. 89–131.
- [111] A. Bitsch et al. "Inflammatory CNS Demyelination: Histopathologic Correlation with In Vivo Quantitative Proton MR Spectroscopy". In: *American Journal of Neuroradiology* 20.9 (Oct. 1999), 1619 LP –1627.
- [112] D. L. Taylor et al. "Investigation into the Role of N-Acetylaspartate in Cerebral Osmoregulation". In: *Journal of Neurochemistry* 65.1 (Nov. 2002), pp. 275–281.
- [113] M. Erecińska and I. A. Silver. "Metabolism and role of glutamate in mammalian brain". In: *Progress in Neurobiology* 35.4 (Jan. 1990), pp. 245–296.
- [114] F. Fonnum. "Glutamate: A Neurotransmitter in Mammalian Brain". In: *Journal of Neurochemistry* 42.1 (Jan. 1984), pp. 1–11.

1.6. References

- [115] C. A. Tamminga et al. "Glutamate dysfunction in hippocampus: Relevance of dentate gyrus and CA3 signaling". In: *Schizophrenia Bulletin* 38.5 (Sept. 2012), pp. 927–935.
- [116] F. Schubert et al. "Glutamate concentrations in human brain using single voxel proton magnetic resonance spectroscopy at 3 Tesla". In: *NeuroImage* 21.4 (Apr. 2004), pp. 1762–1771.
- [117] D. Wong, A. L. Schranz, and R. Bartha. "Optimized in vivo brain glutamate measurement using long-echo-time semi-LASER at 7 T". In: *NMR in Biomedicine* 31.11 (Nov. 2018), e4002.
- [118] R. Rupasingh et al. "Reduced hippocampal glutamate in Alzheimer disease". In: *Neurobiology of Aging* 32.5 (May 2011), pp. 802–810.
- [119] C. J. Stagg et al. "Relationship between physiological measures of excitability and levels of glutamate and GABA in the human motor cortex". In: *Journal of Physiology* 589.23 (Dec. 2011), pp. 5845–5855.
- [120] N. R. Sibson et al. "Stoichiometric coupling of brain glucose metabolism and glutamatergic neuronal activity". In: *Proceedings of the National Academy of Sciences* 95.1 (Jan. 1998), pp. 316–321.
- [121] M. Yudkoff et al. "Tricarboxylic acid cycle in rat brain synaptosomes. Fluxes and interactions with aspartate aminotransferase and malate/aspartate shuttle." In: *The Journal of biological chemistry* 269.44 (Nov. 1994), pp. 27414–20.
- [122] M. Erecińska et al. "Glucose and Synaptosomal Glutamate Metabolism: Studies with [15N]Glutamate". In: *Journal of Neurochemistry* 51.3 (Sept. 1988), pp. 892–902.
- [123] J. A. Stanley and N. Raz. "Functional magnetic resonance spectroscopy: The "new" MRS for cognitive neuroscience and psychiatry research". In: *Frontiers in Psychiatry* 9.MAR (2018), p. 76.

- [124] J. Penner et al. "Increased glutamate in the hippocampus after galantamine treatment for Alzheimer disease". In: *Progress in Neuro-Psychopharmacology and Biological Psychiatry* 34.1 (Feb. 2010), pp. 104–110.
- [125] M. J. Berridge. "The Inositol Trisphosphate/Calcium Signaling Pathway in Health and Disease". In: *Physiological Reviews* 96.4 (Oct. 2016), pp. 1261–1296.
- [126] R. Vadnal, L. Parthasarathy, and R. Parthasarathy. "Role of Inositol in the Treatment of Psychiatric Disorders". In: *CNS Drugs* 7.1 (Jan. 1997), pp. 6–16.
- [127] W. Huang et al. "Brain metabolite concentration and dementia severity in Alzheimer's disease: a (1)H MRS study." In: *Neurology* 57.4 (Aug. 2001), pp. 626–32.
- [128] B. L. Miller et al. "Alzheimer disease: depiction of increased cerebral myo-inositol with proton MR spectroscopy." In: *Radiology* 187.2 (May 1993), pp. 433–437.
- [129] R. A. Moats et al. "Abnormal cerebral metabolite concentrations in patients with probable alzheimer disease". In: *Magnetic Resonance in Medicine* 32.1 (July 1994), pp. 110–115.
- [130] J. E. Novak et al. "Differentiated Human NT2-N Neurons Possess a High Intracellular Content of myo-Inositol". In: *Journal of Neurochemistry* 72.4 (Dec. 2001), pp. 1431–1440.
- [131] C. D. Rae. "A guide to the metabolic pathways and function of metabolites observed in human brain 1H magnetic resonance spectra". In: *Neurochemical Research* 39.1 (Jan. 2014), pp. 1–36.
- [132] X. C. Wang et al. "Correlation between choline signal intensity and acetylcholine level in different brain regions of rat". In: *Neurochemical Research* 33.5 (May 2008), pp. 814–819.

1.6. References

- [133] K. Kantarci et al. "1H MR spectroscopy in common dementias". In: *Neurology* 63.8 (Oct. 2004), pp. 1393–1398.
- [134] D. J. Meyrhoff et al. "Axonal injury and membrane alterations in Alzheimer's disease suggested by in vivo proton magnetic resonance spectroscopic imaging". In: *Annals of Neurology* 36.1 (July 1994), pp. 40–47.
- [135] S. MacKay et al. "Alzheimer disease and subcortical ischemic vascular dementia: evaluation by combining MR imaging segmentation and H-1 MR spectroscopic imaging." In: *Radiology* 198.2 (Feb. 1996), pp. 537–545.
- [136] G. E. Gibson and J. P. Blass. "Impaired synthesis of acetylcholine in brain accompanying mild hypoxia and hypoglycemia". In: *Journal of Neurochemistry* 27.1 (July 1976), pp. 37–42.
- [137] J. Klein. "Membrane breakdown in acute and chronic neurodegeneration: Focus on choline-containing phospholipids". In: *Journal of Neural Transmission* 107.8-9 (2000), pp. 1027–1063.
- [138] R. J. Wurtman, J. K. Blusztajn, and J.-C. Maire. "'Autocannibalism' of choline-containing membrane phospholipids in the pathogenesis of Alzheimer's disease—A hypothesis". In: *Neurochemistry International* 7.2 (Jan. 1985), pp. 369–372.
- [139] M. Mihara et al. "Magnetic resonance spectroscopic study of Alzheimer's disease and frontotemporal dementia/Pick complex". In: *NeuroReport* 17.4 (Mar. 2006), pp. 413–416.
- [140] U. Weiss et al. "Cognitive impairment: Assessment with brain magnetic resonance imaging and proton magnetic resonance spectroscopy". In: *Journal of Clinical Psychiatry* 64.3 (2003), pp. 235–242.
- [141] X. Xuan, M. Ding, and X. Gong. "Proton magnetic resonance spectroscopy detects a relative decrease of N-acetylaspartate in the hippocampus of patients with dementia with Lewy bodies". In: *Journal of Neuroimaging* 18.2 (Apr. 2008), pp. 137–141.

- [142] J. A. Molina et al. "Proton magnetic resonance spectroscopy in dementia with Lewy bodies". In: *European Neurology* 48.3 (2002), pp. 158–163.
- [143] S. Weintraub, A. H. Wicklund, and D. P. Salmon. "The Neuropsychological Profile of Alzheimer Disease". In: *Cold Spring Harbor Perspectives in Medicine* 2.4 (Apr. 2012), a006171–a006171.
- [144] L. Bäckman et al. "Cognitive impairment in preclinical Alzheimer's disease: A meta-analysis." In: *Neuropsychology* 19.4 (2005), pp. 520–531.
- [145] C. A. Gold and A. E. Budson. "Memory loss in Alzheimer's disease: Implications for development of therapeutics". In: *Expert Review of Neurotherapeutics* 8.12 (Dec. 2008), pp. 1879–1891.
- [146] A. E. Budson and B. H. Price. "Memory Dysfunction". In: *New England Journal of Medicine* 352.7 (Feb. 2005), pp. 692–699.
- [147] J. M. Gardiner. "Episodic memory and autonoetic consciousness: A first-person approach". In: *Philosophical Transactions of the Royal Society B: Biological Sciences*. Vol. 356. 1413. 2001, pp. 1351–1361.
- [148] E. Tulving. "Episodic Memory: From Mind to Brain". In: *Annual Review of Psychology* 53.1 (Feb. 2002), pp. 1–25.
- [149] L. Nyberg. "Structural Basis of Episodic Memory". In: *Learning and Memory: A Comprehensive Reference*. Academic Press, Jan. 2008, pp. 99–112.
- [150] M. Moscovitch et al. "Episodic Memory and Beyond: The Hippocampus and Neocortex in Transformation". In: *Annual Review of Psychology* 67.1 (2016), pp. 105–134.
- [151] D. Wechsler. "A Standardized Memory Scale for Clinical Use". In: *Journal of Psychology: Interdisciplinary and Applied* 19.1 (Jan. 1945), pp. 87–95.

1.6. References

- [152] A. Rey. "L'examen psychologique dans les cas d'encéphalopathie traumatique. (Les problems.). [The psychological examination in cases of traumatic encepholopathy. Problems.]" In: *Archives de Psychologie* 28 (1941), pp. 215–285.
- [153] P. A. Osterrieth. "Le test de copie d'une figure complexe; contribution à l'étude de la perception et de la mémoire. [Test of copying a complex figure; contribution to the study of perception and memory.]" In: *Archives de Psychologie* 30 (1944), pp. 206–356.
- [154] S. Craft et al. "Memory improvement following induced hyperinsulinemia in Alzheimer's disease". In: *Neurobiology of Aging* 17.1 (Jan. 1996), pp. 123–130.
- [155] K. L. Possin et al. "Distinct neuroanatomical substrates and cognitive mechanisms of figure copy performance in Alzheimer's disease and behavioral variant frontotemporal dementia". In: *Neuropsychologia* 49.1 (Jan. 2011), pp. 43–48.
- [156] S. Weintraub et al. "Version 3 of the Alzheimer Disease Centers' Neuropsychological Test Battery in the Uniform Data Set (UDS)". In: *Alzheimer Disease and Associated Disorders* 32.1 (2018), pp. 10–17.
- [157] J. C. Morris. "Clinical Dementia Rating: A reliable and valid diagnostic and staging measure for dementia of the Alzheimer type". In: *International Psychogeriatrics* 9.SUPPL. 1 (Dec. 1997), pp. 173–176.
- [158] M. F. Folstein, S. E. Folstein, and P. R. McHugh. ""Mini-mental state": A practical method for grading the cognitive state of patients for the clinician". In: *Journal of Psychiatric Research* 12.3 (Nov. 1975), pp. 189–198.
- [159] Z. S. Nasreddine et al. "The Montreal Cognitive Assessment, MoCA: A Brief Screening Tool For Mild Cognitive Impairment". In: *Journal of the American Geriatrics Society* 53.4 (Apr. 2005), pp. 695–699.
- [160] R. M. Reitan. "Validity of the trail making test as an indicator of organic brain damage". In: *Perceptual and Motor Skills* 8.7 (Dec. 1958), p. 271.

- [161] J. A. Yesavage et al. "Development and validation of a geriatric depression screening scale: A preliminary report". In: *Journal of Psychiatric Research* 17.1 (Jan. 1982), pp. 37–49.
- [162] C. Janus, M. Chishti, and D. Westaway. "Transgenic mouse models of Alzheimer's disease". In: *Biochimica et Biophysica Acta (BBA) - Molecular Basis of Disease* 1502.1 (July 2000), pp. 63–75.
- [163] M. Kitazawa, R. Medeiros, and F. M. Laferla. "Transgenic mouse models of Alzheimer disease: developing a better model as a tool for therapeutic interventions." In: *Current Pharmaceutical Design* 18.8 (2012), pp. 1131–47.
- [164] G. A. Elder, M. A. Gama Sosa, and R. De Gasperi. "Transgenic Mouse Models of Alzheimer's Disease". In: *Mount Sinai Journal of Medicine* 77.1 (Jan. 2010), pp. 69–81.
- [165] K. Hsiao et al. "Correlative memory deficits, A β elevation, and amyloid plaques in transgenic mice". In: *Science* 274.5284 (Oct. 1996), pp. 99–102.
- [166] R. G. Morris et al. "Place navigation impaired in rats with hippocampal lesions". In: *Nature* 297.5868 (June 1982), pp. 681–683.
- [167] T. L. Spires-Jones et al. "Impaired spine stability underlies plaque-related spine loss in an Alzheimer's disease mouse model". In: *American Journal of Pathology* 171.4 (Oct. 2007), pp. 1304–1311.
- [168] H. Dong et al. "Spatial relationship between synapse loss and β -amyloid deposition in Tg2576 mice". In: *Journal of Comparative Neurology* 500.2 (Jan. 2007), pp. 311–321.
- [169] K. Duff et al. "Increased amyloid- β 42(43) in brains of mice expressing mutant presenilin 1". In: *Nature* 383.6602 (Oct. 1996), pp. 710–713.
- [170] L. Holcomb et al. "Accelerated Alzheimer-type phenotype in transgenic mice carrying both mutant amyloid precursor protein and presenilin 1 transgenes". In: *Nature Medicine* 4.1 (Jan. 1998), pp. 97–100.

1.6. References

- [171] D. R. Borchelt et al. "Accelerated amyloid deposition in the brains of transgenic mice coexpressing mutant presenilin 1 and amyloid precursor proteins". In: *Neuron* 19.4 (Oct. 1997), pp. 939–945.
- [172] M. Garcia-Alloza et al. "Characterization of amyloid deposition in the APP^{swe}/PS1^{dE9} mouse model of Alzheimer disease". In: *Neurobiology of Disease* 24.3 (Dec. 2006), pp. 516–524.
- [173] A. Volianskis et al. "Episodic memory deficits are not related to altered glutamatergic synaptic transmission and plasticity in the CA1 hippocampus of the APP^{swe}/PS1^{ΔE9}-deleted transgenic mice model of β -amyloidosis". In: *Neurobiology of Aging* 31.7 (July 2010), pp. 1173–1187.
- [174] C. Janus et al. "Behavioral abnormalities in APP^{Swe}/PS1^{dE9} mouse model of AD-like pathology: comparative analysis across multiple behavioral domains". In: *Neurobiology of Aging* 36.9 (Sept. 2015), pp. 2519–2532.
- [175] R. Lalonde et al. "Exploratory activity and spatial learning in 12-month-old APP 695 SWE/co + PS1/ Δ E9 mice with amyloid plaques". In: *Neuroscience Letters* 390.2 (Dec. 2005), pp. 87–92.
- [176] G. Roks et al. "Mutation screening of the tau gene in patients with early-onset Alzheimer's disease". In: *Neuroscience Letters* 277.2 (Dec. 1999), pp. 137–139.
- [177] M. G. Spillantini et al. "Mutation in the tau gene in familial multiple system tauopathy with presenile dementia". In: *Proceedings of the National Academy of Sciences* 95.13 (June 2002), pp. 7737–7741.
- [178] J. Lewis et al. "Neurofibrillary tangles, amyotrophy and progressive motor disturbance in mice expressing mutant (P301L)tau protein". In: *Nature Genetics* 25.4 (Aug. 2000), pp. 402–405.

- [179] S. Oddo et al. "Triple-Transgenic Model of Alzheimer's Disease with Plaques and Tangles: Intracellular A β and Synaptic Dysfunction". In: *Neuron* 39.3 (July 2003), pp. 409–421.
- [180] L. M. Billings et al. "Intraneuronal A β causes the onset of early Alzheimer's disease-related cognitive deficits in transgenic mice". In: *Neuron* 45.5 (Mar. 2005), pp. 675–688.
- [181] K. Duff and F. Suleman. "Transgenic mouse models of Alzheimer's disease: How useful have they been for therapeutic development?" In: *Briefings in Functional Genomics and Proteomics* 3.1 (2004), pp. 47–59.
- [182] T. W. Nixon et al. "Compensation of gradient-induced magnetic field perturbations". In: *Journal of Magnetic Resonance* 192.2 (June 2008), pp. 209–217.
- [183] I. Tkáč et al. "In vivo ¹H NMR spectroscopy of rat brain at 1 ms echo time". In: *Magnetic Resonance in Medicine* 41.4 (Apr. 1999), pp. 649–656.
- [184] M. Garwood and L. DelaBarre. "The return of the frequency sweep: designing adiabatic pulses for contemporary NMR." In: *Journal of magnetic resonance (San Diego, Calif. : 1997)* 153.2 (Dec. 2001), pp. 155–77.
- [185] P. A. Bottomley. "Spatial localization in NMR spectroscopy in vivo". In: *Annals of the New York Academy of Sciences* 508.1 Physiological (Nov. 1987), pp. 333–48.
- [186] J. Frahm et al. "Localized high-resolution proton NMR spectroscopy using stimulated echoes: Initial applications to human brain in vivo". In: *Magnetic Resonance in Medicine* 9.1 (Jan. 1989), pp. 79–93.
- [187] G. Oz and I. Tkáč. "Short-echo, single-shot, full-intensity proton magnetic resonance spectroscopy for neurochemical profiling at 4 T: validation in the cerebellum and brainstem." In: *Magnetic resonance in medicine* 65.4 (Apr. 2011), pp. 901–10.

1.6. References

- [188] A. A. De Graaf, J. E. Van Dijk, and W. M. M. J. BoéE. "QUALITY: quantification improvement by converting lineshapes to the lorentzian type". In: *Magnetic Resonance in Medicine* 13.3 (Mar. 1990), pp. 343–357.
- [189] M. Marjańska et al. "Localized ^1H NMR spectroscopy in different regions of human brain in vivo at 7 T: T2 relaxation times and concentrations of cerebral metabolites". In: *NMR in Biomedicine* 25.2 (Feb. 2012), pp. 332–339.
- [190] R. Bartha et al. "Spectroscopic lineshape correction by QUECC: combined QUALITY deconvolution and eddy current correction." In: *Magnetic resonance in medicine* 44.4 (Oct. 2000), pp. 641–5.
- [191] U. Klose. "In vivo proton spectroscopy in presence of eddy currents". In: *Magnetic Resonance in Medicine* 14.1 (Apr. 1990), pp. 26–30.
- [192] A. van den Boogaart et al. "Time and frequency domain analysis of NMR data compared: an application to 1D ^1H spectra of lipoproteins." In: *Magnetic resonance in medicine* 31.4 (Apr. 1994), pp. 347–58.
- [193] P. B. Barker et al. "Quantitation of proton NMR spectra of the human brain using tissue water as an internal concentration reference". In: *NMR in Biomedicine* 6.1 (Jan. 1993), pp. 89–94.
- [194] J. Near et al. "Frequency and phase drift correction of magnetic resonance spectroscopy data by spectral registration in the time domain". In: *Magnetic Resonance in Medicine* 73.1 (Jan. 2015), pp. 44–50.
- [195] S. W. Provencher. "Automatic quantitation of localized in vivo ^1H spectra with LCModel". In: *NMR in Biomedicine* 14.4 (June 2001), pp. 260–264.
- [196] J. Penner and R. Bartha. "Semi-LASER (^1H) MR spectroscopy at 7 Tesla in human brain: Metabolite quantification incorporating subject-specific macromolecule removal." In: *Magnetic resonance in medicine* 12.1 (July 2014), pp. 4–12.

- [197] R. Bartha. "Effect of signal-to-noise ratio and spectral linewidth on metabolite quantification at 4 T". In: *NMR in Biomedicine* 20.5 (Aug. 2007), pp. 512–521.
- [198] J. Arm et al. "Diurnal variability of cerebral metabolites in healthy human brain with 2D localized correlation spectroscopy (2D L-COSY)". In: *Journal of Magnetic Resonance Imaging* 50.2 (2019), pp. 592–601.
- [199] H. M. Feldman et al. "Diffusion Tensor Imaging: A Review for Pediatric Researchers and Clinicians". In: *Journal of Developmental and Behavioral Pediatrics* 31.4 (May 2010), pp. 346–56.
- [200] A. L. Alexander et al. "Diffusion Tensor Imaging of the Brain". In: *Neurotherapeutics* 4.3 (July 2007), pp. 316–329. arXiv: Neurotherapeutics.2007July;4(3):316–329.
- [201] S.-K. Song et al. "Dysmyelination revealed through MRI as increased radial (but unchanged axial) diffusion of water." In: *NeuroImage* 17.3 (Nov. 2002), pp. 1429–36.
- [202] P. Mukherjee et al. "Diffusion tensor MR imaging and fiber tractography: theoretic underpinnings". In: *AJNR American journal of neuroradiology* 29.4 (2008), pp. 632–641.
- [203] O. Friman, G. Farneback, and C.-F. Westin. "A Bayesian approach for stochastic white matter tractography". In: *IEEE Transactions on Medical Imaging* 25.8 (Aug. 2006), pp. 965–978.
- [204] A. J. Sherbondy et al. "ConTrack: Finding the most likely pathways between brain regions using diffusion tractography". In: *Journal of Vision* 8.9 (July 2008), pp. 15–15.

2

Reduced hippocampal glutamate and posterior cingulate NAA in MCI and AD is associated with episodic memory performance and white matter integrity in the cingulum

A version of this chapter has been accepted with minor revisions at the Journal of Alzheimer's Disease: Dickson Wong, Samir Atiya, Jennifer Fogarty, Manuel Montero-Odasso, Stephen H. Pasternak, Chris Brymer, Michael J. Borrie, Robert Bartha, "Reduced hippocampal glutamate and posterior cingulate N-acetyl aspartate in mild cognitive impairment and Alzheimer's disease is associated with episodic memory performance and white matter integrity in the cingulum," October 2019.

Abstract: Identification of biological changes underlying the early symptoms of Alzheimer's disease (AD) will help to identify and stage individuals prior to symptom onset. The limbic system, which supports episodic memory and is impaired early in AD is a primary target. In this study, brain metabolism and microstructure evaluated by high field (7 Tesla) proton magnetic resonance spectroscopy (^1H -MRS) and diffusion tensor imaging (DTI) were evaluated in the limbic system of eight individuals with mild cognitive impairment (MCI), nine with AD, and sixteen normal elderly controls (NEC). Left hippocampal glutamate and posterior cingulate *N*-acetyl aspartate concentrations were reduced in MCI and AD compared to NEC. Differences in DTI metrics indicated volume and white matter loss along the cingulum in AD compared to NEC. Metabolic and microstructural changes were associated with episodic memory performance assessed using *Craft Story 21 Recall* and *Benson Complex Figure Copy*. The current study suggests that metabolite concentrations measured using ^1H -MRS may provide insight into the underlying metabolic and microstructural processes of episodic memory impairment.

2.1 Introduction

Alzheimer's disease (AD), the most common form of dementia, is a neurodegenerative disorder of the brain that results in progressive impairments across cognitive domains such as memory, language, and executive function [1]. Although neurofibrillary tangles and amyloid plaques are hallmarks of AD pathology, the biological mechanisms underlying the development of AD are complex and heterogeneous. No clear cause [1] or chain of events have been identified that lead to the clinical presentation of AD [2].

Clinically, AD progression is considered a continuum, beginning with an asymptomatic phase that transitions into a symptomatic predementia phase called mild cognitive impairment (MCI) due to AD, followed by a symptomatic dementia phase called probable AD. However, identifying where an individual lies along the disease continuum requires subjective clinical judgment, with greater diagnostic uncertainty early in the disease continuum. Incorporating biomarkers of AD pathology, such as measures of amyloid-beta ($A\beta$) load, could help reduce this uncertainty [3, 4]. Additionally, volumetric measures of brain structure derived from magnetic resonance imaging (MRI) [5], white matter microstructural integrity derived from diffusion tensor imaging (DTI) [6], functional connectivity derived from functional MRI (fMRI) [7], and glucose uptake measured by fluorodeoxyglucose positron emission tomography (FDG-PET) [8] provide complementary information that can also aid in staging the disease. Despite the availability of these sophisticated measures it remains difficult to predict when and who will progress from mild cognitive impairment to AD. Even though disease-modifying treatments for AD are being investigated [9], they are not yet clinically available. Nevertheless, improving the ability to place an individual along the AD continuum, especially during the predementia phases, will help patients receive timely care and symptomatic treatment that could improve their quality of life [10].

Both the hippocampus and the posterior cingulate cortex (PCC) are known to be involved early in the pathological progression of AD [11]. Interestingly, both the hippocampus and PCC are connected by white matter fibres that run through the cingulum and are components of the Papez brain circuit, also known as the medial limbic system [12, 13, 14, 15, 16]. Damage to the grey matter and white matter structures of the Papez circuit is associated with episodic memory impairment [17, 18, 19]. Episodic memory impairment is among the earliest and most severe cognitive changes in AD [20], and is considered the most clinically relevant for assessing AD patients [21]. Structural changes in both the hippocampus and posterior cingulate cortex [22, 17, 5, 23, 24, 25], as well as changes in white matter microstructural integrity within the cingulum [22, 26, 6, 27, 28, 29, 30] have previously been shown in AD and MCI.

In addition to brain structure, measures of brain metabolism may provide insight into disease stage, particularly since there is evidence that metabolic changes may precede changes in cellular microstructure, neuronal density and death [31, 32, 33]. This suggests that measurement of brain metabolism could aid in the prediction of cognitive decline prior to the detection of structural changes at early stages of the disease. Though FDG-PET is a common measure of *in vivo* brain metabolism in AD, a less expensive, more accessible, and non-invasive method is proton magnetic resonance spectroscopy (^1H -MRS) [34]. Several metabolites relevant to neuronal function can be simultaneously measured by ^1H -MRS in specific brain regions. Previous studies have shown decreased *N*-acetyl aspartate (NAA) to creatine (Cr) ratio [35, 36, 37, 38, 39], decreased NAA concentration [40, 41, 42], and decreased glutamate (Glu) concentration [43, 39] in the hippocampus and posterior cingulate cortex (PCC) of individuals with AD.

Although previous studies have independently shown altered brain metabolite levels in the posterior cingulate and hippocampus as well as altered microstructure in the cingulum in people with MCI and AD, it is unclear whether these changes occur simultaneously

in the same individuals. The purpose of the current study was to determine whether altered metabolism in the hippocampus and PCC was associated with altered white matter microstructure in the cingulum of individuals with MCI and AD. Measuring metabolism using ^1H -MRS and white matter microstructure using DTI within regions of the Papez circuit that are associated with episodic memory could provide valuable information to help support a diagnosis of MCI or probable AD. Thus, the main objectives of this study were to: (1) correlate ^1H -MRS measurements in the hippocampus and PCC with MRI-derived measures of microstructural integrity in the cingulum, and (2) correlate ^1H -MRS measurements in the hippocampus and PCC with measurements of episodic memory performance. We hypothesized that glutamate and NAA concentrations as measured by ^1H -MRS would be lower in the PCC and left hippocampus of individuals with AD, and significantly correlated with both MRI-derived measures of microstructural integrity in the cingulum and measurements of episodic memory performance.

2.2 Materials and Methods

2.2.1 Subjects

In total, 33 subjects were recruited from the Aging Brain and Memory Clinic at Parkwood Institute and the Geriatric Clinic at the Mount Hope Centre for Long Term Care in London, Ontario, Canada. Of these, sixteen subjects were cognitively normal elderly controls (NEC), eight subjects had a clinical diagnosis of mild cognitive impairment (MCI), and nine subjects had a clinical diagnosis of probable AD. This study was approved by the Western University Health Sciences Research Ethics Board. Informed consent was acquired according to the Declaration of Helsinki.

MCI and AD subjects were diagnosed according to the most recent core clinical criteria put forward by the National Institute of Aging and Alzheimer's Association (NIA-AA) working Groups [3, 4]. The MCI criteria were consistent with the previously published

2.2. Materials and Methods

Petersen criteria [44, 45, 46]. The AD criteria were consistent with the National Institute of Neurological and Communicative Disorders and Stroke/Alzheimer's Disease and Related Disorder's Association (NINCDS/ADRDA) criteria [47]. Clinical head CTs and MRIs were also used to investigate non-AD causes of cognitive impairment such as white matter loss or lacunar infarcts. Any subject with a significant number of lacunar infarcts, a single strategically located lacunar infarct, or significant white matter loss (>25%) were not considered for this study.

Additional exclusion criteria for the study were: (1) uncontrolled mood or psychiatric symptoms in the 6 months prior to study enrolment; (2) use of anti-depressant with anti-cholinergic side effects; (3) use of psychoactive medication excluding anti-depressants, neuroleptics, chronic anxiolytics, opioid pain relievers, or sedative hypnotics within the four weeks prior to study enrolment; (4) enrolment in a clinical trial using an investigational medication; and (5) contraindications to ultra-high field MRI scanning. All subjects were aged between 55-90 years old and had a Geriatric Depression Score (GDS) less than 6. Subjects taking cholinesterase inhibitors and/or memantine were included if they were on a stable dose for at least 12 weeks prior to study enrolment. In general, the inclusion, exclusion, and diagnostic criteria used in this study were consistent with the criteria used by the Alzheimer's Disease Neuroimaging Initiative 2 (ADNI2) study [48].

2.2.2 Data Acquisition

2.2.2.1 Magnetic Resonance Imaging

All subjects were scanned on a 7 T/70 cm Siemens MAGNETOM (Siemens, Erlangen, Germany) head-only MRI system at the Centre for Functional and Metabolic Mapping, Roebarts Research Institute with an 8-channel transmit, 32-channel receive whole head array [49]. The scanner is equipped with eight 1000W radiofrequency amplifiers and a gradient

system (80 mT/m maximum gradient strength, 350 mT/m/s slew rate) that includes second order, third order, and Z4 shims. Whole-brain, 3D T_1 -weighted anatomical images and T_1 maps were acquired using the MP2RAGE pulse sequence [50] with 0.75 mm isotropic resolution, a repetition time (TR) of 6000 ms, and an echo-time (TE) of 2.83 ms.

2.2.2.2 Magnetic Resonance Spectroscopy

^1H -MRS data were acquired from all subjects using an implementation of the semi-LASER (localization by adiabatic selective refocusing) sequence described in detail elsewhere [51, 52, 53]. Voxel positions were manually positioned within the high-resolution, 3D T_1 weighted anatomical images using anatomical landmarks. Examples of the voxel placements are given in Figure 2.1a and Figure 2.1b. Water suppressed and unsuppressed ^1H -MRS data were collected from a $23 \times 12 \times 12 \text{ mm}^3$ voxel in the left hippocampus (Figure 2.1a) and a $16 \times 20 \times 18 \text{ mm}^3$ voxel in the PCC (Figure 2.1b) with the following parameters: TR=7500 ms, TE=60 ms, number of points=2048, bandwidth=6024 Hz, averages=64 for the water suppressed data, averages=4 for the water unsuppressed data. Hippocampal spectroscopy data could not be acquired in two NEC subjects, one MCI subject, and three AD subjects. PCC spectroscopy data were successfully acquired from all subjects.

2.2.2.3 Diffusion Weighted Imaging

Diffusion weighted images covering the whole brain were also acquired from all subjects using a single-shell, multi-shot, diffusion-weighted, spin-echo, echo-planar imaging (EPI) sequence with $b=1000 \text{ s/mm}^2$, 64 gradient directions, $2 \times 2 \times 2 \text{ mm}^3$ resolution, TR=5100 ms, and TE=50.2 ms. To facilitate corrections of distortions induced by the EPI sequence, two $b=0 \text{ s/mm}^2$ images were acquired with the same sequence – one with the phase encode direction in the anterior-to-posterior direction and the other with the phase encode direction in the posterior-to-anterior direction.

2.2. Materials and Methods

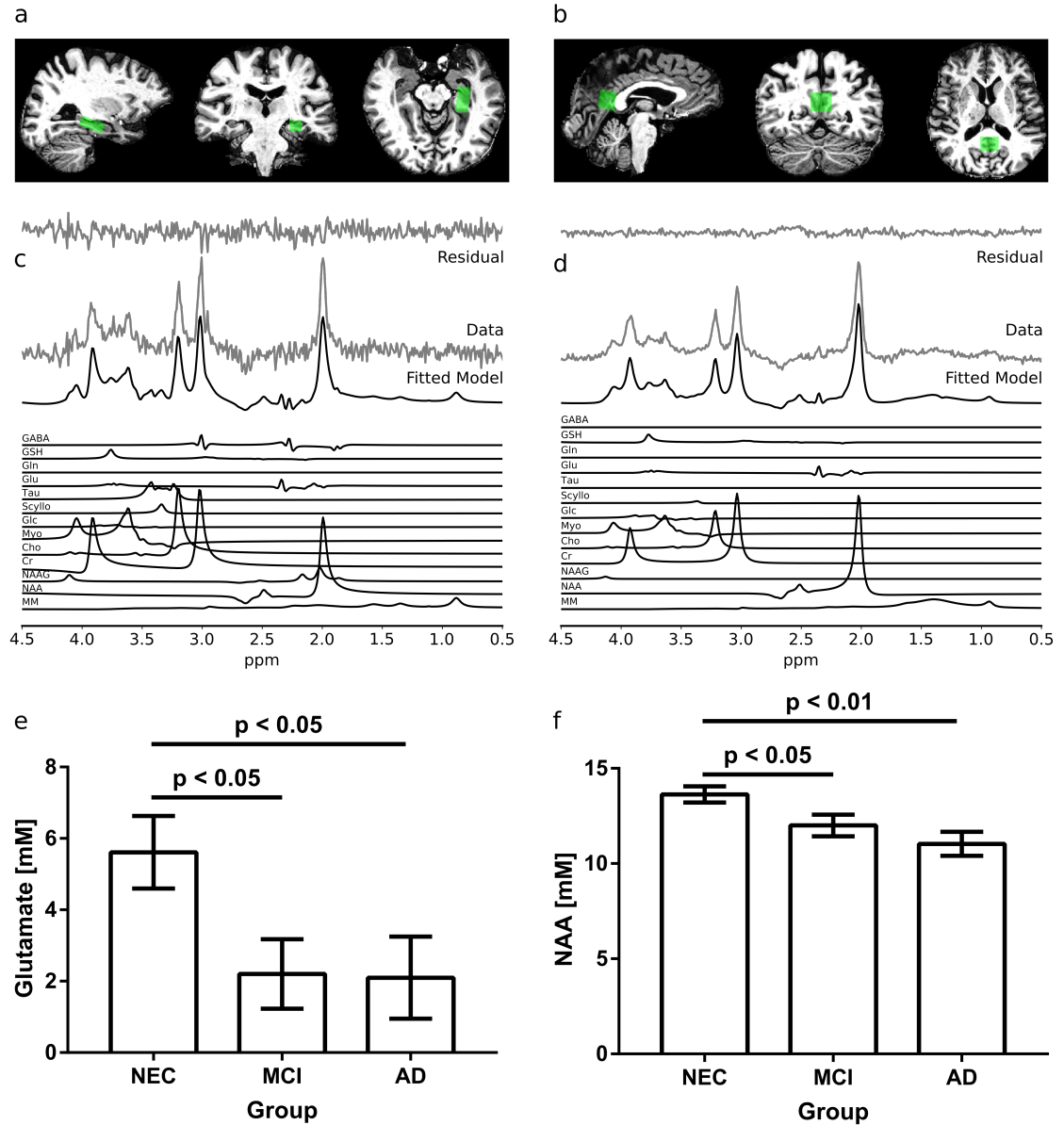


FIGURE 2.1: Examples of spectroscopy voxel placement and representative spectra in the left hippocampus (a, c) and PCC (b, d). The fitted model is shown in (c) and (d) along with the individual metabolite components. In the left hippocampus (e), MCI and AD subjects had significantly lower glutamate concentrations measured by ^1H -MRS than NEC subjects ($p < 0.05$). In the PCC (f), the average N-acetyl aspartate (NAA) concentrations measured by ^1H -MRS were lower in MCI and AD compared to NEC subjects ($p < 0.05$). Standard errors are shown in (e) and (f).

2.2.2.4 Cognitive Testing

Subjects were first assessed using the Clinical Dementia Rating (CDR) scale and the Geriatric Depression Scale (GDS) to ensure that the inclusion criteria for the study were met. Since MCI and AD subjects were already assessed using the mini-mental state examination (MMSE) and the Montreal cognitive assessment (MoCA) as part of standard clinical care, the episodic memory of study subjects was tested using neuropsychological tests not used in clinic to avoid learning effects. Specifically, the Craft Story 21 Recall (CSR) [54] and the Benson Complex Figure Copy (BCFC) [55] tests from the National Alzheimer's Coordinating Centre Neuropsychological Battery Version 3.0 [56] were used. Research staff administering the cognitive testing were trained by a licensed neuropsychological in accordance with Washington University protocols. Raw test scores were converted into age, sex, and years of education adjusted z-scores based on published norms [56]. Test z-scores were used for all further analyses. One NEC subject did not agree to provide information about their years of education and was therefore excluded from all analyses involving their cognitive testing data.

2.2.3 Data Processing

2.2.3.1 Post-Processing of Acquired Images

Brain extraction was performed on the T_1 weighted anatomical images, T_1 maps, and diffusion weighted images using a registration-based method. First, a transformation between T_1 -space and standard MNI152-space was found by registering the T_1 weighted anatomical image and the MNI152 T_1 weighted template. The registration was performed by first using a 6 degree-of-freedom (DOF) linear registration, followed by a 12 DOF linear registration, and non-linear registration. Linear and non-linear registrations were performed using FMRIB's linear image registration tool (FLIRT) [57, 58] and FMRIB's non-linear imaging registration tool (FNIRT), respectively. These tools are part of FMRIB's Software Library

(FSL), version 5.0.10 [59, 60, 61]. Using the resulting transformation matrix, the MNI152 brain mask was then transformed in T_1 -space and applied to the anatomical images and T_1 -maps.

Since EPI sequences are prone to susceptibility distortions, the diffusion weighted images were distortion-corrected using an estimated susceptibility off-resonance field, derived from the two $b=0$ s/mm³ images acquired with opposite phase encode directions. The topup tool from FSL [62] was used to apply this correction. Other distortions induced by eddy currents and subject motion were then corrected using the FSL eddy tool [63]. This processing also generated a distortion-corrected $b=0$ s/mm³ image.

A transformation from T_1 -space to diffusion-space was found by linearly registering the T_1 weighted anatomical image and the distortion-corrected $b=0$ s/mm³ image using the FSL `epi_reg` script. Applying the previously found MNI152-space to T_1 -space transformation matrix and the T_1 -space to diffusion-space transformation matrices in series transformed the MNI152 brain mask into diffusion-space for brain extraction of the diffusion weighted images. Then, using the FSL `dtifit` command-line program, a diffusion tensor model was fitted to every voxel within the brain-extracted diffusion weighted images, and subject-specific fraction anisotropy (FA), radial diffusivity (RD), and axial diffusivity (AxD) maps were produced. An example of a subject-specific FA map generated from diffusion tensor fitting of brain-extracted diffusion weighted images is shown in Figure 2.3a.

2.2.3.2 Quantification of Metabolite Concentrations

The ¹H-MRS data were first lineshape and eddy current corrected using combined QUALITY deconvolution and eddy current correction (QUECC) [64] with 400 QUALITY (quantification improvement by converting lineshapes to the Lorentzian type) points [65]. Residual water in the water suppressed spectrum was removed by subtracting peaks between 4.2 ppm and 5.7 ppm identified by a Hankel singular value decomposition fitting routine that required no prior knowledge.

Simulated 7 T semi-LASER prior knowledge templates that included an empirically measured macromolecule model were fitted in the time-domain to the water suppressed data using in-house software called fitMAN [66], which uses a Levenberg-Marquardt algorithm [67] to minimize the difference between the data and the template. A detailed description of the simulations and macromolecule model were described previously [53]. Briefly, the following metabolites were included in the prior knowledge template used to fit the water suppressed data from the PCC: NAA, *N*-acetylaspartyl glutamate (NAAG), choline (Cho), creatine (Cr), *myo*-inositol (Myo), glutamate (Glu), glutamine (Gln), glutathione (GSH), phosphorylethanolamine (PEth), *scyllo*-inositol (Scyllo), taurine (Tau), alanine (Ala), glucose (Glc), γ -aminobutyric acid (GABA), glycine (Gly), and lactate (Lac). The multiplets of NAA were fitted independently, because they experience a different rate of T_2 relaxation than the singlet at 2.01 ppm [68]. The prior knowledge template used to fit the water suppressed data from the left hippocampus did not include PEth and Gly, because the lower signal-to-noise ratio (SNR) of these data made it difficult to reliably fit these low amplitude signals.

To reduce the number of variables to be fitted, many parameters describing the line-shapes of the metabolites were constrained within the prior knowledge template (Table 2.1). Within metabolites, the peak amplitudes, shifts, and phases were fixed relative to one another. Relative peak amplitudes were not fixed between metabolites, since these are expected to vary across subjects. Relative peak positions and phases between some metabolites were fixed. For example, the positions and phases of low-amplitude metabolites (e.g. Ala, GABA, Lac) were linked to the positions and phases of higher-amplitude metabolites (e.g. NAA, *myo*-inositol, glutamate). A summary of the parameter constraints is given in Table 2.1.

Hippocampal and PCC metabolite concentrations ($[M]$) were obtained as previously described [69] by using the fitted and corrected amplitudes of the metabolite signals (\hat{S}_m), the corrected water signal amplitude (\hat{S}_W) from each spectroscopy voxel as an internal

2.2. Materials and Methods

Spectroscopy Voxel	Reference metabolite	Linked metabolites		Comments
		Shift	Phase	
Left Hippocampus	NAA	NAAG, Lac, Asp, Glu, Gln, GSH, GABA	NAAG, Lac, Asp, Glu, Gln, GSH, GABA, Myo, Ala, Glc, Scyllo, Tau	<ul style="list-style-type: none"> Shifts, phases, and amplitudes for Cho and Cr were not fixed relative to any reference metabolite. Cho and Cr were fitted independently.
	Myo	Ala, Glc, Scyllo, Tau		<ul style="list-style-type: none"> Relative peak amplitudes were not fixed between metabolites, since these may vary across subjects.
Posterior Cingulate Cortex	NAA	NAAG, Lac, Asp	NAAG, Lac, Asp, Ala, Glc, Gly, PEth, Scyllo, Tau, GABA	<ul style="list-style-type: none"> A single linewidth parameter was defined for all metabolites.
	Myo	Ala, Glc, Gly, PEth, Scyllo, Tau		<ul style="list-style-type: none"> A single delay time parameter was defined for all metabolites.
	Glu	Gln, GSH, GABA	Gln, GSH	

TABLE 2.1: A summary of relationships between metabolite parameters in the prior knowledge template [66]. Peak positions (shifts) and phases of low-amplitude metabolites were linked to the shifts and phases of higher-amplitude metabolites. Within metabolites, peak amplitudes, shifts, and phases were fixed relative to one another. The following metabolites were included in the prior knowledge template used to fit ^1H -MRS data from the PCC: NAA, NAAG, Cho, Cr, Myo, Glu, Gln, GSH, PEth, Scyllo, Tau, Ala, Glc, GABA, Gly and Lac. The prior knowledge template used to fit ^1H -MRS data from the left hippocampus did not include PEth and Gly.

reference, and the concentration of pure water (55.14 M) (Equation (2.1)):

$$[M] = \frac{\hat{S}_m}{\hat{S}_W} \times 55.14 \text{ M} \times \frac{1}{f_{GM} + f_{WM}} \quad (2.1)$$

where f_{GM} and f_{WM} are, respectively, the grey matter (GM) fraction and white matter (WM) fraction in the spectroscopy voxels. Multiplication by $\frac{1}{f_{GM} + f_{WM}}$ in Equation (2.1) produces tissue concentrations. Without this factor, concentrations within the entire volume of the spectroscopy voxel would be calculated. Since metabolite signals detected by ^1H -MRS originate from the tissue and not the cerebrospinal fluid (CSF), such voxel concentrations are biased by the CSF partial volume. Instead, tissue concentrations, which are not affected by the amount of CSF in the voxel, were calculated in the present study.

The corrected water signal amplitudes from the hippocampus and PCC were obtained by fitting the water unsuppressed data acquired from the respective regions with a prior knowledge template containing a single Lorentzian at 4.7 ppm. The fitted amplitude was first corrected for the number of averages used during data acquisition (N_{avg}^W), for any gain and scaling factors applied to the data (G^W), and for the number of ^1H -MRS visible nuclei in water (ρ^W). Next, a correction for the T_1 and T_2 relaxation rates of water in GM, WM, and CSF was applied. This requires the GM, WM, and CSF fractions in the spectroscopy voxels, as well as the T_1 and T_2 values of water in each tissue compartment. To estimate the GM, WM, and CSF fractions in the spectroscopy voxels, image voxels in the T_1 weighted anatomical images were first classified as GM, WM, or CSF using FMRIB's Automated Segmentation Tool (FAST) [70]. Then, within each spectroscopy voxel, the number of GM, WM, and CSF image voxels were divided by the total number of image voxels to obtain the GM fraction (f_{GM}), the WM fraction (f_{WM}), and CSF fraction (f_{CSF}), respectively. The T_1 values used for this correction were 2.1 s, 1.2 s, and 4.4 s for water in GM, WM, and CSF, respectively, and were obtained directly from literature [71]. The T_2 value of water in GM, WM, and CSF were estimated using T_2 measurements made by [68] in the occipital

2.2. Materials and Methods

lobe, motor cortex, and cerebellum. Estimated T_2 relaxation time constants of water were 47 ms, 45 ms, and 66 ms for GM, WM, and CSF, respectively. A correction for the relative proton density of water in GM (α_{GM}^W), WM (α_{WM}^W), and CSF (α_{CSF}^W) as compared to that of pure water was also incorporated into this correction. Values used for α_{GM}^W , α_{WM}^W , and α_{CSF}^W were 0.82, 0.73, and 1.00, respectively, and were obtained from [72]. The corrections applied to the fitted water signal amplitude (A_W) are summarized in Equation (2.2) adapted from [69], where R_{GM}^W , R_{WM}^W , and R_{CSF}^W are relaxation correction terms using the tissue specific T_1 and T_2 relaxation rates of water. For example, $R_{GM}^W = \left(1 - e^{\frac{-TR}{T_{1,GM}^W}}\right) \left(e^{\frac{-TE}{T_{2,GM}^W}}\right)$, where $T_{1,GM}^W$ is the T_1 of water in GM (2.1 s) and $T_{2,GM}^W$ is the T_2 of water in GM (47 ms). R_{WM}^W and R_{CSF}^W are similarly defined.

$$\hat{S}_W = \frac{A_W}{N_{avg}^W \rho^W G^W (f_{GM} \alpha_{GM}^W R_{GM}^W + f_{WM} \alpha_{WM}^W R_{WM}^W + f_{CSF} \alpha_{CSF}^W R_{CSF}^W)} \quad (2.2)$$

The fitted amplitudes of the metabolite signals were also corrected for the number of averages used during data acquisition (N_{avg}^m), for any gain and scaling factors applied to the data (G^m), for the number of ^1H -MRS visible nuclei in the metabolite (ρ^m), and for the T_1 and T_2 relaxation rates of metabolites in grey matter (GM) and white matter (WM). T_1 values of metabolites in GM and WM were obtained from literature, while T_2 values of metabolites in GM and WM were estimated using measurements made by Marjańska *et al.* [68] in the motor cortex and cerebellum, Wong *et al.* [53] in the motor cortex, and Ryan *et al.* [73] in the motor cortex.

Reported tissue fractions and metabolite T_2 values were incorporated into the estimation. The T_1 and T_2 values used for relaxation rate correction are summarized in Table 2.2. All corrections applied to the fitted metabolite amplitudes are summarized in Equation (2.3) from [69], where K is the number of peaks for metabolite m and A_k^m is the k th peak of the metabolite. R_{GM}^m and R_{WM}^m are relaxation correction terms using the T_1 and T_2 relaxation rates of metabolite m in GM and WM. For example, $R_{GM}^m = \left(1 - e^{\frac{-TR}{T_{1,GM}^m}}\right) \left(e^{\frac{-TE}{T_{2,GM}^m}}\right)$,

where $T_{1,GM}^m$ is the T_1 of metabolite m in GM and $T_{2,GM}^m$ is the T_2 of metabolite m in GM. R_{WM}^W is similarly defined.

$$\hat{S}_m = \frac{\sum_k^K A_k^m}{N_{avg}^m \rho^m G^m \left(\frac{f_{GM}}{f_{GM}+f_{WM}} R_{GM}^m + \frac{f_{WM}}{f_{GM}+f_{WM}} R_{WM}^m \right)} \quad (2.3)$$

2.2.3.3 Tractography and Diffusion Metrics in the Cingulum

To study the relationship between spectroscopy measurements to MRI-derived measures of neuronal injury in the cingulum, the left cingulum of each subject was reconstructed using diffusion-based tractography. Two separate segments, as defined by Wakana *et al.* [77], were identified: the cingulate gyrus portion that runs along the cingulate gyrus, and the hippocampal portion that runs along the ventral side of the hippocampus. As shown in Figure 2.2, the cingulate gyrus portion passed through the spectroscopy voxel placed in the PCC, while the hippocampal portion passed through both spectroscopy voxels.

The cingulate gyrus portion was identified using whole-brain tractography followed by an atlas-based technique to select only those tracts that belonged to the cingulum. First, the T_1 weighted anatomical image was transformed into diffusion-space using the previously found transformation matrix. From this image, a WM mask was generated using FSL FAST. Then, Bayesian probabilistic tracking with a diffusion tensor model [78] was performed on the brain-extracted diffusion weighted images (Figure 2.3a) using every voxel in the WM mask as a seed voxel. The produced tracts were refined using an exclusion region of interest (ROI) defined based on the left cingulum/cingulate gyrus mask (label #5) from the 2 mm probabilistic John's Hopkins white matter tractography atlas thresholded at zero [79, 80]. This thresholded atlas was included with FSL. The mask was transformed from MNI152-space into the subject-specific diffusion-space using the previously found transformation matrices (Figure 2.3b¹). Only tracts that lay completely within this mask were retained. Any tracts that touched the edge of the mask were discarded. Tracts that were shorter than

2.2. Materials and Methods

Metabolite	T ₁ [s]		Reference	T ₂ [ms]		Reference
	GM	WM		GM	WM	
NAA	1.83	1.9	Xin <i>et al.</i> [74]	224	143	Estimated using reported values from Marjańska <i>et al.</i> [68], Wong <i>et al.</i> [53], and Ryan <i>et al.</i> [73]
NAAG	1.21	0.94		224 ^b	143 ^b	
Ala	1.28 ^a	1.19 ^a		201 ^a	71 ^a	
GABA	1.334 ^d	1.334 ^d	Andreychenko <i>et al.</i> [75]	87 ^d	87 ^d	Andreychenko <i>et al.</i> [75]
Asp	1.28 ^a	1.19 ^a	Xin <i>et al.</i> [74]	201 ^a	71 ^a	Estimated using reported values from Marjańska <i>et al.</i> [68], Wong <i>et al.</i> [53], and Ryan <i>et al.</i> [73]
Cho	.151	1.32		248	102	
Cre	1.74	1.78		148	119	
Glc	1.28 ^a	1.19 ^a		201 ^a	71 ^a	
Glu	1.61	1.75		176	57	
Gln	1.64	1.74		176 ^c	57 ^c	
GSH	1.14	1.06		86	89	
Gly	1.28 ^a	1.19 ^a		201 ^a	71 ^a	
Myo	1.28	1.19		201	71	
Scy	1.31	1.23		148	115	
Lac	1.28 ^a	1.19 ^a		201 ^a	71 ^a	
PEth	1.31	1.32		201	71	
Tau	2.15	2.09		142	86	

^a T₁ and T₂ values of metabolites which could not be determined were assumed to be similar to that of Myo [76, 68].

^b T₂ values of NAAG were assumed to be similar to that of NAA [68].

^c T₂ values of Gln were assumed to be similar to that of Glu [68].

^d T₁ and T₂ values of GABA were assumed to be the same in both GM and WM, as Andreychenko *et al.* [75] did not report separate values for GM and WM.

TABLE 2.2: A summary of the metabolite-specific T₁ and T₂ values used for relaxation correction of the fitted metabolite signals. T₁ values were obtained directly from the literature, whereas T₂ values were estimated using different reported values in literature (see text for details). The same T₁ and T₂ values were used for spectra acquired from both the hippocampus and the PCC.

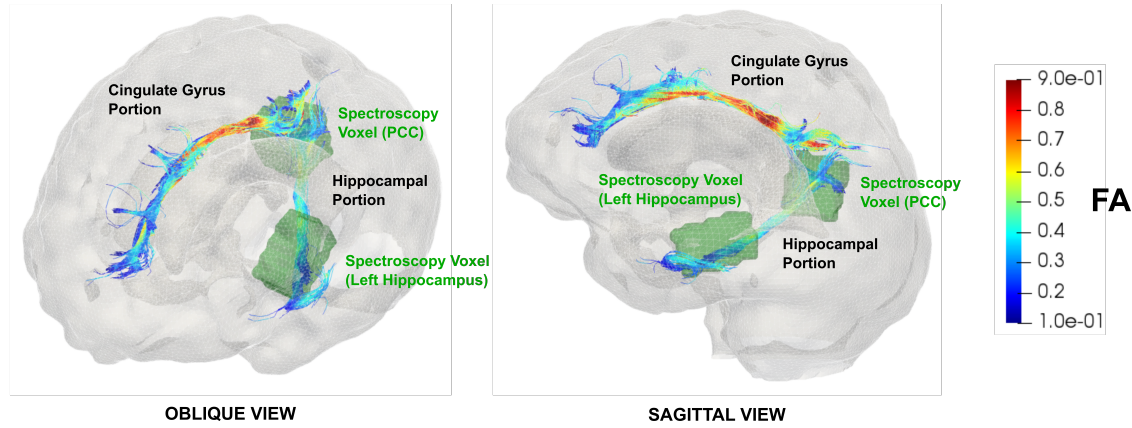


FIGURE 2.2: Three dimensional transparent whole brain (grey) of a single subject in two different orientations showing the position of the spectroscopy (green shaded regions) in relation to the left cingulum fibre tracts reconstructed using diffusion-based probabilistic tractography. Two separate segments as defined by Wakana *et al.* [77] were identified (black labels): the cingulate gyrus portion that runs along the cingulate gyrus, and the hippocampal portion that runs along the ventral side of the hippocampus. The cingulate gyrus portion passed through the spectroscopy voxel (green shaded region) placed in the PCC, while the hippocampal portion passed through both spectroscopy voxels (green shaded regions). The colours in the fibre tracts represent the FA values along the cingulum.

the mean tract length minus one standard deviation were also discarded. An example of the result is shown in Figure 2.3c¹.

The hippocampal portion of the cingulum was also identified using Bayesian tractography. However, instead of using an atlas, the tractography was constrained by the spectroscopy voxels. Every image voxel within the left hippocampal spectroscopy voxel was used to seed the tractography and every image voxel within the PCC spectroscopy voxel was used as a waypoint. With this approach, only tracts that began in the hippocampal spectroscopy voxel and passed through the PCC spectroscopy voxel were identified. Tracts were grouped based on geometric similarity using spectral clustering [81, 82] and only the cluster of tracts with a geometry that matched the hippocampal portion of the cingulum was retained (Figure 2.3b²). Of those tracts, any that were shorter than the mean tract length of the cluster minus one standard deviation were also discarded. An example of the result is shown in Figure 2.3c².

The identified tracts were then modelled as cubic B-splines and re-parameterized to 33 vertices to facilitate between-group statistical analysis [83]. Diffusion metrics were assigned to each vertex of the B-spline by selecting the metric value from the corresponding image voxel in the previously generated FA, RD, and AxD maps. An example of this is shown in Figure 2.2, Figure 2.3c¹, and Figure 2.3c², where the colours represent the FA measurement along the tracts. Tissue T_1 values were also assigned to each vertex, by first transforming the T_1 map to diffusion-space using the previously found transformation matrix, and then selecting the T_1 value from the corresponding image voxel. The metrics were averaged across corresponding vertices to obtain mean measures of FA, RD, AxD, and T_1 along the cingulum. An example of the mean FA plotted with respect to position along the cingulum for a single subject is shown in Figure 2.3d¹ and Figure 2.3d².

2.2.4 Statistical Analyses

Statistical analyses for the spectroscopy data were performed using GraphPad Prism 7.00 for Windows (GraphPad Software, La Jolla, California, United States of America). Before analysis, outliers were first identified using Grubbs' method [84] with the significance level (α) set to 0.05. As a result, one AD subject was an outlier and removed from the analysis of the hippocampal spectroscopy data. A one-way analysis of variance (ANOVA) was performed for each measured metabolite to identify between-group differences at $\alpha = 0.05$. If a significant difference among group means was found, a post-hoc between-group comparison using Fisher's least significant differences (LSD) test was performed. For three groups at $\alpha = 0.05$, Fisher's LSD guarantees that the familywise error rate (FWER) does not exceed 0.05 [85].

Cognitive testing data were analyzed in a similar way. An ANOVA was performed for each of the scores obtained from the CSR and BCFC tests to identify between-group differences at $\alpha = 0.05$. If the group effect was significant, a post-hoc LSD test with $\alpha = 0.05$ was performed to identify statistically significant differences between groups.

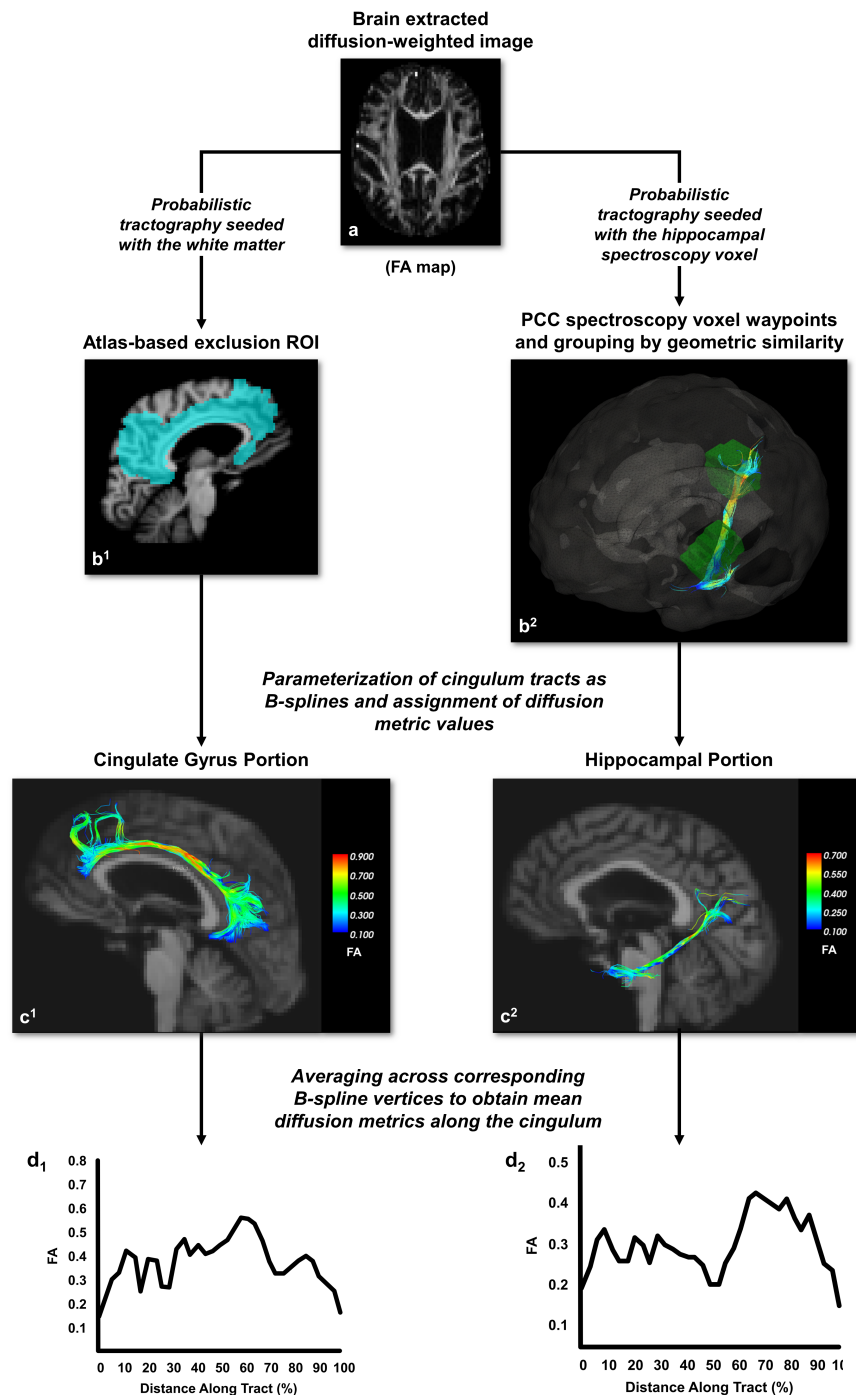


FIGURE 2.3: Diffusion-based tractography of the left cingulum. For both the cingulate gyrus portion and hippocampal portion of the cingulum, Bayesian probabilistic tracking with a diffusion tensor model [78] was performed on the brain-extracted diffusion weighted images shown in (a).

2.2. Materials and Methods

FIGURE 2.3: The produced tracts were refined using an atlas-based exclusion region of interest (b^1), to identify the cingulate gyrus portion of the cingulum (c^1). Using the spectroscopy voxels as seeds and waypoints, and discarding those tracts that were not geometrically similar to the hippocampal portion of the cingulum (b^2), the hippocampal portion of the cingulum was identified (c^2). The identified tracts of the cingulum were modelled as B-splines, and diffusion metrics were assigned to each vertex of the B-spline, as shown in (c^1) and (c^2), where the colours represent the FA values along the cingulum. These metrics were averaged across corresponding vertices to obtain mean measures along the cingulum, as shown in (d^1) and (d^2).

To determine whether along-cingulum metrics changed between groups, a linear mixed effect regression as described in [83] was performed for each metric and for each pairwise comparison. The regression contains a vertex-by-group interaction that tests whether the effect of group on a metric varies based on position along the tract. If an ANOVA of the vertex-by-group interaction term was significant at $\alpha = 0.05$, linear mixed effect regressions were performed at each vertex to test whether there was an effect of group on a metric. If the effect was significant at a level of $\alpha = 0.05$, the metric was considered to be different between groups at that tract position. Statistical analyses of along-cingulum diffusion measures were performed in R [86].

For both the hippocampal and cingulate gyrus portions of the cingulum, the diffusion metric values in the largest continuous region of statistical difference between groups were averaged and used to examine association with the spectroscopy measurements that were significantly different between groups. The averaged diffusion metric values were also correlated with the CSR and BCFC scores. Finally, the spectroscopy measurements that differed between groups were correlated with the CSR and BCFC scores. All correlations were Pearson correlations performed at the one-tailed α of 0.05 using GraphPad Prism 7.00.

2.3 Results

2.3.1 Magnetic Resonance Spectroscopy

Spectra acquired in the hippocampus (Figure 2.1c) had an average (\pm SD) SNR of 28 ± 10 , defined as the height of the absolute signal at the position of the NAA CH_3 peak divided by the standard deviation (SD) of the noise. The average (\pm SD) linewidth was 17.4 ± 6.3 Hz. The voxel contained on average (\pm SD) $56 \pm 8\%$ grey matter, $25 \pm 6\%$ white matter, and $19 \pm 9\%$ CSF. There was a significant group effect on glutamate concentration in the left hippocampus ($F(2,24) = 3.61$, $p < 0.05$). As shown in Figure 2.1e, post-hoc analysis indicated that MCI and AD subjects had significantly lower left hippocampal glutamate levels than NECs ($p < 0.05$). Group differences were not detected in other metabolite concentrations in the left hippocampus.

Spectra acquired in the PCC (Figure 2.1d) had an average (\pm SD) SNR of 94 ± 24 and an average (\pm SD) linewidth of 14.0 ± 3.5 Hz. The voxel contained on average (\pm SD) $52 \pm 7\%$ grey matter, $29 \pm 6\%$ white matter, and $19 \pm 8\%$ CSF. In the PCC, a significant group effect on NAA concentration was found ($F(2,30) = 6.91$, $p < 0.01$). Post-hoc analysis indicated that AD subjects had significantly lower NAA levels in the PCC than NECs ($p < 0.01$, Figure 2.1f). MCI subjects also had significantly lower NAA levels in the PCC than NECs ($p < 0.05$, Figure 2.1f). Group differences were not detected in other metabolite concentrations in the PCC.

2.3.2 Diffusion in the Cingulum

In the hippocampal portion of the cingulum, no significant vertex-by-group effect was found for the FA metric (Figure 2.4b). No significant vertex-by-group effects were found for any metric when comparing NEC subjects to MCI subjects. However, when comparing NEC subjects to AD subjects, a significant vertex-by-group effect was found for the

2.3. Results

RD ($F(32,640) = 1.68, p < 0.05$), AxD ($F(32,640) = 2.78, p < 1 \times 10^{-6}$), and T_1 ($F(32,640) = 1.935, p < 0.01$, Figure 2.4e) metrics. A significant vertex-by-group effect was also found for the RD ($F(32,352) = 1.78, p < 0.01$), AxD ($F(32,352) = 1.95, p < 0.01$), and T_1 ($F(32,352) = 2.08, p < 0.001$) metrics when comparing MCI subjects to AD subjects. Along-tract analyses showed that the AD group had significantly higher RD ($p < 0.05$, Figure 2.4c), AxD ($p < 0.05$, Figure 2.4d), and T_1 ($p < 0.05$, Figure 2.4e) in the first 25% of the hippocampal cingulum than the NEC and MCI groups. These differences are shown in the p -value plots provided in Figure 2.4b-e, where $p < 0.05$ between groups is highlighted in green.

In the cingulate gyrus portion of the cingulum, no significant vertex-by-group effect was found for any metric when comparing NEC subjects to MCI subjects. A significant vertex-by-group effect was found for the FA ($F(32,704) = 1.82, p < 0.01$) and RD ($F(32,704) = 1.46, p < 0.05$) when comparing NEC subjects to AD subjects. When comparing MCI subjects to AD subjects, a significant vertex-by-group effect was also found for the FA ($F(32,448) = 1.52, p < 0.05$), and RD ($F(32,448) = 1.95, p < 0.01$) metrics. No other significant vertex-by-group effects were found. Along-tract analyses showed that the AD group had significantly lower FA ($p < 0.05$, Figure 2.5b) and higher RD ($p < 0.05$, Figure 2.5c) than the NEC and MCI groups in the last 60-90% of the cingulate gyrus portion of the cingulum.

2.3.3 Tests of Episodic Memory

Significant group effects were found for the CSR verbatim z-scores (immediate: $F(2,31) = 15.9, p < 0.0001$; delayed: $F(2,31) = 20.92, p < 0.0001$) and the CSR paraphrase z-scores (immediate: $F(2,31) = 16.44, p < 0.0001$; delayed: $F(2,31) = 28.45, p < 0.0001$). Post-hoc analysis showed that MCI and AD subjects had lower verbatim scores than NEC subjects (immediate: $p < 0.001$, delayed: $p < 0.0001$). MCI and AD subjects also had lower

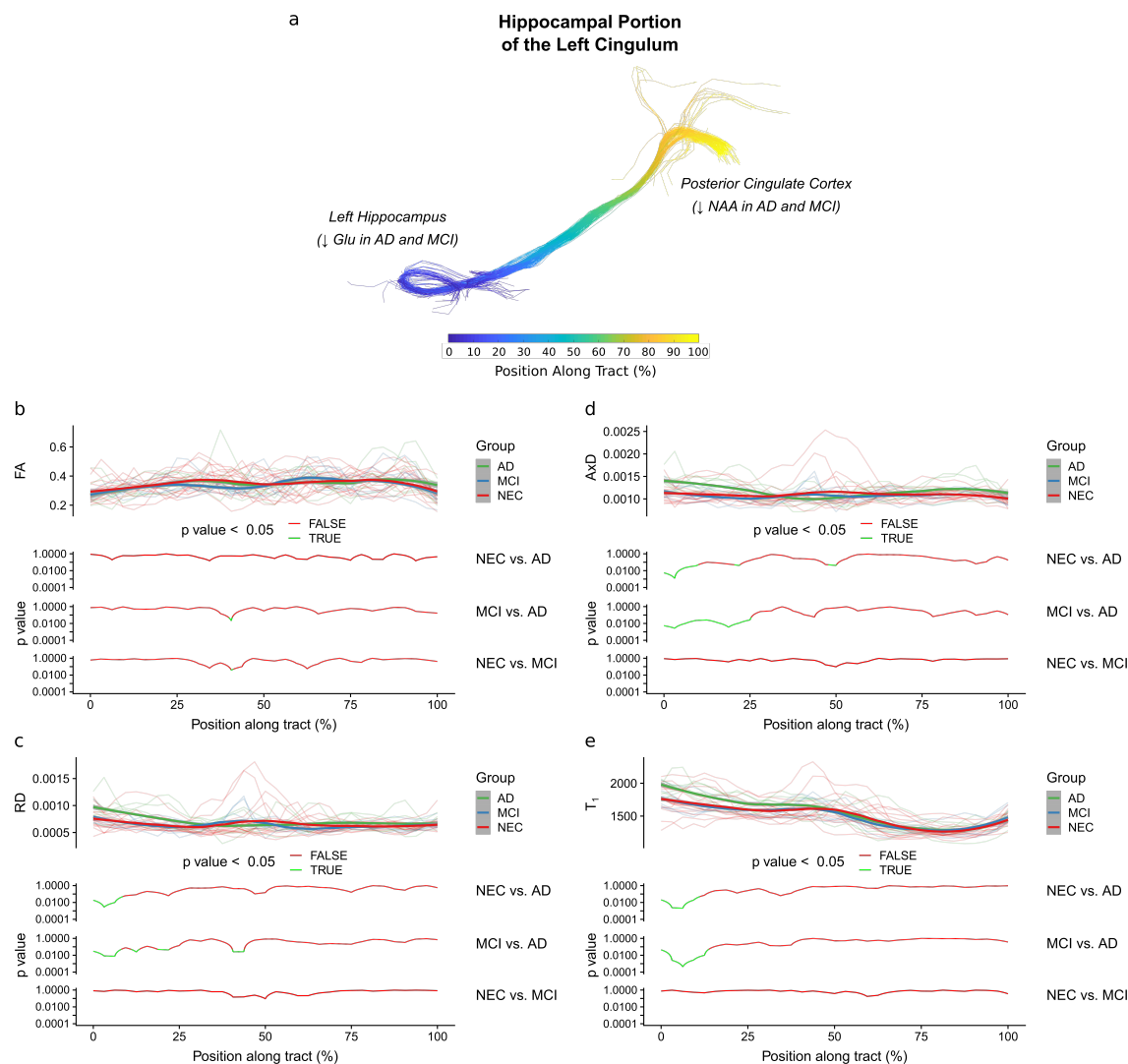


FIGURE 2.4: Diffusion metrics plotted as a function of the position along the hippocampal portion of the cingulum. The position along this tract is defined in (a), with the start of the tract in the left hippocampus and the end of the tract in the posterior cingulate cortex. In each of (b), (c), (d), and (e), the diffusion metric of individual subjects at each position along the tract are shown semi-transparently in the background of the top panels and are overlaid with the smoothed estimates of the group means (thick lines). The pointwise 95% confidence intervals are shown in grey. In the bottom panels, the results of between-group analyses are plotted with respect to position. No differences between groups were found along the tract for the FA metric (b). As shown in (c), (d), and (e), respectively, the AD group had significantly higher RD ($p < 0.05$), AxD ($p < 0.05$), and T_1 ($p < 0.05$) in the first 25% of the hippocampal cingulum than the NEC and MCI groups. This pattern of changes in the AD group may be interpreted as the result of a loss of neurons in the hippocampus.

2.3. Results

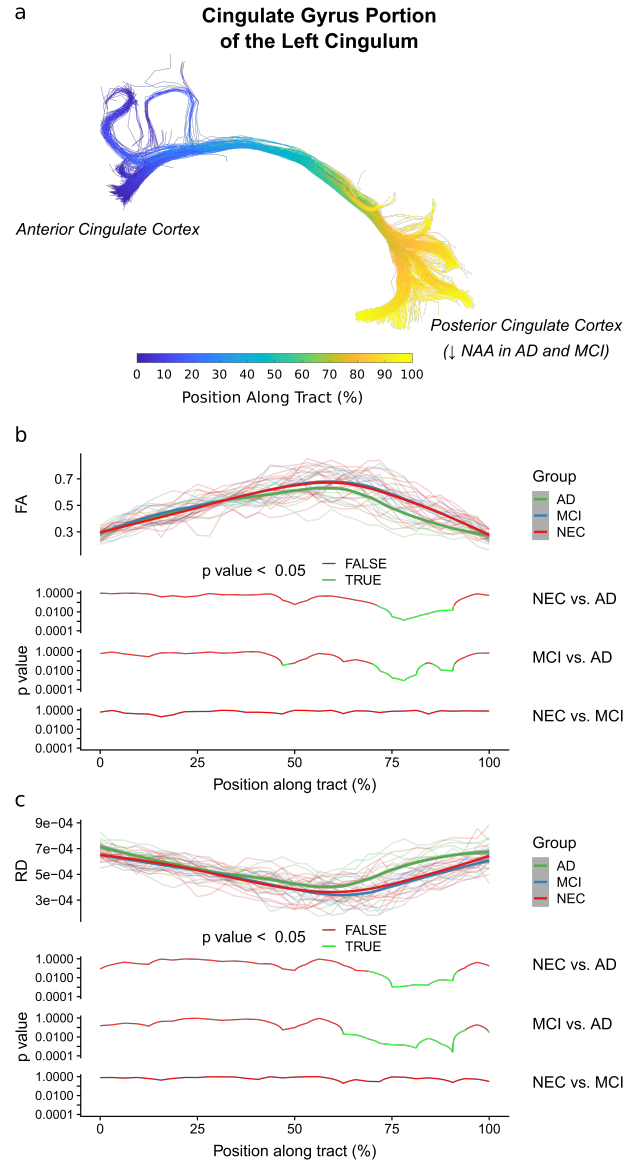


FIGURE 2.5: Diffusion metrics (FA and RD) as a function of the position along the cingulate gyrus portion of the cingulum. The position along this tract is defined in (a), with the start of the tract in the anterior cingulate cortex and the end of the tract in the posterior cingulate cortex. In (b) and (c), the diffusion metric of individual subjects at each position along the tract are shown semi-transparently in the background of the top panels and are overlaid with the smoothed estimates of the group means (thick lines). The pointwise 95% confidence intervals are shown in grey. In the bottom panels, the results of between-group analyses are plotted with respect to position. As shown in (b) and (c), respectively, the AD group had significantly lower FA ($p < 0.05$) and higher RD ($p < 0.05$) than the NEC and MCI groups in the last 60-90% of the cingulate gyrus portion of the cingulum. This pattern of changes in the AD group may be interpreted as a demyelination process.

paraphrase scores (immediate: $p < 0.001$, delayed: $p < 0.0001$). For the BCFC test, a significant group effect was found for the BCFC delayed verbatim z-score ($F(2,31) = 17.9$, $p < 0.0001$). Post-hoc analysis revealed that MCI and AD subjects had lower scores than NEC subjects ($p < 0.0001$). Means and standard deviations of the test scores are provided in Supplementary Table 2.S1.

2.3.4 Correlations

Metabolite levels in the hippocampus and PCC shown to be different between groups were examined for associations with diffusion measures in the cingulum (Figure 2.6). Specifically, left hippocampal glutamate level was inversely correlated with the average RD ($r = -0.40$, $p < 0.05$, Figure 2.6a) and AxD ($r = -0.51$, $p < 0.01$, Figure 2.6b) in the first 25% of the hippocampal cingulum. NAA levels in the PCC were also inversely correlated with the average RD ($r = -0.46$, $p < 0.01$, Supplemental Figure 2.S1a) and AxD ($r = -0.35$, $p < 0.05$, Supplemental Figure 2.S1b) in this portion of the cingulum. In the last 60-90% of the cingulate gyrus portion of the cingulum, NAA level in the PCC was inversely correlated with RD ($r = -0.42$, $p < 0.05$, Figure 2.6c), T_1 ($r = -0.61$, $p < 0.001$, Figure 2.6d), and positively correlated with FA ($r = 0.37$, $p < 0.05$, Figure 2.6e).

Metabolite levels in the hippocampus and PCC that were different between groups were also examined for associations with measures of episodic memory performance (Figure 2.7). Left hippocampal glutamate levels were positively correlated with the delayed CSR paraphrase z-score ($r = 0.40$, $p < 0.01$, Figure 2.7a), the delayed BCFC z-score ($r = 0.40$, $p < 0.05$, Figure 7b), and the delayed CSR verbatim z-score ($r = 0.39$, $p < 0.05$, Supplemental Figure 2.S2). NAA levels in the PCC were also positively correlated with CSR and BCFC z-scores. Specifically, NAA in the PCC was correlated with the delayed CSR paraphrase z-score ($r = 0.43$, $p < 0.01$, Figure 2.7c), the delayed BCFC z-score ($r = 0.46$, $p < 0.01$, Figure 2.7d), the immediate CSR verbatim z-score ($r = 0.43$, $p < 0.01$, Supplemental Figure 2.S3a), the immediate CSR paraphrase z-score ($r = 0.47$, $p < 0.01$,

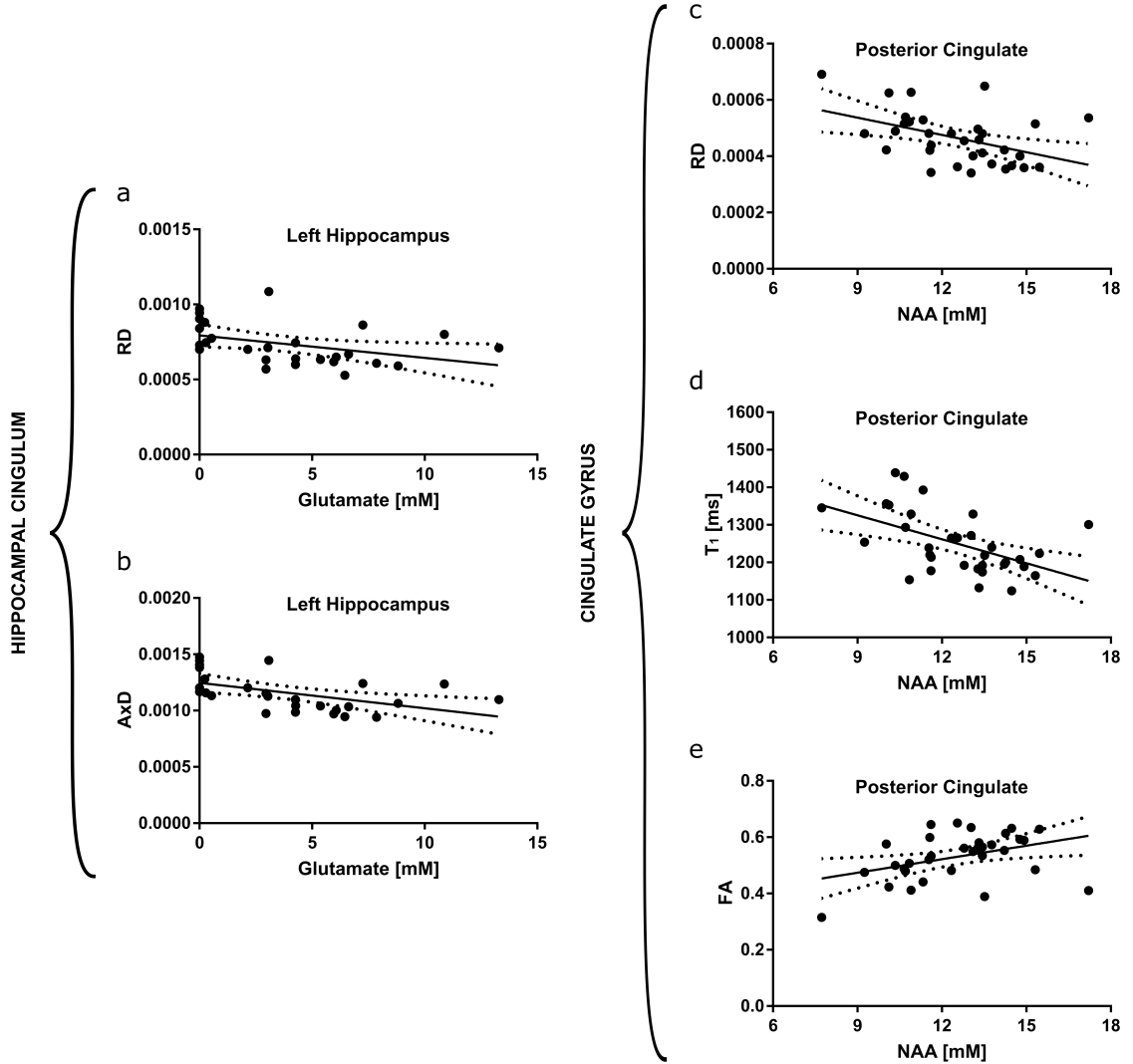


FIGURE 2.6: Significant correlations between the left hippocampal glutamate concentration and the average RD ($r = -0.40$, $p < 0.05$) and AxD ($r = -0.51$, $p < 0.01$) in the first 25% of the hippocampal portion of the cingulum are shown with 95% confidence bands in (a) and (b), respectively. Significant correlations between the NAA concentration in the PCC and the average RD ($r = -0.42$, $p < 0.05$), T_1 ($r = -0.61$, $p < 0.001$), and the average FA ($r = 0.37$, $p < 0.05$) in the last 60-90% of the cingulate gyrus portion of the cingulum are shown with 95% confidence bands in (c), (d), and (e), respectively.

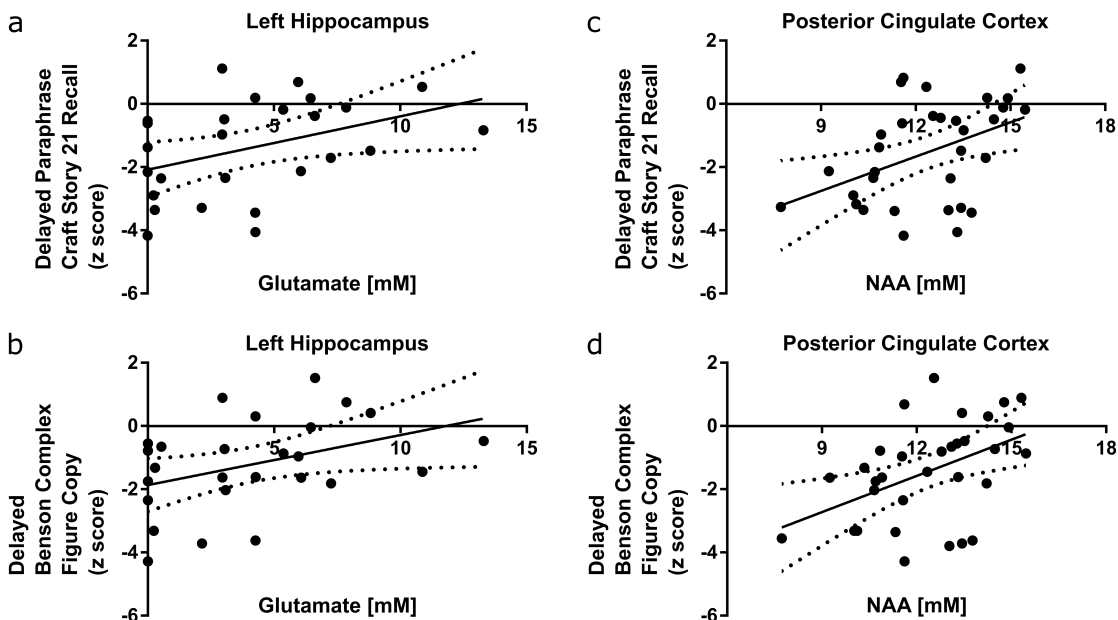


FIGURE 2.7: Significant correlations between left hippocampal glutamate concentration and the delayed Craft Story 21 Recall (CSR) paraphrase score ($r = 0.40$, $p < 0.05$) and the delayed Benson Complex Figure copy (BCFC) score ($r = 0.39$, $p < 0.05$) are shown with 95% confidence bands in (a) and (b), respectively. Significant correlations between posterior cingulate NAA concentration and the delayed CSR paraphrase score ($r = 0.43$, $p < 0.05$) and the delayed BCFC score ($r = 0.46$, $p < 0.01$) are shown with 95% confidence bands in (b) and (c), respectively.

Supplemental Figure 2.S3b), and the delayed CSR verbatim z-score ($r = 0.39$, $p < 0.05$, Supplemental Figure 2.S3c).

2.4 Discussion

Using ^1H -MRS at 7 T, this study measured concentrations of metabolites within the episodic memory system of people with normal cognition and of people with a clinical diagnosis of MCI and probable AD. Significant decreases in left hippocampal glutamate concentration and in posterior cingulate cortex NAA concentrations were found (Figure 2.1) in the MCI and AD groups. Within the cingulum, diffusion-based indicators of white-matter microstructural integrity showed that the AD group had significantly higher RD,

AxD, and T_1 in the first 25% of the hippocampal cingulum (Figure 2.4) and significantly lower FA and higher RD in the last 60-90% of the cingulate gyrus portion of the cingulum (Figure 2.5) compared to the NEC and MCI groups. Both hippocampal glutamate concentration and NAA concentration in the PCC were significantly associated with altered water diffusion and T_1 relaxation within the cingulum (Figure 2.6), as well as episodic memory performance measured by the CSR and BCFC neuropsychological tests (Figure 2.7).

2.4.1 Posterior Cingulate Cortex

Compared to NEC subjects, both MCI and AD subjects had significantly lower NAA concentration in the PCC. This result is consistent with previous studies that have also reported lower NAA concentration in the PCC of AD and MCI subjects compared to NECs [43, 41, 42].

Since NAA synthesis in the brain requires acetyl-coenzyme A (acetyl CoA) levels that exceed neuronal metabolic requirements [87], a decrease in NAA concentration in the PCC likely indicates that energy reserves are low in this region. Indeed, studies using FDG-PET have consistently shown energy deficits in the PCC of people with AD [88, 89, 90, 91]. This energy deficit would result in lower acetyl CoA levels and compromise NAA synthesis.

Impaired NAA synthesis could have detrimental downstream effects. NAA is synthesized in neurons, but the enzyme that catabolizes NAA into its component aspartate and acetate moieties is localized exclusively to oligodendrocytes [92, 93, 94]. The sequential action of this enzyme, aspartoacylase II (ASPA-II), along with acetyl CoA synthetase-1 (AceCS-1), will convert NAA-derived acetate into acetyl CoA, which could be used by oligodendrocytes for the synthesis of myelin-associated lipids [95]. Thus, impaired NAA synthesis could negatively affect myelin repair and remyelination processes.

MRI-derived measures of white matter microstructural integrity in the current study are consistent with this interpretation. Specifically, the last 60-90% of the cingulate gyrus

portion of the cingulum, which corresponds anatomically to the posterior cingulate cortex (Figure 2.2, Figure 2.3c¹), showed significant differences in MRI-derived measures of microstructural integrity between AD subjects and NEC subjects. AD subjects had lower FA, higher RD, but no difference in AxD. This pattern of changes in diffusion metrics is characteristic of an underlying demyelination process [96]. Further, NAA concentration in the PCC was significantly associated with this pattern of change – that is, lower NAA concentration was associated with lower FA and higher RD. These results, together with the finding that a lower NAA concentration in the PCC was significantly associated with worse CSR and BCFC scores, suggests that NAA deficit in the PCC of people with AD could indicate a demyelinating process in the region that manifests as poorer episodic memory performance.

Importantly, lower NAA concentrations were observed in both MCI and AD subjects compared to NEC subjects, whereas differences in diffusion metrics were only observed in AD subjects compared to NECs. This suggests that a decrease in the posterior cingulate NAA concentration may precede microstructural changes indicative of demyelination in the region, although a longitudinal study would be required to confirm this hypothesis.

2.4.2 Hippocampus

In the left hippocampus, lower glutamate levels in MCI and AD subjects were observed in the current study. Consistent with this result, a previous study by our group [39] at 4T in a different cohort also found significantly lower hippocampal glutamate concentration in AD subjects compared to NEC subjects, but no significant differences between MCI and NEC subjects. The lower glutamate levels observed in MCI subjects in the current study is likely due to the increased sensitivity of 7 T MR spectroscopy or could be attributed to differences in the cohort studied. An important methodological difference to consider is that Rupsingh *et al.* positioned the spectroscopy voxel in the right hippocampus, while the left hippocampus was examined in the present study. Measurements in the left hippocampus

may be sensitive to earlier changes exhibited at the MCI stage, as it is well-known that left hippocampal atrophy precedes right hippocampal atrophy in AD [23, 97].

The MRI-derived measures of microstructural integrity showed that compared to NEC subjects, AD subjects had significantly greater RD, AxD, and T_1 in the first 25% of the left hippocampal cingulum, which corresponds anatomically to the left hippocampus (Figure 2.2, Figure 2.3c²). The pattern of RD and AxD changes is characteristic of increased CSF [98], which could result from overall tissue atrophy. The observed T_1 differences also support this interpretation, as the T_1 of CSF water is greater than the T_1 of tissue bound water [71]. Thus, the reduced left hippocampal glutamate concentrations observed in AD subjects may be a result of a loss of neurons in the hippocampus, a region of the brain that is highly dependent on glutamate signalling [99, 100].

Interestingly, these microstructural changes were not observed in the MCI subjects, which suggests that the reduced glutamate concentration observed in the MCI subjects was not the result of the loss of glutamatergic neurons. Rather, it may be related to an energy deficit in the hippocampus. Reduced glucose metabolism will reduce citrate production in neurons, in turn reducing ATP production via the tricarboxylic acid (TCA) cycle. Indeed, reduced glucose metabolism in the hippocampus of individuals with MCI have been previously reported [31, 101]. To meet the energy demands of the neuron, glutamate and oxaloacetate can be used by aspartate aminotransferase (AAT) as alternative substrates for α -ketoglutarate production in a truncated TCA cycle [102]. Interestingly, excess acetate is produced in this process, which may be acetylated into NAA by *L*-aspartate *N*-acetyltransferase (Asp-NAT). Increased NAA production would facilitate the AAT reaction, by removing the product inhibition from acetate. In fact, there is evidence of an upregulated rate of NAA synthesis in AD [103]. Increased NAA production and increased glutamate consumption due to neuronal energy deficit could also explain why a significant reduction in left hippocampal glutamate concentration, but no difference in left hippocampal NAA concentration, was observed in the present study.

This result from the current study is consistent with results previously published by our group in the right hippocampus, in which no differences in right hippocampal NAA concentration were found [39]. However, others have reported NAA concentration differences in mean bilateral hippocampal NAA concentrations between AD and NEC subjects [40], as well as significant differences in left hippocampal NAA concentrations between NEC, MCI, and AD subjects [41]. Methodological differences with respect to the corrections for the relaxation rates of metabolite signal in each of the GM, WM, and CSF compartments of the spectroscopy voxel could explain why lower NAA was not observed in either the current study or in Rupsingh *et al.*

Left hippocampal glutamate concentration was also observed to be significantly associated with better CSR and BCFC scores. This, together with the previously discussed results, suggests that lower glutamate concentration in the left hippocampus could indicate impaired neuro-energetics or a loss of glutamatergic neurons, ultimately manifesting as poorer episodic memory performance.

2.4.3 Study Limitations

There are several limitations to the present study that should be considered. First, the generalizability of the results is limited by the small sample size. Nevertheless, significant differences in metabolite concentrations and diffusion metrics were observed, which may be due to the improved precision of both spectroscopy and diffusion tensor imaging at the high magnetic field (7 T) used. In particular, the size of the group effect as measured using Hays' ω^2 [104] was large for both the hippocampal glutamate concentration ($\omega^2 = 0.162$) and the posterior cingulate NAA concentration ($\omega^2 = 0.264$), implying that the study was sufficiently powered. The results of the present study are also consistent with prior studies, providing further confidence in the results. Specifically, other studies have independently shown decreased glutamate in the hippocampus [39, 105], decreased NAA in the posterior cingulate cortex [42, 43, 105, 106], and microstructural changes in the limbic system [22, 30,

107, 108] in individuals with AD. Also, power was increased for all correlational analyses as these were done using all study subjects with successfully acquired spectroscopy data (N=27 for hippocampal data and N=33 for PCC data), without consideration for group membership.

Second, participants of this study with AD likely reflected a subset of the clinical population. In addition to changes in episodic memory, many individuals diagnosed with AD also present with neuropsychiatric symptoms such as apathy, anxiety, agitation, and depression which typically worsen as the disease progresses [109, 110]. However, the exclusion criteria used in the present study excluded potential participants with neuropsychiatric symptoms. All participants in the current study had GDS scores that were less than 6, indicating none had depressive symptoms. Thus, MCI and AD participants of this study likely reflect a clinical population with mild disease that lies earlier along the AD continuum. Furthermore, the inclusion of only subjects without neuropsychiatric symptoms eliminates this variable as a cause of the metabolic and microstructural changes observed in the current study.

Third, the present study used single-voxel ^1H -MRS to study metabolite concentrations in the left hippocampus and the posterior cingulate cortex. The metabolite concentration measured using single-voxel ^1H -MRS is the average tissue concentration within the entire spectroscopy voxel. As a result, it is not possible to discern whether the observed differences in hippocampal glutamate concentrations arise from the metabolic pool or the neurotransmitter pool. In the PCC, it is also not possible to say whether the observed differences in the NAA concentration are localized to the neuronal compartment, the oligodendrocyte compartment, or both compartments. Another point of caution is that the method of metabolite quantification used in the present study incorporated T_1 and T_2 relaxation correction using values obtained from literature and assumed that metabolite T_1 and T_2 values in GM and WM do not change with disease. This was done as it wasn't possible to measure

subject-specific metabolite T_1 and T_2 values due to scan-time constraints. It is also important to note here that a field strength of 7 Tesla was used in the present study. ^1H -MRS at ultra-high magnetic fields (4 Tesla and above) benefits from increased SNR and greater spectral dispersion. This is especially important for glutamate detection, as there is better separation of glutamate from the overlapping resonances of glutamine and GABA. However, at clinical field strengths (3 Tesla and below), focused detection of glutamate changes may benefit from spectral editing techniques such as MEGA-sLASER or MEGA-PRESS [111, 112].

Fourth, an atlas-based method of tractography was used, rather than the gold standard of guiding the tractography using manually drawn inclusion and exclusion ROIs. Although an atlas-based method does not suffer from problems such as operator experience, intra- and inter-operator reproducibility, and ROI placement feasibility [113], it is affected by the quality of the registration between the subject scan and the atlas. However, even with just a simple linear registration to the atlas, Zhang *et al.* has shown good agreement between manually-guided tractography and an atlas-based technique employing the same atlas as that used in the present study [114]. Despite the potential loss of precision with an atlas-based approach to tractography, we were still able to show statistically significant differences in diffusion metrics along the cingulum between groups.

2.5 Conclusion

This cross-sectional study compared metabolite concentrations in the left hippocampus and in the PCC between people with MCI, people with AD, and NECs. NAA concentration in the PCC and glutamate concentration in the left hippocampus were significantly lower in both MCI and AD subjects and were significantly associated with both MRI-derived measures of microstructural changes in the cingulum and with episodic memory performance. The observed metabolite differences and associated microstructural differences are

consistent with brain energy deficits caused by AD pathology. Thus, metabolite concentrations measured using ^1H -MRS may provide valuable insight into the underlying metabolic and microstructural processes of episodic memory impairment.

2.6 Acknowledgements

This study was funded by the Premier Research Grant from the Alzheimer Foundation of London and Middlesex, the Canada First Research Excellence Fund (CFREF), Brain Canada, and the Canadian Institutes of Health Research MD/PhD Studentship. Thanks to Charlene Bartha for assistance with subject recruitment, to Jason Kai for assistance with the tractography analyses, and to Trevor Szekeres and Joe Gati for help in acquiring the imaging and spectroscopy data.

2.7 References

- [1] P. Scheltens et al. "Alzheimer's disease". In: *The Lancet* 388.10043 (July 2016), pp. 505–517.
- [2] H. W. Querfurth and F. M. LaFerla. "Alzheimer's Disease". In: *New England Journal of Medicine* 362.4 (Jan. 2010), pp. 329–344.
- [3] M. S. Albert et al. "The diagnosis of mild cognitive impairment due to Alzheimer's disease: Recommendations from the National Institute on Aging-Alzheimer's Association workgroups on diagnostic guidelines for Alzheimer's disease". In: *Alzheimer's and Dementia* 7.3 (May 2011), pp. 270–279. arXiv: NIHMS150003.
- [4] G. M. McKhann et al. "The diagnosis of dementia due to Alzheimer's disease: Recommendations from the National Institute on Aging-Alzheimer's Association workgroups on diagnostic guidelines for Alzheimer's disease". In: *Alzheimer's and Dementia* 7.3 (May 2011), pp. 263–269. arXiv: NIHMS150003.

- [5] C. R. Jack et al. “¹¹C PiB and structural MRI provide complementary information in imaging of Alzheimer’s disease and amnesic mild cognitive impairment”. In: *Brain* 131.3 (Mar. 2008), pp. 665–680.
- [6] K. Kantarci et al. “White-matter integrity on DTI and the pathologic staging of Alzheimer’s disease”. In: *Neurobiology of Aging* 56 (Aug. 2017), pp. 172–179.
- [7] R. Sperling. “The potential of functional MRI as a biomarker in early Alzheimer’s disease”. In: *Neurobiology of Aging* 32.SUPPL. 1 (Dec. 2011), S37–S43. arXiv: NIHMS150003.
- [8] L. Mosconi et al. “Pre-clinical detection of Alzheimer’s disease using FDG-PET, with or without amyloid imaging”. In: *Journal of Alzheimer’s Disease* 20.3 (2010), pp. 843–854. arXiv: NIHMS150003.
- [9] D. Galimberti and E. Scarpini. “Disease-modifying treatments for Alzheimer’s disease”. In: *Therapeutic Advances in Neurological Disorders* 4.4 (July 2011), pp. 203–216.
- [10] P. R. Solomon and C. A. Murphy. “Early diagnosis and treatment of Alzheimer’s disease”. In: *Expert Review of Neurotherapeutics* 8.5 (2008), pp. 769–780.
- [11] H. Wang et al. “Magnetic Resonance Spectroscopy in Alzheimer’s Disease: Systematic Review and Meta-Analysis”. In: *J Alzheimers Dis* 46.4 (2015), pp. 1049–1070.
- [12] E. J. Bubb, C. Metzler-Baddeley, and J. P. Aggleton. “The cingulum bundle: Anatomy, function, and dysfunction”. In: *Neuroscience and Biobehavioral Reviews* 92 (Sept. 2018), pp. 104–127.
- [13] C. Granziera et al. “In-vivo magnetic resonance imaging of the structural core of the Papez circuit in humans”. In: *NeuroReport* 22.5 (Mar. 2011), pp. 227–231.
- [14] Y. Kobayashi and D. G. Amaral. “Macaque monkey retrosplenial cortex: II. Cortical afferents”. In: *The Journal of Comparative Neurology* 466.1 (Nov. 2003), pp. 48–79.

2.7. References

- [15] S. Mori and M. Aggarwal. "In vivo magnetic resonance imaging of the human limbic white matter". In: *Frontiers in Aging Neuroscience* 6.NOV (2014), p. 321.
- [16] A. Shah, S. S. Jhavar, and A. Goel. "Analysis of the anatomy of the Papez circuit and adjoining limbic system by fiber dissection techniques". In: *Journal of Clinical Neuroscience* 19.2 (Feb. 2012), pp. 289–298.
- [17] M. Hornberger et al. "In vivo and post-mortem memory circuit integrity in frontotemporal dementia and Alzheimer's disease". In: *Brain* 135.10 (Oct. 2012), pp. 3015–3025.
- [18] S. N. Lockhart et al. "Episodic memory function is associated with multiple measures of white matter integrity in cognitive aging". In: *Frontiers in Human Neuroscience* 6 (Mar. 2012), p. 56.
- [19] R. H. Tan et al. "Beyond the temporal pole: Limbic memory circuit in the semantic variant of primary progressive aphasia". In: *Brain* 137.7 (July 2014), pp. 2065–2076.
- [20] L. Bäckman et al. "Cognitive impairment in preclinical Alzheimer's disease: A meta-analysis." In: *Neuropsychology* 19.4 (2005), pp. 520–531.
- [21] C. A. Gold and A. E. Budson. "Memory loss in Alzheimer's disease: Implications for development of therapeutics". In: *Expert Review of Neurotherapeutics* 8.12 (Dec. 2008), pp. 1879–1891.
- [22] I. H. Choo et al. "Posterior cingulate cortex atrophy and regional cingulum disruption in mild cognitive impairment and Alzheimer's disease". In: *Neurobiology of Aging* 31.5 (May 2010), pp. 772–779.
- [23] J. H. Morra et al. "Automated mapping of hippocampal atrophy in 1-year repeat MRI data from 490 subjects with Alzheimer's disease, mild cognitive impairment, and elderly controls". In: *NeuroImage* 45.1 (Mar. 2009), S3–S15.

- [24] J. Mutlu et al. "Connectivity disruption, atrophy, and hypometabolism within posterior cingulate networks in Alzheimer's disease". In: *Frontiers in Neuroscience* 10.DEC (2016), p. 582.
- [25] N. Schuff et al. "MRI of hippocampal volume loss in early Alzheimers disease in relation to ApoE genotype and biomarkers". In: *Brain* 132.4 (Apr. 2009), pp. 1067–1077.
- [26] A. Fellgiebel et al. "Color-coded diffusion-tensor-imaging of posterior cingulate fiber tracts in mild cognitive impairment". In: *Neurobiology of Aging* 26.8 (Aug. 2005), pp. 1193–1198.
- [27] D. Medina et al. "White matter changes in mild cognitive impairment and AD: A diffusion tensor imaging study". In: *Neurobiology of Aging* 27.5 (May 2006), pp. 663–672.
- [28] Y. Nakata et al. "Diffusion abnormality in posterior cingulate fiber tracts in Alzheimer's disease: Tract-specific analysis". In: *Radiation Medicine - Medical Imaging and Radiation Oncology* 26.8 (Oct. 2008), pp. 466–473.
- [29] J. Yu, C. L. Lam, and T. M. Lee. "White matter microstructural abnormalities in amnesic mild cognitive impairment: A meta-analysis of whole-brain and ROI-based studies". In: *Neuroscience and Biobehavioral Reviews* 83 (Dec. 2017), pp. 405–416.
- [30] Y. Zhang et al. "Diffusion tensor imaging of cingulum fibers in mild cognitive impairment and Alzheimer disease". In: *Neurology* 68.1 (Nov. 2007), pp. 13–19. arXiv: NIHMS150003.
- [31] S. De Santi et al. "Hippocampal formation glucose metabolism and volume losses in MCI and AD". In: *Neurobiology of Aging* 22.4 (July 2001), pp. 529–539.

2.7. References

- [32] C. R. Jack et al. "Hypothetical model of dynamic biomarkers of the Alzheimer's pathological cascade". In: *The Lancet Neurology* 9.1 (Jan. 2010), pp. 119–128. arXiv: NIHMS150003.
- [33] E. M. Reiman et al. "Hippocampal volumes in cognitively normal persons at genetic risk for Alzheimer's disease". In: *Annals of Neurology* 44.2 (Aug. 1998), pp. 288–291.
- [34] G. Öz et al. "Clinical Proton MR Spectroscopy in Central Nervous System Disorders". In: *Radiology* 270.3 (Mar. 2014), pp. 658–679.
- [35] R. M. R. Dixon et al. "Longitudinal quantitative proton magnetic resonance spectroscopy of the hippocampus in Alzheimer's disease". In: *Brain* 125.10 (Oct. 2002), pp. 2332–2341.
- [36] K. Kantarci et al. "Longitudinal 1H MRS changes in mild cognitive impairment and Alzheimer's disease". In: *Neurobiology of Aging* 28.9 (Sept. 2007), pp. 1330–1339.
- [37] K. Kantarci et al. "1H magnetic resonance spectroscopy, cognitive function, and apolipoprotein E genotype in normal aging, mild cognitive impairment and Alzheimer's disease." In: *Journal of the International Neuropsychological Society : JINS* 8.7 (Nov. 2002), pp. 934–42.
- [38] M. E. Murray et al. "Early Alzheimer's disease neuropathology detected by proton MR spectroscopy." In: *The Journal of Neuroscience* 34.49 (Dec. 2014), pp. 16247–55.
- [39] R. Rupsingh et al. "Reduced hippocampal glutamate in Alzheimer disease". In: *Neurobiology of Aging* 32.5 (May 2011), pp. 802–810.
- [40] C. M. L. Foy et al. "Hippocampal Proton MR Spectroscopy in Early Alzheimer's Disease and Mild Cognitive Impairment". In: *Brain Topography* 24.3-4 (Oct. 2011), pp. 316–322.

- [41] T. Watanabe, A. Shiino, and I. Akiguchi. "Hippocampal metabolites and memory performances in patients with amnesic mild cognitive impairment and Alzheimer's disease". In: *Neurobiology of Learning and Memory* 97.3 (Mar. 2012), pp. 289–293.
- [42] T. Watanabe, A. Shiino, and I. Akiguchi. "Absolute quantification in proton magnetic resonance spectroscopy is useful to differentiate amnesic mild cognitive impairment from Alzheimer's disease and healthy aging." In: *Dement Geriatr Cognitive Disorders* 30.1 (2010), pp. 71–7.
- [43] N. Fayed et al. "Brain Glutamate Levels Are Decreased in Alzheimer's Disease". In: *American Journal of Alzheimer's Disease & Other Dementias* 26.6 (Sept. 2011), pp. 450–456.
- [44] R. C. Petersen. "Mild cognitive impairment as a diagnostic entity". In: *Journal of Internal Medicine* 256.3 (Sept. 2004), pp. 183–194.
- [45] R. C. Petersen et al. "Mild cognitive impairment: Clinical characterization and outcome". In: *Archives of Neurology* 56.3 (Mar. 1999), pp. 303–308. arXiv: NIHMS150003.
- [46] B. Winblad et al. "Mild cognitive impairment - Beyond controversies, towards a consensus: Report of the International Working Group on Mild Cognitive Impairment". In: *Journal of Internal Medicine* 256.3 (Sept. 2004), pp. 240–246.
- [47] G. McKhann et al. "Clinical diagnosis of Alzheimer's disease: Report of the NINCDS-ADRDA Work Group* under the auspices of Department of Health and Human Services Task Force on Alzheimer's Disease". In: *Neurology* 34.7 (July 1984), pp. 939–939.
- [48] M. W. Weiner et al. "The Alzheimer's Disease Neuroimaging Initiative: A review of papers published since its inception". In: *Alzheimer's & Dementia* 9.5 (Sept. 2013), e111–e194.

2.7. References

- [49] K. M. Gilbert et al. "An parallel-transmit, parallel-receive coil for routine scanning on a 7T head-only scanner". In: *Proceedings of the 23rd Annual Meeting of ISMRM*. Toronto, 2015, p. 0623.
- [50] J. P. Marques et al. "MP2RAGE, a self bias-field corrected sequence for improved segmentation and T1-mapping at high field". In: *NeuroImage* 49.2 (Jan. 2010), pp. 1271–1281.
- [51] M. Garwood and L. DelaBarre. "The return of the frequency sweep: designing adiabatic pulses for contemporary NMR." In: *Journal of magnetic resonance (San Diego, Calif. : 1997)* 153.2 (Dec. 2001), pp. 155–77.
- [52] G. Oz and I. Tkáč. "Short-echo, single-shot, full-intensity proton magnetic resonance spectroscopy for neurochemical profiling at 4 T: validation in the cerebellum and brainstem." In: *Magnetic resonance in medicine* 65.4 (Apr. 2011), pp. 901–10.
- [53] D. Wong, A. L. Schranz, and R. Bartha. "Optimized in vivo brain glutamate measurement using long-echo-time semi-LASER at 7 T". In: *NMR in Biomedicine* 31.11 (Nov. 2018), e4002.
- [54] S. Craft et al. "Memory improvement following induced hyperinsulinemia in Alzheimer's disease". In: *Neurobiology of Aging* 17.1 (Jan. 1996), pp. 123–130.
- [55] K. L. Possin et al. "Distinct neuroanatomical substrates and cognitive mechanisms of figure copy performance in Alzheimer's disease and behavioral variant frontotemporal dementia". In: *Neuropsychologia* 49.1 (Jan. 2011), pp. 43–48.
- [56] S. Weintraub et al. "Version 3 of the Alzheimer Disease Centers' Neuropsychological Test Battery in the Uniform Data Set (UDS)". In: *Alzheimer Disease and Associated Disorders* 32.1 (2018), pp. 10–17.
- [57] M. Jenkinson et al. "Improved optimization for the robust and accurate linear registration and motion correction of brain images". In: *NeuroImage* 17.2 (Oct. 2002), pp. 825–841. arXiv: arXiv:1011.1669v3.

- [58] M. Jenkinson and S. Smith. "A global optimisation method for robust affine registration of brain images". In: *Medical Image Analysis* 5.2 (June 2001), pp. 143–156.
- [59] M. Jenkinson et al. "FSL". In: *NeuroImage* 62.2 (Aug. 2012), pp. 782–790. arXiv: arXiv:1401.4122v2.
- [60] S. M. Smith et al. "Advances in functional and structural MR image analysis and implementation as FSL". In: *NeuroImage* 23.SUPPL. 1 (Jan. 2004), S208–S219.
- [61] M. W. Woolrich et al. "Bayesian analysis of neuroimaging data in FSL." In: *NeuroImage* 45.1 Suppl (Mar. 2009), S173–S186.
- [62] J. L. Andersson, S. Skare, and J. Ashburner. "How to correct susceptibility distortions in spin-echo echo-planar images: Application to diffusion tensor imaging". In: *NeuroImage* 20.2 (Oct. 2003), pp. 870–888. arXiv: 1011.1669.
- [63] J. L. Andersson and S. N. Sotiropoulos. "An integrated approach to correction for off-resonance effects and subject movement in diffusion MR imaging". In: *NeuroImage* 125 (Jan. 2016), pp. 1063–1078. arXiv: 15334406.
- [64] R. Bartha et al. "Spectroscopic lineshape correction by QUECC: combined QUALITY deconvolution and eddy current correction." In: *Magnetic resonance in medicine* 44.4 (Oct. 2000), pp. 641–5.
- [65] A. A. De Graaf, J. E. Van Dijk, and W. M. M. J. BoéE. "QUALITY: quantification improvement by converting lineshapes to the lorentzian type". In: *Magnetic Resonance in Medicine* 13.3 (Mar. 1990), pp. 343–357.
- [66] R. Bartha, D. J. Drost, and P. C. Williamson. "Factors affecting the quantification of short echo in-vivo ¹H MR spectra: prior knowledge, peak elimination, and filtering." In: *NMR in biomedicine* 12.4 (June 1999), pp. 205–16.
- [67] J. H. Griesmer. "Society for Industrial and Applied Mathematics (A5)". In: *Science* 151.3712 (Feb. 1966), pp. 859–860. arXiv: arXiv:1011.1669v3.

2.7. References

- [68] M. Marjańska et al. "Localized ^1H NMR spectroscopy in different regions of human brain in vivo at 7 T: T2 relaxation times and concentrations of cerebral metabolites". In: *NMR in Biomedicine* 25.2 (Feb. 2012), pp. 332–339.
- [69] C. Gasparovic et al. "Use of tissue water as a concentration reference for proton spectroscopic imaging". In: *Magnetic Resonance in Medicine* 55.6 (June 2006), pp. 1219–1226.
- [70] Y. Zhang, M. Brady, and S. Smith. "Segmentation of brain MR images through a hidden Markov random field model and the expectation-maximization algorithm". In: *IEEE Transactions on Medical Imaging* 20.1 (2001), pp. 45–57.
- [71] W. D. Rooney et al. "Magnetic field and tissue dependencies of human brain longitudinal $^1\text{H}_2\text{O}$ relaxation in vivo". In: *Magnetic Resonance in Medicine* 57.2 (Feb. 2007), pp. 308–318.
- [72] R. A. de Graaf. *In Vivo NMR Spectroscopy*. 2nd ed. Chichester, UK: John Wiley & Sons, Ltd, Oct. 2007.
- [73] K. Ryan et al. " ^1H MR spectroscopy of the motor cortex immediately following transcranial direct current stimulation at 7 Tesla". In: *PLoS ONE* 13.8 (Aug. 2018). Ed. by T. Yuan, e0198053.
- [74] L. Xin et al. "Proton T1 relaxation times of metabolites in human occipital white and gray matter at 7 T". In: *Magnetic Resonance in Medicine* 69.4 (Apr. 2013), pp. 931–936.
- [75] A. Andreychenko et al. "In vivo GABA T2 determination with J-refocused echo time extension at 7 T". In: *NMR in Biomedicine* 26.11 (Nov. 2013), pp. 1596–1601.
- [76] R. Kreis et al. "Integrated data acquisition and processing to determine metabolite contents, relaxation times, and macromolecule baseline in single examinations of individual subjects". In: *Magnetic Resonance in Medicine* 54.4 (Oct. 2005), pp. 761–768.

- [77] S. Wakana et al. "Reproducibility of quantitative tractography methods applied to cerebral white matter". In: *NeuroImage* 36.3 (July 2007), pp. 630–644. arXiv: NIHMS150003.
- [78] O. Friman, G. Farneback, and C.-F. Westin. "A Bayesian approach for stochastic white matter tractography". In: *IEEE Transactions on Medical Imaging* 25.8 (Aug. 2006), pp. 965–978.
- [79] K. Hua et al. "Tract probability maps in stereotaxic spaces: Analyses of white matter anatomy and tract-specific quantification". In: *NeuroImage* 39.1 (Jan. 2008), pp. 336–347. arXiv: NIHMS150003.
- [80] S. Mori and B. J. Crain. *MRI atlas of human white matter*. Elsevier, 2005, p. 239.
- [81] C. Fowlkes et al. "Spectral Grouping Using the Nyström Method". In: *IEEE Transactions on Pattern Analysis and Machine Intelligence* 26.2 (Feb. 2004), pp. 214–225.
- [82] U. Von Luxburg. "A tutorial on spectral clustering". In: *Statistics and Computing* 17.4 (Dec. 2007), pp. 395–416. arXiv: 0711.0189.
- [83] J. B. Colby et al. "Along-tract statistics allow for enhanced tractography analysis". In: *NeuroImage* 59.4 (Feb. 2012), pp. 3227–3242. arXiv: NIHMS150003.
- [84] F. E. Grubbs. "Procedures for Detecting Outlying Observations in Samples". In: *Technometrics* 11.1 (1969), pp. 1–21.
- [85] D. C. Howell. *Fundamental Statistics for the Behavioral Sciences*. 8th ed. 2013, p. 649.
- [86] R Development Core Team. *R: A Language and Environment for Statistical Computing*. Vienna, Austria, 2008.
- [87] P. S. Ariyannur et al. "Methamphetamine-induced neuronal protein NAT8L is the NAA biosynthetic enzyme: Implications for specialized acetyl coenzyme A metabolism in the CNS". In: *Brain Research* 1335 (June 2010), pp. 1–13.

2.7. References

- [88] A. Del Sole et al. "Individual cerebral metabolic deficits in Alzheimer's disease and amnesic mild cognitive impairment: An FDG PET study". In: *European Journal of Nuclear Medicine and Molecular Imaging* 35.7 (July 2008), pp. 1357–1366.
- [89] S. Minoshima et al. "Alzheimer's disease versus dementia with Lewy bodies: Cerebral metabolic distinction with autopsy confirmation". In: *Annals of Neurology* 50.3 (Sept. 2001), pp. 358–365.
- [90] L. Mosconi et al. "Multicenter Standardized 18F-FDG PET Diagnosis of Mild Cognitive Impairment, Alzheimer's Disease, and Other Dementias". In: *Journal of Nuclear Medicine* 49.3 (Mar. 2008), pp. 390–398. arXiv: NIHMS150003.
- [91] R. Ossenkoppele et al. "Longitudinal imaging of Alzheimer pathology using [11C]PIB, [18F]FDDNP and [18F]FDG PET". In: *European Journal of Nuclear Medicine and Molecular Imaging* 39.6 (June 2012), pp. 990–1000.
- [92] M. H. Baslow et al. "Expression of aspartoacylase activity in cultured rat macroglial cells is limited to oligodendrocytes." In: *Journal of molecular neuroscience : MN* 13.1-2 (1999), pp. 47–53.
- [93] C. N. Madhavarao et al. "Immunohistochemical localization of aspartoacylase in the rat central nervous system." In: *The Journal of comparative neurology* 472.3 (May 2004), pp. 318–29.
- [94] J. R. Moffett et al. "Extensive aspartoacylase expression in the rat central nervous system". In: *GLIA* 59.10 (Oct. 2011), pp. 1414–1434.
- [95] J. R. Moffett et al. "N-Acetylaspartate in the CNS: From neurodiagnostics to neurobiology". In: *Progress in Neurobiology* 81.2 (Feb. 2007), pp. 89–131.
- [96] H. M. Feldman et al. "Diffusion Tensor Imaging: A Review for Pediatric Researchers and Clinicians". In: *Journal of Developmental and Behavioral Pediatrics* 31.4 (May 2010), pp. 346–56.

- [97] P. M. Thompson et al. "Mapping hippocampal and ventricular change in Alzheimer disease". In: *NeuroImage* 22.4 (Aug. 2004), pp. 1754–1766.
- [98] A. L. Alexander et al. "Diffusion Tensor Imaging of the Brain". In: *Neurotherapeutics* 4.3 (July 2007), pp. 316–329. arXiv: Neurotherapeutics.2007July;4(3):316–329.
- [99] A. Barco, C. H. Bailey, and E. R. Kandel. "Common molecular mechanisms in explicit and implicit memory". In: *Journal of Neurochemistry* 97.6 (June 2006), pp. 1520–1533.
- [100] C. A. Tamminga et al. "Glutamate dysfunction in hippocampus: Relevance of dentate gyrus and CA3 signaling". In: *Schizophrenia Bulletin* 38.5 (Sept. 2012), pp. 927–935.
- [101] P. J. Nestor et al. "Limbic hypometabolism in Alzheimer's disease and mild cognitive impairment". In: *Annals of Neurology* 54.3 (Sept. 2003), pp. 343–351.
- [102] M. Yudkoff et al. "Tricarboxylic acid cycle in rat brain synaptosomes. Fluxes and interactions with aspartate aminotransferase and malate/aspartate shuttle." In: *The Journal of biological chemistry* 269.44 (Nov. 1994), pp. 27414–20.
- [103] K. Harris et al. "Regulation of NAA-synthesis in the human brain in vivo: Canavan's disease, Alzheimer's disease and schizophrenia". In: *Advances in Experimental Medicine and Biology*. Vol. 576. Springer US, 2006, pp. 263–273.
- [104] S. Olejnik and J. Algina. "Generalized Eta and Omega Squared Statistics: Measures of Effect Size for Some Common Research Designs". In: *Psychological Methods* 8.4 (Dec. 2003), pp. 434–447.
- [105] L. Su et al. "Whole-brain patterns of 1H-magnetic resonance spectroscopy imaging in Alzheimer's disease and dementia with Lewy bodies". In: *Translational Psychiatry* 6.8 (Aug. 2016), e877–e877.

2.7. References

- [106] J. M. Schott et al. "Short echo time proton magnetic resonance spectroscopy in Alzheimer's disease: A longitudinal multiple time point study". In: *Brain* 133.11 (Nov. 2010), pp. 3315–3322.
- [107] C. E. Sexton et al. "A meta-analysis of diffusion tensor imaging in mild cognitive impairment and Alzheimer's disease". In: *Neurobiology of Aging* 32.12 (Dec. 2011), 2322.e5–2322.e18.
- [108] G. Catheline et al. "Distinctive alterations of the cingulum bundle during aging and Alzheimer's disease". In: *Neurobiology of Aging* 31.9 (Sept. 2010), pp. 1582–1592.
- [109] J. T. Tschanz et al. "Progression of cognitive, functional, and neuropsychiatric symptom domains in a population cohort with alzheimer dementia: The cache county dementia progression study". In: *American Journal of Geriatric Psychiatry* 19.6 (June 2011), pp. 532–542.
- [110] K. L. Lanctôt et al. "Neuropsychiatric signs and symptoms of Alzheimer's disease: New treatment paradigms". In: *Alzheimer's and Dementia: Translational Research and Clinical Interventions* 3.3 (Sept. 2017), pp. 440–449.
- [111] M. Mescher et al. "Simultaneous in vivo spectral editing and water suppression". In: *NMR in Biomedicine* 11.6 (Oct. 1998), pp. 266–272.
- [112] M. Mescher et al. "Solvent suppression using selective echo dephasing". In: *Journal of Magnetic Resonance - Series A* 123.2 (Dec. 1996), pp. 226–229.
- [113] Y. Zhang et al. "Atlas-guided tract reconstruction for automated and comprehensive examination of the white matter anatomy". In: *NeuroImage* 52.4 (Oct. 2010), pp. 1289–1301. arXiv: NIHMS150003.
- [114] W. Zhang et al. "Automated fiber tracking of human brain white matter using diffusion tensor imaging". In: *NeuroImage* 42.2 (Aug. 2008), pp. 771–777.

2.8 Supplementary Figures

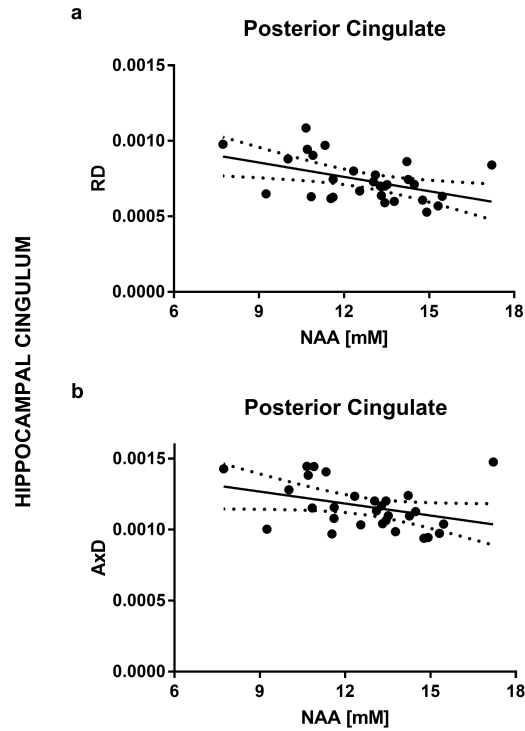


FIGURE 2.S1: Significant correlations between NAA levels in the PCC and the average RD ($r = -0.46$, $p < 0.01$) and AxD ($r = -0.35$, $p < 0.05$) in the first 25% of the hippocampal portion of the cingulum are shown with 95% confidence bands in (a) and (b), respectively.

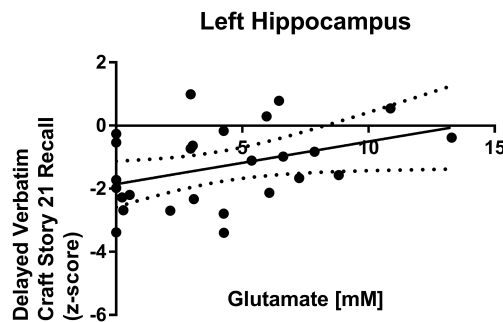


FIGURE 2.S2: Left hippocampal glutamate levels were positively correlated with the delayed CSR verbatim z-score ($r = 0.39$, $p < 0.05$).

2.8. Supplementary Figures

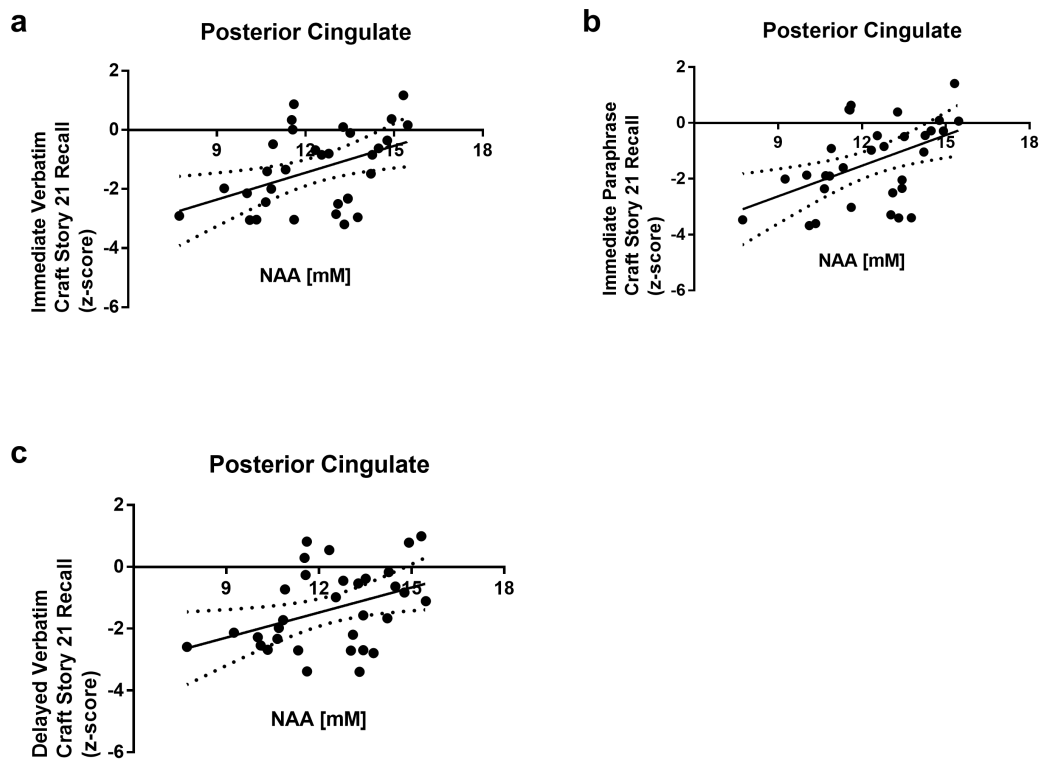


FIGURE 2.S3: As shown in (a), NAA concentration in the PCC was correlated with the immediate CSR verbatim score ($r = 0.43$, $p < 0.01$). As shown in (b), NAA in the PCC was correlated with the immediate CSR paraphrase score ($r = 0.47$, $p < 0.01$). As shown in (c), NAA in the PCC was correlated with the delayed CSR verbatim z-score ($r = 0.39$, $p < 0.05$).

2.9 Supplementary Tables

Group	Craft Story Recall (Immediate)						Craft Story Recall (Delayed)					
	Verbatim			Paraphrase			Verbatim			Paraphrase		
	Mean	SD	SE	Mean	SD	SE	Mean	SD	SE	Mean	SD	SE
NEC	-0.43	0.99	0.25	-0.37	0.95	0.24	-0.37	0.91	0.23	-0.22	0.87	0.22
MCI	-2.57	1.06	0.35	-2.69	1.29	0.43	-2.68	1.16	0.39	-3.20	1.35	0.45
AD	-1.90	0.82	0.27	-2.08	0.96	0.32	-2.10	0.65	0.22	-2.47	0.93	0.31
	Benson Complex Figure Copy (Immediate)						Benson Complex Figure Copy (Delayed)					
	Mean		SD		SE		Mean		SD		SE	
NEC	0.025		1.18		0.29		-0.22		0.94		0.24	
MCI	-0.96		1.99		0.66		-2.78		1.66		0.55	
AD	-0.40		1.19		0.40		-2.58		1.08		0.37	

TABLE 2.S1: The group means, standard deviations (SD), and standard errors (SE) of the Craft Story 21 Recall and Benson Complex Figure Copy z-scores are shown in this table.

2.10 Co-Authorship Statement

Material in this chapter is in revision for publication in the Journal of Alzheimer's Disease as of September 16, 2019. Some of the material presented in this chapter was also presented at the Alzheimer's Association International Conference on Alzheimer's Disease (2018; Poster #IC-P-114/P1-448). Dickson Wong was the main contributor for the material presented in this chapter – performing most of the study design, software development, data acquisition, data analysis, and manuscript preparation. Co-authors on this chapter were Samir Atiya, Jennifer Fogarty, Manuel Montero-Odasso, Stephen Pasternak, Chris Brymer, Michael Borrie, and Robert Bartha. Samir Atiya was involved in the recruitment of participants and in the acquisition of the MRI and neuropsychological data. Jennifer Fogarty trained Dickson Wong and Samir Atiya to perform neuropsychological testing and assisted in scoring the tests. Manuel Montero-Odasso, Stephen Pasternak, Chris Brymer, and

2.10. Co-Authorship Statement

Michael Borrie recruited participants. Michael Borrie and Robert Bartha provided guidance in the study design, interpretation of the data, and in the preparation of the manuscript and conference presentations.

Estimated percentage of the work for Chapter 2 conducted solely by Dickson Wong: 85%

3

Optimized in vivo glutamate measurement using long-echo-time semi-LASER at 7 T

A version of this chapter has been published in NMR in Biomedicine: Dickson Wong, Amy L. Schranz, and Robert Bartha, "Optimized in vivo brain glutamate measurement using long-echo-time semi-LASER at 7 T," NMR Biomed., vol. 31, no. 11, p. e4002, Nov. 2018.

Abstract: A short echo time (T_E) is commonly used for brain glutamate measurement by ^1H MRS to minimize drawbacks of long T_E such as signal modulation to J evolution and T_2 relaxation. However, J coupling causes the spectral patterns of glutamate to change with T_E , and the shortest achievable T_E may not produce the optimal glutamate measurement. The purpose of this study was to determine the optimal T_E for glutamate measurement at 7 T using semi-LASER (localization by adiabatic selective refocusing). Time-domain simulations were performed to model the T_E dependence of glutamate signal energy, a measure of glutamate signal strength, and were verified against measurements made in the human sensorimotor cortex (five subjects, $2 \times 2 \times 2 \text{ cm}^3$ voxel, 16 averages) on a 7 T MRI scanner. Simulation showed a local maximum of glutamate signal energy at $T_E = 107 \text{ ms}$. In vivo, $T_E = 105 \text{ ms}$ produced a low Cramér-Rao lower bound of $6.5 \pm 2.0\%$ across subjects, indicating high-quality fits of the prior knowledge model to in vivo data. $T_E = 105 \text{ ms}$ also produced the greatest glutamate signal energy with the smallest inter-subject glutamate-to-creatine ratio (Glu/Cr) coefficient of variation (CV), 4.6%. Using these CVs, we performed sample size calculations to estimate the number of participants per group required to detect a 10% change in Glu/Cr between two groups with 95% confidence. 13 were required at $T_E = 45 \text{ ms}$, the shortest achievable echo time on our 7 T MRI scanner, while only 5 were required at $T_E = 105 \text{ ms}$, indicating greater statistical power. These results indicate that $T_E = 105 \text{ ms}$ is optimum for in vivo glutamate measurement at 7 T with semi-LASER. Using long T_E decreases power deposition by allowing lower maximum RF pulse amplitudes in conjunction with longer RF pulses. Importantly, long T_E minimizes macromolecule contributions, eliminating the requirement for acquisition of separate macromolecule spectra or macromolecule fitting techniques, which add additional scan time or bias the estimated glutamate fit.

3.1 Introduction

Glutamate is the primary excitatory neurotransmitter in the brain enabling synaptic communication between neurons [1]. Levels of glutamate have been shown to be altered in several neurological conditions including Alzheimer's disease [2] and epilepsy [3]. Such changes are thought to precede structural alterations and may be a valuable biomarker for disease detection and treatment.

Proton MRS (^1H -MRS) may be used to non-invasively and directly measure levels of metabolites, such as glutamate. Using chemical shift imaging or single-voxel acquisition techniques, spectra can be acquired from specific brain regions relevant to various neurological diseases, such as the primary motor cortex [4], the hippocampus [2], and the anterior cingulate cortex [5]. Although glutamate can be difficult to resolve at clinical field strengths, ^1H -MRS at ultra-high magnetic fields, such as 4 T and above, benefits from increased signal-to-noise ratio (SNR) and greater spectral dispersion. These factors lead to better separation of glutamate from the overlapping resonances of glutamine and γ -aminobutyric acid (GABA), increasing quantification accuracy and precision [6, 7].

However, high-field ^1H -MRS suffers from increased chemical shift displacement error, increased B_1 inhomogeneity, greater power deposition, and shorter T_2^* relaxation times. Localization by adiabatic selective refocusing (LASER) [7, 8], or variants such as semi-LASER [9, 10], can overcome many of these limitations by utilizing adiabatic full passage (AFP) refocusing pulses. AFP pulses are robust to B_1 inhomogeneity and have a bandwidth independent of B_1 amplitude, reducing the chemical shift displacement error and producing well-defined excitation profiles. A downside to AFP pulses is that they must be made relatively long to reduce peak B_1 amplitude and stay below power deposition limits. Also, to refocus non-linear phase dispersion across an excited slice, AFP pulses must be used in pairs, increasing the total number of RF pulses that are played out. These requirements typically limit the minimum achievable echo times to be in the 38–50 ms range at 7 T [11, 10],

in contrast to the widely used spectroscopy sequences PRESS (point-resolved spectroscopy [12]) and STEAM (stimulated echo acquisition mode [13]), where echo times under 10 ms can be achieved at high field [14, 15, 16, 17].

To detect and measure strongly J -coupled spin systems such as glutamate using ^1H -MRS, the shortest achievable echo time is normally used to minimize signal modulation due to J evolution and T_2 relaxation. However, J coupling causes the spectral patterns of glutamate to change in a complex pattern as a function of echo time. Thus, it is possible that the shortest achievable echo time does not produce the optimal glutamate measurement using semi-LASER at 7 T, and that a longer echo time is preferred. Shorter echo times also increase the contribution of macromolecule resonances that overlap with glutamate resonances [18], which confounds metabolite fitting and quantification. A longer echo time would remove this complication.

The purpose of this study was to determine the optimal echo time for glutamate measurement at 7 T using semi-LASER. Time-domain simulations were initially performed to model the echo-time dependence of the glutamate signal energy, a measure of glutamate signal strength. Human in vivo experiments and phantom in vitro experiments performed on a 7 T MRI scanner showed a similar echo-time dependence to the simulations. In vivo, the shortest achievable echo time was suboptimal, as both glutamate signal energy and measurement precision were maximized at longer echo times.

3.2 Methods

3.2.1 Time-domain simulations

To investigate glutamate signal amplitude changes as a function of echo time, the glutamate spectrum was simulated for 7 T using the PyGAMMA library of the VeSPA (Versatile Simulation, Pulses and Analysis) software suite [19]. Direct use of the PyGAMMA code library rather than the VeSPA graphical user interface allowed the exact replication of the RF

3.2. Methods

pulse shapes from the MRI scanner, the calibration of the pulses to ensure adiabaticity, and the running of multiple simulations in parallel, all within a single Python program. The simulations only included the RF pulses of the semi-LASER sequence. No spatial localization was included in the simulations, as RF pulse bandwidths minimized chemical shift artefacts. Previously measured chemical shift and J -coupling constants [20] were used to define the glutamate spin system. These values were used by PyGAMMA to perform time-domain density matrix calculations and to incorporate J -coupling effects into the simulation outputs. Positions, amplitudes, and phases of the glutamate peaks were obtained from the simulations. Using these parameters, the glutamate free-induction decay (FID) signal was reconstructed as a function of time (t) using

$$FID(t) = e^{-\frac{t+T_E}{T_2}} e^{-\pi\alpha t} \sum_k c_k e^{j(2\pi\omega_k t + \phi_k)} \quad (3.1)$$

where T_E is echo time, T_2 is the T_2 relaxation time constant of glutamate in the motor cortex (98 ms) [21], ω_k is the chemical shift, c_k is the amplitude, and ϕ_k is the phase of the k th peak of glutamate. α is the Lorentzian linewidth for all peaks and was set to 10 Hz, which was typically observed in our in vivo data collected from the sensorimotor cortex. Equation (3.1) is consistent with the model equation described by Bartha et al. [22], which was used in the present study to analyse in vivo spectra. This consistency allows the direct comparison of simulation results with in vivo results.

After reconstruction of the glutamate FID, the energy of the signal, a measure of signal strength, was calculated using [23]

$$E = \int_0^T |FID(t)|^2 dt \quad (3.2)$$

where T is the total acquisition time of the FID. Signal energy was used as the optimization metric rather than simply optimizing over peak area in the frequency domain because the magnitude of the FID incorporates both peak area and T_2 information [24].

This process was repeated for echo times ranging from 45 ms to 215 ms (1 ms step size). These echo times represent the shortest and longest achievable echo times for semi-LASER on our 7 T MRI scanner.

3.2.2 ^1H -MRS acquisition

3.2.2.1 Hardware and shimming

All ^1H -MRS data were collected on a 7 T/70 cm Siemens MAGNETOM (Siemens, Erlangen, Germany) head-only MRI system at the Centre for Functional and Metabolic Mapping, Roberts Research Institute. An 8-channel transmit, 32-channel receive whole head array [25] that can achieve a maximum transmit B_1 of 16 μT in the sensorimotor cortex was used.

The scanner is equipped with eight 1000 W RF amplifiers and a gradient system (80 mT/m maximum gradient strength, 350 mT/m/s slew rate) that includes second order, third order, and Z4 shims. Prior to data collection, localized B_0 and B_1 shimming were performed. The B_0 field was optimized using a two-echo gradient recalled echo shimming technique [26, 27, 28, 29]. The B_1 field was optimized using an algorithm in which the phases of the transmit channels were set to add constructively within the MRS voxel. This maximized the B_1 field in the MRS voxel, producing the most power efficient shim. B_1 field optimization incorporated field mapping as outlined by Curtis et al [30].

3.2.2.2 Pulse sequence

The semi-LASER pulse sequence was used to acquire all spectral data. This sequence has been described in detail by Öz and Tkáč [9]. In the current implementation, a 4 ms asymmetric, slice-selective, sinc excitation pulse [31] and 8 ms hyperbolic secant AFP refocusing pulses (HS4, $R = 25$) [10] were used. Interleaved VAPOR (variable pulse power and optimized relaxation delays) water suppression and outer-volume suppression (OVS) preceded the semi-LASER sequence. The VAPOR scheme was identical to that described by

Öz and Tkáč [9]. The OVS scheme was also identical, except that the crusher gradients ranged from 1 to 7 ms in duration and from 1 to 6 mT/m in strength. Prior to each experiment, the strength of the excitation pulse and the flip angle for VAPOR water suppression were optimized. The readout time was 340 ms with a 166 μ s dwell-time ($N = 2048$, $SW = 6024$ Hz).

3.2.3 In vivo data

3.2.3.1 Acquisition

In vivo ^1H -MRS data were obtained from five healthy individuals (four males, one female, average age 25 ± 3 years). Informed consent was obtained according to the procedures approved by the Health Sciences Research Ethics Board at The University of Western Ontario. ^1H -MRS data were collected from a single $2 \times 2 \times 2 \text{ cm}^3$ voxel in the left sensorimotor cortex (see Figure 3.2e later) at echo times ranging from 45 ms to 215 ms (10 ms step size). Both water suppressed (16 averages) and unsuppressed (4 averages) data were acquired. To minimize T_1 saturation effects, a T_R of 7500 ms was used, which is roughly five times the T_1 value of the 2.01 ppm *N*-acetyl aspartate (NAA) singlet at 7 T [32]. The total acquisition time was approximately 2 h.

3.2.3.2 Post-processing

All in vivo spectra were lineshape and eddy current corrected using combined QUALITY deconvolution and eddy current correction (QUECC) with 400 QUALITY (quantification improvement by converting lineshapes to the Lorentzian type) points [6]. To remove any residual water not suppressed by VAPOR, resonances between 4.2 ppm and 5.7 ppm were fitted using a Hankel singular value decomposition fitting routine requiring no prior knowledge [33] and subtracted from the spectrum.

The quality of the acquired data was assessed by calculating the linewidths of the water signal and by measuring the in vivo SNR. The water signal linewidths were calculated by fitting a single Lorentzian peak to the unsuppressed water spectra. SNR was measured by dividing the height of the absolute signal at the position of the NAA CH_3 peak by the standard deviation (SD) of the noise after Fourier transforming the first 100 ms of the FID.

3.2.3.3 Prior knowledge

Simulated, echo-time-specific 7 T semi-LASER prior knowledge templates were used to fit the post-processed spectra. The metabolite spectra were modelled with PyGAMMA [19] using previously measured metabolite-specific shifts and coupling constants [20] and the RF pulses of the semi-LASER pulse sequence. The following metabolites were included in the prior knowledge template: NAA, *N*-acetylaspartyl glutamate (NAAG), choline (Cho), creatine (Cr), *myo*-inositol, glutamate, glutamine, glutathione, phosphorylethanolamine (PEth), *scyllo*-inositol (Scyllo), taurine (Tau), alanine (Ala), glucose (Glc), GABA, glycine (Gly), and lactate (Lac). Glutamate and glutamine were included as separate metabolites, since the increased spectral dispersion at 7 T allows these metabolites to be resolved in vivo [7]. The multiplets of NAA and NAAG were fitted independently, because the multiplets experience a different rate of T_2 relaxation from the singlets [21, 34]. From the simulations, the peak positions, amplitudes, and phases, as well as the number of peaks, were obtained for each metabolite. These parameters were used to create the corresponding model function using Equation (3.1) in Bartha et al. [22]

A macromolecule model created using previously acquired macromolecule data was also included in the prior knowledge template. As described by Penner and Bartha[11], these data were acquired from 12 healthy participants at 7 T using a semi-LASER sequence with a double-inversion metabolite-nulling method. Two datasets were acquired per participant and all 24 datasets were averaged. Eleven Lorentzian lineshapes were used to parameterize the averaged macromolecule data (Figure 3.1) and were included in the prior

knowledge template.

Metabolite lineshapes were constrained in the prior knowledge template before fitting to the in vivo data. Since QUECC correction was used, all metabolite peaks were modelled as Lorentzian functions. A single Lorentzian linewidth parameter and a single delay time was defined for all metabolite peaks. Within metabolites, the peak amplitudes, shifts, and phases were fixed relative to one another. Relative peak amplitudes were not fixed between metabolites, since these may vary across subjects. Relative peak positions and phases between some metabolites were fixed. For example, the positions and phases of low-amplitude metabolites (e.g. Ala, GABA, Lac) were linked to the positions and phases of higher-amplitude metabolites (e.g. NAA, *myo*-inositol, glutamate). These constraints are summarized in Table 3.1.

Macromolecule lineshapes were also constrained. Relative amplitudes and linewidths between macromolecule resonances were fixed, and one phase parameter was defined for all macromolecular resonances.

3.2.3.4 Spectral fitting

The prior knowledge templates were fitted to the post-processed in vivo spectra using the fitMAN [22] software developed in-house. fitMAN uses a Levenberg–Marquardt minimization algorithm [35] to minimize the difference between the prior knowledge template and the in vivo data in the time domain. Initial parameter values of metabolites and macromolecule basis functions were manually adjusted such that the prior knowledge template resembled the data to be fit. After fitting, the quality of the model fit was assessed using Cramér-Rao lower bounds (CRLBs). At each echo time, CRLBs were calculated for all fitted metabolites and averaged across the five subjects. From the fitted model, glutamate peak positions, amplitudes, and phases were obtained. Using these parameters, the glutamate FID signal was reconstructed using Equation (3.1), with α set to 10 Hz. The energies of the reconstructed glutamate signals were calculated using Equation (3.2).

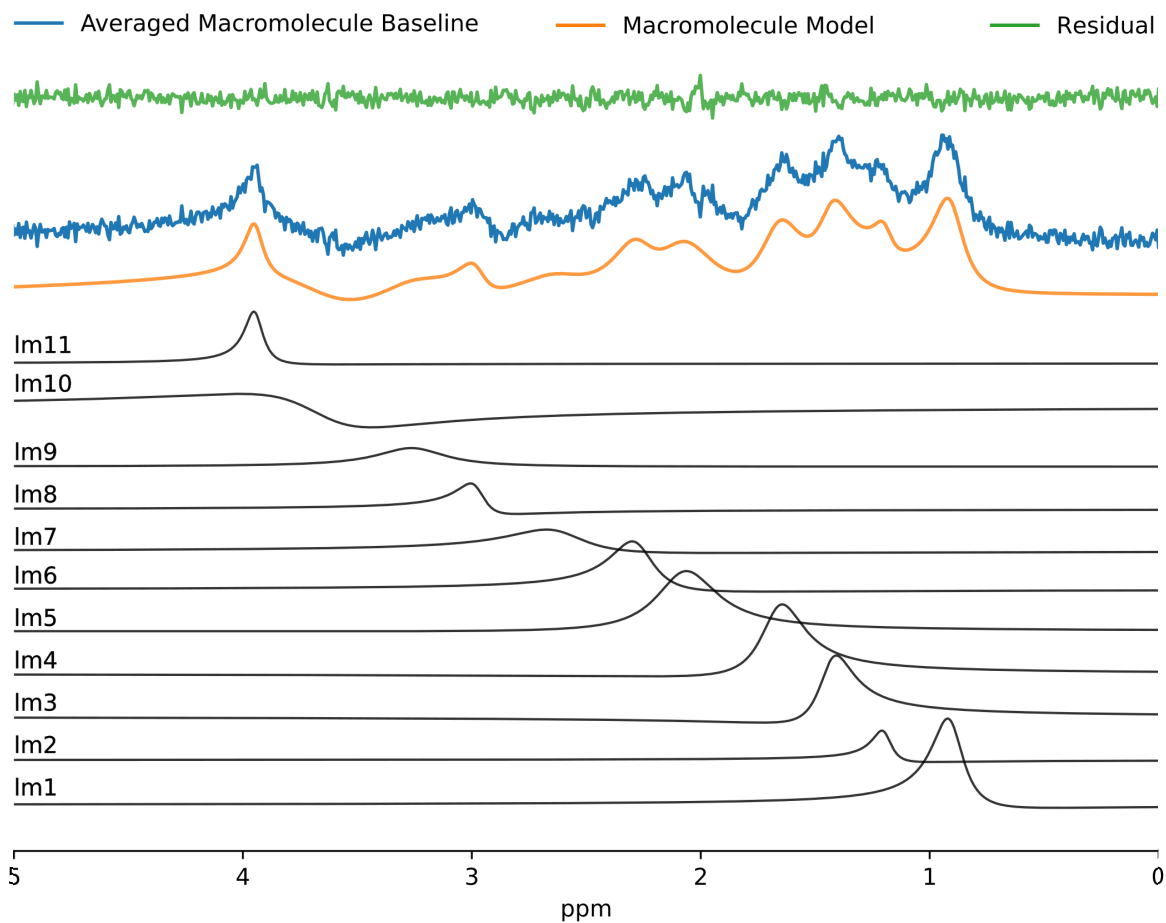


FIGURE 3.1: The macromolecule model included in the prior knowledge template is shown in orange. To create the model, an average macromolecule baseline was parameterized with 11 Lorentzian lineshapes (lm1-lm11). The average macromolecule baseline was obtained by averaging 24 *in vivo* metabolite-nulled spectra acquired at 7 T with semi-LASER.

3.2. Methods

Reference Metabolite	Linked Metabolites		Comments
	Shift	Phase	
NAA	NAAG, Lac	NAAG, PETH, Scyllo, Tau, Ala, Glc, GABA, Gly, Lac	<ul style="list-style-type: none"> • Shifts, phases, and amplitudes for Cho and Cr were not fixed relative to any reference metabolite. Cho and Cr were fitted independently. • Relative peak amplitudes were not fixed between metabolites, since these may vary across subjects. • A single linewidth parameter was defined for all metabolites. • A single delay time parameter was defined for all metabolites.
Myo	Ala, Glc, Gly, PETH, Scyllo, Tau	Phases of other metabolites were not fixed to Myo.	
Glu	Glu, Gln, GSH, GABA	Glu, Gln, GSH	

TABLE 3.1: A summary of relationships between metabolite parameters in the prior knowledge template. Peak shifts and phases of low-amplitude metabolites were linked to the shifts and phases of higher-amplitude metabolites. Within metabolites, the peak amplitudes, shifts, and phases were fixed relative to one another. The following metabolites were included in the prior knowledge template: NAA, NAAG, Cho, Cr, *myo*-inositol (Myo), glutamate (Glu), glutamine (Gln), glutathione (GSH), PETH, Scyllo, Tau, Ala, Glc, GABA, Gly, and Lac.

Similarly, peak positions, amplitudes, and phases were obtained for other typical metabolites of interest, including NAA, Cr, Cho, *myo*-inositol, and glutathione. As above, their FID signals were reconstructed and their signal energies calculated for each echo time. These results are presented in Supplementary Figure 3.S1.

3.2.3.5 Glutamate-to-creatine ratio (Glu/Cr)

At each echo time, Glu/Cr was calculated by dividing the sums of amplitudes of glutamate and Cr resonances after T_2 correction:

$$\frac{\sum_{k,Glu} c_{k,Glu} / e^{-TE/T_{2,Glu}}}{\sum_{k,Cr} c_{k,Cr} / e^{-TE/T_{2,Cr}}} \times \frac{1/\rho_{Glu}}{1/\rho_{Cr}} \quad (3.3)$$

where $\sum_{k,Glu} c_{k,Glu}$ is the sum of the amplitudes of all k glutamate resonances, $\sum_{k,Cr} c_{k,Cr}$ is the sum of the amplitudes of all k resonances from the $N(CH_3)$ group of creatine, $T_{2,Glu}$ is the T_2 relaxation time-constant of glutamate, $T_{2,Cr}$ is the T_2 relaxation time-constant of the $N(CH_3)$ group of creatine, ρ_{Glu} is the number of glutamate protons, and ρ_{Cr} is the number of protons of the $N(CH_3)$ group of Cr.

The T_2 values used above were determined by fitting a two-parameter (amplitude and T_2) mono-exponential function to the in vivo metabolite amplitudes obtained from Subjects V1-V4 using a Levenberg–Marquardt minimization (the `lm` method in SciPy’s [36] `optimize.curve_fit()` function). The results were averaged to obtain the final T_2 values. The goodness of fit was evaluated by correlating the fitted result with the raw data using SciPy’s [36] `stats.spearmanr()` function. This function returns Spearman’s correlation coefficient, r_s , and a two-sided p -value for a hypothesis test whose null hypothesis is that two sets of data are uncorrelated. T_2 values were also measured for other metabolites of interest, including NAA, choline, *myo*-inositol, and glutathione.

3.2.3.6 Effect of macromolecule contribution

At shorter echo times, the increased contribution of macromolecule resonances that overlap with glutamate resonances [18] confounds glutamate fitting and quantification. To demonstrate this effect, variations of the macromolecule model were included in the prior knowledge template used to fit the $T_E = 45$ ms data from Subject V1. The amplitude of the lm5 and lm6 macromolecule lineshapes was changed from 20% of its original value to 220% of its original value (see Figure 3.4d later). The data from Subject V1 were then fit using the same methods as described above, and the signal energies calculated.

3.2.3.7 Sample size calculations

To assess the practical impact of the choice of echo time on future study design, we performed a sample size calculation to estimate the number of participants per group required to detect a 10% change in Glu/Cr between two groups with a 95% confidence level given a specific echo time. This calculation is given in Equation (3.4), a modified version of the formula described by Fox et al. [37]:

$$n = \left\lceil (u + v)^2 \times \frac{(2 \times \sigma_{TE}^2)}{(\Delta \times \mu_{TE})^2} \right\rceil \quad (3.4)$$

where $u = 1.28$ for 90% power, $v = 1.96$ for a 95% confidence level, $\Delta = 0.1$ for a 10% change, σ_{TE} is the SD of in vivo Glu/Cr at echo time T_E , and μ_{TE} is the mean in vivo Glu/Cr at echo-time T_E . This calculation assumes that the SD of Glu/Cr stays constant with changes in Glu/Cr.

3.2.4 In vitro data

3.2.4.1 Acquisition

In vitro data were obtained from a 900 mL aqueous phantom. The phantom contained glutamate, glutamine, and GABA at concentrations of 92.5mM, 45mM, and 15mM, respectively. These concentrations are approximately 10 times the average physiological concentrations in the normal adult human brain [20]. The conductivity of the phantom was adjusted to be similar to that of the human brain by adding sodium chloride (5 g). No relaxation agent was added. The phantom was adjusted to have a pH of 7.04 at room temperature with the addition of sodium hydroxide. Water suppressed in vitro ^1H -MRS data were collected from a $2.5 \times 2.5 \times 2.5 \text{ cm}^3$ voxel placed in the centre of the phantom at echo times ranging from 45 ms to 215 ms (5 ms step size). Since no relaxation agent was added, only a single-shot FID was acquired at each echo time. To allow the magnetization to return to equilibrium, a delay of 1 min was used between each acquisition.

3.2.4.2 Post-processing, prior knowledge, and spectral fitting

The methods of post-processing, generating prior knowledge, and spectral fitting used for the in vitro spectra was the same as described above for the in vivo spectra, except for the following changes. Although the quality of the acquired data was also assessed via water signal linewidth and SNR, the in vitro SNR was calculated differently. Instead of using the signal of the NAA CH_3 peak, SNR was measured using the height of the tallest peak of the absolute spectra.

The prior knowledge template used to fit the in vitro data was also different. Instead of including all metabolites, only glutamate, glutamine, and GABA were included in the prior knowledge template. Relative peak positions and phases between glutamate, glutamine, and GABA were not fixed and a separate Lorentzian linewidth parameter was defined for

each metabolite. After spectral fitting, the FID signals and signal energies were calculated for all three metabolites.

3.3 Results

3.3.1 Spectral quality

Examples of spectra collected in vivo are shown in Figure 3.2c, d. Examples of spectra collected in vitro are shown in Figure 3.3c, d. The spectra shown in Figure 3.2 and Figure 3.3 are representative of the high-quality, artefact-free data obtained from the semi-LASER sequence in this study. Excellent water suppression and outer-volume suppression was consistently achieved across all echo times. Localized B_0 shimming produced narrow water linewidths in vivo and in vitro. The in vivo mean (\pm SD) water signal linewidth across all subjects and all echo times was 10.1 ± 1.1 Hz and the in vitro mean (\pm SD) water signal linewidth across all echo times was 4.4 ± 0.2 Hz. The in vivo mean (\pm SD) SNR across all subjects and echo times was 119 ± 30 and was observed to decrease with echo time. Linear regression of the SNRs averaged across subjects showed a 0.58 SNR decrease for every 1 ms echo time ($p < 0.0001$). The in vitro mean (\pm SD) SNR across all echo times was 542 ± 193 . In vitro SNR also decreased with echo time, with linear regression showing an SNR decrease of 3 for every 1 ms echo time ($p < 0.0001$).

3.3.2 Echo-time dependence of glutamate signal energy

The results from the time-domain simulations and the in vivo acquisition are summarized in Figure 3.2. Time-domain simulations (Figure 3.2a) showed that the relationship between glutamate signal energy and echo time is not a simple exponential decay between $T_E = 45$ ms and $T_E = 215$ ms, but rather a curve with two local maxima. The glutamate signal energy was greatest at $T_E = 45$ ms, with another local maximum observed at 107 ms.

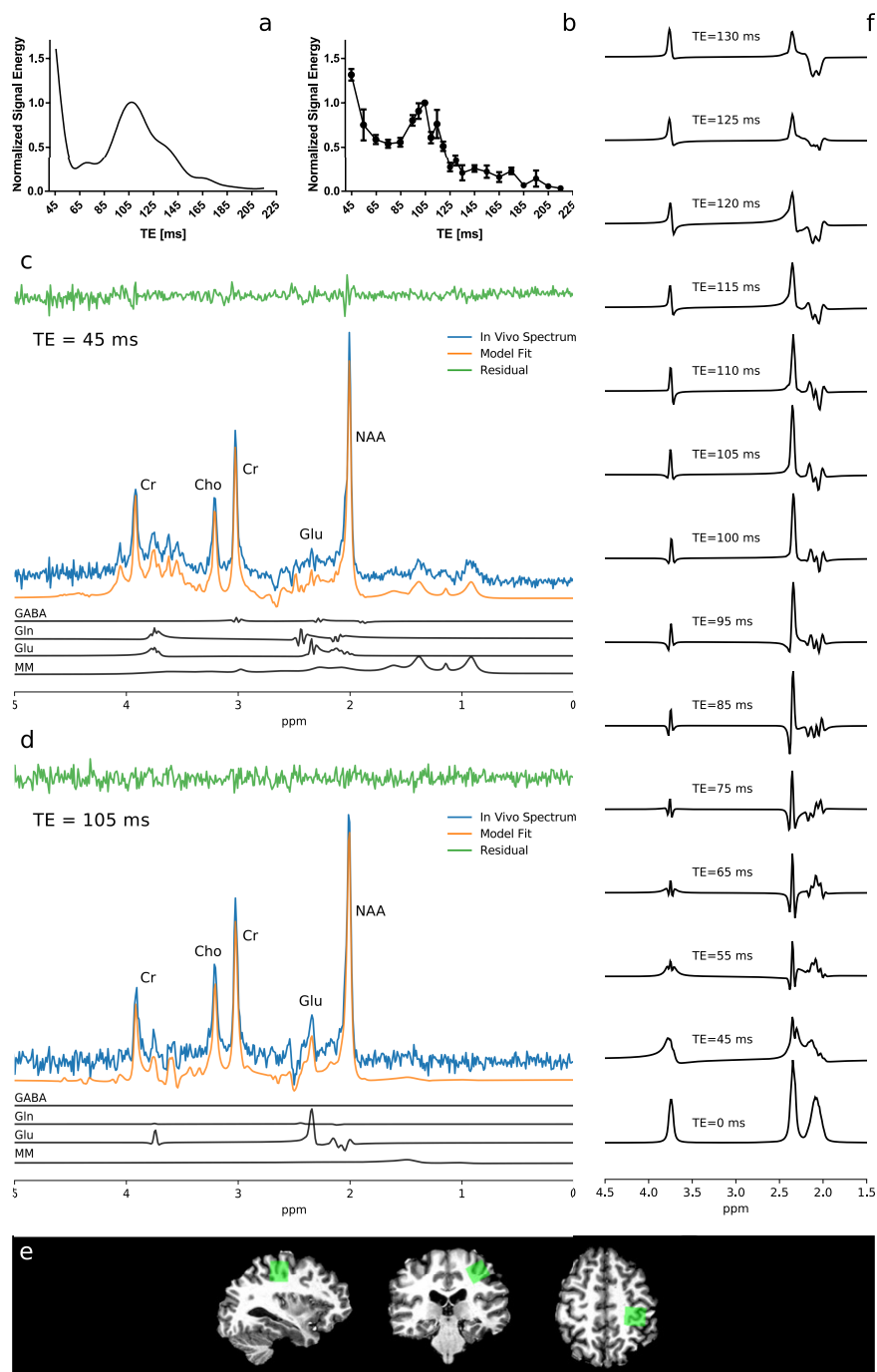


FIGURE 3.2: a, b, The calculated signal energies of glutamate from simulated data (a) and average in vivo data (b) are plotted from $T_E = 45$ ms to $T_E = 215$ ms. Standard errors are shown for the in vivo data.

3.3. Results

FIGURE 3.2: Signal energies were normalized to the maximum signal energy to allow comparison between experiments. The maximal signal energy occurred at 45 ms for the simulated data, and at 45 ms for the in vivo data. A secondary local maximum occurred at 107 ms and 105 ms for the simulated and in vivo data, respectively. c, d, Examples of in vivo ^1H -MRS spectra collected from a $2 \times 2 \times 2 \text{ cm}^3$ voxel in the left sensorimotor cortex at $T_E = 45 \text{ ms}$ and $T_E = 105 \text{ ms}$ respectively using the semi-LASER sequence. The orange line shows the result after fitting the spectrum with the simulated prior knowledge template. The residual following fitting is shown by the green line. At $T_E = 105 \text{ ms}$, the resonances from macromolecules are reduced, and the main glutamate peak at about 2.3 ppm appears prominently. e, The voxel position. f, When examining the in vivo glutamate spectral pattern as a function of echo time, the main glutamate peak at about 2.3 ppm is entirely in phase at $T_E = 105 \text{ ms}$. A simulated glutamate spectrum generated from a pulse-acquire experiment ($T_E = 0 \text{ ms}$) with a 10 Hz linewidth is included for reference.

The in vivo (Figure 3.2b) results showed the same pattern of variation in the glutamate signal as a function of echo time. In almost perfect agreement with the simulations, the in vivo spectra also had the greatest glutamate signal energy at 45 ms, with another local maximum observed at 105 ms. The in vivo echo-time dependence of signal energy for other metabolites of interest (NAA, Cr, Cho, *myo*-inositol, and glutathione) are shown in Supplementary Figure 3.S1.

In vitro, the glutamate signal also varied with echo time in a similar way (Figure 3.3a). Like the simulated and in vivo results, the curve had two local maxima. Glutamate signal energy was greatest at $T_E = 100 \text{ ms}$, with another local maximum observed at 45 ms. Comparing the glutamate signal energy with the glutamine and GABA signal energies with respect to echo time revealed that the maximal difference in signal energy between glutamate and glutamine signals occurred at $T_E = 105 \text{ ms}$ (Figure 3.3b). The maximal difference in signal energy between glutamate and GABA signals occurred at $T_E = 100 \text{ ms}$.

3.3.3 In vivo spectral fitting quality

In vivo glutamate CRLBs plotted across echo time are shown in Figure 3.4a. All glutamate CRLBs between $T_E = 45 \text{ ms}$ and $T_E = 145 \text{ ms}$ were under 20%. The minimum glutamate CRLB ($6.2 \pm 0.9\%$) occurred at $T_E = 100 \text{ ms}$, which is close to the echo time at which the

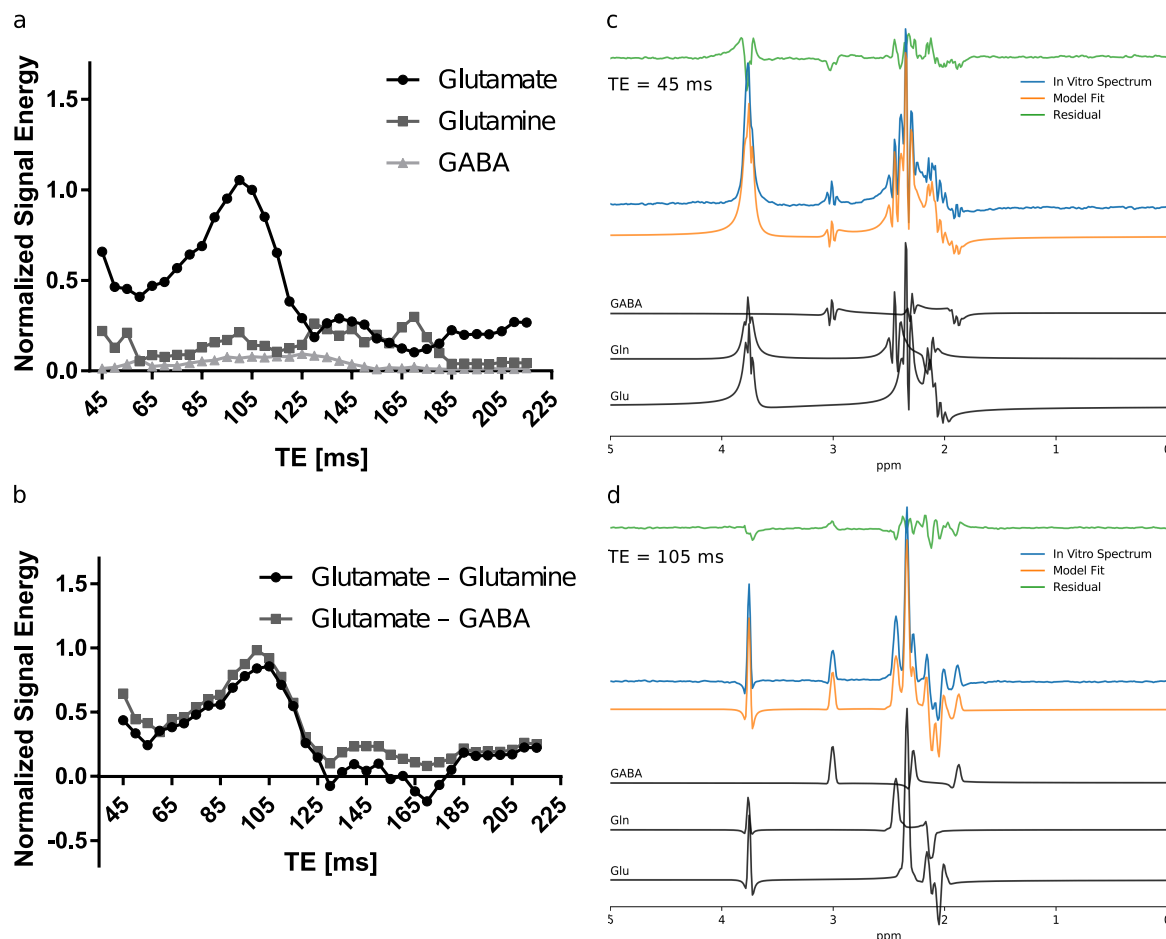


FIGURE 3.3: a, The calculated signal energies of glutamate, glutamine, and GABA from *in vitro* data obtained using a mixed-metabolite phantom from $T_E = 45 \text{ ms}$ to $T_E = 215 \text{ ms}$. Signal energies were normalized to the signal energy of glutamate at $T_E = 105 \text{ ms}$. The maximal signal energy for glutamate occurred at 100 ms, with a secondary local maximum at 45 ms. b, The differences in signal energy between the glutamate signal and the glutamine and GABA signals from $T_E = 45 \text{ ms}$ to $T_E = 215 \text{ ms}$. The maximal difference in signal energy occurred at $T_E = 105 \text{ ms}$ for glutamate versus glutamine, and at $T_E = 100 \text{ ms}$ for glutamate versus GABA. c, d, Examples of *in vitro* ^1H -MRS spectra collected from a $2.5 \times 2.5 \times 2.5 \text{ cm}^3$ voxel in the centre of the phantom at $T_E = 45 \text{ ms}$ and $T_E = 105 \text{ ms}$ respectively. Since the average linewidth of the phantom spectra was 4 Hz, a 6 Hz exponential filter was applied to the phantom spectra such that the linewidth matched what was typically observed in our *in vivo* data (10 Hz). At $T_E = 105 \text{ ms}$, peaks of glutamate and glutamine in the 2–3 ppm range that are present at $T_E = 45 \text{ ms}$ are reduced, resulting in little overlap between the peaks of the three metabolites in the 2–3 ppm region.

3.3. Results

secondary glutamate signal energy maximum was observed in vivo ($T_E = 105$ ms, CRLB = $6.5 \pm 2.0\%$).

Inter-subject coefficients of variation (CVs) of Glu/Cr were also calculated. Glu/Cr CVs are plotted as a function of echo time in Figure 3.4b. All Glu/Cr CVs between $T_E = 45$ ms and $T_E = 130$ ms were below 25%. The minimum Glu/Cr CV (4.6%) was observed at $T_E = 105$ ms. Glu/Cr at $T_E = 105$ ms was 0.95 ± 0.04 .

At the shorter echo times, the glutamate fit is directly influenced by the macromolecule fit. Specifically, the energy of the glutamate signal decreased (Figure 3.4c) as the amplitude of the lm5 and lm6 lineshapes in the macromolecule model was increased (Figure 3.4d).

3.3.4 Sample size calculations

The estimated number of participants per group required to detect a 10% change in Glu/Cr between two groups with a 95% confidence level at each echo time is shown in Figure 3.5. The minimum estimated required number of participants was 5 per group and occurred at $T_E = 105$ ms. The estimated required number of participants at $T_E = 45$ ms was 13 per group.

3.3.5 T_2 relaxation times

The average T_2 relaxation times of the metabolites are shown in Table 3.2. The quality of the exponential fits, indicated by the average Spearman's correlation coefficient r_s , and associated p -values, are also shown in Table 3.2. The associated p -values were all less than 0.01 for the listed metabolites, indicating a significant correlation between the raw data and the exponential fit.

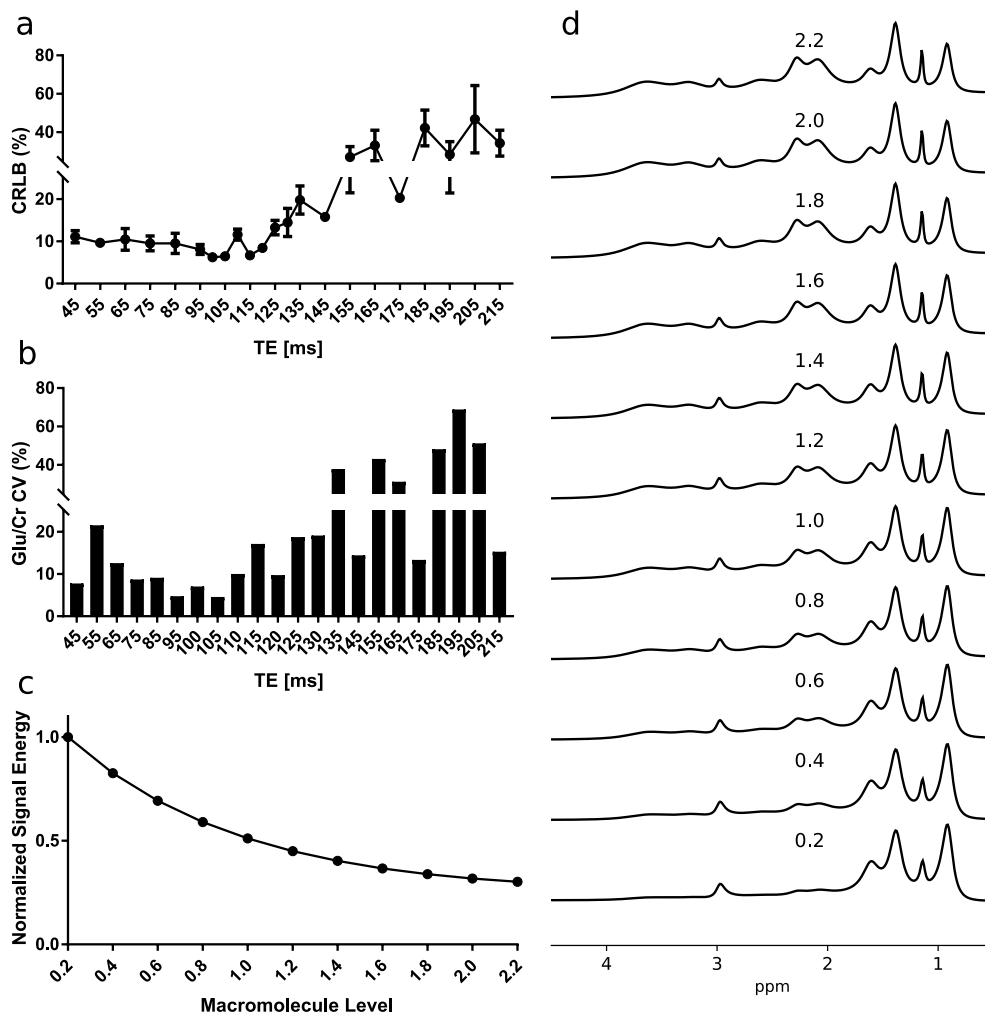


FIGURE 3.4: a, CRLBs for the glutamate fit are plotted as a function of echo time with standard errors shown. The minimum glutamate CRLB was $6.2 \pm 0.9\%$ at $T_E = 100$ ms, which is close to the echo time at which the secondary glutamate signal energy maximum was observed *in vivo* (105 ms). The glutamate CRLB at $T_E = 105$ ms was $6.5 \pm 2.0\%$. b, Inter-subject coefficients of variance of Glu/Cr are plotted against echo time. The minimum Glu/Cr CV was 4.6% at $T_E = 105$ ms. c, The energy of the glutamate signal fitted to *in vivo* data acquired at $T_E = 45$ ms from Subject V1 as a function of the lm5 and lm6 macromolecule amplitude. d, The macromolecule model was varied by changing the lm5 and lm6 macromolecule line shape from 20% of its original value to 220% of its original value. The altered macromolecule model was incorporated into the prior knowledge template used to fit the $T_E = 45$ ms *in vivo* data of Subject V1.

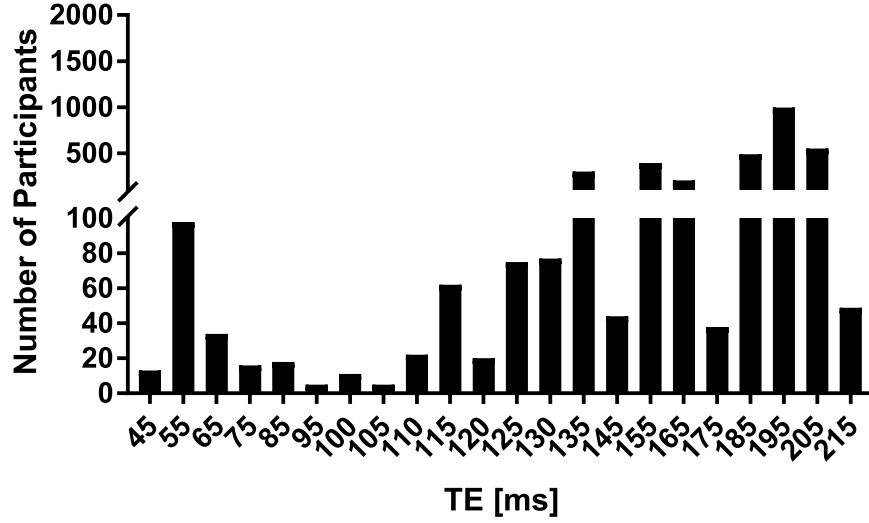


FIGURE 3.5: Estimated number of participants per group required to detect a 10% change in Glu/Cr between two groups at a 95% confidence level are plotted across echo time. The minimum required number of participants per group was 5 at $T_E = 105$ ms. The number of participants per group required at $T_E = 45$ ms was 13.

Metabolite	Group	Type	T_2 (ms)	r_s	p
NAA	2CH_3	Singlet	138 ± 11	0.96	< 0.001
	3CH_2	Multiplet	69 ± 4	0.86	< 0.001
Creatine	$N(CH_3)$	Singlet	120 ± 1	0.99	< 0.001
	2CH_2	Singlet	87 ± 3	0.97	< 0.001
Choline	Entire molecule	Singlet	128 ± 9	0.90	< 0.001
Myo-inositol	Entire molecule	Multiplet	102 ± 8	0.78	< 0.001
Glutamate	Entire molecule	Multiplet	72 ± 5	0.95	< 0.001
Glutathione	Entire molecule	Multiplet	63 ± 16	0.82	< 0.01

TABLE 3.2: T_2 values (mean \pm SD) of various metabolites of interest measured from a voxel in the sensorimotor cortex of Subjects V1, V2, V3, and V4. Statistically significant fits were obtained with $r_s \geq 0.80$, except for *myo*-inositol, which had $r_s = 0.78$.

3.4 Discussion

The goal of this work was to determine the optimal echo time for glutamate measurement at 7 T using the semi-LASER pulse sequence. Time-domain simulations of the glutamate system showed a local signal energy maximum at an echo time of 107 ms. This echo time was in agreement with the results from the in vivo and in vitro experiments, which showed a local signal energy maximum at 105 ms and 100 ms, respectively. Additionally, the lowest in vivo CRLBs, indicating the highest-quality model fits, and the lowest measurement variability associated with Glu/Cr, were achieved at $T_E = 100$ –105 ms. Taken together these results indicate that $T_E = 105$ ms maximizes glutamate signal energy in vivo while also maximizing glutamate measurement precision, and suggests that this echo time is optimal for in vivo glutamate measurement at 7 T with semi-LASER.

This result is counter-intuitive, as the current practice in ^1H -MRS is to use the shortest achievable echo time to maximize the signal of J -coupled metabolites, including glutamate. Previous phantom work by Zhong and Ernst [14] at 4 T using the PRESS sequence compared the resonances of glutamate at $T_E = 8$ ms and $T_E = 30$ ms. They found virtually no dephasing due to J coupling and minimal signal loss at $T_E = 8$ ms compared with $T_E = 30$ ms, suggesting increased SNR and improved metabolite quantitation.

Along this line of reasoning, the shortest possible echo times have traditionally been selected when using the semi-LASER sequence at high field. A variety of echo times have been chosen, as the minimum T_E achieved depends strongly on hardware capabilities, pulse settings, and sequence parameters [38]. These dependencies include the maximum available B_1 amplitude, pulse duration, and crusher gradient duration. Echo times as short as 36 ms (Reference [39]) and 38 ms (Reference [11]) have been achieved at 7 T. An even shorter echo time of 26 ms (Reference [40]) was achieved using 16 RF amplifiers (1 kW each), which provided greater B_1 amplitude, allowing for shorter adiabatic pulses. Trapezoidal adiabatic pulses, which can achieve more spectral bandwidth with less B_1 amplitude

than hyperbolic secant adiabatic pulses, also allows for shorter pulse lengths and thus even shorter echo times. For example, Boer et al. [41] achieved an echo-time of 25 ms using trapezoidal adiabatic pulses, despite having only two 4 kW RF amplifiers. With only eight 1 kW RF amplifiers and conventional hyperbolic secant pulses, the minimum achievable echo-time was 45 ms in the current study.

Regardless of the available hardware, acquiring short-echo-time spectra has the added complication of a more pronounced macromolecule signal, which complicates the subsequent fitting and quantification of metabolites, particularly glutamate. In fact, Zhong and Ernst showed that the intensity of the macromolecule peak at 0.9 ppm doubled at $T_E = 8$ ms compared with $T_E = 30$ ms [14]. Several approaches can be used to estimate the macromolecule contribution including spline fitting (LCModel [42]), measuring the macromolecule signal using inversion recovery techniques and including the lineshape as a basis function in the prior knowledge template [38, 39, 40, 41, 43], use of a parameterized mathematical model of the macromolecules in the prior knowledge template [6, 22, 44, 45], or acquisition of a subject-specific metabolite-nulled macromolecule spectrum that is subtracted from the full spectrum [11, 46]. Not surprisingly, Schaller et al. [45] showed that the approach used to remove the macromolecule signal when using short echo times can significantly impact glutamate quantification, which contributes to variability in the glutamate measurement and complicates the comparison of glutamate levels from studies that use different methods for macromolecule signal removal. The current study has also demonstrated that the magnitude of the estimated macromolecule contribution to the spectrum significantly impacts the measured glutamate level. The use of long echo times to minimize macromolecule contributions greatly reduced measurement variability.

In the present study, we observed the greatest in vivo glutamate signal at the shortest echo time ($T_E = 45$ ms). However, the glutamate fit at that echo time was highly variable between subjects, probably due to variations in the macromolecule model contribution. Uncertainty in the $T_E = 45$ ms measurement was evidenced by the CVs of Glu/Cr and the

CRLBs of the glutamate fits. Both improved as the echo time approached 105 ms, with the lowest Glu/Cr CV occurring at 105 ms. This lower variability translated into practical benefits for study design. The estimated number of participants per group required to detect a 10% change in Glu/Cr between two groups at $T_E = 105$ ms was 5, compared with 13 at $T_E = 45$ ms. However, it should be noted that the signal of other metabolites decreases at longer echo times (Supplementary Figure 3.S1) and that the use of a long-echo-time measurement of glutamate may result in greater measurement variability for other metabolites in the spectrum.

The measured Glu/Cr of 0.95 ± 0.04 at $T_E = 105$ ms was in good agreement with previous measurements in healthy individuals. For example, using a 7 T system, Choi et al. [47] reported a Glu/Cr of 1.16 ± 0.11 measured using PRESS ($T_E = 100$ ms) and 1.22 ± 0.13 measured using STEAM ($T_E = 14$ ms) in the medial prefrontal cortex. Using ^1H -MRS imaging at 7 T (free induction decay acquisition with acquisition delay $T_E^* = 1.3$ ms), Bogner et al. reported Glu/Crs of 0.99 ± 0.16 in a white matter voxel in the right frontal lobe, 1.07 ± 0.1 in a gray matter voxel in the center of the frontal lobe, and 1.0 ± 0.14 in a white matter voxel in the left frontal lobe [48]. Similarly, using a spectrally selective refocusing method at 3 T ($T_E = 128$ ms), Choi et al. reported a Glu/Cr of 1.21 ± 0.06 in the prefrontal cortex [49]. Therefore, the use of long T_E to measure Glu/Cr provides measurements comparable to those made using shorter echo times with different pulse sequences and at lower field strengths when correction for number of protons and T_2 relaxation is incorporated.

The necessary T_2 correction required when using a long T_E may be a disadvantage when incorporating spectroscopic measurements in multi-modality MR imaging protocols, as is the case with most clinical studies. In these studies, it is usually infeasible to perform a T_2 measurement for each participant due to the lengthy scan time required. Use of literature values for T_2 correction is generally accepted in the field of ^1H -MRS, although errors in measured metabolite levels could occur due to T_2 changes in disease. When short T_E is used, T_2 correction is still required, but measured metabolite levels are less sensitive to

T_2 differences. However, increased sensitivity to T_2 may be an acceptable trade-off for the demonstrated improvement in measurement variability at $T_E = 105$ ms.

The glutamate CRLBs that we reported (Figure 3.4a) were higher than previously reported CRLBs in other ^1H -MRS studies performed with a similar number of participants at 7 T. For example, Choi et al [47] reported a mean glutamate CRLB of 2% across six healthy subjects when using PRESS at $T_E = 100$ ms. Similarly, Pradhan et al. [50] reported mean glutamate CRLBs of 2.5–4.8% across four healthy subjects when using semi-LASER at $T_E = 32$ ms. The higher glutamate CRLBs that we report can be attributed to methodological differences. First, Choi et al. and Pradhan et al. used spectroscopy voxels that are approximately three times larger than the voxel used in the present study. Second, Choi et al. and Pradhan et al. used 64 averages (four times more than the present study) and 32 averages (twice as many as the present study), respectively, to collect water-suppressed spectroscopy data. The larger voxel sizes and greater number of averages combine to produce spectra with greater SNR, resulting in a lower CRLB. In fact, Pradhan et al. report an SNR of 135 ± 28 at $T_E = 32$ ms. Replicating their method of SNR calculation with our $T_E = 45$ ms data, we obtain an SNR of 59 ± 11 . Thus, it is unsurprising that we obtained higher glutamate CRLBs. However, we did achieve a glutamate CRLB comparable to the 4.8% CRLB reported by Pradhan et al. in the centrum semiovale at the proposed optimal echo time of $T_E = 105$ ms (CRLB = $6.5 \pm 2.0\%$). The greater number of averages reported by Choi et al. and Pradhan et al. is typical of clinical spectroscopy studies. More averages would improve SNR and lower the glutamate CRLBs. As a result, Glu/Cr variability across subjects would decrease, subsequently increasing statistical power to detect differences in Glu/Cr at $T_E = 105$ ms.

The determination of the optimal T_E for glutamate measurement has previously been studied using PRESS at 7 T and 3 T [47, 51, 52], but not for semi-LASER. Notably, Snyder and Wilman [51] used numerical simulation to optimize the PRESS timings at various field strengths. The results showed that an echo time of 105 ms ($T_{E1} = 20$ ms, $T_{E2} = 85$ ms)

yielded optimal separation of glutamate and glutamine peaks and optimal glutamate and glutamine amplitudes at 7 T. Similarly, Choi et al. [47] verified this result by collecting in vivo spectra from the medial prefrontal cortex of six healthy volunteers, finding that $T_E = 100$ ms provided improved resolution of these metabolites, reduced macromolecule signal, and a more reliable measurement.

These results are consistent with the current study using semi-LASER. Specifically, our in vitro experiments showed that $T_E = 100$ ms maximized the difference between glutamate and GABA signal energies, while $T_E = 105$ ms maximized the difference between the glutamate and glutamine signal energies (Figure 3.3b). This suggests that the glutamine and GABA signals are reduced relative to glutamate at $T_E = 100$ – 105 ms. Comparing the in vitro spectra at $T_E = 45$ ms (Figure 3.3c) and at $T_E = 105$ ms (Figure 3.3d) reveals that some peaks of glutamate and glutamine in the 2–3 ppm range that are present at $T_E = 45$ ms are reduced at $T_E = 105$ ms. The remaining peaks at $T_E = 105$ ms have little overlap in the 2–3 ppm region, resulting in better separation between the glutamate and glutamine spectra.

Others have also taken different approaches to detect glutamate, including using spectral editing to separate glutamate from overlapping resonances [53, 54]. Using MEGA-PRESS at 3 T, Waddell et al. reported a Glu/Cr of 1.16 ± 0.10 in the anterior cingulate and 0.70 ± 0.07 in the cerebellar vermis [54]. These measurements are comparable to the Glu/Cr reported in this study (0.95 ± 0.04 at $T_E = 105$ ms in the sensorimotor cortex). The inter-subject Glu/Cr CV reported by Waddell et al. was 8.9% in the anterior cingulate and 11% in the cerebellar vermis. Both are higher than the value we achieved at $T_E = 105$ ms with the semi-LASER sequence (4.0%). Spectral editing also has several drawbacks. Since the echo time of the editing sequence is determined by the J coupling of the metabolite, a T_E of around 70 ms is required for glutamate detection [53, 54, 55], leading to co-editing of macromolecules and requiring incorporation of methods to reduce the macromolecule contribution. Quantification of metabolite concentrations also becomes more complicated, requiring additional corrections for editing efficiency, co-editing, and chemical exchange

in addition to the corrections for relaxation and B_1 inhomogeneities that are already necessary for quantification of unedited spectra [56]. Further study directly comparing spectral editing and long-echo-time semi-LASER is needed to determine which technique measures glutamate with greater accuracy and precision at 7 T.

There are some limitations of this study that should be considered. First, only one approach to modelling the macromolecule contributions at short echo times was utilized in the current study. Other approaches as described above may improve glutamate measurement reproducibility at short echo times. However, all such techniques introduce uncertainty. Therefore, use of such techniques would probably not result in a better CV than that achieved at $T_E = 105$ ms. Second, the absolute concentration of glutamate was not measured in vivo. This is because high-resolution structural scans were not acquired in order to keep the total scan time to 2 h. Such images are needed to determine the tissue partial volume within the voxel for accurate metabolite quantification.

3.5 Conclusions

In vivo, the semi-LASER sequence at $T_E = 105$ ms produced the greatest glutamate signal energy while also maximizing glutamate measurement precision, and consequently increasing statistical power to detect differences in Glu/Cr. Therefore, we conclude that $T_E = 105$ ms is the preferred echo time for in vivo glutamate measurement at 7 T with semi-LASER. Using this long echo time has several advantages. It allows the use of a lower maximum B_1 in conjunction with longer RF and gradient pulses, resulting in less power deposition into the tissue. As shown by in vitro measurements in the present study, overlap between glutamate, glutamine, and GABA peaks are minimal at $T_E = 105$ ms. Most importantly, macromolecule contributions at $T_E = 105$ ms are minimal, eliminating the need for macromolecule removal or fitting techniques that add additional scan time or can directly bias the estimated glutamate fit.

3.6 Acknowledgement

Funding provided by The Alzheimer Foundation of London and Middlesex. The authors wish to thank Siemens for providing the semi-LASER sequence, Gülin Öz for helpful discussion on sequence implementation, and Jagroop Doad for help with creating the mixed-metabolite phantom.

3.7 References

- [1] F. Fonnum. "Glutamate: A Neurotransmitter in Mammalian Brain". In: *Journal of Neurochemistry* 42.1 (Jan. 1984), pp. 1–11.
- [2] R. Rupsingh et al. "Reduced hippocampal glutamate in Alzheimer disease". In: *Neurobiology of Aging* 32.5 (May 2011), pp. 802–810.
- [3] W.-F. Peng et al. "Increased ratio of glutamate/glutamine to creatine in the right hippocampus contributes to depressive symptoms in patients with epilepsy." In: *Epilepsy & behavior : E&B* 29.1 (Oct. 2013), pp. 144–9.
- [4] I. Kowalczyk, N. Duggal, and R. Bartha. "Proton magnetic resonance spectroscopy of the motor cortex in cervical myelopathy". In: *Brain* 135.2 (Feb. 2012), pp. 461–468.
- [5] R. Taylor et al. "Functional magnetic resonance spectroscopy of glutamate in schizophrenia and major depressive disorder: anterior cingulate activity during a color-word Stroop task." In: *NPJ schizophrenia* 1.1 (Dec. 2015), p. 15028.
- [6] R. Bartha et al. "Comparison of the Quantification Precision of Human Short Echo Time 1H Spectroscopy at 1.5 and 4.0 Tesla". In: *Magnetic Resonance in Medicine* 192.2 (Aug. 2000), pp. 185–192.

3.7. References

- [7] I. Tkáč et al. "In vivo ^1H NMR spectroscopy of the human brain at high magnetic fields: metabolite quantification at 4T vs. 7T." In: *Magnetic Resonance in Medicine* 62.4 (Oct. 2009), pp. 868–79. arXiv: NIHMS150003.
- [8] M. Garwood and L. DelaBarre. "The return of the frequency sweep: designing adiabatic pulses for contemporary NMR." In: *Journal of magnetic resonance (San Diego, Calif. : 1997)* 153.2 (Dec. 2001), pp. 155–77.
- [9] G. Oz and I. Tkáč. "Short-echo, single-shot, full-intensity proton magnetic resonance spectroscopy for neurochemical profiling at 4 T: validation in the cerebellum and brainstem." In: *Magnetic resonance in medicine* 65.4 (Apr. 2011), pp. 901–10.
- [10] T. W. J. Scheenen, A. Heerschap, and D. W. J. Klomp. "Towards ^1H -MRSI of the human brain at 7T with slice-selective adiabatic refocusing pulses." In: *Magma (New York, N.Y.)* 21.1-2 (Mar. 2008), pp. 95–101.
- [11] J. Penner and R. Bartha. "Semi-LASER (^1H) MR spectroscopy at 7 Tesla in human brain: Metabolite quantification incorporating subject-specific macromolecule removal." In: *Magnetic resonance in medicine* 12.1 (July 2014), pp. 4–12.
- [12] P. A. Bottomley. "Spatial localization in NMR spectroscopy in vivo". In: *Annals of the New York Academy of Sciences* 508.1 Physiological (Nov. 1987), pp. 333–48.
- [13] J. Frahm et al. "Localized high-resolution proton NMR spectroscopy using stimulated echoes: Initial applications to human brain in vivo". In: *Magnetic Resonance in Medicine* 9.1 (Jan. 1989), pp. 79–93.
- [14] K. Zhong and T. Ernst. "Localized in vivo human ^1H MRS at very short echo times". In: *Magnetic Resonance in Medicine* 52.4 (Oct. 2004), pp. 898–901.
- [15] G. Öz et al. "Proton MRS of the unilateral substantia nigra in the human brain at 4 tesla: Detection of high GABA concentrations". In: *Magnetic Resonance in Medicine* 55.2 (Feb. 2006), pp. 296–301.

- [16] V. Mlynárik et al. "Very short echo time proton MR spectroscopy of human brain with a standard transmit/receive surface coil." In: *Magnetic resonance in medicine : official journal of the Society of Magnetic Resonance in Medicine / Society of Magnetic Resonance in Medicine* 44.6 (Dec. 2000), pp. 964–7.
- [17] I. Tkáč et al. "In vivo ^1H NMR spectroscopy of the human brain at 7 T." In: *Magnetic resonance in medicine* 46.3 (Sept. 2001), pp. 451–6.
- [18] K. L. Behar et al. "Analysis of macromolecule resonances in ^1H NMR spectra of human brain". In: *Magnetic Resonance in Medicine* 32.3 (Sept. 1994), pp. 294–302.
- [19] B. Soher et al. "VeSPA: Integrated applications for RF pulse design, spectral simulation and MRS data analysis". In: *Proceedings of the 19th Annual Meeting ISMRM* 19.19 (2011), p. 1410.
- [20] V. Govindaraju, K. Young, and A. A. Maudsley. "Proton NMR chemical shifts and coupling constants for brain metabolites". In: *NMR in biomedicine* 13.3 (2000), pp. 129–153.
- [21] M. Marjańska et al. "Localized ^1H NMR spectroscopy in different regions of human brain in vivo at 7 T: T_2 relaxation times and concentrations of cerebral metabolites". In: *NMR in Biomedicine* 25.2 (Feb. 2012), pp. 332–339.
- [22] R. Bartha, D. J. Drost, and P. C. Williamson. "Factors affecting the quantification of short echo in-vivo ^1H MR spectra: prior knowledge, peak elimination, and filtering." In: *NMR in biomedicine* 12.4 (June 1999), pp. 205–16.
- [23] G. Cariolaro. "Classical Signal Theory". In: *Unified Signal Theory*. London: Springer London, 2011, pp. 17–79.
- [24] R. A. de Graaf. *In Vivo NMR Spectroscopy*. 2nd ed. Chichester, UK: John Wiley & Sons, Ltd, Oct. 2007.

- [25] K. M. Gilbert et al. "An parallel-transmit, parallel-receive coil for routine scanning on a 7T head-only scanner". In: *Proceedings of the 23rd Annual Meeting of ISMRM*. Toronto, 2015, p. 0623.
- [26] A. Greiser et al. "Improved Cardiac Shimming In A Clinical Setting By Multi-Frame Fieldmap Acquisition and Automatic ROI Extension". In: *Journal of Cardiovascular Magnetic Resonance* 9.2 (2007), pp. 239–240.
- [27] J. E. Schneider and P. Jezard. "Development of a rapid, automated shim approach for cardiac MR in mice in vivo". In: *Proceedings of the International Society for Magnetic Resonance in Medicine* 19.2 (2006).
- [28] M. Schär et al. "Local linear shimming for cardiac SSFP imaging at 3T". In: *Proceedings of the International Society for Magnetic Resonance in Medicine* 10 (2002).
- [29] M. Schär et al. "Cardiac SSFP Imaging at 3 Tesla". In: *Magnetic Resonance in Medicine* 51.4 (Apr. 2004), pp. 799–806.
- [30] A. T. Curtis et al. "Slice-by-slice B1+ shimming at 7 T." In: *Magnetic resonance in medicine* 68.4 (Oct. 2012), pp. 1109–16.
- [31] I. Tkáč et al. "In vivo ^1H NMR spectroscopy of rat brain at 1 ms echo time". In: *Magnetic Resonance in Medicine* 41.4 (Apr. 1999), pp. 649–656.
- [32] R. Otazo et al. "Signal-to-noise ratio and spectral linewidth improvements between 1.5 and 7 Tesla in proton echo-planar spectroscopic imaging." In: *Magnetic resonance in medicine* 56.6 (Dec. 2006), pp. 1200–10.
- [33] A. van den Boogaart et al. "Time and frequency domain analysis of NMR data compared: an application to 1D ^1H spectra of lipoproteins." In: *Magnetic resonance in medicine* 31.4 (Apr. 1994), pp. 347–58.

- [34] D. K. Deelchand et al. "Measurement of transverse relaxation times of J-coupled metabolites in the human visual cortex at 4 T". In: *Magnetic Resonance in Medicine* 67.4 (Apr. 2012), pp. 891–897.
- [35] J. H. Griesmer. "Society for Industrial and Applied Mathematics (A5)". In: *Science* 151.3712 (Feb. 1966), pp. 859–860. arXiv: arXiv:1011.1669v3.
- [36] E. Jones, T. Oliphant, P. Peterson, et al. *SciPy: Open source scientific tools for Python*. 2001.
- [37] N. C. Fox et al. "Using Serial Registered Brain Magnetic Resonance Imaging to Measure Disease Progression in Alzheimer Disease". In: *Archives of Neurology* 57.3 (Mar. 2000), p. 339.
- [38] A. Fuchs et al. "SPECIAL semi-LASER with lipid artifact compensation for 1H MRS at 7 T". In: *Magnetic Resonance in Medicine* 69.3 (Mar. 2013), pp. 603–612.
- [39] I. Betina Ip et al. "Combined fMRI-MRS acquires simultaneous glutamate and BOLD-fMRI signals in the human brain". In: *NeuroImage* 155 (July 2017), pp. 113–119.
- [40] M. Terpstra et al. "Test-retest reproducibility of neurochemical profiles with short-echo, single-voxel MR spectroscopy at 3T and 7T". In: *Magnetic Resonance in Medicine* 76.4 (Oct. 2016), pp. 1083–1091.
- [41] V. O. Boer et al. "7-T 1H MRS with adiabatic refocusing at short TE using radiofrequency focusing with a dual-channel volume transmit coil". In: *NMR in Biomedicine* 24.9 (2011), pp. 1038–1046.
- [42] S. W. Provencher. "Automatic quantitation of localized in vivo 1H spectra with LCModel". In: *NMR in Biomedicine* 14.4 (June 2001), pp. 260–264.

- [43] P. Bednařík et al. "Neurochemical and BOLD Responses during Neuronal Activation Measured in the Human Visual Cortex at 7 Tesla". In: *Journal of Cerebral Blood Flow & Metabolism* 35.4 (Apr. 2015), pp. 601–610.
- [44] R. Kreis et al. "Integrated data acquisition and processing to determine metabolite contents, relaxation times, and macromolecule baseline in single examinations of individual subjects". In: *Magnetic Resonance in Medicine* 54.4 (Oct. 2005), pp. 761–768.
- [45] B. Schaller et al. "Quantification of the neurochemical profile using simulated macromolecule resonances at 3 T". In: *NMR in Biomedicine* 26.5 (May 2013), pp. 593–599.
- [46] M. N. E. Kassem and R. Bartha. "Quantitative proton short-echo-time LASER spectroscopy of normal human white matter and hippocampus at 4 tesla incorporating macromolecule subtraction". In: *Magnetic Resonance in Medicine* 49.5 (May 2003), pp. 918–927.
- [47] C. Choi et al. "Improvement of resolution for brain coupled metabolites by optimized ^1H MRS at 7T". In: *NMR in Biomedicine* 23.9 (Nov. 2010), pp. 1044–1052.
- [48] W. Bogner et al. "High-resolution mapping of human brain metabolites by free induction decay ^1H MRSI at 7T". In: *NMR in Biomedicine* 25.6 (June 2012), pp. 873–882.
- [49] C. Choi et al. "Measurement of brain glutamate and glutamine by spectrally-selective refocusing at 3-tesla". In: *Magnetic Resonance in Medicine* 55.5 (May 2006), pp. 997–1005.
- [50] S. Pradhan et al. "Comparison of single voxel brain MRS AT 3T and 7T using 32-channel head coils". In: *Magnetic Resonance Imaging* 33.8 (2015), pp. 1013–1018. arXiv: 15334406.

- [51] J. Snyder and A. Wilman. "Field strength dependence of PRESS timings for simultaneous detection of glutamate and glutamine from 1.5 to 7 T". In: *Journal of Magnetic Resonance* 203.1 (Mar. 2010), pp. 66–72.
- [52] A. Yahya, B. Mädler, and B. G. Fallone. "Exploiting the chemical shift displacement effect in the detection of glutamate and glutamine (Glx) with PRESS". In: *Journal of Magnetic Resonance* 191.1 (2008), pp. 120–127.
- [53] R. L. O’Gorman et al. "In vivo detection of GABA and glutamate with MEGA-PRESS: Reproducibility and gender effects". In: *Journal of Magnetic Resonance Imaging* 33.5 (May 2011), pp. 1262–1267.
- [54] K. W. Waddell et al. "Anterior cingulate and cerebellar GABA and Glu correlations measured by ^1H J-difference spectroscopy." In: *Magnetic resonance imaging* 29.1 (Jan. 2011), pp. 19–24.
- [55] A. Andreychenko et al. "In vivo GABA T_2 determination with J-refocused echo time extension at 7 T". In: *NMR in Biomedicine* 26.11 (Nov. 2013), pp. 1596–1601.
- [56] W. Bogner et al. "1D-spectral editing and 2D multispectral in vivo ^1H -MRS and ^1H -MRSI - Methods and applications". In: *Analytical Biochemistry* 529 (July 2017), pp. 48–64.

3.8 Supplementary Figures

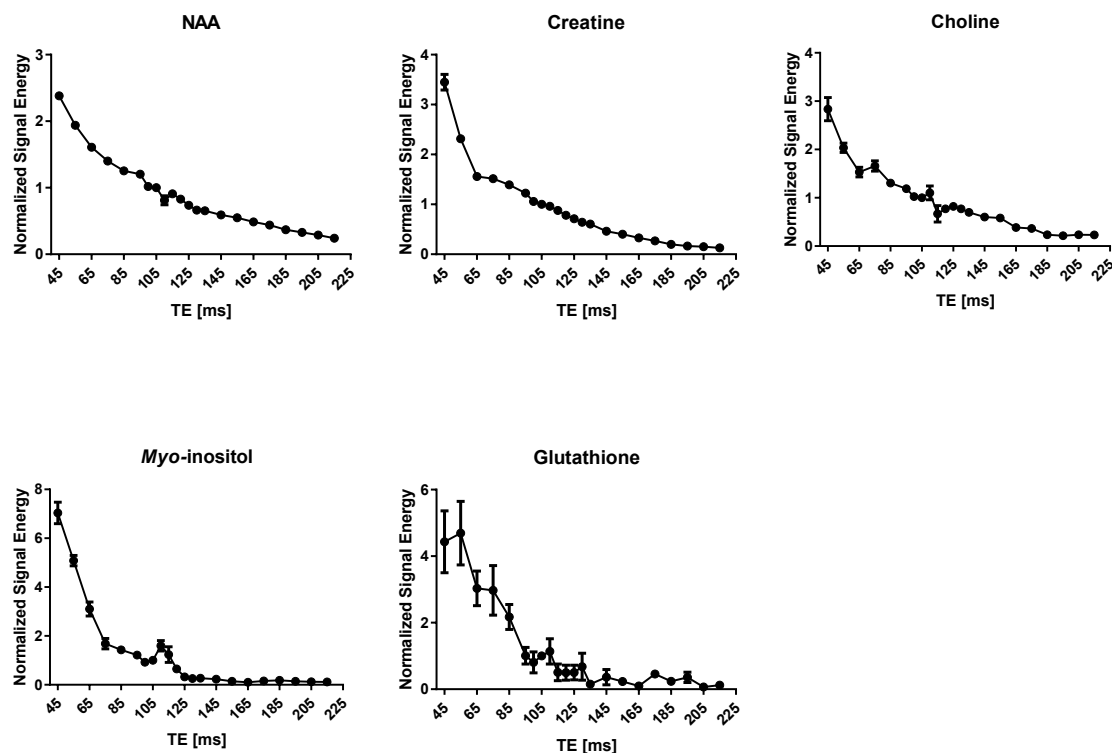


FIGURE 3.S1: The calculated signal energies of NAA, creatine, choline, *myo*-inositol, and glutathione from average in vivo data are plotted from TE = 45 ms to TE = 215 ms.

3.9 Co-Authorship Statement

The material in Chapter 3 is published in NMR in Biomedicine in a manuscript entitled *Optimized in vivo brain glutamate measurement using long-echo-time semi-LASER at 7T* (Received: September 20, 2017, Revised: July 3, 2018, Accepted: July 6, 2018). Material from this chapter was also presented at the International Society for Magnetic Resonance in Medicine Conference (2017; Abstract #5510). Dickson Wong was the main contributor for the material presented in this chapter – performing most of the study design, software development,

data acquisition, data analysis, and manuscript preparation. Co-authors on this chapter were Dickson Wong, Amy L. Schranz, and Robert Bartha. Amy L. Schranz assisted in data acquisition, study design, and the development of the mixed-metabolite phantom. Robert Bartha was involved in the design of the study, interpretation of the data, and provided guidance for data analysis and manuscript preparation.

Estimated percentage of the work for Chapter 3 conducted solely by Dickson Wong: 90%

4

Chronic Vitamin D deficiency in adult APP/PS1 mice: Effect on memory performance and brain metabolite levels

A version of this chapter is in preparation for publication: Dickson Wong, Miranda Bellyou, Alex Li, Marco Prado, Olivier Beauchet, Cédric Annweiler, Manuel Montero-Odasso, Robert Bartha, "Chronic Vitamin D deficiency in adult APP/PS1 mice: Effect on memory performance and brain metabolite levels," In preparation. Jun 2019.

Abstract: Amyloid-beta ($A\beta$) plaques and neurofibrillary tangles are the pathological hallmarks of Alzheimer's disease (AD), but their contribution to neurodegeneration in AD remains unclear. Calcium dysregulation and oxidative stress are additional biological mechanisms thought to be involved in the AD process. Vitamin D (VitD) is a secosteroid hormone that can act in the brain to protect against the effects of calcium dysregulation and oxidative stress, suggesting that VitD deficiency may potentially exacerbate AD progression. However, literature on VitD deficiency in AD remains inconsistent. The purpose of this study was to thoroughly evaluate the role of chronic VitD deficiency in an adult transgenic mouse model of AD. 6 month old APP_{Swe}/PS1 Δ E9 mice were fed either a VitD deficient diet (< 1 IU/kg VitD₃) or a nutritionally sufficient control diet (1000 IU/kg VitD₃). Longitudinal serum 25(OH)D levels were measured using radioimmunoassay. Magnetic resonance spectroscopy, magnetic resonance imaging, and the Barnes and Morris water mazes were used to assess longitudinal neurochemical, anatomical, and spatial memory changes, respectively. Measurements were made at 6 months, 9 months, 12 months, and 15 months of age. VitD deficiency did not change ventricle volume, an MRI marker of neuronal loss, but did result in changes in metabolite concentrations consistent with astrogliosis and gliosis. Overall VitD deficient mice also performed better or improved on measures of spatial memory than mice on the control diet. Since the APP_{Swe}/PS1 Δ E9 mouse is a mild model of $A\beta$ toxicity, the results of this study suggest that VitD deficiency may improve memory by upregulating beneficial astrogliosis in the prodromal stages of AD.

4.1 Introduction

Alzheimer's disease (AD) is a neurodegenerative disorder of the brain, presenting as progressive impairment over several cognitive domains [1]. Although it is well established that amyloid beta ($A\beta$) plaques and neurofibrillary tangles (NFTs) are the pathological hallmarks of AD, their contribution to neurodegeneration in AD is less clear. Additional biological mechanisms thought to be involved in the disease process include calcium dysregulation and oxidative stress [2].

Calcium dysregulation involves the activation of *L*-type voltage gated calcium channels (LVGCC) [3]. These channels have increased activity and expression due to $A\beta$ [4, 5, 6, 7], leading to increased intracellular calcium. The extra calcium may be taken up by mitochondria, producing increased reactive oxygen species (ROS) [8, 9]. Interestingly, the secosteroid hormone Vitamin D (VitD) can help protect neurons against ROS-induced damage. Specifically, VitD can enhance the expression of antioxidants and detoxifying enzymes [10] and can lower LVGCC expression and reduce *L*-type currents in neurons [11, 12]. Other protective effects of VitD include the regulation of neurotrophic factors and the reduction of inflammation [13]. Additionally, both VitD receptors and the 1α -hydroxylase enzyme that converts VitD into its biologically active form are known to be expressed in the human brain and are localized to brain regions affected by AD such as the hippocampus and the cingulate gyrus [14]. Together, this suggests a role for VitD in AD, with VitD deficiency potentially exacerbating AD progression.

In line with this view, epidemiological studies have shown that VitD deficiency is prevalent in AD [15] and is associated with a substantially increased risk for AD [16]. In addition, low VitD has been associated with impaired cognition, a greater rate of cognitive decline [17, 18], and increased incidence of AD [19]. In contrast, two studies have shown no association of VitD levels with episodic memory function in older adults [20, 21]. Research using rodent models of aging and AD is also inconsistent, with some studies showing

worsened spatial memory after VitD deficiency but no effect of supplementation [22, 23]. and other studies showing the opposite effect. These studies showed no effect of VitD deficiency on spatial memory [24, 25], but better spatial memory after VitD supplementation [24, 26].

In light of this contradictory evidence, the aim of the present study was to thoroughly evaluate the role of chronic VitD deficiency in AD by establishing VitD deficiency in an adult transgenic AD mouse model and to comprehensively examine the resulting longitudinal neurochemical, anatomical, and memory changes in the brain. Neurochemical changes were assessed using proton magnetic resonance spectroscopy (^1H -MRS), while anatomical changes were assessed using high resolution magnetic resonance imaging (MRI) – both techniques that are well established in the study of AD in humans. Memory was carefully assessed by using two independent spatial tasks and measuring potential confounding variables. Spatial tasks were chosen as they mimic aspects of episodic memory [27], the type of memory that is one of the earliest and most severely affected in human AD [28]. Based on previous evidence in humans and rodent models, we hypothesized that VitD deficiency would decrease *N*-acetyl aspartate (NAA) concentrations (a ^1H -MRS marker of neuronal health), increase ventricle volume (an MRI marker of volume loss), and worsen spatial memory performance.

4.2 Methods

4.2.1 Subjects

60 male transgenic (Tg) mice carrying the Swedish mutation of the human amyloid precursor protein (APP_{Swe}) and the exon-9 deleted mutation of the human presenilin-1 protein ($\text{PS1}\Delta\text{E9}$) on a (C57BL/6 x C3H)F2 genetic background were obtained from Jackson Laboratories (JAX MMRC Stock #034829; Bar Harbour, ME, USA) at 10 weeks of age. A cohort of 5 mice arrived every two weeks until 60 mice were obtained. Upon arrival, mice

were housed individually in standard tub cages under fluorescent lighting on a 12/12 h day/night schedule (lights on at 7 am) with *ad libitum* access to food and water. Other than a covered shelter, mice were provided no environmental enrichment. Mice were euthanized at 15 months of age. All animal experiments were performed by the same individual between the hours of 9 am and 6 pm. Ethics approval for this study was obtained from the University of Western Ontario Animal Use Subcommittee.

4.2.2 Diets and Vitamin D Status

All mice were fed a standard AIN-76A rodent diet from Research Diets Inc. (D10001; New Brunswick, NJ, USA) from 10 weeks of age to 6 months of age. This control diet contained 1000 IU Vitamin D₃ (VitD₃) per kg. The 56 mice that survived to 6 months of age were randomized to one of four groups. The control group (n=14) continued to receive the control diet for the remainder of the study. The number of mice receiving the control diet was 14 at 9 months of age, and 13 at 12 and 15 months of age. The other three groups (n=42) received a VitD deficient (VitD-) diet from Research Diets Inc. (D08090903; New Brunswick, NJ, USA) with < 1 IU VitD₃ per kg from 6 months to 9 months of age. The VitD- diet is identical to the standard AIN-76A diet, except no VitD was included in the diet's vitamin mix. One group (n=14) continued to receive the VitD- diet for the remainder of the study. The other two groups received further interventions that are not presented herein. The number of mice receiving the VitD deficient diet was 41 at 9 months of age, 13 at 12 months of age, and 10 at 15 months of age. A summary of the study design is shown in Figure 4.1a.

To verify that the diets were affecting VitD levels in the mice as intended, a tail nick procedure was performed on each mouse under anaesthesia and blood was drawn from the tail. This was performed at all time points. To ensure that the anaesthesia did not affect behavioural measurements, blood samples were acquired after all behavioural studies were complete. After collection, blood samples were sent to Heartland Assays (Ames, IA, USA) for radioimmunoassay to determine the serum 25(OH)D levels.

4.2. Methods

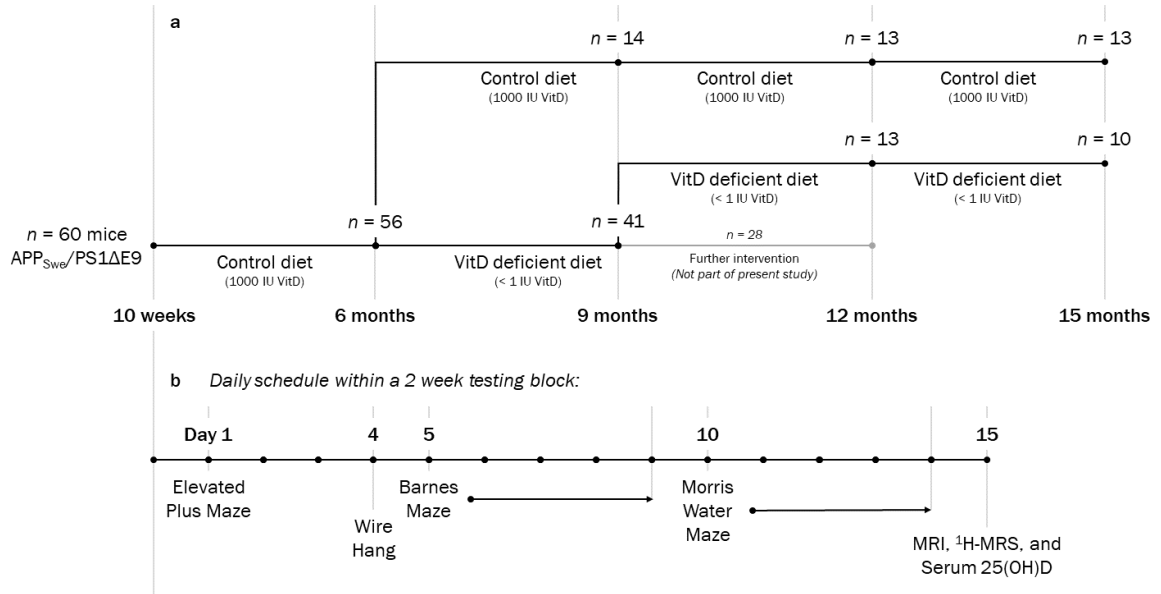


FIGURE 4.1: A summary of the study design is shown in (a). 10 week old $APP_{Swe}/PS1\Delta E9$ mice received the AIN-76A control diet containing 1000 IU Vitamin D (VitD) from 10 weeks to 6 months of age. 14 mice continued to receive this diet for the remainder of the study. Starting at 6 months of age, the remainder of the mice received a VitD deficient diet, which was identical to the control diet except that it contained < 1 IU VitD. 41 of these mice survived to 9 months of age. Of these 41 mice, 13 continued to receive the VitD deficient diet, while the other 28 received further intervention not presented herein. At each time point, all mice were assessed over a 2 week period according the schedule summarized in (b). Mice were tested on the elevated plus maze on Day 1, the wire hang experiment on Day 4, the Barnes maze on Days 5-9, and the Morris water maze on Days 10-14. Blood was collected for measurement of serum 25(OH)D levels after the behavioural testing was completed, so anaesthesia would not affect the behavioural measurements. For the same reason, the scanning session to collect MRI and 1H -MRS data was also scheduled after all behavioural measurements were completed.

4.2.3 Behavioural Studies

Behavioural studies were performed on all mice at 6, 9, 12, and 15 months of age. At each time point, mice completed the behaviour studies before any diet changes occurred. Mice were evaluated over a two week period, beginning with the elevated plus maze (EPM) on the first day. On the fourth day, mice underwent the wire hang test. On days 5 to 9, mice were evaluated on the Barnes maze (BM). Finally, on days 10 to 14, mice were evaluated on the Morris water maze (MWM). While the Barnes maze was performed at every time point, the MWM was performed only at 12 months and 15 months of age. A summary of the behavioural assessment schedule is shown in Figure 4.1b.

4.2.3.1 Morris Water Maze

The Morris water maze (MWM) is a task frequently used to assess spatial memory and learning. The MWM consisted of a submerged target platform made of clear plastic placed in the centre of one quadrant of a round pool with a 2 metre diameter. The pool contained clear water heated to a temperature of 25 degrees Celsius to prevent hypothermia [29]. The water was filled to a level such that mice could still see distal visual cues in the room, but could not jump out of the maze once they were on the platform. Visual cues were on three of the four walls of the MWM testing room. The room was lit with two incandescent light bulbs located at two adjacent corners of the room. An overhead webcam mounted on the ceiling recorded all mouse activity.

Mice were evaluated over a five day period. For the first four days, mice were trained to find the target platform with four trials per day. Each trial began with the mouse entering the maze from either the North, South, East, or West locations. For each mouse, the set of starting locations were constructed in a semi-random fashion such that all four locations were used and one trial each day was from each of the four locations [30]. Trials began as soon as the mouse entered the water and ended once the mouse found the target platform

or the maximum trial time of 90 seconds was reached. If the mouse did not find the target platform, it was gently guided to the platform by the experimenter. Regardless of how the mouse arrived at the target platform, it remained there for 20 seconds once it found the platform. At the end of the 20 seconds, the mouse was returned to its home cage. The four trials were conducted in a spaced fashion, with the all mice completing the first trial before the first mouse began its second trial. Mice waiting for their turn in the maze were placed in cages with no access to food or water located behind an opaque curtain, where they had no view of the maze or the room cues. After the four training days, a probe trial was conducted on the fifth day to assess reference memory. For the probe trial, the submerged target platform was removed, and mice were allowed to explore the maze freely until the maximum trial time of 60 seconds was reached. In this case, the starting position for each mouse was random. Videos of the training and probe trials were analyzed using Any-MAZE software (Stoetling Co., Wood Dale, IL, USA) and in-house software written in Python (Python Software Foundation, <https://www.python.org/>) using the OpenCV 3.4.3 libraries (OpenCV Team, <https://opencv.org/>). Metrics obtained from Any-MAZE software included the time to find the platform (primary latency), distance travelled to find the target (primary path length), average proximity to the target, and time spent in the quadrant containing the target platform (target quadrant time). The in-house software was used to generate spatial maps of mouse activity (Figure 4.2a) for the probe trials, which were used to compare probe trial activity in the MWM between groups and between time points.

Since mice were tested in the MWM at both 12 months of age and 15 months of age, the location of the target platform was changed for each time point to minimize longitudinal learning effects. At 12 months of age, mice were randomized without consideration of diet group membership to be trained to find the target platform in either Quadrant 1 or Quadrant 2. At 15 months of age, mice that were trained to find the target platform in Quadrant 1 at 12 months of age were then trained to find the target platform in Quadrant 3. Similarly,

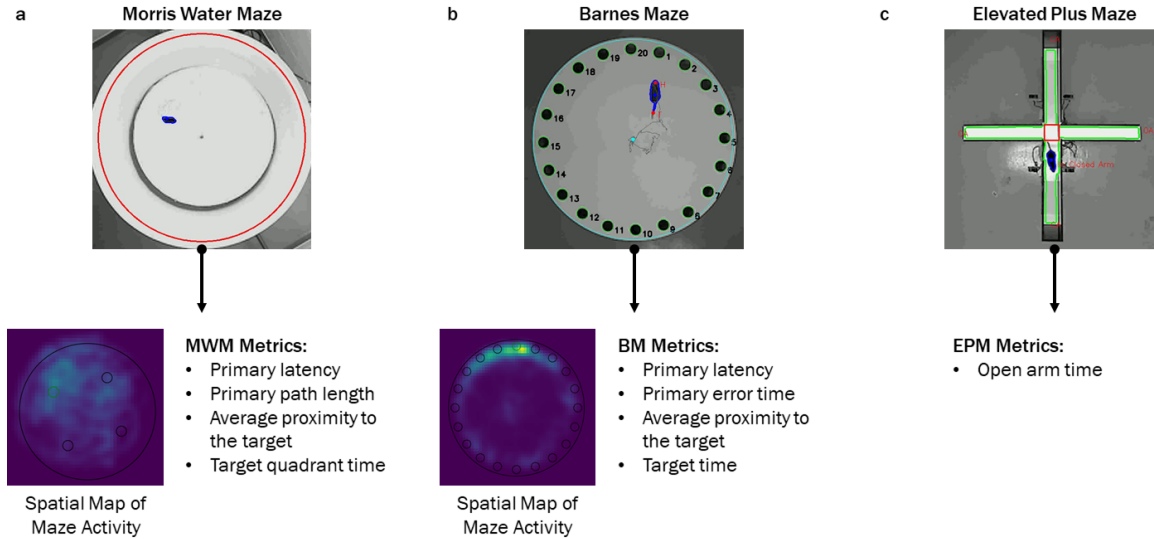


FIGURE 4.2: In house software written using Python and OpenCV 3.4.3 was used to automatically track mouse activity from recorded videos of experimental sessions. An example of the mouse tracking in the Morris water maze (MWM) is shown in (a), with the mouse outlined in blue and the edge of the tank shown in red. From the video tracking, spatial maps of maze activity may be generated, where a brighter green colour indicates more time spent by mice at that location. Several relevant MWM metrics may be obtained. An example of mouse tracking in the Barnes maze (BM) is shown in (b). The mouse is outlined in the blue, its head and tail are identified in red, and the BM apparatus is outlined in green. Like with the MWM, spatial maps of mouse activity and relevant BM metrics may be obtained. An example of mouse tracking in the elevated plus maze (EPM) is shown in the (c). The mouse is outlined in blue, and the edges of the EPM are shown in green. The regions of the EPM are labelled in red, with the “OA” labels corresponding to the open arms, the “CA” labels corresponding to the closed arms, and the red square corresponding to the centre region. The mouse was considered to be completely within a region of the maze if the centroid of the mouse segmentation was in the region.

mice that were trained to find the target platform in Quadrant 2 at 12 months of age were then trained to find the target platform in Quadrant 4 at 15 months of age.

4.2.3.2 Barnes Maze

Although studies investigating the effect of Vitamin D on spatial memory and learning have mostly employed the MWM [22, 23, 24, 25], the Barnes maze (BM) task was used in the present study as an alternative method for assessment of spatial memory and learning. The BM offers an advantage over the MWM, since differences in speed, anxiety, and locomotor ability are automatically controlled for [31]. The BM consisted of a white, circular platform (92 cm in diameter), elevated 105 cm above the floor (San Diego Instruments, San Diego, CA, USA). The platform had 20 equally spaced holes that were 5 cm in diameter, with 7.5 cm between holes. A false box or a target box made of black-coloured plastic could be placed underneath any of the holes. The BM testing room was lit with fluorescent lighting located on the ceiling, and a single visual cue was placed on three of the four walls. The distal visual cues were a circle, square, and triangle printed in black ink on a white sheet of paper [32]. Also on the ceiling was an overhead webcam that recorded all mouse activity.

Mice were evaluated over a five-day testing period. For the first four days, mice were trained to find the target box. Each training day consisted of four trials. Trials began with the mouse being placed inside a start tube (20 cm in diameter). When the start tube was removed, the mouse could roam freely and the video recording was started. A beeping alarm from a digital timer was used during the trial as a mild aversive stimulus. Trials were stopped when the mouse found the target box and climbed completely inside or if the maximum trial time of 180 seconds was reached. If the mouse did not find the target during the trial, the experimenter gently guided the mouse to the hole containing the target box with his hand. The base of the tail was then gently pulled in the direction away from the target hole, which encouraged the mouse to move towards the target hole and

climb into the target box. Once the mouse was in the target box, whether by its own volition or with help from the experimenter, it remained in the box for 1 minute before it was returned to its home cage. Trials were conducted in a spaced fashion, wherein the first trial of all mice being tested were completed before the second trial of the first mouse began. Between trials, the maze, the target box, and the false boxes were cleaned with a 10% alcohol solution to remove odours and the maze was rotated 90 degrees to prevent mice from using intra-maze cues. After four training days were completed, a 90 second probe trial was conducted on the fifth day to assess reference memory. The probe trial was conducted in the same way as the training trials, except that the target box was replaced with a false box and trials were not stopped early for any reason. Videos of the training and probe trials were analyzed using in-house software written in Python, which used OpenCV 3.4.3 libraries to automatically segment the Barnes maze apparatus, identify the hole locations, and track the mouse head, tail, and centre of mass (Figure 4.2b). Each hole zone was defined as the hole plus 1 cm around the hole, and a mouse was considered to have entered a hole zone if the head was in the zone. Metrics including the latency time to find the target hole (primary latency), the time spent at false holes before finding the target (primary error time), average proximity to the target hole, and the time spent at the target hole (target time) were measured by the software. The software also generated spatial maps of mouse activity (Figure 4.2b) for the probe trials, which were used to compare probe trial activity in the BM between groups and between time points.

Since mice were tested in the Barnes maze at 6 months, 9 months, 12 months, and 15 months of age, the location of the target box was changed for each time point to minimize longitudinal learning effects. Specifically, at 6 months of age, mice were randomized to be trained at either target hole 1, 6, 11, or 16 without consideration for diet group membership. Mice that were trained to find target hole 1 at 6 months of age were then trained to find target hole 6 at 9 months of age, target hole 11 at 12 months of age, and then target hole 16 at 15 months of age. Similarly, mice that were trained to find target hole 6 at 6 months

of age were then trained to find target hole 11 at 9 months of age, and so on. This target assignment scheme was also used for mice randomized to target hole 11 and 16 at 6 months of age.

4.2.3.3 Confounding Variables of Spatial Learning and Memory

Some variables that could confound a mouse's performance in the BM and MWM were measured. Weight was measured, since it could be a confounding variable for the MWM as a mouse's buoyancy depends on its weight. A mouse's physical ability and motivation to complete a maze (i.e. anxiety-like behaviour) was also assessed, since these could confound a mouse's performance in the BM and MWM. Physical ability was assessed by measuring neuromuscular function and grip strength with the wire hang test, while anxiety-like behaviour was assessed using the elevated plus maze (EPM).

4.2.3.3.1 Wire Hang

Neuromuscular function and grip strength were measured using a wire hang test. A standard wire cage top was used as the experiment apparatus. The edges of the wire cage were taped off, preventing the mice from reaching the edges and climbing onto the other side when inverted. To perform the experiment, a mouse was gently placed on the wire cage top. The wire cage top was then gently shaken to induce the mice to grip onto the apparatus. Next, the cage top was inverted and suspended 40 cm above a large tub cage filled with bedding. The total time that the mouse was able to hang inverted was measured. Each mouse performed 5 trials of the wire hang experiment. The longest and shortest wire hang times were removed and the remaining 3 times were averaged.

4.2.3.3.2 Elevated Plus Maze

Anxiety-like behaviour was assessed using the EPM (Med Associates Inc., Fairfax, VT, USA). The maze consisted of four arms that were 34.9 cm long and 6.07 cm wide. Two

of the arms were closed with walls that were 19.13 cm tall, while the other two arms were open arms without walls. The centre of the maze was a square region with sides that were 6.1 cm in length. Experiments began with the animals being placed at the centre. The animals were then allowed to roam freely for 10 minutes. Activity was recorded with a webcam placed directly above the maze. The video recorded by the webcam was analyzed using in-house software written in Python. Using the OpenCV 3.4.3 libraries, the analysis software automatically segmented the open and closed arm regions of the maze, identified the mouse outline, and tracked the mouse location (Figure 4.2c). A mouse was considered to be completely within a region of the maze if the centroid of the mouse segmentation was in the region. The total amount of time spent in open arm regions (open arm time) is considered a valid index of anxiety [33] and was recorded.

4.2.4 Magnetic Resonance Imaging and Ventricle Volume

Ventricle volume, a valid metric of neuronal loss and AD progression in humans [34], was measured in the mice using MRI. MRI data were acquired from a subset of mice receiving either the control diet or VitD- diet. 8 mice receiving the control diet were scanned at 6 months of age, with follow-up scans of the same mice performed at 9 months, 12 months, and 15 months of age. For mice receiving the VitD- diet, 8 were scanned at 6 months, 24 were scanned at 9 months, 8 were scanned at 12 months, and 8 were scanned at 15 months. Where possible, the same mice were followed longitudinally.

Mice were scanned in a Varian 9.4 Tesla small-bore MRI scanner (Palo Alto, CA, USA) at the Centre for Functional and Metabolic Mapping, Robarts Research Institute using an Agilent Millipede MP30 radio-frequency (RF) coil (Santa Clara, CA, USA). High-resolution 3D anatomical images (Figure 4.3a) were acquired using the TrueFISP (fast imaging with steady state precession) sequence [35] with the following parameters: TR/TE=7/3.5 ms, flip angle=70°, FOV=19.2 × 19.2 × 14.4 mm³, matrix=128 × 128 × 96, resolution=150 × 150 × 150 μm³, coronal slice orientation, reception bandwidth=32051 Hz (250 Hz/pixel),

4.2. Methods

6 averages. TrueFISP images have excellent tissue/CSF contrast that facilitates ventricle segmentation.

To segment the ventricles, voxels in the image were classified as either tissue or CSF. This segmentation was performed using in-house software written in Python using the NiBabel v2.1.0 libraries [36] and VTK 8.0.1 libraries [37]. First, a pulse-coupled neural network (PCNN) [38] was used for brain extraction (Figure 4.3b). Then, an estimated distribution of image voxel intensities was obtained from the brain extracted image using Gaussian kernel density estimation. Voxels with intensities below the 93.5th percentile were considered tissue, while voxels with intensities above the 93.5th percentile were considered to be CSF (Figure 4.3c). With only the CSF voxels, a discrete marching cubes algorithm was used to generate closed isosurfaces of all CSF volumes. Surfaces that corresponded to the lateral and 3rd ventricles were manually selected (Figure 4.3d). The volume enclosed by these surfaces were calculated and recorded as the estimated ventricle volume.

4.2.5 Magnetic Resonance Spectroscopy

4.2.5.1 Acquisition

Proton magnetic resonance spectroscopy (^1H -MRS) data were acquired in all mice during the same MRI session used to acquire the images to assess ventricle volume. In vivo ^1H -MRS data were acquired using a localization by adiabatic selective refocusing (LASER) sequence [39] from a $2 \times 6 \times 3 \text{ mm}^3$ voxel encompassing both hippocampi (Figure 4.4a). The spectroscopy voxel was manually positioned using anatomical landmarks on 2D fast-spin echo (2D-FSE) anatomical images (TR/TE=4000/10 ms; FOV= $19.2 \times 19.2 \text{ mm}^2$, TE=10 ms, matrix= 128×128 , slice thickness=0.5 mm). Both water suppressed and water unsuppressed data were acquired with the following parameters: TR=3250 ms, TE=18.9 ms, bandwidth=6000 Hz, averages=128 for water unsuppressed data, and averages=8 for the water unsuppressed data. The adiabatic full passage pulse used (AFP) was a hyperbolic secant

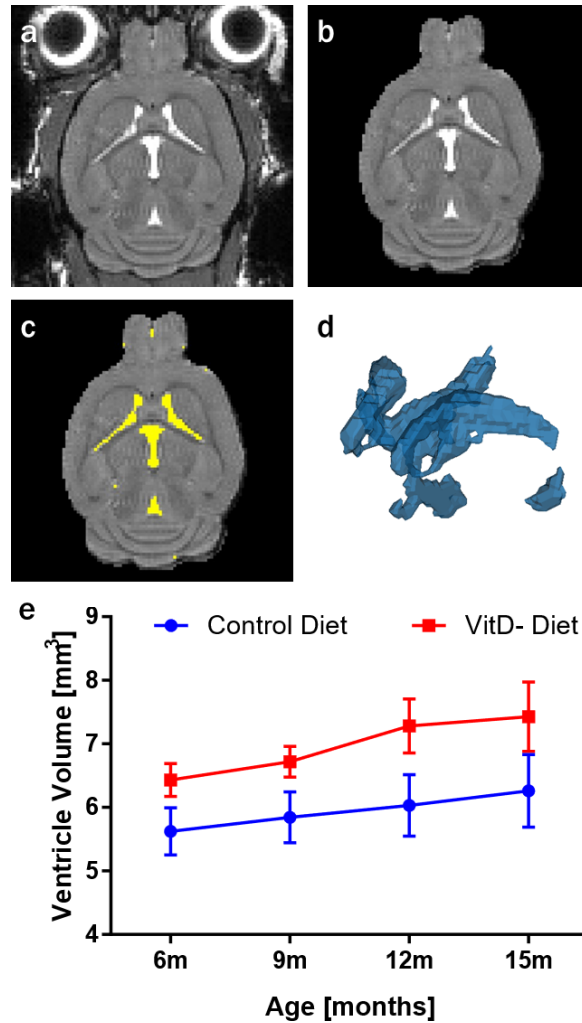


FIGURE 4.3: An example of a high-resolution ($150 \times 150 \times 150 \mu\text{m}^3$) TrueFISP image with excellent tissue/cerebrospinal fluid (CSF) contrast for ventricule segmentation is shown in (a). A pulse-coupled neural network was first used to segment the brain from the surrounding structures (b). Then, an estimated distribution of image voxel intensities was obtained from the brain extracted image using Gaussian kernel density estimation with voxels having intensities below the 93.5th percentile being considered tissue, and voxels having intensities above the 93.5th percentile being considered CSF. The identified CSF voxels are labelled with yellow and shown in (c). Next, a discrete marching cubes algorithm was used to generate closed isosurfaces of all CSF volumes. Finally, surfaces that corresponded to the lateral and 3rd ventricles were manually selected (d), and the total enclosed volume was recorded as the ventricule volume. Ventricule volume is plotted with respect to age in (e). Standard errors are shown. Ventricule volume showed no significant effect of age, diet, or age-by-diet interaction indicating that ventricule volume did not significantly change with age and did not differ significantly between mice on a control diet and mice on a vitamin D deficient (VitD-) diet.

4.2. Methods

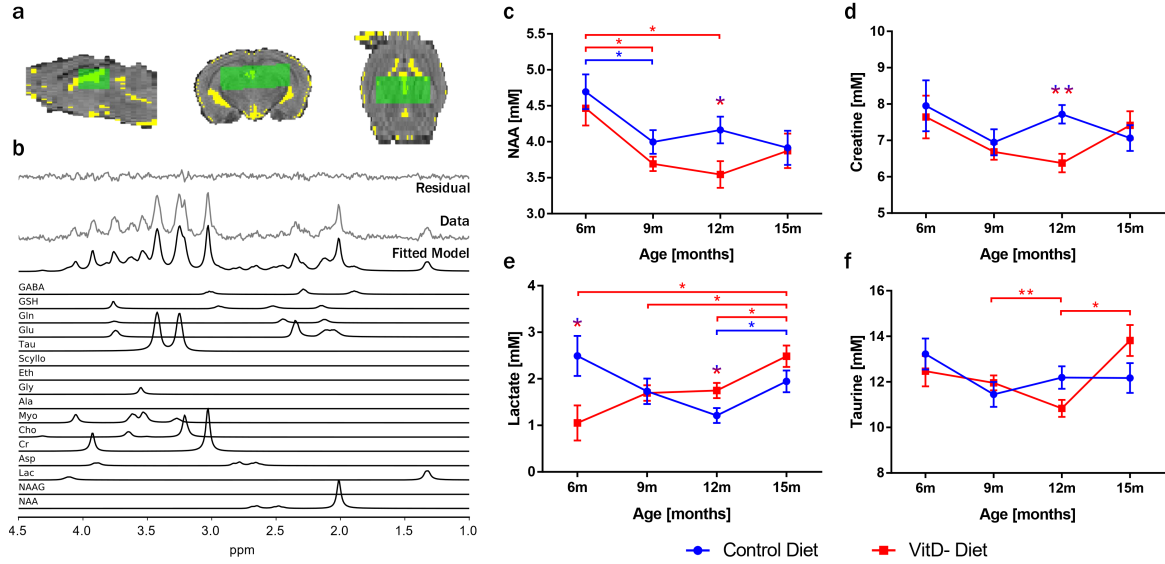


FIGURE 4.4: An example of a brain extracted 2D fast-spin echo (2D-FSE) anatomical image is shown in (a). The $2 \times 6 \times 3 \text{ mm}^3$ spectroscopy voxel encompassing both hippocampi is labelled in green. Voxels that are cerebrospinal fluid (CSF), identified using the same segmentation method as described for ventricle segmentation, are shown in yellow. This enabled the calculation of the fraction of the spectroscopy voxel that was tissue and the fraction that was CSF. An example of post-processed ^1H -MRS spectra acquired from the hippocampal region is shown in (b). The fitted prior knowledge template is also shown, along with the individual metabolite components. Longitudinal measurements of NAA, creatine (Cr), lactate (Lac), and taurine concentrations are plotted in (c), (d), and (e), respectively. Data were analyzed using linear mixed models (see text for details) and the estimated marginal means are shown with standard errors. Statistically significant Sidak-corrected post-hoc comparisons ($p < 0.05$: *, $p < 0.01$: **) are indicated with asterisks. Differences between time points are shown with red brackets for the control diet group and blue brackets for the vitamin D deficient diet group. Between group differences are indicated with asterisks only.

(HS2) pulse with a time-bandwidth product of 15. Water suppression was achieved using the VAPOR (variable pulse power and optimized relaxation delays) scheme that preceded the LASER sequence. A metabolite-suppressed macromolecule only spectrum was also acquired using a single inversion recovery technique interleaved with the LASER acquisition of the full (macromolecule + metabolite) spectrum. At each time point, the scanning session always occurred after all behavioural studies were complete to ensure that anaesthesia did not affect the behavioural measurements (Figure 4.1b).

4.2.5.2 Post-Processing

The ^1H -MRS data were first lineshape and eddy current corrected using combined QUALITY deconvolution and eddy current correction (QUECC) [40] with 400 QUALITY points [41]. Residual water in the water suppressed spectrum was removed by subtracting peaks between 4.2 ppm and 5.7 ppm identified by a Hankel singular value decomposition (HSVD) fitting routine that required no prior knowledge. HSVD fitting was also used to generate a noiseless model of acquired macromolecule spectra, which was subtracted from the water suppressed full spectrum to obtain a metabolite-only spectrum.

Metabolite-only spectra were then fitted with prior knowledge templates (Figure 4.4b) using a Levenberg-Marquardt minimization algorithm [42]. Water unsuppressed spectra were fitted with a prior knowledge template containing a single Lorentzian at 4.7 ppm to obtain the amplitude of the water signal. For the water suppressed spectra, an echo-time specific, simulated 9.4 T LASER prior knowledge template generated using density matrix simulations was used. Simulations were performed using Python code written in-house that utilized the PyGAMMA library of the VeSPA (Versatile Simulation, Pulses and Analysis) software suite [43]. Metabolites included in this prior knowledge template included *N*-acetyl aspartate (NAA), aspartate (Asp), lactate (Lac), alanine (Ala), glutamate (Glu), glutamine (Gln), glutathione (GSH), creatine (Cr), taurine, choline (Cho), glycerophosphorylcholine (GroPCho), phosphorylcholine (PCho), *scyllo*-inositol (Scyllo), *myo*-inositol (Myo), glucose (Glc), and glycine (Gly). To reduce the number of variables to be fitted, parameters describing the lineshapes of the metabolites were constrained within the prior knowledge template. Within metabolites, peak amplitudes, shifts, and phases were fixed relative to one another. Relative peak amplitudes were not fixed between metabolites, since these are expected to vary across mice. Relative peak positions and phases between some metabolites were fixed. The positions and phases of low-amplitude metabolites were linked to the

4.2. Methods

Reference Metabolite	Linked Metabolites		Comments
	Shift	Phase	
NAA	Asp	Asp, Glc, Gly, Lac, Ala, Scyllo, Myo	<ul style="list-style-type: none"> • Shifts for Cr were not fixed relative to any reference metabolite. • A separate linewidth parameter was defined for Glu, Gln, and GSH. A single linewidth parameter was defined for all other metabolites. • A single delay parameter was defined for all metabolites.
Lac	Ala		
Glu	Gln, GSH, GABA	Gln, GSH, GABA	
Tau	Cho, Scyllo, Myo, Glc, Gly	Cr, Cho	

TABLE 4.1: A summary of relationships between metabolite parameters in the prior knowledge template [44]. Peak positions (shifts) and phases of low-amplitude metabolites were linked to the shifts and phases of higher-amplitude metabolites. Within metabolites, peak amplitudes, shifts, and phases were fixed relative to one another. The following metabolites were included in the prior knowledge template used to fit ^1H -MRS data: NAA, Asp, Lac, Ala, Glu, Gln, GSH, Cr, Tau, Cho, GroPCho, PCho, Scyllo, Myo, Glc, and Gly.

positions and phases of high-amplitude metabolites such as NAA, Tau, and Glu. A summary of the parameter constraints are provided in Table 4.1.

4.2.5.3 Metabolite Quantification

Hippocampal metabolite concentrations were obtained as previously described [45] using the fitted and corrected amplitudes of the metabolite signal and the water signal. Corrections for the relaxation rates of metabolites in tissue and CSF incorporated T_1 and T_2 values obtained from literature (Table 4.2) as well as tissue and CSF fractions obtained from the 2D-FSE anatomical images. The same T_1 and T_2 values were used for both the white matter (WM) and grey matter (GM) tissue compartments, as these compartments could not be separated within the 2D-FSE anatomical images. However, the cerebrospinal fluid (CSF)

compartment could be separated from the overall tissue compartment using the same segmentation method as described above for the 3D TrueFISP volumes (Figure 4.4a). This enabled the calculation of the GM, WM and CSF partial volume within the spectroscopy voxel.

4.2.6 Statistical Analyses

4.2.6.1 Analysis of Longitudinal Data

Longitudinal changes in serum 25(OH)D level, behavioural metrics, ventricle volume measurements, and metabolite levels were analyzed using linear mixed models with the age of the mouse, the mouse's diet (control diet or VitD- diet), and the age-by-diet interaction as fixed effects. Repeated observations on the same mice were accounted for using an unstructured covariance matrix term, and maximum likelihood estimation was used to produce the statistical models. If any fixed effects were significant, post-hoc tests of simple main effects and comparisons of covariate-adjusted estimated marginal means were performed to identify statistically significant differences between time points and between groups. A Sidak correction [51] was applied to control for multiple comparisons.

For the BM and MWM metrics, the mouse's wire hang time, weight, mean speed during the trial, and open arm time in the EPM were used as covariates in the statistical models. Since successful completion of the BM task requires the mouse to make a choice between a false box and the target box, a wrong choice involves the same motor ability as the correct choice. Thus, differences in motor ability are inherently controlled for in the BM's design. As a result, reduced models with only the mouse's open arm time in the EPM as a covariate were used to analyze the BM data. All statistical analyses were performed using the mixed command in IBM SPSS Statistics version 25 (IBM, Armonk, NY, USA).

4.2. Methods

Metabolite	T ₁ [s]			T ₂ [ms]		
	Tissue	CSF	Reference	Tissue	CSF	Reference
NAA	1.6740		[46]	321		[47]
Ala	1.3701 ^a			161 ^a		
GABA	1.3701 ^a			161 ^a		
Asp	1.3701 ^a			161 ^a		
Cho, GroP- Cho, PCho	1.3484			445		
Cr	1.6792			104		
Glc	1.3701			161		
Glu	1.4975			70		
Gln	1.4975 ^b			56		
GSH	1.3701 ^a			161 ^a		
Gly	1.3701 ^a			161 ^a		
Myo	1.3701			161		
Scyllo	1.3701 ^a			161 ^a		
Lac	1.3701 ^a			161 ^a		
Taurine	2.3289			162		
Water	2.0567	4.2867	[46, 48]	44	111.3	[48, 47]

^a T₁ and T₂ values of metabolites which were not available in literature were assumed to be similar to that of Myo [49, 50].

^b The T₁ value of Gln was assumed to be similar to Glu because the Glx (Glu + Gln) was measured in [46].

TABLE 4.2: A summary of the metabolite-specific T₁ and T₂ values used for relaxation correction of the fitted metabolite signals. T₁ and T₂ values are obtained directly from the literature.

4.2.6.2 Analysis of Spatial Maps of Mouse Activity

A permutation testing method typically used to compare surface dose maps for radiotherapy [52] was used to compare spatial maps of probe trial activity in the BM and MWM between groups and between time points. Briefly, the method calculates a test statistic from the activity maps that summarizes the overall difference in maze activity between groups. Then the method randomly permutes the group labels to generate a null distribution, from which an adjusted p value threshold for statistical significance is calculated. Finally, regions where pixel-wise comparisons meet this threshold are considered significantly different. Permutation testing gives strong control over false positives, whereas directly comparing activity between groups at each pixel of the map does not. To reduce the amount of computation needed, activity maps were resampled to 10% of the original image resolution before applying the method.

4.3 Results

4.3.1 Vitamin D Status

The linear mixed model for serum 25(OH)D levels (Figure 4.5) showed a significant effect of age ($F(3, 36) = 95.366$, $p < 0.001$), diet ($F(1, 36) = 321.941$, $p < 0.001$), and age-by-diet interaction ($F(3, 36) = 85.994$, $p < 0.001$). Post-hoc univariate tests showed that VitD levels decreased with age in both the control (significant effect of age: $F(3, 35) = 6.065$, $p < 0.01$) and VitD- diet groups (significant effect of age: $F(3, 42) = 253.769$, $p < 0.001$). Mice on the control diet had higher serum 25(OH)D levels than mice on the VitD- diet at 9 months (significant effect of diet: $F(1, 55) = 240.726$, $p < 0.001$), 12 months (significant effect of diet: $F(1, 31) = 537.911$, $p < 0.001$), and 15 months of age (significant effect of diet: $F(1, 28) = 37.996$, $p < 0.001$).

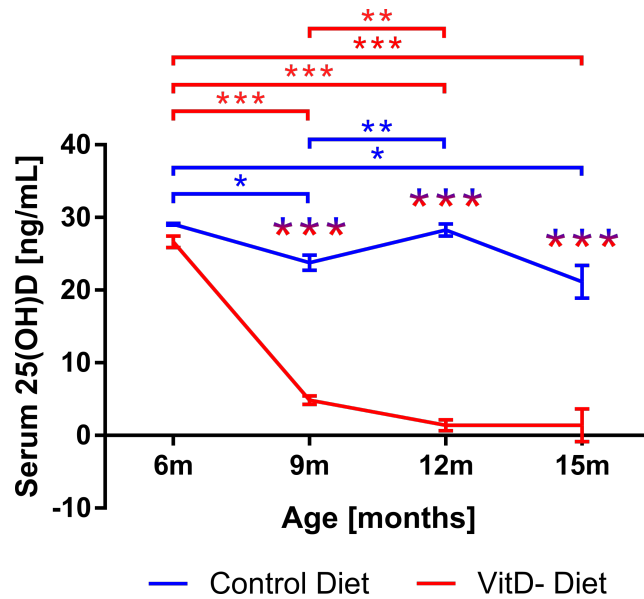


FIGURE 4.5: Serum 25(OH)D levels as measured by radioimmunoassay were analyzed using linear mixed models. The estimated marginal means with standard errors are shown. Statistically significant Sidak-corrected post-hoc comparisons ($p < 0.05$: *, $p < 0.01$: **, $p < 0.001$: ***) are indicated with the asterisks. Differences between time points are shown with red brackets for the control diet group and blue brackets for the vitamin D deficient (VitD-) diet group. Between group differences are indicated with asterisks only. VitD levels decreased with age in both the control diet and VitD- diet mice, with control diet mice having higher serum 25(OH)D levels than mice on the VitD- diet at 9 months, 12 months, and 15 months of age.

4.3.2 Morris Water Maze

4.3.2.1 Training Phase

At 12 months of age, analysis of primary latency (Figure 4.6a) showed a significant effect of training day ($F(3,27) = 10.616$, $p < 0.001$). Univariate post-hoc tests showed that there was a decrease in the time to find the platform with training day in mice receiving both the control diet ($F(3,27) = 8.590$, $p < 0.001$) and the VitD- diet ($F(3,27) = 3.152$, $p < 0.05$). Primary latency over the training days were not different between groups as there was no significant effect of diet ($F(1,30) = 0.204$, $p = 0.665$) or age-by-diet interaction ($F(1,26) = 0.741$, $p = 0.537$). Analysis of primary path length (Figure 4.6b) showed similar results, with a significant effect of training day ($F(3,27) = 10.184$, $p < 0.001$). Univariate post-hoc tests revealed a significant decrease in distance travelled to find the target with training day in both control diet mice ($F(3,27) = 7.866$, $p < 0.01$) and VitD- diet mice ($F(3,27) = 3.253$, $p < 0.05$), but no significant differences between groups (diet effect: $F(1,30) = 0.688$, $p = 0.413$; age-by-diet effect: $F(3,26) = 0.549$, $p = 0.653$). In line with these results, average proximity to target during training trials (Figure 4.6c) decreased with time as there was a significant effect of training day ($F(3,25) = 6.118$, $p < 0.01$). Post-hoc tests of average proximity to target revealed that mice on the VitD- diet were further away from the target on average during day 4 of training than mice on the control diet ($F(1,33) = 8.424$, $p < 0.01$). Together, these results suggests that mice on both diets were able to learn the MWM task at 12 months of age.

At 15 months of age, there was no significant effect of training day, diet, or day-by-diet interaction in the analyses of primary latency and primary path length. Analysis of the average proximity to target during training trials revealed a significant effect of training day (Figure 4.6c; $F(3,24) = 3.654$, $p < 0.05$), but post-hoc tests showed no differences between training days or between groups. This indicates that mice did not improve in maze performance with training. However, performance in MWM as measured by primary

latency, primary path length, and proximity to target was better on Day 1 of training at 15 months of age compared to Day 1 of training at 12 months of age, indicating that mice had retained the MWM task rules from testing at 12 months of age.

4.3.2.2 Probe Trial

Analyses of the MWM probe trial showed significant effects of age for the primary latency (Figure 4.6d; $F(1,36) = 13.383$, $p < 0.01$) and average proximity to the target platform location (Figure 4.6e; $F(1,36) = 11.294$, $p < 0.01$) metrics. A significant effect of age was also found when analyzing the time spent in the quadrant of the maze containing the location of the target platform (Figure 4.6f; $F(1,36) = 7.195$, $p < 0.05$). Post-hoc univariate analyses of these metrics showed a significant effect of age only for mice on the VitD- diet. For these mice, primary latency decreased with age ($F(1,34) = 12.646$, $p < 0.01$), average proximity to target decreased with age ($F(1,34) = 17.676$, $p < 0.001$), and target quadrant time increased with age ($F(1,34) = 10.335$, $p < 0.01$). Together, this indicates that the performance in the probe trial of VitD- diet mice, but not control diet mice, improved from 12 months of age to 15 months of age.

Significant age-by-diet interactions were found for the average proximity to target metric ($F(1,25) = 8.090$, $p < 0.01$) and target quadrant time metric ($F(1,25) = 4.278$, $p < 0.05$). Post-hoc analyses showed that 12 month old VitD- mice were, on average, further away from the location of the target than 12 month old control diet mice ($F(1,31) = 7.096$, $p < 0.05$) during the probe trial. This indicates that VitD- mice had worse recall of the platform location than control diet mice at 12 months of age. However, no regional differences between control diet mice and VitD- mice were detected on the spatial maps of MWM activity at 12 months of age. At 15 months of age, post-hoc analyses of primary latency showed that VitD- diet mice found the target location faster than mice on the control diet ($F(1,28) = 5.347$, $p < 0.05$). However, no regional differences were detected on

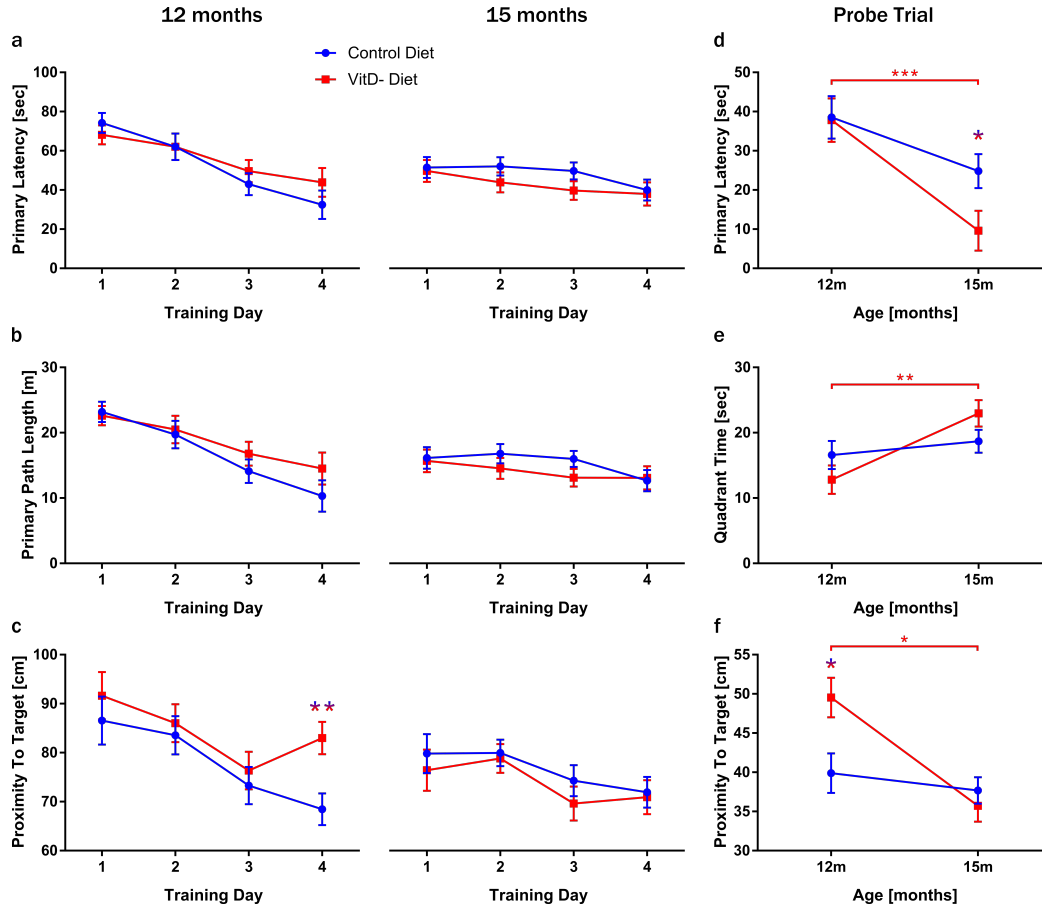


FIGURE 4.6: The performance of APP_{Swe}/PS1ΔE9 mice in the Morris water maze (MWM) is shown in blue for mice on the control diet and in red for mice on the Vitamin D deficient (VitD-) diet. Metrics obtained from both the training (a–c) and the probe (d–f) trials were analyzed using linear mixed models with wire hang time, weight, mean speed in the MWM, and open arm time in the elevated plus maze as covariates. The covariate-adjusted estimated marginal means with standard errors are shown. Statistically significant Sidak-corrected post-hoc comparisons ($p < 0.05$: *, $p < 0.01$: **, $p < 0.001$: ***) are indicated with the asterisks. Differences between time points are shown with red brackets for the control diet group and blue brackets for the VitD- diet group. Between group differences are indicated with asterisks only. For clarity, only between group differences are shown for the training data. Metrics measuring spatial learning included primary latency (a) and primary error time (b), which both decreased with training day at 12, but not 15 months of age. Average proximity to the target platform (c) decreased with training day at 12 and 15 months of age, but 12 month old VitD- diet mice were further away from the target than control diet mice on day 4 of training. Probe trial metrics measuring spatial memory included primary latency (d), time spent in the quadrant containing the target location (e), and average proximity to the target location (f), which all indicated improvement with age for VitD- diet mice, but not for control diet mice. Compared to control diet mice, VitD- diet mice performed worse on the proximity to target metric at 12 months of age (f), but better on the primary latency metric at 15 months of age (d).

spatial maps of MWM activity. There were also no regional differences detected on spatial maps of MWM activity between time points.

4.3.3 Barnes Maze

4.3.3.1 Training Phase

Linear mixed model analyses revealed a significant effect of training day for the latency time to find the target hole (primary latency; Figure 4.7a) and the time spent at false holes before finding the target (primary error time; Figure 4.7b) at 6 months (primary latency: $F(3,56) = 126.643$, $p < 0.001$; primary error time: $F(3,56) = 96.571$, $p < 0.001$), 9 months (primary latency: $F(3,55) = 36.431$, $p < 0.001$; primary error time: $F(3,55) = 32.043$, $p < 0.001$), 12 months (primary latency: $F(3,26) = 9.244$, $p < 0.001$; primary error time: $F(3,26) = 10.007$, $p < 0.001$), and 15 months (primary latency: $F(3,24) = 4.834$, $p < 0.01$; primary error time: $F(3,24) = 5.547$, $p < 0.01$). Similarly, analyses of average proximity to target (Figure 4.7c) also revealed a significant effect of training day at 6 months ($F(3,56) = 52.204$, $p < 0.001$), 9 months ($F(3,55) = 21.316$, $p < 0.001$), 12 months ($F(3,26) = 12.403$, $p < 0.001$), and 15 months ($F(3,24) = 3.865$, $p < 0.05$) of age. Together, this indicates that mice were able to learn the BM task at all ages.

Though no significant diet and day-by-diet effects were detected any time point, post-hoc univariate tests showed some group differences. At 12 months of age, VitD- diet mice had lower primary latency on day 2 of training than control diet mice (Figure 4.7a; $F(1,26) = 4.424$, $p < 0.05$), indicating that VitD- diet mice may have learned the task faster than control diet mice. At 15 months of age, VitD- diet mice had higher primary error time than control diet mice (Figure 4.7b; $F(1,24) = 4.643$, $p < 0.05$) on day 1 of training at 15 months of age, indicating that control diet mice may be remembering the BM task rules from previous testing at 12 months of age, while VitD- diet mice were not.

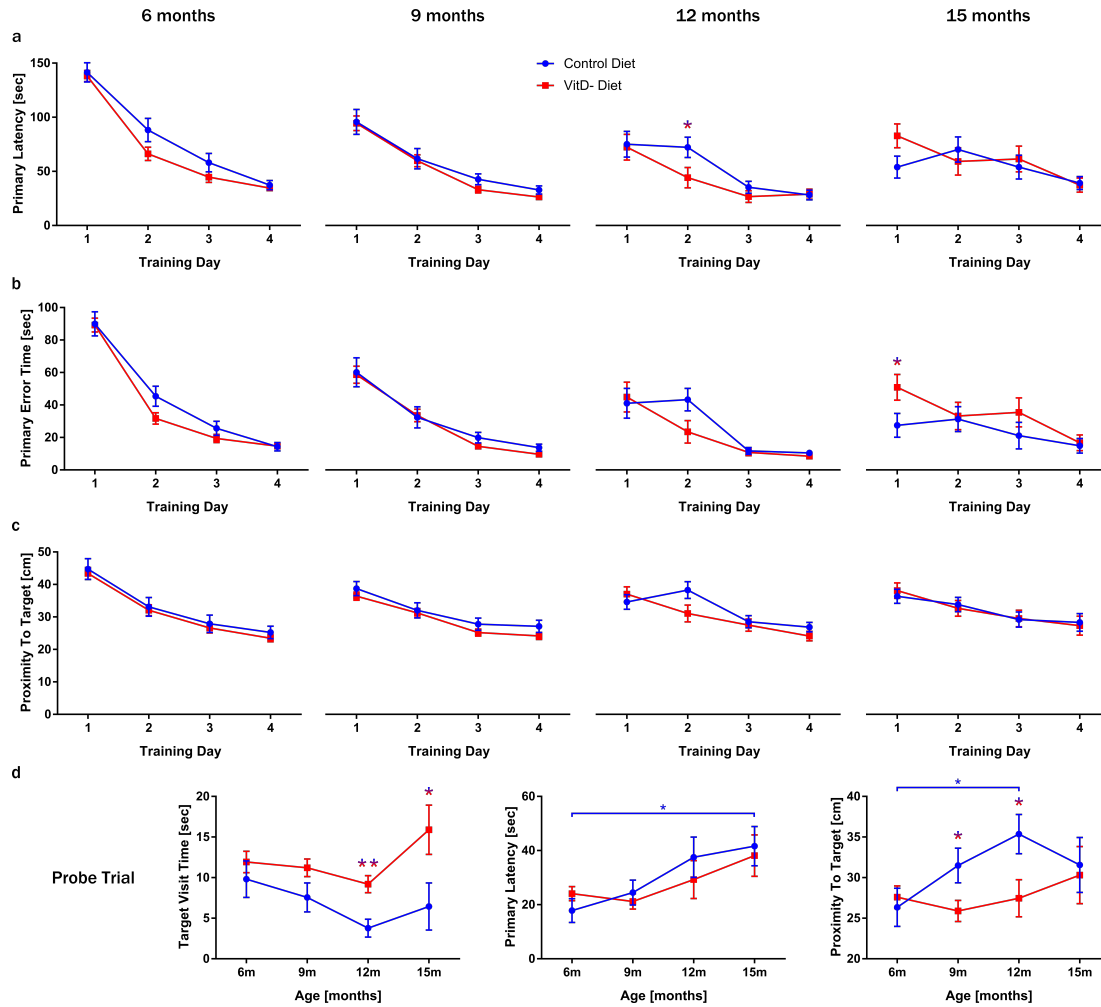


FIGURE 4.7: The performance of APP_{Swe}/PS1ΔE9 mice in the Barnes maze (BM) is shown in blue for mice on the control diet and in red for mice on the Vitamin D deficient (VitD-) diet. Metrics obtained from both the training (a–c) and the probe (d) trials were analyzed using linear mixed models with open arm time in the elevated plus maze as a covariate. The covariate-adjusted estimated marginal means with standard errors are shown. Statistically significant Sidak-corrected post-hoc comparisons ($p < 0.05$: *, $p < 0.01$: **, $p < 0.001$: ***) are indicated with the asterisks. Differences between time points are shown with red brackets for the control diet group and blue brackets for the VitD- diet group. Between group differences are indicated with asterisks only. For clarity, only between group differences are shown for the training data. Metrics measuring spatial learning included the latency to find the target hole (a), the time spent at false holes before finding the target (b), and the average proximity to the target (c), which all decreased with training day at every time point, indicating mice were able to learn the BM task. Metrics measuring spatial learning in the probe trial (d) included target visit time, primary latency, and average proximity to the target. These metrics worsened with age for the control mice, but not the VitD- diet mice. Compared to control diet mice, VitD- diet mice spent more time at the target hole at 12 and 15 months of age. They also remained closer to the target hole during the probe trial at 9 and 12 months of age.

4.3.3.2 Probe Trial

Analyses of the BM probe trial (Figure 4.7d) revealed a significant effect of age for the target visit time ($F(3,34) = 4.652, p < 0.01$), with post-hoc univariate analyses showing that as mice on the control diet grew older, target visit time decreased ($F(3,27) = 3.633, p < 0.05$). In line with these results, a significant effect of age for primary latency was also observed ($F(3,36) = 3.666, p < 0.05$), with post-hoc univariate analyses showing that primary latency for control mice increased with age. No worsening of BM performance with age was seen in VitD- diet mice. This is corroborated further by the regional differences in BM activity of control diet mice between time points (Figure 4.8). Permutation testing revealed that mice on the control diet spent less time at the target hole when they were 12 or 15 months of age than at 6 months of age. The BM activity for VitD- mice differed when comparing activity at 9 months vs. 15 months of age, but this difference occurred at a false hole. No other regional differences in BM activity across time points were observed in the VitD- diet mice.

There was also a significant effect of diet for the target visit time metric ($F(3,34) = 10.454, p < 0.01$), with post-hoc analyses showing that control diet mice spent less time at the target than VitD- diet mice at 12 months of age ($F(1,26) = 12.869, p < 0.01$) and 15 months of age ($F(1,25) = 5.069, p < 0.05$). For the average proximity to target metric, there was a significant age-by-diet effect ($F(3,30) = 3.350, p < 0.05$), with post-hoc tests showing that control diet mice were further away from the target hole on average than control diet mice at both 9 months of age ($F(1,55) = 5.124, p < 0.05$) and 12 months of age ($F(1,27) = 5.685, p < 0.05$). Together, this indicates that control diet mice may have worse recall of the target hole location than VitD- mice at 9, 12, and 15 months of age. However, no regional differences of BM activity between groups were detected on spatial activity maps at any time point.

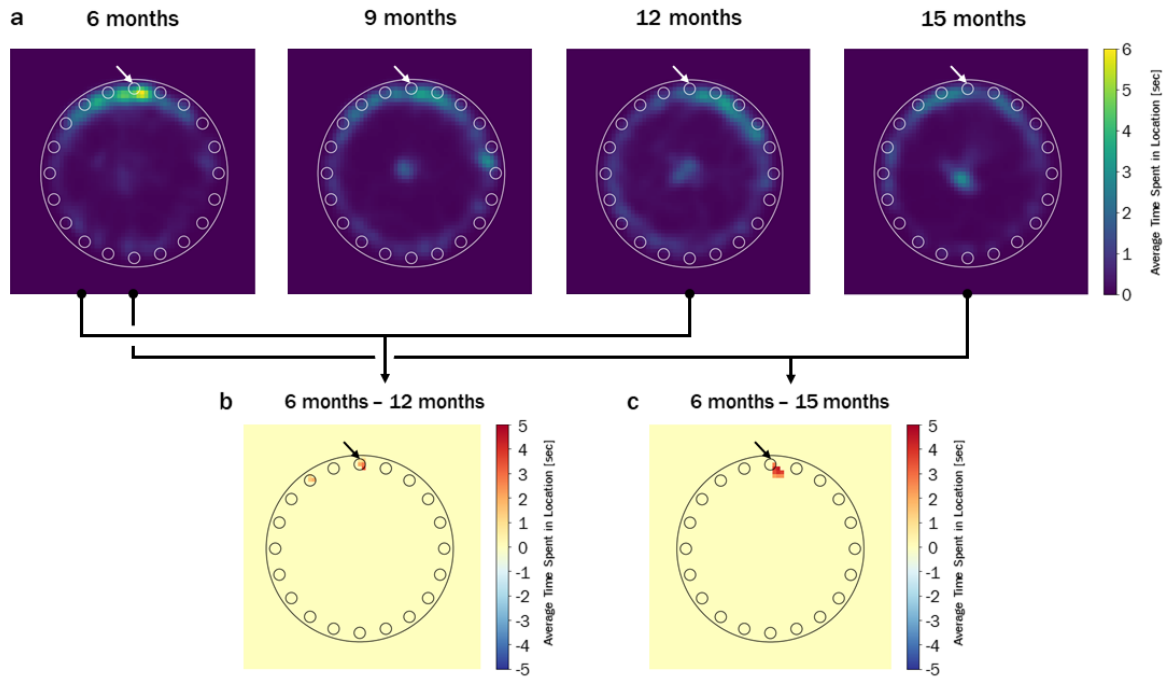


FIGURE 4.8: Average maps of probe trial activity in the Barnes maze (BM) are shown for APP_{Swe}/PS1ΔE9 mice on the control diet at 6 months, 9 months, 12 months, and 15 months of age (a). A brighter green colour on the map indicates more time spent by mice in that location, while the arrow indicates the location of the target hole. Maps were compared between time points using a permutation testing method that has strong control over false positives (see text for details). The results of these comparisons are shown in (b) and (c). Only areas that differ in activity at a significance level of $p < 0.05$ are shown. Permutation testing revealed that 6 month old control diet mice spent an average of 5 seconds more at the target hole than 12 month old (b) and 15 month old (c) control diet mice.

4.3.4 Confounding Variables of Spatial Learning and Memory

4.3.4.1 Weight and Wire Hang Time

Analysis of weight change over time revealed a significant effect of age ($F(3,35) = 14.725$, $p < 0.001$), diet ($F(1,46) = 7.236$, $p < 0.05$), and age-by-diet interaction ($F(3,35) = 3.185$, $p < 0.05$). Post-hoc univariate analyses revealed an increase in weight with age for both the control diet mice ($F(3,32) = 6.701$, $p < 0.01$) and the VitD- diet mice ($F(3,44) = 12.822$, $p < 0.001$). Post-hoc analyses also showed that VitD- mice were heavier than control mice at 6 months ($F(1,56) = 5.079$, $p < 0.05$), 9 months ($F(1,53) = 6.055$, $p < 0.05$), and 12 months of age ($F(1,40) = 14.007$, $p < 0.01$).

Analysis of wire hang time revealed a significant effect of age ($F(3,37) = 15.931$, $p < 0.001$). There was also a significant effect of weight on the wire hang time ($F(1,103) = 18.803$, $p < 0.001$). Post-hoc analyses (adjusted for weight) revealed a decrease in wire hang time with age for both the control diet mice ($F(3,28) = 7.289$, $p < 0.01$) and VitD- diet mice ($F(3,46) = 11.872$, $p < 0.001$). No diet and age-by-diet main effects were detected, and no between group differences were detected in post-hoc analyses at any time point.

Between-group and across-time differences in weight and wire hang time justified their inclusion as covariates when analyzing MWM data.

4.3.4.2 Open Arm Time in the EPM

Analysis of the total amount of time spent in open arm regions revealed a significant effect of age ($F(3,27) = 13.561$, $p < 0.001$), but no significant effects of diet or age-by-diet interaction. Post-hoc analyses showed that the time spent in open arm regions decreased with age for both control diet mice ($F(3,24) = 3.476$, $p < 0.05$) and VitD- diet mice ($F(3,36) = 12.822$, $p < 0.001$), indicating that anxiety levels increased with age for all mice. There were no differences between groups at any time point. Changes of anxiety levels over time justified the inclusion of open arm time as covariates in the analysis of MWM and BM data.

4.3.5 Ventricle Volume

Analyses of ventricle volume (Figure 4.3e) showed no significant effect of age, diet, or age-by-diet interaction. This indicates that mice on a control diet had the same ventricle volume as mice on the VitD- diet and that ventricle volume remained stable across time.

4.3.6 Magnetic Resonance Spectroscopy

Analysis of NAA concentration in the hippocampus as measured by ^1H -MRS (Figure 4.4c) revealed a significant effect of age ($F(3,22) = 9.164, p < 0.001$) and diet ($F(1,31) = 5.693, p < 0.05$). Post-hoc univariate analyses revealed that NAA concentration decreased with age for both control diet mice ($F(3,10) = 6.868, p < 0.01$) and the VitD- diet mice ($F(3,18) = 3.777, p < 0.05$). Post-hoc analyses also showed that 12 month old control diet mice had higher NAA concentrations than 12 month old VitD- diet mice ($F(1,14) = 5.537, p < 0.05$). At 12 months of age, higher NAA concentrations were associated with lower average proximity to the target platform location in the MWM probe trial (Figure 4.9a; two-tailed Pearson correlation: $r = -0.6127, p < 0.05$).

A significant effect of age ($F(3,23) = 4.274, p < 0.05$) and age-by-diet interaction ($F(3,23) = 3.134, p < 0.05$) was observed for the Cr concentration (Figure 4.4d). Post-hoc analyses revealed that 12 month old control diet mice had higher Cr concentrations than 12 month old VitD- diet mice ($F(1,14) = 13.684, p < 0.01$). Like for NAA, higher Cr concentrations were associated with lower average proximity to the target platform location in the MWM probe trial (Figure 4.9b; two-tailed Pearson correlation: $r = -0.6148, p < 0.05$).

In the analysis of Lac concentration (Figure 4.4e), there was a significant effect of age ($F(3,20) = 7.528, p < 0.01$) and age-by-diet interaction ($F(3,20) = 3.918, p < 0.05$). Post-hoc analyses showed that Lac concentration decreased with age for control diet mice ($F(3,13) = 4.123, p < 0.01$), while it increased with age for the VitD- diet mice ($F(3,20) = 5.867, p < 0.001$). Post-hoc analyses also revealed that mice in the VitD- diet

group had lower Lac concentrations at baseline (6 months of age) than mice in the control diet group ($F(1, 16) = 6.305$, $p < 0.05$). By 12 months of age, VitD- diet mice had higher Lac concentrations than control diet mice ($F(1, 14) = 5.443$, $p < 0.05$). The increase in Lac concentration over time was correlated with BM probe trial performance over time for the VitD- diet mice. Specifically, a greater increase in Lac concentration from 12 months to 15 months of age was associated with a smaller increase in primary latency (Figure 4.9c; two-tailed Pearson correlation: $r = -0.9043$, $p < 0.05$). In other words, a greater increase in lactate was associated with less worsening in BM probe trial performance.

For taurine concentration (Figure 4.4f), a significant age-by-diet interaction was observed ($F(3, 12) = 6.616$, $p < 0.01$). Post-hoc univariate analyses showed a significant age effect for VitD- diet mice only ($F(3, 16) = 5.619$, $p < 0.01$), indicating that taurine concentration changed with age for these mice. Indeed, 12 month old VitD- diet mice had lower taurine levels than 9 month old ($p < 0.05$) and 15 month old VitD- mice ($p < 0.05$).

4.4 Discussion

The goal of this study was to thoroughly evaluate the role of chronic VitD deficiency in AD using adult APP_{Swe}/PS1ΔE9 mice. Since mice on the VitD- diet had significantly lower serum 25(OH)D levels than mice on the control diet at 9 months, 12 months, and 15 months of age (Figure 4.5), chronic VitD deficiency was successfully established in this transgenic model. This resulted in neurochemical changes detected using ¹H-MRS, such as decreased hippocampal NAA and Cr concentrations as well as increased Lac and taurine concentrations. Chronic VitD deficiency also appeared to result in better spatial memory performance as measured on the BM and MWM. These results are discussed in more detail below.

In the present study, chronic VitD deficiency did not appear to result in differences of ventricle size (Figure 4.3) as measured by MRI, a valid metric of neuronal loss and AD progression in humans [34]. This result is not surprising, as APP_{Swe}/PS1ΔE9 mice typically

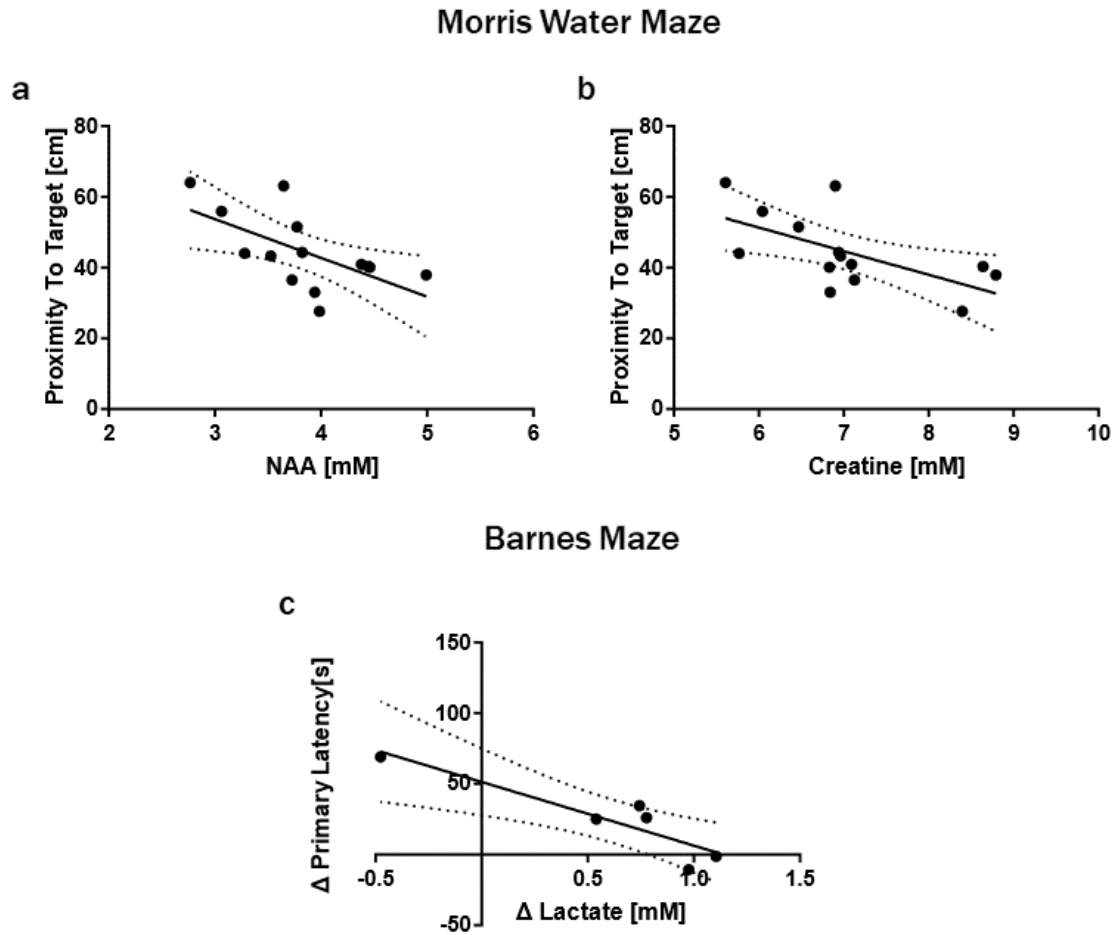


FIGURE 4.9: The correlation between NAA concentration in the hippocampus of 12 month old APP_{Swe}/PS1ΔE9 mice as measured by ¹H-MRS and average proximity to the target platform location in the MWM probe trial is shown in (a). Increased NAA concentrations were associated with lower average proximity (two-tailed Pearson correlation: $r = -0.6127$, $p < 0.05$). Creatine concentration in the hippocampus of 12 month old mice were also associated with lower average proximity in the MWM probe trial (two-tailed Pearson correlation: $r = -0.6148$, $p < 0.05$), as shown in (b). The 12 to 15 month change in primary latency in the BM probe trial of APP_{Swe}/PS1ΔE9 mice on the Vitamin D deficient (VitD-) diet is plotted against the 12 to 15 month change in hippocampal lactate (Lac) concentration as measured by ¹H-MRS in (c). A greater increase in Lac concentration from 12 to 15 months of age was associated with a smaller increase in primary latency (two-tailed Pearson correlation: $r = -0.9043$, $p < 0.05$).

only exhibit modest neuronal loss [53] with no statistically significant total brain volume or shape change from 6 months to 13 months of age [54].

On the other hand, neurochemical changes in the brain were detected using ^1H -MRS (Figure 4.4). Decreases in hippocampal NAA and Cr (Figure 4.4c, d) with age were observed in APP_{Swe}/PS1 Δ E9 mice on both the control and VitD- diets and. At 12 months of age, lower NAA and Cr concentrations were associated with lower spatial memory recall in the mice as measured by the MWM probe trial (Figure 4.9a, b). This result is consistent with measurements of NAA and Cr concentrations in humans, both of which decrease with AD progression and are associated with a decline in global cognitive function [55, 56]. VitD deficiency appears to accelerate this decline, since VitD- diet mice had lower hippocampal NAA and Cr concentrations than control diet mice at 12 months of age. But, by 15 months of age, hippocampal NAA and Cr levels of control diet mice had declined to that of VitD- mice. Since NAA synthesis in the brain requires acetyl-coenzyme A levels that exceed neuronal metabolic requirements [57] and Cr is essential for brain energy homeostasis [58], decreasing NAA and Cr concentrations could reflect an increasing brain energy deficit, a view supported by reduced brain glucose uptake in AD as measured by FDG-PET [59, 60]. This reduction in glucose uptake could be offset by lactate, an important source of energy in the brain [61, 62, 63]. Interestingly, the present study shows that VitD deficiency increases the level of lactate in the brain (Figure 4.4e). APP_{Swe}/PS1 Δ E9 mice on a VitD- diet showed increasing hippocampal lactate concentrations with age, while mice on a control diet showed decreasing lactate concentrations. At 12 months of age, VitD- diet mice had increased levels of lactate compared to control diet mice. In addition to being an energy source, lactate is also a signalling molecule in the brain that activates neuro-protective mechanisms, promotes increased blood flow and fuel delivery, and is important for long term memory formation [64]. The attenuated decline in spatial memory as measured by BM probe trial performance (Figure 4.9c) in VitD- diet mice in the present study supports the notion that increasing lactate concentrations over time may help preserve

memory function.

Increased lactate in the brain is likely a result of increased astrocyte metabolism, since astrocyte metabolism is primarily via aerobic glycolysis, producing lactate to sustain neuronal activity [65]. Thus, it is possible that VitD deficiency is increasing astrocyte activation in the mice, resulting in increased lactate levels. Though we are not aware of any studies that have directly shown the effect of VitD deficiency on astrocytes, VitD administration has been shown to suppress astrocyte activation *in vivo* [66]. Suppression of astrocyte activation is likely detrimental, as studies using transgenic mouse models that allow for conditional ablation of reactive astrocytes have shown that astrocyte activation is essential for restricting inflammation, limiting neuronal injury, and preserving neuronal function in central nervous system injury and disease [67, 68].

In the context of AD, it has been shown that nerve cells resistant to A β toxicity have increased markers of aerobic glycolysis [69], and overexpression of these markers confer resistance to A β [70]. Further, reactive astrogliosis in conjunction with improved memory function has been observed in response to taurine administration in APP/PS1 mice [71]. In the present study, taurine levels remained stable for APP_{Swe}/PS1 Δ E9 mice on the control diet, but increased from 12 months of age to 15 months of age in mice on the VitD-diet. In addition, decreased NAA, decreased Cr, and increased lactate (as observed in APP_{Swe}/PS1 Δ E9 mice on the VitD-diet) have been demonstrated to be associated with high macrophage and glial density [72, 73]. Microglial activity has a protective role in AD, including phagocytosing A β and clearing A β aggregates from the brain [74]. Together, the neurochemical changes observed suggest that VitD deficiency could be conferring some neuroprotection in AD.

The behavioural results of the present study supports this interpretation. Though APP_{Swe}/PS1 Δ E9 mice on both the control diet and VitD-diet exhibited spatial learning with few differences (Figure 4.6a-c and Figure 4.7a-c), stark differences in spatial memory function were observed in the BM and MWM probe trials. In the MWM probe trials, VitD

deficient APP_{Swe}/PS1 Δ E9 mice were further away from the target platform location than mice on the control diet at 12 months of age (Figure 4.6f), but performance improved from 12 months to 15 months of age (Figure 4.6d-f), with VitD- diet mice finding the target location faster than control diet mice at 15 months of age (Figure 4.6d). In contrast, mice on the control diet did not display improvement in MWM probe trial performance. In the BM probe trials, VitD deficient APP_{Swe}/PS1 Δ E9 mice spent more time at the target hole at 12 and 15 months of age and were closer to the target hole during the probe trial at 9 and 12 months of age compared to control diet mice (Figure 4.7d). Analysis of overall BM activity showed that control diet mice spent less time at the target hole when they were 12 or 15 months of age than at 6 months of age (Figure 4.8), suggesting worsening BM probe trial performance. In contrast, no differences between time-points in BM activity at the target hole were observed in the VitD- diet mice. Improvement in probe trial performance with age and better performance in the MWM at 15 months of age coupled with better probe trial performance by APP_{Swe}/PS1 Δ E9 mice on a VitD- diet at 9 months, 12 months, and 15 months in the BM suggests that chronic VitD deficiency helped to preserve spatial memory function.

To our knowledge, this is the first study evaluating VitD deficiency over the course of 9 months in an APP/PS1 mouse model of AD. One other study compared a low VitD diet (500 IU/kg VitD₃ in the feed) to a control diet (1000 IU/kg VitD₃ in the feed) and a high VitD diet (1000 IU/kg VitD₃ in the feed + 1000 IU intramuscular injection every 2 weeks) in quercetin-supplemented APP/PS1 mice from 3 months of age to 8 months of age [75]. Interestingly, they also found that mice on the low VitD diet had the best spatial memory performance as measured by the MWM maze, though it is unclear whether their observed effect was due to a VitD deficiency alone, or due to an interaction between quercetin and VitD status. Another study used a rat model of AD, where AD was induced via intracerebroventricular injection of A β 1-42 [22]. In that study, AD rats given a diet devoid of VitD for 2 months performed worse in the MWM maze than rats given a normal diet with sufficient

VitD. This is consistent with our observation that APP_{Swe}/PS1ΔE9 mice on a VitD- diet perform worse in the MWM than mice on a control diet after 6 months of VitD deficiency. However, after 9 months of VitD deficiency, we found that APP_{Swe}/PS1ΔE9 mice on a VitD- diet actually performed better in the MWM. Thus, VitD deficiency may be detrimental in the short term, but beneficial in the long term. More literature is available regarding VitD supplementation than VitD deprivation in mouse models of AD, with most studies finding that VitD supplementation confers a benefit [26, 76, 77, 78]. VitD supplementation was not performed in the current study and the results presented herein do not refute or corroborate the benefits of VitD supplementation in AD. It is entirely plausible that both chronic VitD supplementation and chronic VitD deprivation confer benefit in AD.

Though the current study did not look at *ex vivo* histology, indirect measurement of *in vivo* biological processes were assessed using ¹H-MRS. To our knowledge, this was the first study to demonstrate longitudinal changes of *in vivo* brain metabolite levels due to VitD deficiency in a mouse model of AD. Many studies have looked at longitudinal changes in APP/PS1 mice on a standard, nutritionally sufficient diet, with the most consistent changes reported being decreases in NAA and Glu levels relative to creatine [79, 80, 81, 82] as well as increases in Myo relative to creatine [80, 81]. However, in our mice, no effect of age was observed for the Glu or Myo concentration. Instead, an effect of age was observed for the Cr concentration, suggesting that some of the previously reported changes could have been driven by a change in Cr concentration rather than true changes in NAA, Glu or Myo.

The lack of *ex vivo* histology is a limitation of the current study. A reactive astrogliosis process was inferred from measurements made using ¹H-MRS, but this should be verified using histology. However, since a longitudinal design was used, *ex vivo* histology would have required sacrificing a proportion of the mice at each time point, significantly increasing the cost and reducing the statistical power of the study. Another point of caution with regards to ¹H-MRS measurements in the current study was the use of literature values of metabolite T_1 and T_2 in tissue (Table 4.2) to calculate metabolite concentrations. There is a

4.5. Conclusion

possibility that these T_1 and T_2 values may not be appropriate, as they were measured in wild-type mice and rats [46, 48, 47] and could be different in APP_{Swe}/PS1 Δ E9 mice.

The lack of measurements made in wild-type mice was another limitation of the current study. Comparing measurements made in VitD deficient APP_{Swe}/PS1 Δ E9 mice to VitD deficient wild-type mice would have allowed us to determine whether the effect of VitD deficiency is specific to AD or not. However, because the specific question being addressed in this study is how VitD deficiency affects the AD process, APP_{Swe}/PS1 Δ E9 mice on a control diet served as a sufficient control group.

The fact that an APP_{Swe}/PS1 Δ E9 mouse model of AD was studied is very important to consider when interpreting the results of this study. This is because the APP_{Swe}/PS1 Δ E9 mouse is considered a mild model of A β toxicity. This model displays only modest neuronal loss [53], and only abundant A β accumulation by 9 months of age [83], without development of tau pathology [84]. Thus, AD pathology in APP/PS1 mice is probably consistent with prodromal or mild AD and the results of this study may not apply in moderate or severe AD. In other words, VitD deficiency may only be beneficial early on in the AD process, but may either have no effect or be detrimental in later stages of AD. Additional studies are needed in more aggressive models of AD to clarify the role of VitD deficiency in moderate to severe AD.

4.5 Conclusion

This longitudinal study thoroughly evaluated the role of chronic VitD deficiency in AD. VitD deficiency was successfully established in adult transgenic APP_{Swe}/PS1 Δ E9 after 3 months on a VitD deficient diet and was maintained for 12 months. Relative to APP_{Swe}/PS1 Δ E9 mice on a nutritionally sufficient control diet, VitD deficiency did not change ventricle volume, an MRI marker of neuronal loss. However, VitD deficiency did

result in decreased NAA and Cr concentration as compared to control diet mice and increased Lac and taurine concentration with age, which is consistent with astrogliosis and gliosis. Increased Lac in VitD deficient mice was associated with attenuated decline in spatial memory performance as measured on the BM probe trial. Overall, VitD deficient mice performed better or improved on measures of spatial memory than control diet mice. Together, our observations in VitD deficient APP_{Swe}/PS1 Δ E9 mice suggest that VitD deficiency may improve memory by upregulating beneficial reactive astrogliosis in the prodromal stages of AD. Further studies are needed to determine the impact of VitD deficiency and supplementation in patients with mild AD.

4.6 Acknowledgements

This study was supported by the Schulich School of Medicine at the University of Western Ontario, University of Angers, Brain Canada, the Canada First Research Excellence Fund, and the Canadian Institutes of Health Research MD/PhD Studentship. Thanks to Matthew Cowan for assistance with the mouse behaviour experiments.

4.7 References

- [1] P. Scheltens et al. "Alzheimer's disease". In: *The Lancet* 388.10043 (July 2016), pp. 505–517.
- [2] H. W. Querfurth and F. M. LaFerla. "Alzheimer's Disease". In: *New England Journal of Medicine* 362.4 (Jan. 2010), pp. 329–344.
- [3] I. Bezprozvanny and M. P. Mattson. "Neuronal calcium mishandling and the pathogenesis of Alzheimer's disease". In: *Trends in Neurosciences* 31.9 (Sept. 2008), pp. 454–463.

4.7. References

- [4] S. Kim and H. Rhim. "Effects of amyloid- β peptides on voltage-gated L-type CaV1.2 and CaV1.3 Ca²⁺ channels". In: *Molecules and Cells* 32.3 (Sept. 2011), pp. 289–294.
- [5] N. Daschil et al. "CaV1.2 calcium channel expression in reactive astrocytes is associated with the formation of amyloid- β plaques in an Alzheimer's disease mouse model." In: *Journal of Alzheimer's Disease* 37.2 (Jan. 2013), pp. 439–51.
- [6] A. MacManus. "Enhancement of ⁴⁵Ca²⁺ Influx and Voltage-dependent Ca²⁺ Channel Activity by β -Amyloid-(1–40) in Rat Cortical Synaptosomes and Cultured Cortical Neurons. Modulation By The Proinflammatory Cytokine Interleukin-1 β ." In: *Journal of Biological Chemistry* 275.7 (Feb. 2000), pp. 4713–4718.
- [7] K. Ueda et al. "Amyloid beta protein potentiates Ca²⁺ influx through L-type voltage-sensitive Ca²⁺ channels: a possible involvement of free radicals". In: *Journal of neurochemistry* 68.1 (Jan. 1997), pp. 265–71.
- [8] E. Alberdi et al. "Amyloid β oligomers induce Ca²⁺ dysregulation and neuronal death through activation of ionotropic glutamate receptors". In: *Cell Calcium* 47.3 (Mar. 2010), pp. 264–272.
- [9] C. Supnet and I. Bezprozvanny. "The dysregulation of intracellular calcium in Alzheimer disease". In: *Cell Calcium* 47.2 (Feb. 2010), pp. 183–189.
- [10] M. J. Berridge. "Vitamin D cell signalling in health and disease". In: *Biochemical and Biophysical Research Communications* 460.1 (2015), pp. 53–71.
- [11] L. D. Brewer et al. "Vitamin D Hormone Confers Neuroprotection in Parallel with Downregulation of L-Type Calcium Channel Expression in Hippocampal Neurons". In: *The Journal of Neuroscience* 21.1 (Jan. 2001), pp. 98–108.
- [12] L. D. Brewer et al. "Chronic 1 α ,25-(OH)₂ vitamin D₃ treatment reduces Ca²⁺-mediated hippocampal biomarkers of aging." In: *Cell calcium* 40.3 (Sept. 2006), pp. 277–86.

- [13] A. V. Kalueff, K. O. Eremin, and P. Tuohimaa. "Mechanisms of Neuroprotective Action of Vitamin D3". In: *Biochemistry (Moscow)* 69.7 (July 2004), pp. 738–741.
- [14] D. W. Eyles et al. "Distribution of the vitamin D receptor and 1 alpha-hydroxylase in human brain". In: *Journal of chemical neuroanatomy* 29.1 (Jan. 2005), pp. 21–30.
- [15] M. L. Evatt et al. "Prevalence of vitamin D insufficiency in patients with Parkinson disease and Alzheimer disease". In: *Archives of Neurology* 65.10 (Oct. 2008), pp. 1348–52.
- [16] T. J. Littlejohns et al. "Vitamin D and the risk of dementia and Alzheimer disease". In: *Neurology* 83.10 (Sept. 2014), pp. 920–8.
- [17] D. J. Llewellyn, K. M. Langa, and I. A. Lang. "Serum 25-hydroxyvitamin D concentration and cognitive impairment". In: *Journal of geriatric psychiatry and neurology* 22.3 (Sept. 2009), pp. 188–95.
- [18] D. J. Llewellyn et al. "Vitamin D and risk of cognitive decline in elderly persons". In: *Archives of Internal Medicine* 170.13 (July 2010), pp. 1135–1141.
- [19] C. Annweiler et al. "Higher vitamin D dietary intake is associated with lower risk of Alzheimer's disease: A 7-year follow-up". In: *Journals of Gerontology - Series A: Biological Sciences and Medical Sciences* 67.11 (Nov. 2012), pp. 1205–1211.
- [20] J. S. Buell et al. "Vitamin D is associated with cognitive function in elders receiving home health services". In: *Journals of Gerontology - Series A Biological Sciences and Medical Sciences* 64.8 (Aug. 2009), pp. 888–895.
- [21] D. M. Lee et al. "Association between 25-hydroxyvitamin D levels and cognitive performance in middle-aged and older European men". In: *Journal of Neurology, Neurosurgery and Psychiatry* 80.7 (July 2009), pp. 722–729.

4.7. References

- [22] M. Taghizadeh et al. "Vitamin-D-free regimen intensifies the spatial learning deficit in Alzheimer's disease". In: *International Journal of Neuroscience* 121.1 (Jan. 2011), pp. 16–24.
- [23] M. Taghizadeh, S. A. Talaei, and M. Salami. "Vitamin D deficiency impairs spatial learning in adult rats". In: *Iranian Biomedical Journal* 17.1 (2013), pp. 42–48.
- [24] C. S. Latimer et al. "Vitamin D prevents cognitive decline and enhances hippocampal synaptic function in aging rats". In: *Proceedings of the National Academy of Sciences* 111.41 (2014), E4359–E4366.
- [25] E. M. Brouwer-Brolsma et al. "No role for vitamin D or a moderate fat diet in aging induced cognitive decline and emotional reactivity in C57BL/6 mice". In: *Behavioural Brain Research* 267 (July 2014), pp. 133–143.
- [26] L. Bennett et al. "Vitamin D2-enriched button mushroom (*Agaricus bisporus*) improves memory in both wild type and APP^{swe}/PS1^{dE9} transgenic mice." In: *PloS one* 8.10 (Jan. 2013), e76362.
- [27] J. C. Cassel and A. P. de Vasconcelos. "Importance of the ventral midline thalamus in driving hippocampal functions". In: *Progress in Brain Research*. Vol. 219. Elsevier, Jan. 2015, pp. 145–161.
- [28] L. Bäckman et al. "Cognitive impairment in preclinical Alzheimer's disease: A meta-analysis." In: *Neuropsychology* 19.4 (2005), pp. 520–531.
- [29] H. Iivonen et al. "Hypothermia in mice tested in Morris water maze". In: *Behavioural Brain Research* 141.2 (May 2003), pp. 207–213.
- [30] C. V. Vorhees and M. T. Williams. "Morris water maze: Procedures for assessing spatial and related forms of learning and memory". In: *Nature Protocols* 1.2 (Aug. 2006), pp. 848–858.

- [31] R. S. Reiserer et al. "Impaired spatial learning in the APPSwe + PSEN1DeltaE9 bi-genic mouse model of Alzheimer's disease". In: *Genes, brain, and behavior* 6.1 (Feb. 2007), pp. 54–65.
- [32] K. Gawel et al. "Assessment of spatial learning and memory in the Barnes maze task in rodents—methodological consideration". In: *Naunyn-Schmiedeberg's Archives of Pharmacology* 392.1 (Jan. 2019), pp. 1–18.
- [33] M. Komada, K. Takao, and T. Miyakawa. "Elevated Plus Maze for Mice". In: *Journal of Visualized Experiments* 22 (Dec. 2009), e1088.
- [34] S. M. Nestor et al. "Ventricular enlargement as a possible measure of Alzheimer's disease progression validated using the Alzheimer's disease neuroimaging initiative database". In: *Brain* 131.9 (Sept. 2008), pp. 2443–2454.
- [35] S. Miraux et al. "3D TrueFISP imaging of mouse brain at 4.7T and 9.4T". In: *Journal of Magnetic Resonance Imaging* 28.2 (Aug. 2008), pp. 497–503.
- [36] M. Brett et al. *nibabel: 2.1.0*. Aug. 2016.
- [37] W. Schroeder, K. Martin, and B. Lorensen. *The Visualization Toolkit*. 4th ed. Kitware, 2016.
- [38] N. Chou et al. "Robust Automatic Rodent Brain Extraction Using 3-D Pulse-Coupled Neural Networks (PCNN)". In: *IEEE Transactions on Image Processing* 20.9 (Sept. 2011), pp. 2554–2564.
- [39] M. Garwood and L. DelaBarre. "The return of the frequency sweep: designing adiabatic pulses for contemporary NMR." In: *Journal of magnetic resonance (San Diego, Calif. : 1997)* 153.2 (Dec. 2001), pp. 155–77.
- [40] R. Bartha et al. "Comparison of the Quantification Precision of Human Short Echo Time 1H Spectroscopy at 1.5 and 4.0 Tesla". In: *Magnetic Resonance in Medicine* 192.2 (Aug. 2000), pp. 185–192.

4.7. References

- [41] A. A. De Graaf, J. E. Van Dijk, and W. M. M. J. BoéE. “QUALITY: quantification improvement by converting lineshapes to the lorentzian type”. In: *Magnetic Resonance in Medicine* 13.3 (Mar. 1990), pp. 343–357.
- [42] J. H. Griesmer. “Society for Industrial and Applied Mathematics (A5)”. In: *Science* 151.3712 (Feb. 1966), pp. 859–860. arXiv: arXiv:1011.1669v3.
- [43] B. Soher et al. “VeSPA: Integrated applications for RF pulse design, spectral simulation and MRS data analysis”. In: *Proceedings of the 19th Annual Meeting ISMRM* 19.19 (2011), p. 1410.
- [44] R. Bartha, D. J. Drost, and P. C. Williamson. “Factors affecting the quantification of short echo in-vivo ^1H MR spectra: prior knowledge, peak elimination, and filtering.” In: *NMR in biomedicine* 12.4 (June 1999), pp. 205–16.
- [45] C. Gasparovic et al. “Use of tissue water as a concentration reference for proton spectroscopic imaging”. In: *Magnetic Resonance in Medicine* 55.6 (June 2006), pp. 1219–1226.
- [46] R. A. de Graaf et al. “High magnetic field water and metabolite proton T_1 and T_2 relaxation in rat brain in vivo”. In: *Magnetic Resonance in Medicine* 56.2 (Aug. 2006), pp. 386–394.
- [47] D. K. Deelchand, P. G. Henry, and M. Marjańska. “Effect of Carr-Purcell refocusing pulse trains on transverse relaxation times of metabolites in rat brain at 9.4 Tesla”. In: *Magnetic Resonance in Medicine* 73.1 (Jan. 2015), pp. 13–20.
- [48] Y. T. Kuo et al. “In vivo measurements of T_1 relaxation times in mouse brain associated with different modes of systemic administration of manganese chloride”. In: *Journal of Magnetic Resonance Imaging* 21.4 (Apr. 2005), pp. 334–339.
- [49] R. Kreis et al. “Integrated data acquisition and processing to determine metabolite contents, relaxation times, and macromolecule baseline in single examinations of

- individual subjects". In: *Magnetic Resonance in Medicine* 54.4 (Oct. 2005), pp. 761–768.
- [50] M. Marjańska et al. "Localized ^1H NMR spectroscopy in different regions of human brain in vivo at 7 T: T2 relaxation times and concentrations of cerebral metabolites". In: *NMR in Biomedicine* 25.2 (Feb. 2012), pp. 332–339.
- [51] Z. Šidák. "Rectangular Confidence Regions for the Means of Multivariate Normal Distributions". In: *Journal of the American Statistical Association* 62.318 (June 1967), pp. 626–633.
- [52] C. Chen et al. "Multiple comparisons permutation test for image based data mining in radiotherapy". In: *Radiation Oncology* 8.1 (Dec. 2013), p. 293.
- [53] R. J. Jackson et al. "Human tau increases amyloid β plaque size but not amyloid β -mediated synapse loss in a novel mouse model of Alzheimer's disease". In: *European Journal of Neuroscience* 44.12 (Dec. 2016). Ed. by G. Mallucci, pp. 3056–3066.
- [54] T. J. Vincent et al. "Longitudinal Brain Size Measurements in App/Ps1 Transgenic Mice". In: *Magnetic Resonance Insights* 4 (Jan. 2010), MRI.S5885.
- [55] E. Adalsteinsson et al. "Longitudinal decline of the neuronal marker N-acetyl aspartate in Alzheimer's disease". In: *Lancet* 355.9216 (May 2000), pp. 1696–1697.
- [56] U. Pilatus et al. "Conversion to dementia in mild cognitive impairment is associated with decline of N-actylaspartate and creatine as revealed by magnetic resonance spectroscopy". In: *Psychiatry Research - Neuroimaging* 173.1 (July 2009), pp. 1–7.
- [57] P. S. Ariyannur et al. "Methamphetamine-induced neuronal protein NAT8L is the NAA biosynthetic enzyme: Implications for specialized acetyl coenzyme A metabolism in the CNS". In: *Brain Research* 1335 (June 2010), pp. 1–13.

4.7. References

- [58] C. D. Rae. "A guide to the metabolic pathways and function of metabolites observed in human brain 1H magnetic resonance spectra". In: *Neurochemical Research* 39.1 (Jan. 2014), pp. 1–36.
- [59] A. Del Sole et al. "Individual cerebral metabolic deficits in Alzheimer's disease and amnesic mild cognitive impairment: An FDG PET study". In: *European Journal of Nuclear Medicine and Molecular Imaging* 35.7 (July 2008), pp. 1357–1366.
- [60] R. Ossenkoppele et al. "Longitudinal imaging of Alzheimer pathology using [11C]PIB, [18F]FDDNP and [18F]FDG PET". In: *European Journal of Nuclear Medicine and Molecular Imaging* 39.6 (June 2012), pp. 990–1000.
- [61] D. Smith et al. "Lactate: A preferred fuel for human brain metabolism in vivo". In: *Journal of Cerebral Blood Flow and Metabolism* 23.6 (June 2003), pp. 658–664.
- [62] C. N. Gallagher et al. "The human brain utilizes lactate via the tricarboxylic acid cycle: A 13C-labelled microdialysis and high-resolution nuclear magnetic resonance study". In: *Brain* 132.10 (Oct. 2009), pp. 2839–2849.
- [63] A. Schurr et al. "An Increase in Lactate Output by Brain Tissue Serves to Meet the Energy Needs of Glutamate-Activated Neurons". In: *The Journal of Neuroscience* 19.1 (Jan. 1999), pp. 34–39.
- [64] J. T. Newington, R. a. Harris, and R. C. Cumming. "Reevaluating Metabolism in Alzheimer's Disease from the Perspective of the Astrocyte-Neuron Lactate Shuttle Model". In: *Journal of Neurodegenerative Diseases* 2013 (2013), pp. 1–13.
- [65] N. Rouach et al. "Astroglial metabolic networks sustain hippocampal synaptic transmission". In: *Science* 322.5907 (Dec. 2008), pp. 1551–1555.
- [66] K. P. Jiao et al. "Vitamin D3 repressed astrocyte activation following lipopolysaccharide stimulation in vitro and in neonatal rats". In: *NeuroReport* 28.9 (June 2017), pp. 492–497.

- [67] I. Allaman, M. Bélanger, and P. J. Magistretti. "Astrocyte-neuron metabolic relationships: For better and for worse". In: *Trends in Neurosciences* 34.2 (Feb. 2011), pp. 76–87.
- [68] M. V. Sofroniew. "Reactive astrocytes in neural repair and protection". In: *Neuroscientist* 11.5 (Oct. 2005), pp. 400–407.
- [69] J. T. Newington et al. "Amyloid beta resistance in nerve cell lines is mediated by the warburg effect". In: *PLoS ONE* 6.4 (Apr. 2011). Ed. by H. Okazawa, e19191.
- [70] J. T. Newington et al. "Overexpression of pyruvate dehydrogenase kinase 1 and lactate dehydrogenase A in nerve cells confers resistance to amyloid β and other toxins by decreasing mitochondrial respiration and reactive oxygen species production". In: *Journal of Biological Chemistry* 287.44 (Oct. 2012), pp. 37245–37258.
- [71] H. Y. Kim et al. "Taurine in drinking water recovers learning and memory in the adult APP/PS1 mouse model of Alzheimer's disease". In: *Scientific Reports* 4.1 (May 2014), p. 7467.
- [72] O. A. Petroff et al. "Spectroscopic imaging of stroke in humans: histopathology correlates of spectral changes." In: *Neurology* 42.7 (July 1992), pp. 1349–54.
- [73] J. K. Choi, A. Dedeoglu, and B. G. Jenkins. "Application of MRS to mouse models of neurodegenerative illness". In: *NMR in Biomedicine* 20.3 (May 2007), pp. 216–237.
- [74] D. V. Hansen, J. E. Hanson, and M. Sheng. "Microglia in Alzheimer's disease". In: *Journal of Cell Biology* 217.2 (Feb. 2018), pp. 459–472.
- [75] M. Lv et al. "Effects of Quercetin Intervention on Cognition Function in APP/PS1 Mice was Affected by Vitamin D Status". In: *Molecular Nutrition and Food Research* 62.24 (Dec. 2018), p. 1800621.

4.7. References

- [76] M. Morello et al. "Vitamin D Improves Neurogenesis and Cognition in a Mouse Model of Alzheimer's Disease". In: *Molecular Neurobiology* 55.8 (Aug. 2018), pp. 6463–6479.
- [77] P. Yamini, R. S. Ray, and K. Chopra. "Vitamin D3 attenuates cognitive deficits and neuroinflammatory responses in ICV-STZ induced sporadic Alzheimer's disease". In: *Inflammopharmacology* 26.1 (Feb. 2018), pp. 39–55.
- [78] M. R. Durk et al. "1,25-Dihydroxyvitamin D3 Reduces Cerebral Amyloid- Accumulation and Improves Cognition in Mouse Models of Alzheimer's Disease". In: *Journal of Neuroscience* 34.21 (May 2014), pp. 7091–7101.
- [79] D. Jansen et al. "A Longitudinal Study of Cognition, Proton MR Spectroscopy and Synaptic and Neuronal Pathology in Aging Wild-type and A β PPswe-PS1dE9 Mice". In: *PLoS ONE* 8.5 (May 2013). Ed. by M. V. Schmidt, e63643.
- [80] S. Q. Chen et al. "Age-related changes in brain metabolites and cognitive function in APP/PS1 transgenic mice". In: *Behavioural Brain Research* 235.1 (Nov. 2012), pp. 1–6.
- [81] M. Marjanska et al. "Monitoring disease progression in transgenic mouse models of Alzheimer's disease with proton magnetic resonance spectroscopy". In: *Proceedings of the National Academy of Sciences* 102.33 (Aug. 2005), pp. 11906–11910.
- [82] J. Oberg et al. "Age related changes in brain metabolites observed by ¹H MRS in APP/PS1 mice". In: *Neurobiology of Aging* 29.9 (Sept. 2008), pp. 1423–1433.
- [83] J. L. Jankowsky et al. "Mutant presenilins specifically elevate the levels of the 42 residue β -amyloid peptide in vivo: Evidence for augmentation of a 42-specific γ secretase". In: *Human Molecular Genetics* 13.2 (Jan. 2004), pp. 159–170.
- [84] M. Kitazawa, R. Medeiros, and F. M. Laferla. "Transgenic mouse models of Alzheimer disease: developing a better model as a tool for therapeutic interventions." In: *Current Pharmaceutical Design* 18.8 (2012), pp. 1131–47.

4.8 Co-Authorship Statement

The material in Chapter 4 is in preparation for publication at the Journal of Neurochemistry. Some material presented in this chapter was included in two poster presentations at the Alzheimer's Association International Conference (2017; Poster #P1-082 and Poster #IC-P-044/P2-331). Dickson Wong was the main contributor for the material presented in this chapter – performing most of the study design, software development, data acquisition, data analysis, and manuscript preparation. Co-authors on this chapter were Miranda Bellyou, Alex Li, Marco Prado, Olivier Beauchet, Cédric Annweiler, Manuel Montero-Odasso, and Robert Bartha. Miranda Bellyou handled the animals, ensuring they had a steady food and water supply and received the correct diets at each time point. Miranda Bellyou also monitored the animals while under anaesthesia and collected the blood samples. Alex Li operated the MRI used to acquire all imaging and spectroscopy data. Marco Prado and the staff at the Neurobehavioural Core Facility at Robarts Research Institute trained Dickson Wong on all behavioural tests that were performed. Olivier Beauchet, Cédric Annweiler, Manuel Montero-Odasso, and Robert Bartha provided invaluable guidance in terms of study design, data analysis, interpretation of the data, and manuscript preparation.

Estimated percentage of the work for Chapter 4 conducted solely by Dickson Wong: 85%

5

Summary and Future Work

5.1 Summary

The purpose of this thesis was to study the metabolic and structural changes of specific brain regions as a consequence of Alzheimer's disease (AD) alone and under conditions of AD and Vitamin D deprivation. The scientific investigations that were conducted are summarized in this section.

5.1.1 Reduced hippocampal glutamate and posterior cingulate NAA in MCI and AD is associated with episodic memory performance and white matter integrity in the cingulum

Chapter 2 described a cross-sectional study where brain metabolism and microstructure were evaluated by proton magnetic resonance spectroscopy (^1H -MRS) and diffusion tensor imaging (DTI) in the limbic system of eight individuals with mild cognitive impairment (MCI), nine with Alzheimer's disease (AD), and sixteen elderly controls (NEC). Compared to NEC, posterior cingulate *N*-acetyl aspartate (NAA) concentrations were reduced in MCI and AD. Differences in diffusion metrics of white-matter microstructure were also observed in the region of the cingulum that corresponds anatomically to the posterior cingulate cortex (PCC). Individuals with AD had lower fractional anisotropy (FA) and higher

RD than NECs or individuals with MCI – a pattern consistent with demyelination. Lower posterior cingulate NAA concentrations were correlated with more demyelination (lower FA, greater RD and T_1) and with worse scores on the Craft Story 21 Recall (CSR) and Benson Complex Figure Copy (BCFC) tests of episodic memory, the type of memory supported by the limbic system. Together, this suggested that NAA deficit in the PCC of people with AD could indicate a demyelinating process in the region that manifests as poorer memory performance.

Reduced left hippocampal glutamate concentrations were also found in MCI and AD compared to NECs. In the region of the cingulum that corresponds anatomically to the hippocampus, individuals with AD had greater radial diffusivity (RD), axial diffusivity (AxD) and T_1 values – a pattern consistent with tissue atrophy. RD and AxD values in this region also correlated with hippocampal glutamate levels. Lower hippocampal glutamate levels were associated with more tissue atrophy (greater RD, lower AxD) and with worse scores on the CSR and BCFC tests on episodic memory. These results suggested that lower hippocampal glutamate concentration could indicate impaired neuro-energetics or a loss of glutamatergic neurons, ultimately manifesting as poorer episodic memory performance.

Overall, the results of this study show that metabolite concentrations measured using ^1H -MRS may provide valuable insight into the underlying metabolic and microstructural processes of episodic memory impairment and increase the confidence of a clinical diagnosis of MCI or AD.

5.1.2 Optimized in vivo glutamate measurement using long-echo-time semi-LASER at 7 T

NAA is one of the strongest signals present in a ^1H -MRS spectrum and can be reliably measured in the brain with a variety of acquisition parameters. On the other hand, glutamate is harder to measure because it is a strongly J -coupled spin system and its resonances

overlaps with the resonances of macromolecules, glutamine, and GABA. Therefore, the selection of acquisition parameters are important.

In Chapter 2, glutamate was measured using acquisition parameters that were not optimized. In order to improve and facilitate the measurement of glutamate in future studies, an experiment to find the optimal echo time (T_E) for the measurement of glutamate concentration using ^1H -MRS at 7 T was performed. This experiment was presented in Chapter 3.

Time-domain simulations were performed to model the T_E dependence of glutamate signal energy, a measure of glutamate signal strength. These simulations were verified against *in vivo* measurements made in the sensorimotor cortex of five human participants and *in vitro* measurements made in a mixed-metabolite phantom containing glutamate, glutamine, and GABA. Simulations showed a local maximum of glutamate signal energy at $T_E = 107$ ms. Consistent with this, *in vitro* measurements produced a maximal signal energy for glutamate at $T_E = 100$ ms. *In vivo* measurements showed that $T_E = 105$ ms produced the greatest glutamate signal energy, while also resulting in the smallest inter-subject glutamate-to-creatine ratio (Glu/Cr) coefficient of variation. In other words, $T_E = 105$ ms provides the greatest statistical power to measure *in vivo* differences in Glu/Cr between groups. Together, these results indicate that $T_E = 105$ ms is optimum for *in vivo* glutamate measurement at 7 T with semi-LASER.

5.1.3 Chronic Vitamin D deficiency in adult APP/PS1 mice: Effect on memory performance and brain metabolite levels

Having established in Chapter 2 that ^1H -MRS could be used to provide insight into the underlying metabolic and structural processes of episodic memory impairment in AD, the same approach was applied to study the effects of Vitamin D (VitD) deficiency in a mouse model of AD in Chapter 4. VitD can protect against the effects of calcium dysregulation and oxidative stress, and VitD deficiency is thought to exacerbate AD progression. However,

literature on VitD deficiency in AD remains inconsistent. Thus, the objective of the study was to use ^1H -MRS, shown in Chapter 2 to provide insight into the underlying metabolic and structural processes of episodic memory impairment of AD, to help clarify the role of chronic VitD deficiency in AD.

The effects of Vitamin D (VitD) deficiency were studied longitudinally in a transgenic mouse model of AD ($\text{APP}_{\text{Swe}}/\text{PS1}\Delta\text{E9}$). Mice were fed either a VitD deficiency diet (< 1 IU/kg VitD_3) or a nutritionally sufficient control diet (1000 IU/kg VitD_3) from 6 months to 15 months of age. Comprehensive evaluation of the resulting longitudinal neurochemical, anatomical, and memory changes in the brain were assessed using ^1H -MRS, high resolution MRI, and two independent spatial memory tasks, respectively. The spatial tasks used were the Barnes maze (BM) and Morris water maze (MWM). Longitudinal serum 25(OH)D levels were also measured using radioimmunoassay. Measurements were made at 6 months, 9 months, 12 months, and 15 months of age.

Mice on the VitD deficient diet had significantly lower serum 25(OH)D levels than mice on the control diet at 9 months, 12 months, and 15 months of age, showing that chronic VitD deficiency was successfully established. Neurochemical changes detected included decreased NAA and Cr concentrations and increasing lactate and taurine concentrations in mice on the VitD deficient diet. This pattern of change is consistent with a reactive astrogliosis process. Interestingly, VitD deficiency appeared to result in better performance or improvement in performance in the BM and MWM. Overall, the observations made in VitD deficient $\text{APP}_{\text{Swe}}/\text{PS1}\Delta\text{E9}$ mice suggest that VitD deficiency may improve memory by upregulating beneficial reactive astrogliosis in the prodromal stages of AD.

5.2 Conclusions

The aim of this thesis was to study the metabolic and structural changes in the brain as a result of Alzheimer's disease. Using ^1H -MRS at 7 T, both decreased NAA in the PCC

and decreased glutamate in the hippocampus were detected in individuals with MCI and AD compared to NECs and were associated with changes in diffusion metrics consistent with atrophy and demyelination processes. Importantly, reduced NAA and glutamate concentrations were observed in both MCI and AD compared to NECs, whereas differences in diffusion metrics were only observed in AD subjects compared to NECs. This suggests that changes in brain metabolite concentrations may precede structural changes. This conclusion is supported by the results presented in Chapter 4, which measured metabolite changes longitudinally in APP_{Swe}/PSΔE9 mice. In these mice, NAA concentrations decreased with time, a result consistent with the observation of decreased NAA concentrations in the PCC of individuals with MCI and AD made in Chapter 2, but ventricle volume (a metric of neuronal loss) remained stable with time. Since APP_{Swe}/PSΔE9 mice are considered a model of mild AD, the results may suggest that NAA concentrations decrease in the early, mild stages of AD before neuronal loss occurs in the more severe stages.

In human participants, brain metabolite concentrations measured using ¹H-MRS were associated with decreased episodic memory performance as measured using neuropsychological testing (Chapter 2). Similarly, in transgenic AD mice, brain metabolite concentrations were associated with decreased spatial memory performance, a proxy measure of episodic memory in rodents (Chapter 4). These results suggest that brain metabolite concentrations could indicate biological changes that underlie early symptoms of AD. Since the progression of AD is a continuum, progressing from an asymptomatic phase to MCI and to AD, measuring such biological changes could help clinicians stage individuals prior to symptom onset.

To measure these metabolite changes effectively, particularly with difficult-to-measure metabolites of interest such as glutamate, optimal acquisition parameters should be used. In Chapter 3, a long T_E of 105 ms was determined to be optimal for human *in vivo* measurement of glutamate using ¹H-MRS at 7 T. Advantages of using this T_E includes decreased power deposition by allowing lower maximum RF pulse amplitudes in conjunction with

longer RF pulses and decreased macromolecule contributions, eliminating the requirement for acquisition of separate macromolecule or macromolecule fitting techniques, which add additional scan time or bias the glutamate measurement. In comparison to previous studies, this T_E yielded comparable glutamate-to-creatine ratios, but with a smaller coefficient of variation. Use of this T_E for future studies of glutamate concentration in AD should provide more precision and statistical power.

5.3 Future Work

5.3.1 The Clinical Utility of Brain Metabolite Concentrations

The studies performed as part of this thesis suggested that brain metabolite concentrations could indicate biological changes that underlie early symptoms of AD and could be predictive of structural changes that occur later on in the disease process. Though the longitudinal measurements of transgenic AD mice in Chapter 4 showed that metabolite concentrations change over time in AD, only a cross-sectional study was performed in humans (Chapter 2). A comprehensive longitudinal study that tracks brain metabolite concentrations using high-field ^1H -MRS with optimized acquisition parameters, measures of brain structure, and measures of cognitive impairment in a large cohort of older individuals as they progress from the asymptomatic phase to MCI and to AD would be needed to definitively determine the prognostic value of ^1H -MRS and its value in helping clinicians stage individuals along the AD continuum.

Single-voxel ^1H -MRS in the hippocampus and PCC was used in this thesis to study NAA and glutamate concentrations. Though these regions are known to be involved early in the pathological progression of AD, it would be valuable to assess the distribution of NAA and glutamate across the whole brain. Techniques such as magnetic resonance spectroscopic imaging (MRSI) using acquisition parameters optimized for NAA and glutamate measurement could be used to perform such a measurement. The value of assessing the

distribution of metabolites is to identify areas of the brain that would be useful for differentiating AD from other dementias that have different neuropathology, progression, and prognosis. Knowing the best brain areas to make the measurement would be necessary if ^1H -MRS is to be used as a tool to help make a clinical diagnosis of AD.

5.3.2 Optimized Acquisition of Brain Metabolite Signals

Chapter 3 in this thesis showed that measurement of the glutamate signal could benefit from an optimized T_E . The next step would be to use this optimized T_E in a ^1H -MRS study. Since the T_E was determined for 7 T semi-LASER ^1H -MRS specifically, it would also be useful to determine the optimal T_E for glutamate acquisition at other commonly used field strengths, such as 1.5 T, 3 T or 9.4 T, and with other commonly used sequences. The same approach described in this thesis could also be used to determine the optimal T_E s for the measurement of other metabolites using ^1H -MRS. This work could set the foundation for an acquisition method where multiple different T_E s are used, enabling the optimal measurement of a panel of metabolites.

5.3.3 The Role of Vitamin D in Alzheimer's Disease

Finally, Chapter 4 in this thesis comprehensively evaluated the effect of VitD deficiency in APP_{Swe}/PS1 Δ E9 mice. The changes measured using ^1H -MRS suggested that the spatial memory performance associated with VitD deficiency was due to a reactive astrogliosis process. However, this needs to be confirmed with future studies that includes both ^1H -MRS measurements and brain histology in VitD deficient APP_{Swe}/PS1 Δ E9 mice. One approach would be to expose different cohorts of APP_{Swe}/PS1 Δ E9 mice to different durations of VitD deficiency, measuring their metabolite levels using ^1H -MRS, sacrificing them immediately after their scanning session, and analyzing their brains for astrocyte markers such as glial fibrillary acidic protein (GFAP).

Studies of VitD deficiency should also be performed in rodent models of AD pathology that are more aggressive than APP_{Swe}/PS1 Δ E9, such as mice that express 5 familial AD genes (5xFAD mice). This is necessary to evaluate the role of VitD deficiency in moderate to severe AD. It is possible that VitD deficiency is beneficial in mild AD, as was suggested by the results of Chapter 4, but is detrimental in moderate to severe AD.

A natural next step after concretely establishing the role of VitD deficiency in various stages of AD would be to assess whether VitD supplementation could be beneficial. If there is a potential benefit, it would also be important to determine at which point along the AD continuum that VitD supplementation is beneficial. Considering the findings of Chapter 4 that VitD deficiency may be beneficial rather than detrimental in the early stages of AD, it could be that VitD supplementation is only beneficial at later stages of AD.

A

Physics of Magnetization and The Equilibrium Magnetization

A.1 Magnetization

The physical phenomenon of nuclear magnetic resonance arises from the quantum mechanical properties of the protons and neutrons that make up atomic nuclei. As shown in Figure A.1a, protons are composed of three quarks. Quarks are elementary particles with fundamental properties of charge and spin. The charges of the quarks produce a net charge of $+e$ for the proton. The spin of a quark is $1/2$ and the spins of an up quark and a down quark cancel. In a proton, the combination of quarks produces a net spin of $1/2$. Neutrons are also composed of three quarks, combining to produce a net spin of $1/2$ and a net charge of 0 (Figure A.1b).

Since nuclei are made up of combinations of protons and neutrons, nuclei can also have the property of spin. However, not all nuclei have spin; nuclei with an even number of protons and an even number of neutrons have a spin of 0. This is because there is a strong tendency for protons to pair with another proton and a neutron to pair with another neutron. The spins of the quarks cancel in proton-proton and neutron-neutron pairs, producing a net spin of 0. It is only nuclei with an odd number of protons or an odd number

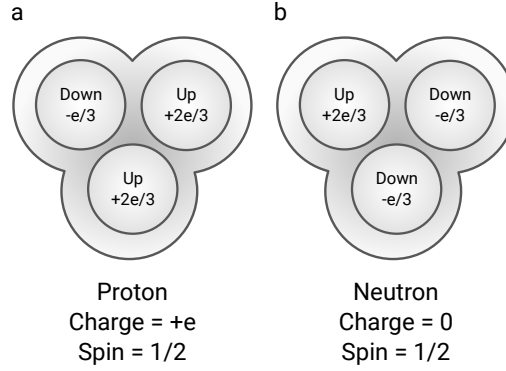


FIGURE A.1: Protons and neutrons are each made of three quarks. (a) A proton has two up quarks and one down quarks, a net charge of $+e$, and a net spin of $1/2$. (b) A neutron has two down quarks and one up quark, with a net charge of 0 and a net spin of $1/2$.

of neutrons that have a non-zero spin. Only nuclei with non-zero spin can undergo nuclear magnetic resonance.

Associated with nuclear spin, I , is the property of spin angular momentum, \vec{L} , which is a vector quantity. Due to Heisenberg's uncertainty principle, the exact direction of \vec{L} is unknown. However, the component of \vec{L} in any direction, i , can be measured,

$$L_i = \hbar I_i \quad I_i \in \{-I, -(I-1) \cdots I-1, I\} \quad (\text{A.1})$$

I_i can take on $2I - 1$ values, which is equal to the number of spin states of the nucleus. The magnitude of \vec{L} is also known and is given by its eigenvalue:

$$|\vec{L}| = \sqrt{I(I-1)} \quad (\text{A.2})$$

Nuclei with angular momentum and charge will also have an associated magnetic moment that can be observed empirically. Analytically, this magnetic moment is given by:

$$\begin{aligned} \vec{\mu} &= \frac{gq}{2m} \vec{L} \\ \vec{\mu} &= \gamma \vec{L} \end{aligned} \quad (\text{A.3})$$

A.1. Magnetization

where q is nuclear charge, m is nuclear mass, \vec{L} is the spin angular momentum and g is the g -factor, a proportionality constant that relates the observed magnetic-moment to the intrinsic spin angular momentum. $\gamma = \frac{gq}{2m}$ is the gyromagnetic ratio unique to each nucleus.

If the nuclei are then placed in a magnetic field, \vec{B}_0 , they will acquire potential energy, U , defined by:

$$U = -\vec{\mu} \cdot \vec{B}_0 \quad (\text{A.4})$$

$$U = \gamma \vec{L} \cdot \vec{B}_0 \quad (\text{by Equation (A.3)})$$

Since \vec{L} is quantized, U is also quantized, and a nuclei may only occupy $2I - 1$ different energy states. The probability that a nucleus is found in a particular energy state, ϵ , is governed by the Boltzmann distribution:

$$P(\epsilon) = \frac{e^{-U_\epsilon/kT}}{\sum_\epsilon e^{-U_\epsilon/kT}} \quad (\text{A.5})$$

where U_ϵ is the energy of state ϵ , k is the Boltzmann constant, and T is the temperature.

In proton magnetic resonance imaging and spectroscopy, the nucleus of interest is 1H , and the magnetic field is oriented along the z -axis (i.e. $\vec{B}_0 = B_0\hat{z}$). A 1H nucleus is made up of a single proton, and therefore has spin $I = 1/2$ and two spin states: $|+\rangle$ and $|-\rangle$. The probability that a 1H nucleus is in an energy state where μ_z is aligned with \vec{B}_0 may be derived from Equation (A.1), (A.3) – (A.5), and the fact that $kT \gg |U|$ at physiological temperatures:

$$P(\epsilon_{\vec{\mu} \parallel \vec{B}_0}) = \frac{\mu_z B_0}{kT} = \frac{\gamma \hbar B_0}{2kT} \quad (\text{A.6})$$

This probability may then be used to determine the net magnetic moment of an ensemble of ^1H nuclei, \vec{M}_0 , also called the equilibrium magnetization:

$$\begin{aligned}\vec{M}_0 &= \text{proton density} \cdot \text{size of } \mu_z \cdot \text{probability of } ^1\text{H nuclei with } \vec{\mu} \parallel \hat{z} \\ &= \rho_0 \cdot \mu_z \cdot \frac{\mu_z B_0}{kT} \hat{z} \\ \vec{M}_0 &= \rho_0 \frac{\gamma^2 \hbar^2 B_0}{4kT} \hat{z}\end{aligned}\tag{A.7}$$

Since \vec{M}_0 is macroscopic, its behaviour may be described without quantum mechanics. In the magnetic field, \vec{B}_0 , \vec{M}_0 will experience a torque given by the following cross-product:

$$\vec{\tau} = \vec{M}_0 \times \vec{B}_0 = \frac{d}{dt} \vec{J}\tag{A.8}$$

At each instant in time, the torque causes a change in the angular momentum of the system, \vec{J} , in the direction of the torque. Since $\vec{M}_0 \parallel \vec{J}$, the \vec{M}_0 also changes in the direction of $\vec{\tau}$, resulting in the clockwise precession of the magnetization around \vec{B}_0 (Figure A.2). The angular frequency of this precession is the Larmor frequency, ω_0 , which is given by:

$$\omega_0 = \gamma B_0\tag{A.9}$$

A.2 Measuring Magnetization

In an MR scanner, the magnetization is measured using a receive coil. There is a time-varying magnetic field associated with the precessing magnetization, which produces magnetic flux through the receive coil. This flux generates an electromotive force (*emf*) in the coil, producing a voltage signal that can be recorded. Using Ampère's Law, the definition

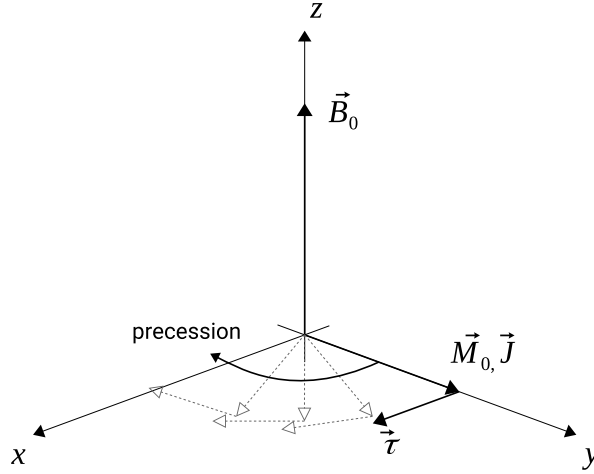


FIGURE A.2: Torque, $\vec{\tau}$, exerted by the magnetic field, \vec{B}_0 , on the magnetization, \vec{M}_0 , changes the angular momentum, \vec{J} , in the direction of $\vec{\tau}$. Since $\vec{M}_0 \parallel \vec{J}$, the \vec{M}_0 also changes in the direction of $\vec{\tau}$, resulting in clockwise precession about \vec{B}_0 .

of magnetic vector potential, and Faraday's Law, the *emf* induced in the coil may derived:

$$\begin{aligned} emf &= \frac{-d}{dt} \Phi(t) \\ &= \frac{-d}{dt} \iiint \vec{M}_0(\vec{r}, t) \cdot \vec{B}_{\text{receive}}(\vec{r}) dV \end{aligned} \quad (\text{A.10})$$

where \vec{B}_{receive} is the sensitivity profile of the receive coil. Coils used for MR imaging are typically designed such that the sensitivity profile is optimized to detect magnetization perpendicular to the direction of \vec{B}_0 . Thus, \vec{M}_0 must be manipulated such that a component of \vec{M}_0 lies within the \hat{x}, \hat{y} -plane.

B

Quantum Mechanical Calculations for the Simulation of Metabolite Spin Systems

B.1 Overview

A mostly classical treatment of the physics of magnetic resonance and ^1H -MRS were given in Sections 1.3 and 1.4 of this thesis. However, J-coupling behaviour for strongly coupled metabolite spin systems could not be adequately described using classical mechanics. In this case, quantum mechanical calculations are needed. These calculations can also be used to produce simulated metabolite spectra that can be part of a prior knowledge template used to analyse *in vivo* data. A brief description of the quantum mechanical calculations needed for these purposes are given in this Appendix.

B.2 Describing the State of a System

In quantum mechanics, the state of a quantum mechanical system, such as a single nuclear spin or a particle, is given by its wave function, $\psi(\vec{r}, t)$. This is analogous to the classical concept of a trajectory and contains all possible information about the particle. The wave

B.2. Describing the State of a System

function is interpreted as the probability amplitudes of the particle's presence:

$$dP(\vec{r}, t) = C |\psi(\vec{r}, t)|^2 d^3\vec{r} \quad (\text{B.1})$$

Associated with the wave function is an element of a linear vector space, F , called Hilbert space. This element, $|\psi\rangle$, is called a “ket” and can be expressed in terms of the basis functions of Hilbert space $|f_i\rangle$:

$$|\psi\rangle = \sum_{i=1}^n \psi_i |f_i\rangle \in F \quad (\text{B.2})$$

A more compact representation of this expression is simply a vector of the coefficients ψ_i :

$$\vec{\psi} = \begin{bmatrix} \psi_1 \\ \psi_2 \\ \vdots \\ \psi_n \end{bmatrix} \quad (\text{B.3})$$

As discussed in Section A.1, the spin-1/2 1H nucleus has two spin states. Expressed in the notation of quantum mechanics, these two states are as follows:

$$|\psi\rangle = |+\rangle = \begin{bmatrix} 1 \\ 0 \end{bmatrix} \quad (\text{B.4})$$

$$|\psi\rangle = |-\rangle = \begin{bmatrix} 0 \\ 1 \end{bmatrix} \quad (\text{B.5})$$

The ket representation of a the system state also has a dual representation called a “bra,” $\langle\psi|$, which is defined as follows for a spin-1/2 system:

$$\langle\psi| = \begin{bmatrix} a^* & b^* \end{bmatrix} \quad (\text{B.6})$$

where $|\psi\rangle = \begin{bmatrix} a \\ b \end{bmatrix}$ and $*$ represents the conjugate.

B.3 Describing Measurable Quantities

Every measurable quantity in a quantum mechanical system is described using an operator. An operator generates one ket from another:

$$\hat{H} |\psi\rangle = |\zeta\rangle \quad (\text{B.7})$$

If $|\zeta\rangle = \lambda |\psi\rangle$, then $|\psi\rangle$ is called the eigenket of the operator \hat{H} , and λ is the eigenvalue of the operator \hat{H} .

Operators also have a matrix representation and can generate one vector representation of a ket from another:

$$\mathbf{H}\vec{\psi} = \vec{\zeta} \quad (\text{B.8})$$

The eigenvalues of the operator \hat{H} is equal to the eigenvalues of the operator matrix \mathbf{H} . These eigenvalues are the only possible values that the quantity can take when it is measured, and each eigenvalue has an associated probability of measurement. The state of the system after a measurement is the eigenket associated with the measured eigenvalue.

In the case of a ^1H nucleus, one of the measurable quantities is its angular momentum along the z-direction, L_z . In quantum mechanics notation, this quantity is represented using the operator \hat{L}_z , which has the associated matrix:

$$\mathbf{L}_z = \begin{bmatrix} \hbar/2 & 0 \\ 0 & -\hbar/2 \end{bmatrix} \quad (\text{B.9})$$

This matrix has eigenvalues $\hbar/2$ and $-\hbar/2$, which are the only two possible values of angular momentum that can be measured. Associated with these eigenvalues are the eigenkets $|+\rangle = [1\ 0]^T$ and $|-\rangle = [0\ 1]^T$, which are the two possible system states of a 1H nucleus (Equation (B.5)).

B.4 Time Evolution of a System State

The time-evolution of the state of a quantum mechanical system is given by Schrödinger's equation:

$$\frac{\delta}{\delta t} |\psi\rangle = -j\hat{H}(t) |\psi(t)\rangle \quad (\text{B.10})$$

where $|\psi(t)\rangle$ is the ket representing the system state, and $\hat{H}(t)$ is the operator representing the energy of the system.

B.5 Describing a Statistical Ensemble of Quantum Mechanical Systems

In 1H -MRS, it is not a single 1H nucleus that is being observed, but rather an ensemble of nuclei. In this case, wave function representations and Schrödinger's equation (B.10) are not very useful, because the exact wave function of every single spin being observed is rarely known. Thus, an ensemble of nuclei must be described statistically.

This can be done using a density operator, $\hat{\sigma}$. $\hat{\sigma}$ has the associated matrix σ , which is defined as follows:

$$\sigma = \sum_{j=1}^N p_j |\psi_j\rangle \langle \psi_j| \quad (\text{B.11})$$

where p_j is the probability of a system being in state $|\psi_j\rangle$. The density matrix can then help us to take the ensemble average of a measurable quantity. For example, the ensemble average of a measurable quantity A is given by:

$$\begin{aligned}\langle \bar{\mathbf{A}} \rangle &= \text{Tr} \{ \sigma \mathbf{A} \} \\ &= \sum_{j=1}^N p_j \langle \psi_j | \mathbf{A} | \psi_j \rangle\end{aligned}\tag{B.12}$$

where Tr is the matrix trace operation. In this equation, $\langle \psi_j | \mathbf{A} | \psi_j \rangle$ is the quantum mechanical average of A . In other words, this is the expected value of A if the system is in state $|\psi_j\rangle$. Since p_j is the probability of the system being in state $|\psi_j\rangle$, Equation (B.12) is simply a statistical average of expected measured values.

B.6 Time Evolution of a Statistical Ensemble of Quantum Mechanical Systems

The time-evolution of a statistical ensemble of quantum mechanical systems is described using the Liouville-von Neumann equation:

$$\frac{\delta}{\delta t} \hat{\sigma} = -j [\hat{H}, \hat{\sigma}]\tag{B.13}$$

In this equation, the square brackets represent the commutator operation: $[A, B] = AB - BA$. The operator \hat{H} is called the Hamiltonian and represents the energy of the ensemble.

In ^1H -MRS, the Hamiltonian is the sum of different Hamiltonians associated with different physical interactions:

$$\hat{H} = \hat{H}_1 + \hat{H}_2 + \hat{H}_3 + \hat{H}_4 + \hat{H}_5 + \dots$$

where \hat{H}_1 is associated the interaction of nuclear spins with the main magnetic field \vec{B}_0 , \hat{H}_2 is associated with the spin-spin interaction, \hat{H}_3 is associated with the J-coupling between spins, \hat{H}_4 is associated with the chemical shift phenomenon, and \hat{H}_5 is associated with the interaction of nuclear spins with the \vec{B}_1 field. Other Hamiltonians associated with other processes could also be part of the sum.

If it can be assumed that the Hamiltonian, \hat{H} , does not change with time, the solution to the Liouville-von Neumann equation in terms of the operator matrices is:

$$\sigma(t) = e^{-j\mathbf{H}t/\hbar} \sigma(0) e^{j\mathbf{H}t/\hbar} \quad (\text{B.14})$$

This is the key equation used to simulate metabolite spin-systems and generate parameter values to produce a constrained prior knowledge template for ^1H -MRS analysis.

B.7 General Procedure for Metabolite Spin-System Simulations

Having established the required mathematics for metabolite spin-system simulations, the general procedure to implement such a simulation can be laid out. Before calculations can begin, a few items need to be defined first:

1. Given a metabolite whose ^1H have specific chemical shielding and J-coupling constants, define a static Hamiltonian for the system:

$$\hat{H} = \hat{H}_{CS} + \hat{H}_J$$

where \hat{H}_{CS} is the chemical shielding Hamiltonian, and \hat{H}_J is the scalar coupling Hamiltonian.

2. Define the RF pulse waveforms using RF pulse files from the MRI scanner.

3. Define the RF pulse sequence using the pulse sequence timings available from the MRI scanner.
4. Define a density matrix for the metabolite spin-system.

Relaxation effects can typically be ignored to simplify the simulations, since a classical treatment of relaxation effects can be applied to the simulation results using known metabolite T_2 values.

Once these items are defined, the density matrix of the metabolite spin-system may be evolved in time under the defined RF pulse sequence using Equation (B.14). During the periods of time in the pulse sequence where no RF pulse is being applied, $\hat{H} = \hat{H}_{CS} + \hat{H}_J$ is simply substituted into Equation (B.14) to evolve $\sigma(t)$. During the periods of time in the pulse sequence where an RF pulse is being applied, a *static* Hamiltonian is defined to describe the interactions of the 1H nuclei with the \vec{B}_1 field *at each time-step* of the RF pulse. The Hamiltonians are substituted into the Equation (B.14) to evolve $\sigma(t)$ under the applied RF pulse.

The resulting density matrix after the pulse sequence is complete can be used to generate expectation values for measurable quantities of interest using Equation (B.12). These quantities can include the metabolite amplitudes, shifts, and phases that result from the application of the pulse sequence. Metabolite amplitudes, shifts, and phases can then be used to generate the metabolite signal models that are included in a prior knowledge template and to constrain the prior knowledge template itself. In the case of a metabolite with strong J-coupling, where the peak splitting behaviour does not follow Pascal's triangle, the calculated metabolite amplitudes, shifts, and phases can be used to describe and visualize the splitting behaviour.

C

Absolute Metabolite Quantification Using an Internal Water Reference

Absolute metabolite concentrations of a metabolite can be calculated by using an internal water reference. This internal water reference is the unsuppressed water signal collected at the same time as the water-suppressed spectra. Instead of using a ratio of each metabolite signal over the signal of a reference metabolite (e.g. creatine), a ratio over the signal of water is used. This is advantageous because the water signal from brain tissue is consistent between individuals, whereas a reference *in vivo* metabolite signal can vary between individuals because its concentration varies.

Using an internal reference to determine metabolite concentration can be written as follows:

$$[M] = \frac{\hat{S}_m}{\hat{S}_W} [W] \quad (\text{C.1})$$

where

$[M]$ = concentration of the metabolite

$[W]$ = concentration of pure water = 55.14 M

\hat{S}_W = corrected water signal

\hat{S}_m = corrected metabolite signal

As Equation (C.1) shows, the measured water signal is mapped to the known concentration of pure water. This mapping is then used to determine what concentration the measured metabolite signal represents. The measured water and metabolite signals are not used directly; they are first corrected for a variety of factors.¹

C.1 Corrections for T_1 and T_2 Relaxation

The most important of these corrections is the correction for T_1 and T_2 relaxation. The objective of the T_1 and T_2 relaxation correction is to determine what the measured signal would be if there was no relaxation. Relaxation of the transverse magnetization is described by the following equation:

$$M_{xy} = M_0 \left(1 - e^{-TR/T_1}\right) \left(e^{-TE/T_2}\right) \quad (C.2)$$

where M_{xy} is the measured signal, and M_0 is the signal before T_1 and T_2 relaxation begins.

Equation (C.2) describes relaxation in a single tissue compartment. However, in the context of *in-vivo* brain metabolite quantification, the GM, WM, and CSF compartments must be considered:

$$\begin{aligned} M_{xy} = & M_{0,GM} \left(1 - e^{-TR/T_{1,GM}}\right) \left(e^{-TE/T_{2,GM}}\right) \\ & + M_{0,WM} \left(1 - e^{-TR/T_{1,WM}}\right) \left(e^{-TE/T_{2,WM}}\right) \\ & + M_{0,CSF} \left(1 - e^{-TR/T_{1,CSF}}\right) \left(e^{-TE/T_{2,CSF}}\right) \end{aligned} \quad (C.3)$$

¹It is important to note that spectroscopic voxel volume is not considered in the present discussion, as it is assumed the unsuppressed water signal and the water-suppressed spectra are measured using the same spectroscopic voxel. If this is not the case, voxel volume would have to be considered.

C.1. Corrections for T_1 and T_2 Relaxation

$M_{0,GM}$, $M_{0,WM}$, and $M_{0,CSF}$ may be expressed in terms of M_0 . Considering only the GM compartment for the moment,

$$M_{0,GM} = f_{GM}\alpha_{GM}M_0$$

where f_{GM} is the volume fraction of GM in the spectroscopic voxel, and α_{GM} is the relative proton density in GM.

To explain why $M_{0,GM} = f_{GM}\alpha_{GM}M_0$, it is important to remember that M_0 is proportional to the total number of protons in the spectroscopic voxel. Since proton density is the number of protons in a volume, multiplying the volume fraction by the relative proton density allows us to determine the fraction of the total number of protons contributed by the GM. This fraction can then be used to properly attribute the proportion of M_0 to GM. Using the same reasoning,

$$M_{0,GM} = f_{WM}\alpha_{WM}M_0$$

$$M_{0,CSF} = f_{CSF}\alpha_{CSF}M_0$$

where f_{WM} is the volume fraction of WM in the spectroscopic voxel, f_{CSF} is the volume fraction of CSF in the spectroscopic voxel, α_{WM} is the relative proton density in WM, and α_{CSF} is the relative proton density in CSF.

Thus, Equation (C.3) may be rewritten as:

$$\begin{aligned} M_{xy} = & f_{GM}\alpha_{GM}M_0 \left(1 - e^{-TR/T_{1,GM}}\right) \left(e^{-TE/T_{2,GM}}\right) \\ & + f_{WM}\alpha_{WM}M_0 \left(1 - e^{-TR/T_{1,WM}}\right) \left(e^{-TE/T_{2,WM}}\right) \\ & + f_{CSF}\alpha_{CSF}M_0 \left(1 - e^{-TR/T_{1,CSF}}\right) \left(e^{-TE/T_{2,CSF}}\right) \end{aligned} \quad (C.4)$$

Since the objective of the T_1 and T_2 relaxation correction is to determine the signal without T_1 or T_2 relaxation, applying a correction for T_1 and T_2 is the same as solving for M_0 . Solving (C.4) for M_0 results in:

$$M_0 = \frac{M_{xy}}{f_{GM}\alpha_{GM}R_{GM} + f_{WM}\alpha_{WM}R_{WM} + f_{CSF}\alpha_{CSF}R_{CSF}} \quad (C.5)$$

where

$$\begin{aligned} R_{GM} &= \left(1 - e^{-TR/T_{1,GM}}\right) \left(e^{-TE/T_{2,GM}}\right) \\ R_{WM} &= \left(1 - e^{-TR/T_{1,WM}}\right) \left(e^{-TE/T_{2,WM}}\right) \\ R_{CSF} &= \left(1 - e^{-TR/T_{1,CSF}}\right) \left(e^{-TE/T_{2,CSF}}\right) \end{aligned}$$

C.1.1 T_1 and T_2 Correction for the Measured Water Signal (S_W)

Equation (C.5) may be applied directly to correct the measured water signal for T_1 and T_2 relaxation:

$$\hat{S}_W = \frac{S_W}{f_{GM}\alpha_{GM}^W R_{GM}^W + f_{WM}\alpha_{WM}^W R_{WM}^W + f_{CSF}\alpha_{CSF}^W R_{CSF}^W} \quad (C.6)$$

where

$\alpha_{GM}^W = 0.82$ = the relative proton density of water in GM as compared to that of pure water

$\alpha_{WM}^W = 0.73$ = the relative proton density of water in WM as compared to that of pure water

$\alpha_{CSF}^W = 1.00$ = the relative proton density of water in CSF as compared to that of pure water

and R_{GM}^W , R_{WM}^W , and R_{CSF}^W are the corresponding relaxation terms of Equation (C.5) using the tissue specific T_1 and T_2 relaxation rates of water. $S_W = A_W$, the amplitude of the fitted

water peak.

C.1.2 T_1 and T_2 Correction for the Measured Metabolite Signal (S_m)

Unlike the measured water signal, Equation (C.5) cannot be directly applied to correct the measured metabolite signal because of a couple of reasons. First, it is assumed that the CSF contribution to the metabolite signal is negligible because there are little to no metabolites in the CSF. No part of the metabolite signal should be attributed to the CSF compartment and any metabolite signal should be equally attributed to the WM and GM compartment. Secondly, the relative proton density in GM, WM, and CSF for metabolites are not known. Because of this, α_{GM} , α_{WM} , and α_{CSF} are assumed to be 1.00 for metabolites. The equation to correct the measured metabolite signal for T_1 and T_2 is then:

$$\hat{S}_m = \frac{S_m}{\frac{f_{GM}}{f_{GM}+f_{WM}}R_{GM}^m + \frac{f_{WM}}{f_{GM}+f_{WM}}R_{WM}^m} \quad (\text{C.7})$$

where R_{GM}^m and R_{WM}^m are the corresponding relaxation terms of Equation (C.5) using the tissue specific T_1 and T_2 relaxation rates of metabolite m . $S_m = \sum_k^K A_k^m$, the sum of the amplitudes of the metabolite as determined by the fitted prior-knowledge model.

C.2 Corrections for Number of Averages (N_{avg}), Number of MRS-visible ^1H Nuclei (ρ), and Gain/Scaling Factors (G)

In addition to corrections for T_1 and T_2 relaxation, the following corrections are applied to the measured water and metabolite signals:

1. A correction for the number of averages used to acquire the water signal
2. A correction for the number of MRS-visible ^1H nuclei in the water molecule

3. Corrections for any gain and scaling factors applied by the scanner and during post-processing

These corrections are applied as follows:

$$\hat{S}_W = \frac{S_W}{N_{\text{avg}}^W \rho^W G^W} \quad (\text{C.8})$$

$$\hat{S}_m = \frac{S_m}{N_{\text{avg}}^m \rho^m G^m} \quad (\text{C.9})$$

C.3 Summary of Corrections for the Measured Water Signal

Combining Equations (C.6) and (C.8), the final equation for the corrected water signal is:

$$\hat{S}_W = \frac{A_W}{N_{\text{avg}}^W \rho^W G^W (f_{GM} \alpha_{GM}^W R_{GM}^W + f_{WM} \alpha_{WM}^W R_{WM}^W + f_{CSF} \alpha_{CSF}^W R_{CSF}^W)} \quad (\text{C.10})$$

C.4 Summary of Corrections for the Measured Metabolite Signal

Combining Equations (C.7) and (C.9), the final equation for the corrected metabolite signal is:

$$\hat{S}_m = \frac{\sum_k^K A_k^m}{N_{\text{avg}}^m \rho^m G^m \left(\frac{f_{GM}}{f_{GM}+f_{WM}} R_{GM}^m + \frac{f_{WM}}{f_{GM}+f_{WM}} R_{WM}^m \right)} \quad (\text{C.11})$$

C.5 Metabolite Quantification Equations

C.5.1 Voxel Concentration

The equation to calculate the concentration of a metabolite with respect to the entire of the spectroscopic voxel volume is obtained by substituting Equations (C.10) and (C.11) into

Equation (C.1):

$$\begin{aligned}
 [M]_{\text{voxel}} = & \left(\frac{\sum_k^K A_k^m}{N_{\text{avg}}^m \rho^m G^m \left(\frac{f_{GM}}{f_{GM}+f_{WM}} R_{GM}^m + \frac{f_{WM}}{f_{GM}+f_{WM}} R_{WM}^m \right)} \right) \\
 & \times \left(\frac{A_W}{N_{\text{avg}}^W \rho^W G^W (f_{GM} \alpha_{GM}^W R_{GM}^W + f_{WM} \alpha_{WM}^W R_{WM}^W + f_{CSF} \alpha_{CSF}^W R_{CSF}^W)} \right)^{-1} \quad (\text{C.12}) \\
 & \times 55.14 \text{ M}
 \end{aligned}$$

Equation (C.12) may be simplified into:

$$\begin{aligned}
 [M]_{\text{voxel}} = & \underbrace{\left(\frac{\sum_k^K A_k^m}{A_W} \right)}_{\text{ratio of measured signals}} \times \underbrace{\left(\frac{f_{GM} \alpha_{GM}^W R_{GM}^W + f_{WM} \alpha_{WM}^W R_{WM}^W + f_{CSF} \alpha_{CSF}^W R_{CSF}^W}{\frac{f_{GM}}{f_{GM}+f_{WM}} R_{GM}^m + \frac{f_{WM}}{f_{GM}+f_{WM}} R_{WM}^m} \right)}_{\text{relaxation correction}} \quad (\text{C.13}) \\
 & \times \underbrace{\left(\frac{N_{\text{avg}}^W}{N_{\text{avg}}^m} \times \frac{\rho^W}{\rho^m} \times \frac{G^W}{G^m} \right)}_{\text{correction for number of averages, number of nuclei, and gain}} \times \underbrace{(55.14 \text{ M})}_{\text{concentration of pure water}}
 \end{aligned}$$

C.5.2 Tissue Concentration

With Equation (C.13), a metabolite concentration with respect to the entire volume of the spectroscopic voxel was found. To determine the concentration of the metabolite in brain tissue alone, the dilution equation can be applied:

$$\begin{aligned}
 c_{\text{tissue}} V_{\text{tissue}} &= c_{\text{voxel}} V_{\text{voxel}} \\
 c_{\text{tissue}} &= c_{\text{voxel}} \frac{V_{\text{voxel}}}{V_{\text{tissue}}} \\
 c_{\text{tissue}} &= c_{\text{voxel}} \frac{1}{f_{GM} + f_{WM}}
 \end{aligned}$$

Thus, the metabolite concentration in brain tissue is:

$$\begin{aligned}
 [M]_{\text{tissue}} = & \underbrace{\left(\frac{\sum_k^K A_k^m}{A_W} \right)}_{\text{ratio of measured signals}} \times \underbrace{\left(\frac{f_{GM}\alpha_{GM}^W R_{GM}^W + f_{WM}\alpha_{WM}^W R_{WM}^W + f_{CSF}\alpha_{CSF}^W R_{CSF}^W}{\frac{f_{GM}}{f_{GM}+f_{WM}} R_{GM}^m + \frac{f_{WM}}{f_{GM}+f_{WM}} R_{WM}^m} \right)}_{\text{relaxation correction}} \\
 & \times \underbrace{\left(\frac{N_{\text{avg}}^W}{N_{\text{avg}}^m} \times \frac{\rho^W}{\rho^m} \times \frac{G^W}{G^m} \right)}_{\text{correction for number of averages, number of nuclei, and gain}} \times \underbrace{(55.14 \text{ M})}_{\text{concentration of pure water}} \times \underbrace{\left(\frac{1}{f_{GM} + f_{WM}} \right)}_{\text{dilution volume correction}}
 \end{aligned} \tag{C.14}$$

Equation (C.14) can be simplified by multiplying the dilution volume correction through the relaxation correction term for the metabolite signal:

$$\begin{aligned}
 [M]_{\text{tissue}} = & \left(\frac{\sum_k^K A_k^m}{A_W} \right) \times \left(\frac{f_{GM}\alpha_{GM}^W R_{GM}^W + f_{WM}\alpha_{WM}^W R_{WM}^W + f_{CSF}\alpha_{CSF}^W R_{CSF}^W}{f_{GM}R_{GM}^m + f_{WM}R_{WM}^m} \right) \\
 & \times \left(\frac{N_{\text{avg}}^W}{N_{\text{avg}}^m} \times \frac{\rho^W}{\rho^m} \times \frac{G^W}{G^m} \right) \times (55.14 \text{ M})
 \end{aligned} \tag{C.15}$$

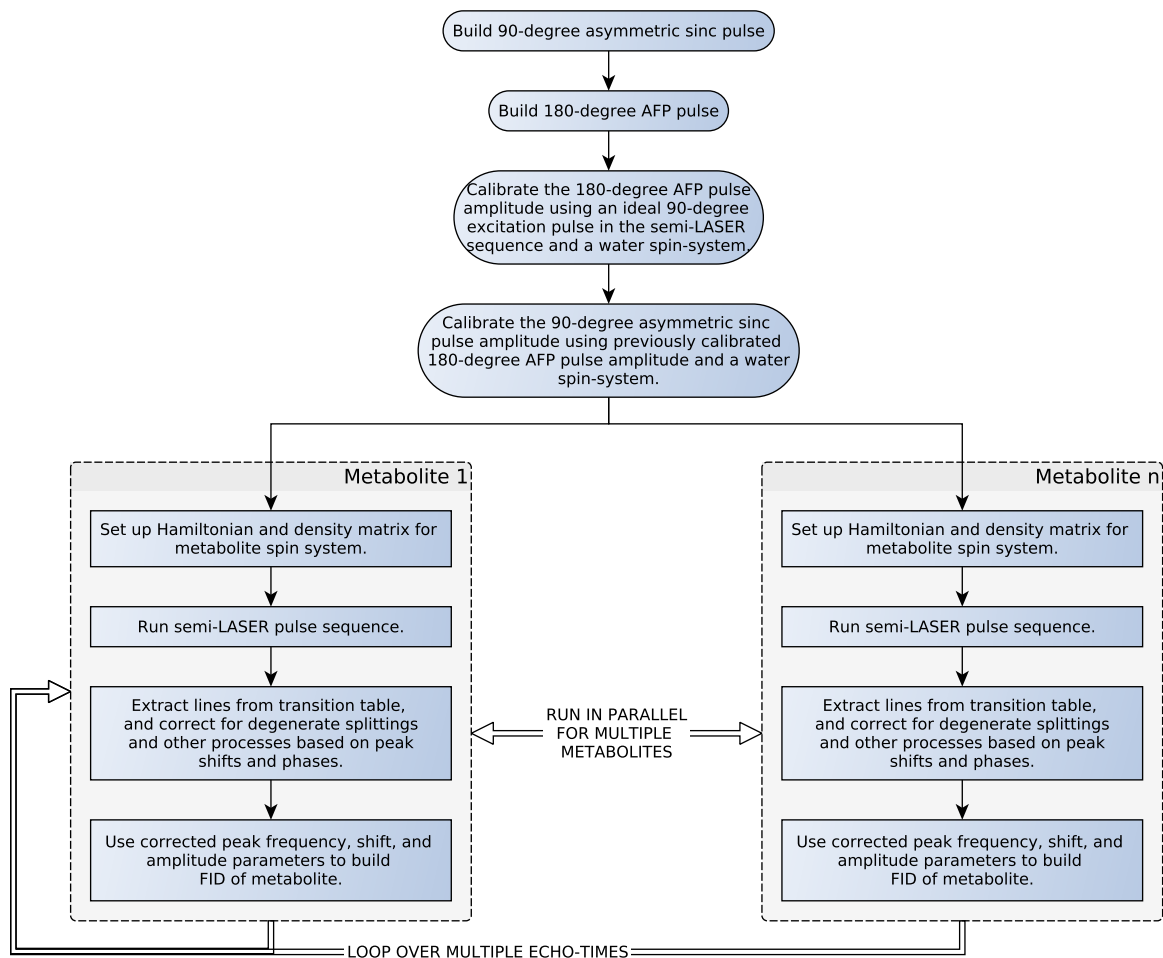
D

Metabolite Simulation Code

Simulated, echo-time-specific 7 T semi-LASER and 9.4 T LASER prior knowledge templates were used to fit the post-processed spectra. These prior knowledge templates were generated with Prior Information Templates (PINTS) software tool written by Dickson Wong. PINTS is part of the MRS Analysis, Generation, and In vivo Quantification (MAGIQ) software suite also written by Dickson Wong. The full code for the MAGIQ software suite is available on the Centre for Functional and Metabolic Mapping's Gitlab Server (<https://git.cfmm.robarts.ca/bartha-lab/MAGIQ>). It will be publicly available as open-source software in the future.

The code relies on the PyGAMMA library of the VeSPA software suite (<https://scion.duhs.duke.edu/vespa/gamma/wiki/PyGamma>) to model the spectra. Using the PyGAMMA library directly instead of using the VeSPA Suite graphical user interface allowed the exact replication of RF pulse shapes from the scanner, the running of calibration experiments for the RF pulses, and the looping over multiple metabolites and echo-times within a single Python program.

Below is a flowchart that provides a high-level description of how the simulated prior knowledge templates were generated.



Also included below is the code for the `MetaboliteSimulation` class used to define a simulation for each metabolite. This code and the annotations should be sufficient for a reader to understand how to set up a simulation, define a pulse sequence, and obtain simulation results using PyGAMMA.

```

import sys
import os
import datetime
5 import time
import glob
import platform
from PyQt5 import QtCore, QtGui, QtWidgets, uic
import subprocess as subprocess
10 import multiprocessing as mp
from collections import defaultdict
from itertools import groupby

import scipy as sp
import scipy.signal as spsg
import numpy as np
import math
from pyfftw.interfaces import scipy_fftpack as fftw
20

import pygamma as pg

from dataclasses import *

class MetaboliteSimulation(QtCore.QObject):
30
    postToConsole = QtCore.pyqtSignal(str)
    outputResults = QtCore.pyqtSignal(object)
    finished = QtCore.pyqtSignal(int)

    def __init__(self, thread_num, insysfile,
        ↪ sim_experiment):
35
        QtCore.QObject.__init__(self)

        self.thread_num = thread_num
        self.insysfile = insysfile
40 self.sim_experiment = sim_experiment

    def simulate(self):
        self.postToConsole.emit(' | Simulating ...
            ↪ ' + self.insysfile)

45
        metab_name = self.insysfile.replace('.sys', '')
            ↪ )

        if self.sim_experiment.b0 == 123.3:
            self.insysfile = 'pints/metabolites/3T_'
                ↪ + self.insysfile
50 elif self.sim_experiment.b0 == 297.2:
            self.insysfile = 'pints/metabolites/7T_'
                ↪ + self.insysfile

```

Import system libraries.

Import math libraries.

Import PyGAMMA for metabolite simulations.

Import custom data classes.

Define the simulation class.

Retrieve the appropriate spin-system definition according to field strength.

Define the semi-LASER pulse sequence.

Load in the current spin-system.

Specify the echo-time-dependent parameters to be used to define delays between RF pulses.

Build a 90-degree excitation pulse from a Siemens *.pta file.

```

elif self.sim_experiment.b0 == 400.2:
    self.insysfile = 'pints/metabolites/9.4
        ↳ T_' + self.insysfile

55     if self.sim_experiment.name == "semi-LASER":

        spin_system = pg.spin_system()
        spin_system.read(self.insysfile)
        for i in range(spin_system.spins()):
            spin_system.PPM(i, spin_system.PPM(
                ↳ i) - self.sim_experiment.
                ↳ RF_OFFSET)

60

        TE = self.sim_experiment.TE
        TE1 = float((TE * 0.31) / 1000.0)
        TE3 = float((TE * 0.31) / 1000.0)
        TE2 = float(TE/1000.0 - TE1 - TE3)
        TE_fill = TE/1000.0 - TE1 - TE2 - TE3

65

70     inpulse90file = self.sim_experiment.
        ↳ inpulse90file
        A_90 = self.sim_experiment.A_90
        PULSE_90_LENGTH = self.sim_experiment.
        ↳ PULSE_90_LENGTH
        gyratio = self.sim_experiment.getGyratio
        ↳ ()

75     pulse90 = Pulse(inpulse90file,
        ↳ PULSE_90_LENGTH)

    n_old = np.linspace(0, PULSE_90_LENGTH,
        ↳ 255)
    n_new = np.linspace(0, PULSE_90_LENGTH,
        ↳ 256)

80     waveform_real = sp.interpolate.
        ↳ InterpolatedUnivariateSpline(
        ↳ n_old, np.real(pulse90.waveform)*
        ↳ A_90)(n_new)
    waveform_imag = sp.interpolate.
        ↳ InterpolatedUnivariateSpline(
        ↳ n_old, np.imag(pulse90.waveform)*
        ↳ A_90)(n_new)
    pulse90.waveform = waveform_real + 1j*(
        ↳ waveform_imag)

85     ampl_arr = np.abs(pulse90.waveform)*
        ↳ gyratio
    phas_arr = np.unwrap(np.angle(pulse90.
        ↳ waveform))*180.0/math.pi

    pulse = pg.row_vector(len(pulse90.
        ↳ waveform))
    ptime = pg.row_vector(len(pulse90.
        ↳ waveform))

```



```

90     for j, val in enumerate(zip(ampl_arr,
    ↪ phas_arr)):
        pulse.put(pg.complex(val[0],val[1])
    ↪ , j)
        ptime.put(pg.complex(pulse90.
    ↪ pulsestep,0), j)

    pulse_dur_90 = pulse.size() * pulse90.
    ↪ pulsestep
95    peak_to_end_90 = pulse_dur_90 - (209 +
    ↪ self.sim_experiment.fudge_factor)
    ↪ * pulse90.pulsestep
    pwf_90 = pg.PulWaveform(pulse, ptime, "
    ↪ 90excite")
    pulc_90 = pg.PulComposite(pwf_90,
    ↪ spin_system, self.sim_experiment.
    ↪ obs_iso)

100    Ureal90 = pulc_90.GetUsum(-1)

    inpulse180file = self.sim_experiment.
    ↪ inpulse180file
    A_180 = self.sim_experiment.A_180
105    PULSE_180_LENGTH = self.sim_experiment.
    ↪ PULSE_180_LENGTH
    gyratio = self.sim_experiment.getGyratio
    ↪ ()

    pulse180 = Pulse(inpulse180file,
    ↪ PULSE_180_LENGTH)

110    n_old = np.linspace(0, PULSE_180_LENGTH,
    ↪ 511)
    n_new = np.linspace(0, PULSE_180_LENGTH,
    ↪ 512)

    waveform_real = sp.interpolate.
    ↪ InterpolatedUnivariateSpline(
    ↪ n_old, np.real(pulse180.waveform)
    ↪ *A_180)(n_new)
    waveform_imag = sp.interpolate.
    ↪ InterpolatedUnivariateSpline(
    ↪ n_old, np.imag(pulse180.waveform)
    ↪ *A_180)(n_new)
115    pulse180.waveform = waveform_real + 1j*(
    ↪ waveform_imag)

    ampl_arr = np.abs(pulse180.waveform)*
    ↪ gyratio
    phas_arr = np.unwrap(np.angle(pulse180.
    ↪ waveform))*180.0/math.pi
    freq_arr = np.gradient(phas_arr)

120    pulse = pg.row_vector(len(pulse180.
    ↪ waveform))

```

Define the propagator for the 90-degree pulse.

Build a AFP pulse from a Siemens *.pta file.

	125	<pre> ptime = pg.row_vector(len(pulse180. ↪ waveform)) for j, val in enumerate(zip(ampl_arr, ↪ phas_arr)): pulse.put(pg.complex(val[0],val[1]) ↪ , j) ptime.put(pg.complex(n_new[1],0), j ↪) pulse_dur_180 = pulse.size() * pulse180. ↪ pulsestep pwf_180 = pg.PulWaveform(pulse, ptime, " ↪ 180afp") pulc_180 = pg.PulComposite(pwf_180, ↪ spin_system, self.sim_experiment. ↪ obs_iso) </pre>
Define the propagator for the AFP pulse.	130	<pre> Ureal180 = pulc_180.GetUsum(-1) </pre>
Initialize the Hamiltonian and density operator matrix for the current spin system.	135	<pre> H = pg.Hcs(spin_system) + pg.HJ(↪ spin_system) D = pg.Fm(spin_system, self. ↪ sim_experiment.obs_iso) ac = pg.acquire1D(pg.gen_op(D), H, self. ↪ sim_experiment.dwell_time) ACQ = ac </pre>
Define the delays between RF pulses using echo-time-dependent parameters.	140	<pre> delay1 = TE1/2.0 + TE_fill/8.0 ↪ - ↪ pulse_dur_180/2.0 - ↪ peak_to_end_90 delay2 = TE1/2.0 + TE_fill/8.0 + TE2/4.0 ↪ + TE_fill/8.0 - pulse_dur_180 delay3 = TE2/4.0 + TE_fill/8.0 + TE2/4.0 ↪ + TE_fill/8.0 - pulse_dur_180 delay4 = TE2/4.0 + TE_fill/8.0 + TE3/2.0 ↪ + TE_fill/8.0 - pulse_dur_180 delay5 = TE3/2.0 + TE_fill/8.0 ↪ - ↪ pulse_dur_180/2.0 </pre>
Define the propagators for each delay period.	150	<pre> Udelay1 = pg.prop(H, delay1) Udelay2 = pg.prop(H, delay2) Udelay3 = pg.prop(H, delay3) Udelay4 = pg.prop(H, delay4) Udelay5 = pg.prop(H, delay5) </pre>
Apply RF pulse propagators and delay propagators in the appropriate sequence to "run the semi-LASER pulse sequence."	155	<pre> sigma0 = pg.sigma_eq(spin_system) # ↪ init sigma1 = Ureal90.evolve(sigma0) ↪ # apply 90-degree pulse sigma0 = pg.evolve(sigma1, Udelay1) </pre>

```

160         sigma1 = Ureal180.evolve(sigma0) #
            ↳ apply AFP1
        sigma0 = pg.evolve(sigma1, Udelay2)
        sigma1 = Ureal180.evolve(sigma0) #
            ↳ apply AFP2
        sigma0 = pg.evolve(sigma1, Udelay3)
        sigma1 = Ureal180.evolve(sigma0) #
            ↳ apply AFP3
        sigma0 = pg.evolve(sigma1, Udelay4)
        sigma1 = Ureal180.evolve(sigma0) #
            ↳ apply AFP4
165         sigma0 = pg.evolve(sigma1, Udelay5)

elif self.sim_experiment.name == "LASER":

    spin_system = pg.spin_system()
    spin_system.read(self.insysfile)
    for i in range(spin_system.spins()):
        spin_system.PPM(i, spin_system.PPM(
            ↳ i) - self.sim_experiment.
            ↳ RF_OFFSET)

    inpulse90file = self.sim_experiment.
        ↳ inpulse90file
    A_90 = self.sim_experiment.A_90
    PULSE_90_LENGTH = self.sim_experiment.
        ↳ PULSE_90_LENGTH
    gyratio = self.sim_experiment.getGyratio
        ↳ ()

    pulse90 = Pulse(inpulse90file,
        ↳ PULSE_90_LENGTH, 'varian')

    n_new = np.linspace(0, PULSE_90_LENGTH,
        ↳ 256)

    waveform_real = np.real(pulse90.waveform
        ↳ )*A_90
    waveform_imag = np.imag(pulse90.waveform
        ↳ )*A_90
    pulse90.waveform = waveform_real + 1j*(
        ↳ waveform_imag)

    ampl_arr = np.abs(pulse90.waveform)*
        ↳ gyratio
    phas_arr = np.unwrap(np.angle(pulse90.
        ↳ waveform))*180.0/math.pi

    pulse = pg.row_vector(len(pulse90.
        ↳ waveform))
    ptime = pg.row_vector(len(pulse90.
        ↳ waveform))
    for j, val in enumerate(zip(ampl_arr,
        ↳ phas_arr)):
195         pulse.put(pg.complex(val[0], val[1])
            ↳ , j)

```

Define the
LASER pulse
sequence.

Load in the
current spin-
system.

Build the AHP
pulse.

Define the propagator for the AHP pulse.

Build the AFP pulse.

```

        ptime.put(pg.complex(pulse90.
            ↪ pulsestep,0), j)

    pulse_dur_90 = pulse.size() * pulse90.
        ↪ pulsestep
    pwf_90 = pg.PulWaveform(pulse, ptime, "
        ↪ 90excite")
    pulc_90 = pg.PulComposite(pwf_90,
        ↪ spin_system, self.sim_experiment.
        ↪ obs_iso)

    Ureal90 = pulc_90.GetUsum(-1)

    inpulse180file = self.sim_experiment.
        ↪ inpulse180file
    A_180 = self.sim_experiment.A_180
    PULSE_180_LENGTH = self.sim_experiment.
        ↪ PULSE_180_LENGTH
    gyratio = self.sim_experiment.getGyratio
        ↪ ()

    pulse180 = Pulse(inpulse180file,
        ↪ PULSE_180_LENGTH, 'varian')

    n_new = np.linspace(0, PULSE_180_LENGTH,
        ↪ 512)

    waveform_real = np.real(pulse180.
        ↪ waveform)*A_180
    waveform_imag = np.imag(pulse180.
        ↪ waveform)*A_180
    pulse180.waveform = waveform_real + 1j*(
        ↪ waveform_imag)

    ampl_arr = np.abs(pulse180.waveform)*
        ↪ gyratio
    phas_arr = np.unwrap(np.angle(pulse180.
        ↪ waveform))*180.0/math.pi
    freq_arr = np.gradient(phas_arr)

    pulse = pg.row_vector(len(pulse180.
        ↪ waveform))
    ptime = pg.row_vector(len(pulse180.
        ↪ waveform))
    for j, val in enumerate(zip(ampl_arr,
        ↪ phas_arr)):
        pulse.put(pg.complex(val[0],val[1])
            ↪ , j)
        ptime.put(pg.complex(n_new[1],0), j
            ↪ )

    pulse_dur_180 = pulse.size() * pulse180.
        ↪ pulsestep
    pwf_180 = pg.PulWaveform(pulse, ptime, "
        ↪ 180afp")

```

Appendix D. Metabolite Simulation Code

```

235     pulc_180 = pg.PulComposite(pwf_180,
        ↪ spin_system, self.sim_experiment.
        ↪ obs_iso)

    Ureal180 = pulc_180.GetUsum(-1)

240     ROF1 = 100E-6 #sec
    ROF2 = 10E-6 #sec
    TCRUSH1 = 0.0008 #sec
    TCRUSH2 = 0.0008 #sec

    ss_grad_rfDelayFront = 0#TCRUSH1 - ROF1
    ss_grad_rfDelayBack = 0#TCRUSH2 - ROF2
    ro_grad_atDelayFront = 0
    ro_grad_atDelayBack = 0

    TE = self.sim_experiment.TE / 1000.
    ipd = (TE - pulse_dur_90 \
        - 6*(ss_grad_rfDelayFront +
        ↪ pulse_dur_180 +
        ↪ ss_grad_rfDelayBack)
        ↪ \
250         - ro_grad_atDelayFront) / 12

    delay1 = ipd + ss_grad_rfDelayFront
    delay2 = ss_grad_rfDelayBack + 2*ipd +
        ↪ ss_grad_rfDelayFront
    delay3 = ss_grad_rfDelayBack + 2*ipd +
        ↪ ss_grad_rfDelayFront
    delay4 = ss_grad_rfDelayBack + 2*ipd +
        ↪ ss_grad_rfDelayFront
    delay5 = ss_grad_rfDelayBack + 2*ipd +
        ↪ ss_grad_rfDelayFront
    delay6 = ss_grad_rfDelayBack + 2*ipd +
        ↪ ss_grad_rfDelayFront
    delay7 = ss_grad_rfDelayBack + ipd +
        ↪ ro_grad_atDelayFront

260     H = pg.Hcs(spin_system) + pg.HJ(
        ↪ spin_system)
    D = pg.Fm(spin_system, self.
        ↪ sim_experiment.obs_iso)
    ac = pg.acquire1D(pg.gen_op(D), H, self.
        ↪ sim_experiment.dwell_time)
    ACQ = ac

265     Udelay1 = pg.prop(H, delay1)
    Udelay2 = pg.prop(H, delay2)
    Udelay3 = pg.prop(H, delay1)
    Udelay4 = pg.prop(H, delay4)
    Udelay5 = pg.prop(H, delay5)
    Udelay6 = pg.prop(H, delay6)
    Udelay7 = pg.prop(H, delay7)
270

```

Define the propagator for the AFP pulse.

Calculate the pulse timings.

Define the delays between RF pulses.

Initialize the Hamiltonian and density operator matrix for the current spin system.

Define the propagators for each delay period.

Apply RF pulse propagators and delay propagators in the appropriate sequence to “run the LASER pulse sequence”.

Extract lines from the transition table.

Using a binning procedure to correct for degenerate splittings and other processes based on peak shifts and phases.

```

275 sigma0 = pg.sigma_eq(spin_system) #
      ↪ init
      sigma1 = Ureal90.evolve(sigma0)
      ↪ # apply 90-degree pulse
280 sigma0 = pg.evolve(sigma1, Udelay1)
      sigma1 = Ureal180.evolve(sigma0) #
      ↪ apply AFP1
      sigma0 = pg.evolve(sigma1, Udelay2)
      sigma1 = Ureal180.evolve(sigma0) #
      ↪ apply AFP2
      sigma0 = pg.evolve(sigma1, Udelay3)
      sigma1 = Ureal180.evolve(sigma0) #
      ↪ apply AFP3
285 sigma0 = pg.evolve(sigma1, Udelay4)
      sigma1 = Ureal180.evolve(sigma0) #
      ↪ apply AFP4
      sigma0 = pg.evolve(sigma1, Udelay5)
      sigma1 = Ureal180.evolve(sigma0) #
      ↪ apply AFP5
290 sigma0 = pg.evolve(sigma1, Udelay6)
      sigma1 = Ureal180.evolve(sigma0) #
      ↪ apply AFP6
      sigma0 = pg.evolve(sigma1, Udelay7)

295 mx = pg.TTable1D(ACQ.table(sigma0))

300 # BINNING
      # Note: Metabolite Peak Normalization and
      ↪ Blending

      # The transition tables calculated by the
      ↪ GAMMA density matrix simulations
      ↪ frequently contain a
      # large number of transitions caused by
      ↪ degenerate splittings and other
      ↪ processes. At the
      # conclusion of each simulation run a routine
      ↪ is called to extract lines from the
      ↪ transition table.
      # These lines are then normalized using a
      ↪ closed form calculation based on the
      ↪ number of spins.
      # To reduce the number of lines required for
      ↪ display, multiple lines are blended by
      ↪ binning them
305 # together based on their PPM locations and
      ↪ phases. The following parameters are
      ↪ used to
      # customize these procedures:

      # Peak Search Range -- Low/High (PPM): the
      ↪ range in PPM that is searched for
      ↪ lines from the
      # metabolite simulation.

```

```

310     # Peak Blending Tolerance (PPM and Degrees):
        ↳ the width of the bins (+/- in PPM and
        ↳ +/- in
    # PhaseDegrees) that are used to blend the
        ↳ lines in the simulation. Lines that
        ↳ are included in the
    # same bin are summed using complex addition
        ↳ based on Amplitude and Phase.

315     b0 = self.sim_experiment.b0
    obs_iso = self.sim_experiment.obs_iso
    tolppm = self.sim_experiment.tolppm
    tolpha = self.sim_experiment.tolpha
320     ppmlo = self.sim_experiment.ppmlo
    ppmhi = self.sim_experiment.ppmhi
    rf_off = self.sim_experiment.RF_OFFSET

    field = b0
    nspins = spin_system.spins()

325     nlines = mx.size()

    tmp = pg.Isotope(obs_iso)
    obs_qn = tmp.qn()

330     qnscale = 1.0
    for i in range(nspins):
        qnscale *= 2*spin_system.qn(i)+1
    qnscale = qnscale / (2.0 * (2.0*obs_qn+1))

335     freqs = []
    outf = []
    outa = []
    outp = []
340     nbin = 0
    found = False

    PI = 3.14159265358979323846
    RAD2DEG = 180.0/PI

345     indx = mx.Sort(0,-1,0)

    for i in range(nlines):
        freqs.append(-1 * mx.Fr(indx[i])/(2.0*PI
            ↳ *field))

350     for i in range(nlines):
        freq = freqs[i]
        if (freq > ppmlo) and (freq < ppmhi):
            val = mx.I(indx[i])
            tmpa = np.sqrt(val.real()**2 + val.
355                ↳ imag()**2) / qnscale
            tmpp = -RAD2DEG * np.angle(val.real
                ↳ ()+1j*val.imag())

            if nbin == 0:
                outf.append(freq)

```

```

360         outa.append(tmpa)
        outp.append(tmpp)
        nbin += 1
    else:
        for k in range(nbin):
365             if (freq >= outf[k]-tolppm)
                ↳ and (freq <= outf[k]+
                ↳ tolppm):
                    if (tmpp >= outp[k]-
                        ↳ tolpha) and (tmpp
                        ↳ <= outp[k]+tolpha)
                        ↳ :
                        ampsum = outa[k]+
                            ↳ tmpa
                        outf[k] = (outa[k]*
                            ↳ outf[k] +
                            ↳ tmpa*freq)/
                            ↳ ampsum
                        outp[k] = (outa[k]*
                            ↳ outp[k] +
                            ↳ tmpa*tmpp)/
                            ↳ ampsum
                        outa[k] += tmpa;
                        found = True

                    if not found:
                        outf.append(freq)
                        outa.append(tmpa)
375                        outp.append(tmpp)
                        nbin += 1
                        found = False

    for i, item in enumerate(outf):
380        outf[i] = item + rf_off
        outp[i] = outp[i] - 90.0

    metab = Metabolite()
385    metab.name = metab_name
    metab.var = 0.0

    for i in range(sp.size(outf)):
        if outf[i] <= 5:
390            metab.ppm.append(outf[i])
            metab.area.append(outa[i])
            metab.phase.append(-1.0*outp[i])

    insysfile = self.insysfile.replace('pints/
        ↳ metabolites/3T_', '')
395    insysfile = self.insysfile.replace('pints/
        ↳ metabolites/7T_', '')
    insysfile = self.insysfile.replace('pints/
        ↳ metabolites/9.4T_', '')

    if insysfile == 'alanine.sys': #
400        metab.A_m = 0.078
        metab.T2 = (87E-3)
    elif insysfile == 'aspartate.sys':

```

Create a new metabolite object using simulated shifts, amplitudes, and phases.

Apply default scaling factors and T2 values. These values are not set in stone; they may be changed by other programs in the MAGIQ software suite.


```

    metab.A_m = 0.117
    metab.T2 = (87E-3)
405 elif insysfile == 'choline_1-CH2_2-CH2.sys':
    ↪ #
    metab.A_m = 0.165
    metab.T2 = (87E-3)
    elif insysfile == 'choline_N(CH3)3_a.sys' or
    ↪ insysfile == 'choline_N(CH3)3_b.sys':
    ↪ #
    metab.A_m = 0.165
410 metab.T2 = (121E-3)
    elif insysfile == 'creatine_N(CH3).sys':
    metab.A_m = 0.296
    metab.T2 = (90E-3)
    elif insysfile == 'creatine_X.sys':
415 metab.A_m = 0.296
    metab.T2 = (81E-3)
    elif insysfile == 'd-glucose-alpha.sys': #
    metab.A_m = 0.049
    metab.T2 = (87E-3)
420 elif insysfile == 'd-glucose-beta.sys': #
    metab.A_m = 0.049
    metab.T2 = (87E-3)
    elif insysfile == 'eth.sys': #
    metab.A_m = 0.320
425 metab.T2 = (87E-3)
    elif insysfile == 'gaba.sys': #
    metab.A_m = 0.155
    metab.T2 = (82E-3)
    elif insysfile == 'glutamate.sys':
430 metab.A_m = 0.898
    metab.T2 = (88E-3)
    elif insysfile == 'glutamine.sys':
    metab.A_m = 0.427
    metab.T2 = (87E-3)
435 elif insysfile == 'glutathione_cysteine.sys':
    metab.A_m = 0.194
    metab.T2 = (87E-3)
    elif insysfile == 'glutathione_glutamate.sys'
    ↪ :
    metab.A_m = 0.194
440 metab.T2 = (87E-3)
    elif insysfile == 'glutathione_glycine.sys':
    metab.A_m = 0.194
    metab.T2 = (87E-3)
    elif insysfile == 'glycine.sys':
445 metab.A_m = 0.068
    metab.T2 = (87E-3)
    elif insysfile == 'gpc_7-CH2_8-CH2.sys': #
    metab.A_m = 0.097
    metab.T2 = (87E-3)
450 elif insysfile == 'gpc_glycerol.sys': #
    metab.A_m = 0.097
    metab.T2 = (87E-3)
    elif insysfile == 'gpc_N(CH3)3_a.sys': #
    metab.A_m = 0.097
455 metab.T2 = (121E-3)
    elif insysfile == 'gpc_N(CH3)3_b.sys': #

```

```

        metab.A_m = 0.097
        metab.T2 = (121E-3)
460     elif insysfile == 'lactate.sys': #
        metab.A_m = 0.039
        metab.T2 = (87E-3)
        elif insysfile == 'myoinositol.sys':
        metab.A_m = 0.578
        metab.T2 = (87E-3)
465     elif insysfile == 'naa_acetyl.sys':
        metab.A_m = 1.000
        metab.T2 = (130E-3)
        elif insysfile == 'naa_aspartate.sys':
        metab.A_m = 1.000
        metab.T2 = (69E-3)
470     elif insysfile == 'naag_acetyl.sys':
        metab.A_m = 0.160
        metab.T2 = (130E-3)
        elif insysfile == 'naag_aspartyl.sys':
        metab.A_m = 0.160
        metab.T2 = (87E-3)
        elif insysfile == 'naag_glutamate.sys':
        metab.A_m = 0.160
        metab.T2 = (87E-3)
480     elif insysfile == 'pcho_N(CH3)3_a.sys': #
        metab.A_m = 0.058
        metab.T2 = (121E-3)
        elif insysfile == 'pcho_N(CH3)3_b.sys': #
        metab.A_m = 0.058
        metab.T2 = (121E-3)
485     elif insysfile == 'pcho_X.sys': #
        metab.A_m = 0.058
        metab.T2 = (87E-3)
        elif insysfile == 'pcr_N(CH3).sys':
        metab.A_m = 0.422
        metab.T2 = (90E-3)
490     elif insysfile == 'pcr_X.sys':
        metab.A_m = 0.422
        metab.T2 = (81E-3)
        elif insysfile == 'peth.sys':
        metab.A_m = 0.126
        metab.T2 = (87E-3)
495     elif insysfile == 'scyllo-inositol.sys':
        metab.A_m = 0.044
        metab.T2 = (87E-3)
500     elif insysfile == 'taurine.sys':
        metab.A_m = 0.117
        metab.T2 = (85E-3)
        elif insysfile == 'water.sys':
        metab.A_m = 1.000
        metab.T2 = (43.60E-3)
505

    # Send save data signal
    self.outputResults.emit(metab)
    self.postToConsole.emit('          | Simulation
    ↳ completed for ... ' + self.insysfile)
    self.finished.emit(self.thread_num)

```

D.1 Spin System Definitions

The simulation code above loads in information about the spin system from an `insysfile`. The `insysfile` is simply a text file that contains the peak shifts and J-coupling constants for a particular metabolite formatted in a way that PyGAMMA expects. An example of an `insysfile` is given below:

```

SysName (2) : gaba
NSpins (0) : 6
Iso(0) (2) : 1H
Iso(1) (2) : 1H
5 Iso(2) (2) : 1H
Iso(3) (2) : 1H
Iso(4) (2) : 1H
Iso(5) (2) : 1H
10 PPM(0) (1) : 2.2840
PPM(1) (1) : 2.2840
PPM(2) (1) : 1.8880
PPM(3) (1) : 1.8880
PPM(4) (1) : 3.0130
PPM(5) (1) : 3.0130
15 J(0,1) (1) : -15.938
J(0,2) (1) : 7.678
J(0,3) (1) : 6.980
J(0,4) (1) : 0.0
J(0,5) (1) : 0.0
20 J(1,2) (1) : 6.980
J(1,3) (1) : 7.678
J(1,4) (1) : 0.0
J(1,5) (1) : 0.0
J(2,3) (1) : -15.000
25 J(2,4) (1) : 8.510
J(2,5) (1) : 6.503
J(3,4) (1) : 6.503
J(3,5) (1) : 8.510
J(4,5) (1) : -14.062
30 Omega (1) : 297.2
```

D.2 RF Pulse Definitions

The simulation code above builds the RF pulses used in the semi-LASER sequence from Siemens *.pta files. These *.pta files are included below.

D.2.1 90-degree Excitation Pulse

```

PULSENAME:      P10.P10NORM
COMMENT:  Asymmetric amplitude modulated RF pulse - BW = 6.77/length, gamma*B1 power
    ↪ for 1ms 90deg = 1.67 kHz, asym factor = 0.23
REFGRAD:  3.105550000
MINSLICE:  1.000000000
5  MAXSLICE: 400.000000000
  AMPINT:   38.391006745
  POWERINT: 35.910179272
  ABSINT:   57.869012713

10 0.001955034      0.000000000      ; (0)
   0.001955034      0.000000000      ; (1)
   0.002932551      0.000000000      ; (2)
   0.002932551      0.000000000      ; (3)
   0.002932551      0.000000000      ; (4)
15 0.003910068      0.000000000      ; (5)
   0.003910068      0.000000000      ; (6)
   0.004887586      0.000000000      ; (7)
   0.004887586      0.000000000      ; (8)
   0.004887586      0.000000000      ; (9)
20 0.005865103      0.000000000      ; (10)
   0.005865103      0.000000000      ; (11)
   0.006842620      0.000000000      ; (12)
   0.006842620      0.000000000      ; (13)
   0.006842620      0.000000000      ; (14)
25 0.007820137      0.000000000      ; (15)
   0.007820137      0.000000000      ; (16)
   0.007820137      0.000000000      ; (17)
   0.007820137      0.000000000      ; (18)
   0.008797654      0.000000000      ; (19)
30 0.008797654      0.000000000      ; (20)
   0.008797654      0.000000000      ; (21)
   0.008797654      0.000000000      ; (22)
   0.008797654      0.000000000      ; (23)
   0.008797654      0.000000000      ; (24)
35 0.008797654      0.000000000      ; (25)
   0.008797654      0.000000000      ; (26)
   0.007820137      0.000000000      ; (27)
   0.007820137      0.000000000      ; (28)
   0.007820137      0.000000000      ; (29)
40 0.006842620      0.000000000      ; (30)
   0.006842620      0.000000000      ; (31)
   0.005865103      0.000000000      ; (32)
   0.004887586      0.000000000      ; (33)
   0.004887586      0.000000000      ; (34)
45 0.003910068      0.000000000      ; (35)

```

D.2. RF Pulse Definitions

	0.002932551	0.000000000	; (36)
	0.001955034	0.000000000	; (37)
	0.000977517	0.000000000	; (38)
	0.000000000	3.141592741	; (39)
50	0.001955034	3.141592741	; (40)
	0.002932551	3.141592741	; (41)
	0.003910068	3.141592741	; (42)
	0.005865103	3.141592741	; (43)
	0.006842620	3.141592741	; (44)
55	0.008797654	3.141592741	; (45)
	0.009775171	3.141592741	; (46)
	0.011730205	3.141592741	; (47)
	0.013685239	3.141592741	; (48)
	0.014662757	3.141592741	; (49)
60	0.016617792	3.141592741	; (50)
	0.018572824	3.141592741	; (51)
	0.020527858	3.141592741	; (52)
	0.021505376	3.141592741	; (53)
	0.023460411	3.141592741	; (54)
65	0.024437929	3.141592741	; (55)
	0.026392963	3.141592741	; (56)
	0.028347995	3.141592741	; (57)
	0.029325513	3.141592741	; (58)
	0.030303029	3.141592741	; (59)
70	0.031280547	3.141592741	; (60)
	0.033235583	3.141592741	; (61)
	0.033235583	3.141592741	; (62)
	0.034213100	3.141592741	; (63)
	0.035190616	3.141592741	; (64)
75	0.035190616	3.141592741	; (65)
	0.036168132	3.141592741	; (66)
	0.036168132	3.141592741	; (67)
	0.035190616	3.141592741	; (68)
	0.035190616	3.141592741	; (69)
80	0.034213100	3.141592741	; (70)
	0.033235583	3.141592741	; (71)
	0.032258064	3.141592741	; (72)
	0.031280547	3.141592741	; (73)
	0.029325513	3.141592741	; (74)
85	0.027370479	3.141592741	; (75)
	0.025415445	3.141592741	; (76)
	0.022482892	3.141592741	; (77)
	0.019550342	3.141592741	; (78)
	0.016617792	3.141592741	; (79)
90	0.013685239	3.141592741	; (80)
	0.009775171	3.141592741	; (81)
	0.005865103	3.141592741	; (82)
	0.001955034	3.141592741	; (83)
	0.001955034	0.000000000	; (84)
95	0.006842620	0.000000000	; (85)
	0.011730205	0.000000000	; (86)
	0.016617792	0.000000000	; (87)
	0.021505376	0.000000000	; (88)
	0.026392963	0.000000000	; (89)
100	0.031280547	0.000000000	; (90)
	0.037145648	0.000000000	; (91)
	0.043010753	0.000000000	; (92)
	0.047898337	0.000000000	; (93)
	0.053763442	0.000000000	; (94)
105	0.059628543	0.000000000	; (95)
	0.064516127	0.000000000	; (96)

Appendix D. Metabolite Simulation Code

	0.070381232	0.000000000	; (97)
	0.075268820	0.000000000	; (98)
	0.080156401	0.000000000	; (99)
110	0.085043989	0.000000000	; (100)
	0.089931577	0.000000000	; (101)
	0.094819158	0.000000000	; (102)
	0.098729230	0.000000000	; (103)
	0.102639295	0.000000000	; (104)
115	0.105571851	0.000000000	; (105)
	0.108504400	0.000000000	; (106)
	0.110459432	0.000000000	; (107)
	0.112414464	0.000000000	; (108)
	0.114369504	0.000000000	; (109)
120	0.115347020	0.000000000	; (110)
	0.115347020	0.000000000	; (111)
	0.115347020	0.000000000	; (112)
	0.113391981	0.000000000	; (113)
	0.112414464	0.000000000	; (114)
125	0.109481916	0.000000000	; (115)
	0.106549367	0.000000000	; (116)
	0.102639295	0.000000000	; (117)
	0.097751714	0.000000000	; (118)
	0.092864126	0.000000000	; (119)
130	0.086021505	0.000000000	; (120)
	0.079178885	0.000000000	; (121)
	0.071358748	0.000000000	; (122)
	0.062561095	0.000000000	; (123)
	0.053763442	0.000000000	; (124)
135	0.043988269	0.000000000	; (125)
	0.033235583	0.000000000	; (126)
	0.021505376	0.000000000	; (127)
	0.009775171	0.000000000	; (128)
	0.002932551	3.141592741	; (129)
140	0.016617792	3.141592741	; (130)
	0.030303029	3.141592741	; (131)
	0.043988269	3.141592741	; (132)
	0.058651026	3.141592741	; (133)
	0.073313780	3.141592741	; (134)
145	0.087976538	3.141592741	; (135)
	0.103616811	3.141592741	; (136)
	0.119257085	3.141592741	; (137)
	0.133919850	3.141592741	; (138)
	0.149560124	3.141592741	; (139)
150	0.165200397	3.141592741	; (140)
	0.179863155	3.141592741	; (141)
	0.194525898	3.141592741	; (142)
	0.208211139	3.141592741	; (143)
	0.221896380	3.141592741	; (144)
155	0.235581622	3.141592741	; (145)
	0.247311831	3.141592741	; (146)
	0.259042025	3.141592741	; (147)
	0.269794732	3.141592741	; (148)
	0.279569894	3.141592741	; (149)
160	0.287390023	3.141592741	; (150)
	0.295210153	3.141592741	; (151)
	0.301075280	3.141592741	; (152)
	0.305962861	3.141592741	; (153)
	0.308895409	3.141592741	; (154)
165	0.310850441	3.141592741	; (155)
	0.310850441	3.141592741	; (156)
	0.308895409	3.141592741	; (157)

D.2. RF Pulse Definitions

	0.305962861	3.141592741	; (158)
	0.301075280	3.141592741	; (159)
170	0.294232637	3.141592741	; (160)
	0.285434991	3.141592741	; (161)
	0.274682313	3.141592741	; (162)
	0.262952089	3.141592741	; (163)
	0.248289347	3.141592741	; (164)
175	0.231671557	3.141592741	; (165)
	0.214076251	3.141592741	; (166)
	0.193548381	3.141592741	; (167)
	0.172043011	3.141592741	; (168)
	0.148582593	3.141592741	; (169)
180	0.123167157	3.141592741	; (170)
	0.095796674	3.141592741	; (171)
	0.067448683	3.141592741	; (172)
	0.037145648	3.141592741	; (173)
	0.004887586	3.141592741	; (174)
185	0.027370479	0.000000000	; (175)
	0.062561095	0.000000000	; (176)
	0.097751714	0.000000000	; (177)
	0.134897366	0.000000000	; (178)
	0.172043011	0.000000000	; (179)
190	0.210166171	0.000000000	; (180)
	0.249266863	0.000000000	; (181)
	0.289345056	0.000000000	; (182)
	0.328445762	0.000000000	; (183)
	0.368523955	0.000000000	; (184)
195	0.408602148	0.000000000	; (185)
	0.448680341	0.000000000	; (186)
	0.488758564	0.000000000	; (187)
	0.527859211	0.000000000	; (188)
	0.565982401	0.000000000	; (189)
200	0.604105592	0.000000000	; (190)
	0.640273690	0.000000000	; (191)
	0.676441848	0.000000000	; (192)
	0.710654914	0.000000000	; (193)
	0.743890524	0.000000000	; (194)
205	0.775171041	0.000000000	; (195)
	0.805474102	0.000000000	; (196)
	0.833822072	0.000000000	; (197)
	0.859237552	0.000000000	; (198)
	0.883675456	0.000000000	; (199)
210	0.906158388	0.000000000	; (200)
	0.925708711	0.000000000	; (201)
	0.943304002	0.000000000	; (202)
	0.958944261	0.000000000	; (203)
	0.971652031	0.000000000	; (204)
215	0.982404709	0.000000000	; (205)
	0.990224838	0.000000000	; (206)
	0.996089935	0.000000000	; (207)
	0.999022484	0.000000000	; (208)
	1.000000000	0.000000000	; (209)
220	0.998044968	0.000000000	; (210)
	0.994134903	0.000000000	; (211)
	0.987292290	0.000000000	; (212)
	0.978494644	0.000000000	; (213)
	0.966764390	0.000000000	; (214)
225	0.953079164	0.000000000	; (215)
	0.937438905	0.000000000	; (216)
	0.919843614	0.000000000	; (217)
	0.900293231	0.000000000	; (218)

230	0.877810359	0.000000000	; (219)
	0.855327487	0.000000000	; (220)
	0.829912007	0.000000000	; (221)
	0.803519070	0.000000000	; (222)
	0.775171041	0.000000000	; (223)
	0.745845556	0.000000000	; (224)
235	0.715542495	0.000000000	; (225)
	0.684261978	0.000000000	; (226)
	0.652003884	0.000000000	; (227)
	0.619745851	0.000000000	; (228)
	0.586510241	0.000000000	; (229)
240	0.552297175	0.000000000	; (230)
	0.518084049	0.000000000	; (231)
	0.483870953	0.000000000	; (232)
	0.449657857	0.000000000	; (233)
	0.416422278	0.000000000	; (234)
245	0.395894438	0.000000000	; (235)
	0.374389052	0.000000000	; (236)
	0.352883667	0.000000000	; (237)
	0.331378311	0.000000000	; (238)
	0.308895409	0.000000000	; (239)
250	0.287390023	0.000000000	; (240)
	0.264907122	0.000000000	; (241)
	0.243401766	0.000000000	; (242)
	0.220918864	0.000000000	; (243)
	0.199413493	0.000000000	; (244)
255	0.177908108	0.000000000	; (245)
	0.157380253	0.000000000	; (246)
	0.136852399	0.000000000	; (247)
	0.117302053	0.000000000	; (248)
	0.097751714	0.000000000	; (249)
260	0.080156401	0.000000000	; (250)
	0.062561095	0.000000000	; (251)
	0.044965789	0.000000000	; (252)
	0.029325513	0.000000000	; (253)
	0.013685239	0.000000000	; (254)
265	0.000000000	0.000000000	; (255)

D.2.2 Adiabatic Full Passage Pulse

	PULSENAME:	HS4_R25.HS4_R25	
	COMMENT:	HS4.0 adiabatic inversion pulse using sech/tanh mod: R=25.0	
	REFGRAD:	11.468075000	
	MINSLICE:	1.000000000	
5	MAXSLICE:	400.000000000	
	AMPINT:	56.670000000	
	POWERINT:	324.724113587	
	ABSINT:	360.759644176	
10	0.010000000	1.421587586	; (0)
	0.010861272	1.268189430	; (1)
	0.011785276	1.114791512	; (2)
	0.012775575	0.961393595	; (3)
	0.013835855	0.807995856	; (4)
15	0.014969926	0.654598236	; (5)
	0.016181717	0.501200855	; (6)

D.2. RF Pulse Definitions

	0.017475275	0.347803652	; (7)
	0.018854763	0.194406718	; (8)
	0.020324456	0.041010056	; (9)
20	0.021888735	-0.112386264	; (10)
	0.023552084	-0.265782207	; (11)
	0.025319088	-0.419177681	; (12)
	0.027194424	-0.572572649	; (13)
	0.029182851	-0.725966990	; (14)
25	0.031289212	-0.879360616	; (15)
	0.033518419	-1.032753468	; (16)
	0.035875447	-1.186145425	; (17)
	0.038365327	-1.339536309	; (18)
	0.040993132	-1.492925882	; (19)
30	0.043763965	-1.646314144	; (20)
	0.046682969	-1.799700856	; (21)
	0.049755275	-1.953085661	; (22)
	0.052986033	-2.106468439	; (23)
	0.056380369	-2.259848833	; (24)
35	0.059943378	-2.413226843	; (25)
	0.063680120	-2.566601515	; (26)
	0.067595594	-2.719972849	; (27)
	0.071694717	-2.873340607	; (28)
	0.075982340	-3.026703835	; (29)
40	0.080463171	3.103123188	; (30)
	0.085141823	2.949770212	; (31)
	0.090022750	2.796423435	; (32)
	0.095110238	2.643083334	; (33)
	0.100408405	2.489751101	; (34)
45	0.105921157	2.336427212	; (35)
	0.111652173	2.183112860	; (36)
	0.117604889	2.029809237	; (37)
	0.123782486	1.876517415	; (38)
	0.130187824	1.723238587	; (39)
50	0.136823505	1.569974303	; (40)
	0.143691748	1.416725993	; (41)
	0.150794446	1.263495326	; (42)
	0.158133104	1.110284209	; (43)
	0.165708825	0.957094550	; (44)
55	0.173522308	0.803928554	; (45)
	0.181573823	0.650788486	; (46)
	0.189863116	0.497676849	; (47)
	0.198389530	0.344596386	; (48)
	0.207151875	0.191549957	; (49)
60	0.216148421	0.038540728	; (50)
	0.225376934	-0.114427961	; (51)
	0.234834641	-0.267352521	; (52)
	0.244518176	-0.420229077	; (53)
	0.254423618	-0.573053539	; (54)
65	0.264546484	-0.725821495	; (55)
	0.274881661	-0.878528297	; (56)
	0.285423487	-1.031169057	; (57)
	0.296165675	-1.183738351	; (58)
	0.307101339	-1.336230636	; (59)
70	0.318223029	-1.488640070	; (60)
	0.329522729	-1.640960455	; (61)
	0.340991765	-1.793185115	; (62)
	0.352621049	-1.945307255	; (63)
	0.364400774	-2.097319365	; (64)
75	0.376320750	-2.249214172	; (65)
	0.388370246	-2.400983572	; (66)
	0.400538027	-2.552618980	; (67)

Appendix D. Metabolite Simulation Code

	0.412812442	-2.704112053	; (68)
	0.425181478	-2.855453491	; (69)
80	0.437632650	-3.006633997	; (70)
	0.450153232	3.125541687	; (71)
	0.462730169	2.974713087	; (72)
	0.475350171	2.824075937	; (73)
	0.487999707	2.673640966	; (74)
85	0.500665188	2.523419619	; (75)
	0.513332844	2.373423100	; (76)
	0.525988936	2.223663330	; (77)
	0.538619637	2.074152708	; (78)
	0.551211178	1.924903512	; (79)
90	0.563750029	1.775928378	; (80)
	0.576222718	1.627240181	; (81)
	0.588615954	1.478852391	; (82)
	0.600916803	1.330778241	; (83)
	0.613112628	1.183031440	; (84)
95	0.625191092	1.035625815	; (85)
	0.637140274	0.888575256	; (86)
	0.648948789	0.741894066	; (87)
	0.660605609	0.595596373	; (88)
	0.672100246	0.449696600	; (89)
100	0.683422863	0.304209113	; (90)
	0.694564164	0.159148410	; (91)
	0.705515265	0.014528991	; (92)
	0.716268241	-0.129634649	; (93)
	0.726815522	-0.273328006	; (94)
105	0.737150252	-0.416536659	; (95)
	0.747266412	-0.559246242	; (96)
	0.757158399	-0.701442420	; (97)
	0.766821384	-0.843110979	; (98)
	0.776251197	-0.984237909	; (99)
110	0.785444319	-1.124809384	; (100)
	0.794397891	-1.264811397	; (101)
	0.803109705	-1.404230714	; (102)
	0.811578035	-1.543053746	; (103)
	0.819801927	-1.681267381	; (104)
115	0.827780843	-1.818858624	; (105)
	0.835514963	-1.955815077	; (106)
	0.843004882	-2.092123985	; (107)
	0.850251675	-2.227773428	; (108)
	0.857257009	-2.362751484	; (109)
120	0.864022851	-2.497046471	; (110)
	0.870551765	-2.630647182	; (111)
	0.876846611	-2.763542652	; (112)
	0.882910550	-2.895721912	; (113)
	0.888747096	-3.027174950	; (114)
125	0.894360244	3.125293970	; (115)
	0.899753988	2.995323896	; (116)
	0.904932737	2.866109371	; (117)
	0.909901023	2.737659693	; (118)
	0.914663732	2.609983921	; (119)
130	0.919225752	2.483090162	; (120)
	0.923592091	2.356986761	; (121)
	0.927767992	2.231681824	; (122)
	0.931758761	2.107182980	; (123)
	0.935569704	1.983497024	; (124)
135	0.939206243	1.860631466	; (125)
	0.942673802	1.738592982	; (126)
	0.945977807	1.617387772	; (127)
	0.949123740	1.497022152	; (128)

D.2. RF Pulse Definitions

	0.952116907	1.377501965	; (129)
140	0.954962790	1.258832932	; (130)
	0.957666695	1.141020417	; (131)
	0.960233867	1.024069428	; (132)
	0.962669551	0.907984972	; (133)
	0.964978814	0.792771637	; (134)
145	0.967166781	0.678433836	; (135)
	0.969238281	0.564975858	; (136)
	0.971198201	0.452401668	; (137)
	0.973051310	0.340714991	; (138)
	0.974802196	0.229919478	; (139)
150	0.976455271	0.120018527	; (140)
	0.978015065	0.011015344	; (141)
	0.979485750	-0.097087011	; (142)
	0.980871379	-0.204285666	; (143)
	0.982176125	-0.310577899	; (144)
155	0.983403683	-0.415961146	; (145)
	0.984557927	-0.520432949	; (146)
	0.985642433	-0.623991072	; (147)
	0.986660659	-0.726633430	; (148)
	0.987616003	-0.828357875	; (149)
160	0.988511682	-0.929162562	; (150)
	0.989350855	-1.029045701	; (151)
	0.990136445	-1.128005624	; (152)
	0.990871370	-1.226040840	; (153)
	0.991558373	-1.323149800	; (154)
165	0.992200136	-1.419331074	; (155)
	0.992799103	-1.514583468	; (156)
	0.993357718	-1.608905792	; (157)
	0.993878305	-1.702296853	; (158)
	0.994363010	-1.794755697	; (159)
170	0.994814038	-1.886281252	; (160)
	0.995233357	-1.976872563	; (161)
	0.995622814	-2.066528797	; (162)
	0.995984256	-2.155249357	; (163)
	0.996319413	-2.243033409	; (164)
175	0.996629953	-2.329880238	; (165)
	0.996917367	-2.415789127	; (166)
	0.997183144	-2.500759602	; (167)
	0.997428775	-2.584791183	; (168)
	0.997655451	-2.667883396	; (169)
180	0.997864485	-2.750035524	; (170)
	0.998057127	-2.831247091	; (171)
	0.998234332	-2.911518097	; (172)
	0.998397291	-2.990848064	; (173)
	0.998546958	-3.069236517	; (174)
185	0.998684287	3.136502266	; (175)
	0.998810112	3.059997559	; (176)
	0.998925269	2.984435320	; (177)
	0.999030590	2.909815550	; (178)
	0.999126792	2.836138487	; (179)
190	0.999214530	2.763404369	; (180)
	0.999294460	2.691613436	; (181)
	0.999367177	2.620765924	; (182)
	0.999433279	2.550861835	; (183)
	0.999493241	2.481901169	; (184)
195	0.999547601	2.413884401	; (185)
	0.999596775	2.346811533	; (186)
	0.999641180	2.280682325	; (187)
	0.999681294	2.215497255	; (188)
	0.999717414	2.151256561	; (189)

Appendix D. Metabolite Simulation Code

200	0.999749899	2.087959766	; (190)
	0.999779046	2.025607347	; (191)
	0.999805212	1.964199066	; (192)
	0.999828637	1.903735280	; (193)
	0.999849498	1.844215989	; (194)
205	0.999868155	1.785641074	; (195)
	0.999884725	1.728010654	; (196)
	0.999899447	1.671324849	; (197)
	0.999912500	1.615583539	; (198)
	0.999924064	1.560786843	; (199)
210	0.999934256	1.506934762	; (200)
	0.999943256	1.454027414	; (201)
	0.999951124	1.402064681	; (202)
	0.999958038	1.351046562	; (203)
	0.999964058	1.300973177	; (204)
215	0.999969304	1.251844525	; (205)
	0.999973893	1.203660607	; (206)
	0.999977887	1.156421423	; (207)
	0.999981284	1.110126972	; (208)
	0.999984264	1.064777255	; (209)
220	0.999986827	1.020372272	; (210)
	0.999988973	0.976912141	; (211)
	0.999990821	0.934396684	; (212)
	0.999992371	0.892826021	; (213)
	0.999993742	0.852200150	; (214)
225	0.999994874	0.812519014	; (215)
	0.999995828	0.773782670	; (216)
	0.999996603	0.735991120	; (217)
	0.999997258	0.699144363	; (218)
	0.999997795	0.663242400	; (219)
230	0.999998212	0.628285170	; (220)
	0.999998569	0.594272733	; (221)
	0.999998868	0.561205149	; (222)
	0.999999166	0.529082298	; (223)
	0.999999344	0.497904211	; (224)
235	0.999999464	0.467670947	; (225)
	0.999999583	0.438382477	; (226)
	0.999999702	0.410038769	; (227)
	0.999999762	0.382639885	; (228)
	0.999999821	0.356185764	; (229)
240	0.999999881	0.330676436	; (230)
	0.999999940	0.306111902	; (231)
	0.999999940	0.282492161	; (232)
	0.999999940	0.259817213	; (233)
	0.999999940	0.238087043	; (234)
245	1.000000000	0.217301667	; (235)
	1.000000000	0.197461069	; (236)
	1.000000000	0.178565279	; (237)
	1.000000000	0.160614267	; (238)
	1.000000000	0.143608049	; (239)
250	1.000000000	0.127546623	; (240)
	1.000000000	0.112429991	; (241)
	1.000000000	0.098258145	; (242)
	1.000000000	0.085031085	; (243)
	1.000000000	0.072748818	; (244)
255	1.000000000	0.061411340	; (245)
	1.000000000	0.051018652	; (246)
	1.000000000	0.041570753	; (247)
	1.000000000	0.033067644	; (248)
	1.000000000	0.025509326	; (249)
260	1.000000000	0.018895797	; (250)

D.2. RF Pulse Definitions

	1.000000000	0.013227058	; (251)
	1.000000000	0.008503108	; (252)
	1.000000000	0.004723949	; (253)
	1.000000000	0.001889580	; (254)
265	1.000000000	0.000000000	; (255)
	1.000000000	0.000000000	; (256)
	1.000000000	0.001889580	; (257)
	1.000000000	0.004723949	; (258)
	1.000000000	0.008503108	; (259)
270	1.000000000	0.013227058	; (260)
	1.000000000	0.018895797	; (261)
	1.000000000	0.025509326	; (262)
	1.000000000	0.033067644	; (263)
	1.000000000	0.041570753	; (264)
275	1.000000000	0.051018652	; (265)
	1.000000000	0.061411340	; (266)
	1.000000000	0.072748818	; (267)
	1.000000000	0.085031085	; (268)
	1.000000000	0.098258145	; (269)
280	1.000000000	0.112429991	; (270)
	1.000000000	0.127546623	; (271)
	1.000000000	0.143608049	; (272)
	1.000000000	0.160614267	; (273)
	1.000000000	0.178565279	; (274)
285	1.000000000	0.197461069	; (275)
	1.000000000	0.217301667	; (276)
	0.999999940	0.238087043	; (277)
	0.999999940	0.259817213	; (278)
	0.999999940	0.282492161	; (279)
290	0.999999940	0.306111902	; (280)
	0.999999881	0.330676436	; (281)
	0.999999821	0.356185764	; (282)
	0.999999762	0.382639885	; (283)
	0.999999702	0.410038769	; (284)
295	0.999999583	0.438382477	; (285)
	0.999999464	0.467670947	; (286)
	0.999999344	0.497904211	; (287)
	0.999999166	0.529082298	; (288)
	0.999998868	0.561205149	; (289)
300	0.999998569	0.594272733	; (290)
	0.999998212	0.628285170	; (291)
	0.999997795	0.663242400	; (292)
	0.999997258	0.699144363	; (293)
	0.999996603	0.735991120	; (294)
305	0.999995828	0.773782670	; (295)
	0.999994874	0.812519014	; (296)
	0.999993742	0.852200150	; (297)
	0.999992371	0.892826021	; (298)
	0.999990821	0.934396684	; (299)
310	0.999988973	0.976912141	; (300)
	0.999986827	1.020372272	; (301)
	0.999984264	1.064777255	; (302)
	0.999981284	1.110126972	; (303)
	0.999977887	1.156421423	; (304)
315	0.999973893	1.203660607	; (305)
	0.999969304	1.251844525	; (306)
	0.999964058	1.300973177	; (307)
	0.999958038	1.351046562	; (308)
	0.999951124	1.402064681	; (309)
320	0.999943256	1.454027414	; (310)
	0.999934256	1.506934762	; (311)

Appendix D. Metabolite Simulation Code

	0.999924064	1.560786843	; (312)
	0.999912500	1.615583539	; (313)
	0.999899447	1.671324849	; (314)
325	0.999884725	1.728010654	; (315)
	0.999868155	1.785641074	; (316)
	0.999849498	1.844215989	; (317)
	0.999828637	1.903735280	; (318)
	0.999805212	1.964199066	; (319)
330	0.999779046	2.025607347	; (320)
	0.999749899	2.087959766	; (321)
	0.999717414	2.151256561	; (322)
	0.999681294	2.215497255	; (323)
	0.999641180	2.280682325	; (324)
335	0.999596775	2.346811533	; (325)
	0.999547601	2.413884401	; (326)
	0.999493241	2.481901169	; (327)
	0.999433279	2.550861835	; (328)
	0.999367177	2.620765924	; (329)
340	0.999294460	2.691613436	; (330)
	0.999214530	2.763404369	; (331)
	0.999126792	2.836138487	; (332)
	0.999030590	2.909815550	; (333)
	0.998925269	2.984435320	; (334)
345	0.998810112	3.059997559	; (335)
	0.998684287	3.136502266	; (336)
	0.998546958	-3.069236517	; (337)
	0.998397291	-2.990848064	; (338)
	0.998234332	-2.911518097	; (339)
350	0.998057127	-2.831247091	; (340)
	0.997864485	-2.750035524	; (341)
	0.997655451	-2.667883396	; (342)
	0.997428775	-2.584791183	; (343)
	0.997183144	-2.500759602	; (344)
355	0.996917367	-2.415789127	; (345)
	0.996629953	-2.329880238	; (346)
	0.996319413	-2.243033409	; (347)
	0.995984256	-2.155249357	; (348)
	0.995622814	-2.066528797	; (349)
360	0.995233357	-1.976872563	; (350)
	0.994814038	-1.886281252	; (351)
	0.994363010	-1.794755697	; (352)
	0.993878305	-1.702296853	; (353)
	0.993357718	-1.608905792	; (354)
365	0.992799103	-1.514583468	; (355)
	0.992200136	-1.419331074	; (356)
	0.991558373	-1.323149800	; (357)
	0.990871370	-1.226040840	; (358)
	0.990136445	-1.128005624	; (359)
370	0.989350855	-1.029045701	; (360)
	0.988511682	-0.929162562	; (361)
	0.987616003	-0.828357875	; (362)
	0.986660659	-0.726633430	; (363)
	0.985642433	-0.623991072	; (364)
375	0.984557927	-0.520432949	; (365)
	0.983403683	-0.415961146	; (366)
	0.982176125	-0.310577899	; (367)
	0.980871379	-0.204285666	; (368)
	0.979485750	-0.097087011	; (369)
380	0.978015065	0.011015344	; (370)
	0.976455271	0.120018527	; (371)
	0.974802196	0.229919478	; (372)

D.2. RF Pulse Definitions

	0.973051310	0.340714991	; (373)
	0.971198201	0.452401668	; (374)
385	0.969238281	0.564975858	; (375)
	0.967166781	0.678433836	; (376)
	0.964978814	0.792771637	; (377)
	0.962669551	0.907984972	; (378)
	0.960233867	1.024069428	; (379)
390	0.957666695	1.141020417	; (380)
	0.954962790	1.258832932	; (381)
	0.952116907	1.377501965	; (382)
	0.949123740	1.497022152	; (383)
	0.945977807	1.617387772	; (384)
395	0.942673802	1.738592982	; (385)
	0.939206243	1.860631466	; (386)
	0.935569704	1.983497024	; (387)
	0.931758761	2.107182980	; (388)
	0.927767992	2.231681824	; (389)
400	0.923592091	2.356986761	; (390)
	0.919225752	2.483090162	; (391)
	0.914663732	2.609983921	; (392)
	0.909901023	2.737659693	; (393)
	0.904932737	2.866109371	; (394)
405	0.899753988	2.995323896	; (395)
	0.894360244	3.125293970	; (396)
	0.888747096	-3.027174950	; (397)
	0.882910550	-2.895721912	; (398)
	0.876846611	-2.763542652	; (399)
410	0.870551765	-2.630647182	; (400)
	0.864022851	-2.497046471	; (401)
	0.857257009	-2.362751484	; (402)
	0.850251675	-2.227773428	; (403)
	0.843004882	-2.092123985	; (404)
415	0.835514963	-1.955815077	; (405)
	0.827780843	-1.818858624	; (406)
	0.819801927	-1.681267381	; (407)
	0.811578035	-1.543053746	; (408)
	0.803109705	-1.404230714	; (409)
420	0.794397891	-1.264811397	; (410)
	0.785444319	-1.124809384	; (411)
	0.776251197	-0.984237909	; (412)
	0.766821384	-0.843110979	; (413)
	0.757158399	-0.701442420	; (414)
425	0.747266412	-0.559246242	; (415)
	0.737150252	-0.416536659	; (416)
	0.726815522	-0.273328006	; (417)
	0.716268241	-0.129634649	; (418)
	0.705515265	0.014528991	; (419)
430	0.694564164	0.159148410	; (420)
	0.683422863	0.304209113	; (421)
	0.672100246	0.449696600	; (422)
	0.660605609	0.595596373	; (423)
	0.648948789	0.741894066	; (424)
435	0.637140274	0.888575256	; (425)
	0.625191092	1.035625815	; (426)
	0.613112628	1.183031440	; (427)
	0.600916803	1.330778241	; (428)
	0.588615954	1.478852391	; (429)
440	0.576222718	1.627240181	; (430)
	0.563750029	1.775928378	; (431)
	0.551211178	1.924903512	; (432)
	0.538619637	2.074152708	; (433)

Appendix D. Metabolite Simulation Code

	0.525988936	2.223663330	; (434)
445	0.513332844	2.373423100	; (435)
	0.500665188	2.523419619	; (436)
	0.487999707	2.673640966	; (437)
	0.475350171	2.824075937	; (438)
	0.462730169	2.974713087	; (439)
450	0.450153232	3.125541687	; (440)
	0.437632650	-3.006633997	; (441)
	0.425181478	-2.855453491	; (442)
	0.412812442	-2.704112053	; (443)
	0.400538027	-2.552618980	; (444)
455	0.388370246	-2.400983572	; (445)
	0.376320750	-2.249214172	; (446)
	0.364400774	-2.097319365	; (447)
	0.352621049	-1.945307255	; (448)
	0.340991765	-1.793185115	; (449)
460	0.329522729	-1.640960455	; (450)
	0.318223029	-1.488640070	; (451)
	0.307101339	-1.336230636	; (452)
	0.296165675	-1.183738351	; (453)
	0.285423487	-1.031169057	; (454)
465	0.274881661	-0.878528297	; (455)
	0.264546484	-0.725821495	; (456)
	0.254423618	-0.573053539	; (457)
	0.244518176	-0.420229077	; (458)
	0.234834641	-0.267352521	; (459)
470	0.225376934	-0.114427961	; (460)
	0.216148421	0.038540728	; (461)
	0.207151875	0.191549957	; (462)
	0.198389530	0.344596386	; (463)
	0.189863116	0.497676849	; (464)
475	0.181573823	0.650788486	; (465)
	0.173522308	0.803928554	; (466)
	0.165708825	0.957094550	; (467)
	0.158133104	1.110284209	; (468)
	0.150794446	1.263495326	; (469)
480	0.143691748	1.416725993	; (470)
	0.136823505	1.569974303	; (471)
	0.130187824	1.723238587	; (472)
	0.123782486	1.876517415	; (473)
	0.117604889	2.029809237	; (474)
485	0.111652173	2.183112860	; (475)
	0.105921157	2.336427212	; (476)
	0.100408405	2.489751101	; (477)
	0.095110238	2.643083334	; (478)
	0.090022750	2.796423435	; (479)
490	0.085141823	2.949770212	; (480)
	0.080463171	3.103123188	; (481)
	0.075982340	-3.026703835	; (482)
	0.071694717	-2.873340607	; (483)
	0.067595594	-2.719972849	; (484)
495	0.063680120	-2.566601515	; (485)
	0.059943378	-2.413226843	; (486)
	0.056380369	-2.259848833	; (487)
	0.052986033	-2.106468439	; (488)
	0.049755275	-1.953085661	; (489)
500	0.046682969	-1.799700856	; (490)
	0.043763965	-1.646314144	; (491)
	0.040993132	-1.492925882	; (492)
	0.038365327	-1.339536309	; (493)
	0.035875447	-1.186145425	; (494)

D.2. RF Pulse Definitions


505	0.033518419	-1.032753468	; (495)
	0.031289212	-0.879360616	; (496)
	0.029182851	-0.725966990	; (497)
	0.027194424	-0.572572649	; (498)
	0.025319088	-0.419177681	; (499)
510	0.023552084	-0.265782207	; (500)
	0.021888735	-0.112386264	; (501)
	0.020324456	0.041010056	; (502)
	0.018854763	0.194406718	; (503)
	0.017475275	0.347803652	; (504)
515	0.016181717	0.501200855	; (505)
	0.014969926	0.654598236	; (506)
	0.013835855	0.807995856	; (507)
	0.012775575	0.961393595	; (508)
	0.011785276	1.114791512	; (509)
520	0.010861272	1.268189430	; (510)
	0.000000000	0.000000000	; (511)

E

Research Ethics Approvals

Research ethics approvals for the studies presented in this thesis are provided on the following pages.

Appendix E. Research Ethics Approvals

	<div style="text-align: right;">Research Ethics</div> <div style="text-align: center;">Western University Health Science Research Ethics Board HSREB Annual Continuing Ethics Approval Notice</div>
<p>Date: September 29, 2016 Principal Investigator: Dr. Michael Borrie Department & Institution: Schulich School of Medicine and Dentistry/Medicine-Dept of, St. Joseph's Health Care London</p> <p>Review Type: Full Board HSREB File Number: 3866 Study Title: Utilizing High Field Magnetic Resonance Spectroscopy as a Biomarker of Mild Cognitive Impairment (REB #12717) Sponsor: Alzheimer Society of Canada</p> <p>HSREB Renewal Due Date & HSREB Expiry Date: Renewal Due -2017/09/30 Expiry Date -2017/10/10</p> <p>The Western University Health Science Research Ethics Board (HSREB) has reviewed the Continuing Ethics Review (CER) Form and is re-issuing approval for the above noted study.</p> <p>The Western University HSREB operates in compliance with the Tri-Council Policy Statement Ethical Conduct for Research Involving Humans (TCPS2), the International Conference on Harmonization of Technical Requirements for Registration of Pharmaceuticals for Human Use Guideline for Good Clinical Practice (ICH E6 R1), the Ontario Freedom of Information and Protection of Privacy Act (FIPPA, 1990), the Ontario Personal Health Information Protection Act (PHIPA, 2004), Part 4 of the Natural Health Product Regulations, Health Canada Medical Device Regulations and Part C, Division 5, of the Food and Drug Regulations of Health Canada.</p> <p>Members of the HSREB who are named as Investigators in research studies do not participate in discussions related to, nor vote on such studies when they are presented to the REB.</p> <p>The HSREB is registered with the U.S. Department of Health & Human Services under the IRB registration number IRB 00000940</p> <div style="background-color: black; width: 250px; height: 20px; margin: 5px 0;"></div> <p>Ethics Officer, on behalf of Dr. Joseph Gilbert, HSREB Chair</p> <p>Ethics Officer: Erika Basile ___ Katelyn Harris ___ Nicole Kaniki ___ Grace Kelly ___ Vikki Trinh <u>1</u> Karen Gopaul ___</p>	
<p><small>Western University, Research, Support Services Bldg., Rm. 5150 London, ON, Canada N6G 1G9 t. 519.661.3036 f. 519.850.2466 www.uwo.ca/research/ethics</small></p>	

From: eSiriusWebServer <[REDACTED]>
Sent: July-11-16 2:33 PM
To: [REDACTED]
Cc: Account Generic 24 <[REDACTED]>; Account Generic 24 <[REDACTED]>
Subject: eSirius Notification - Annual Protocol Renewal APPROVED by the AUS 2012-040::3



2012-040::3:

AUP Number: 2012-040

AUP Title: The Interaction of Vitamin D and Memantine for Alzheimer Disease Treatment

Yearly Renewal Date: 07/01/2016

The YEARLY RENEWAL to Animal Use Protocol (AUP) 2012-040 has been approved, and will be approved for one year following the above review date.

1. This AUP number must be indicated when ordering animals for this project.
2. Animals for other projects may not be ordered under this AUP number.
3. Purchases of animals other than through this system must be cleared through the ACVS office.

Health certificates will be required.

REQUIREMENTS/COMMENTS

Please ensure that individual(s) performing procedures on live animals, as described in this protocol, are familiar with the contents of this document.

The holder of this Animal Use Protocol is responsible to ensure that all associated safety components (biosafety, radiation safety, general laboratory safety) comply with institutional safety standards and have received all necessary approvals. Please consult directly with your institutional safety officers.

Submitted by: Kinchlea, Will D
on behalf of the Animal Use Subcommittee

F

Licenses

Licenses for the reproduction of copyright material contained in the chapters of thesis are provided on the following pages.

**JOHN WILEY AND SONS LICENSE
TERMS AND CONDITIONS**

Jul 12, 2019

This Agreement between The University of Western Ontario -- Dickson Wong ("You") and John Wiley and Sons ("John Wiley and Sons") consists of your license details and the terms and conditions provided by John Wiley and Sons and Copyright Clearance Center.

License Number	4626551222565
License date	Jul 12, 2019
Licensed Content Publisher	John Wiley and Sons
Licensed Content Publication	NMR in Biomedicine
Licensed Content Title	Optimized in vivo brain glutamate measurement using long-echo-time semi-LASER at 7 T
Licensed Content Author	Dickson Wong, Amy L. Schranz, Robert Bartha
Licensed Content Date	Aug 24, 2018
Licensed Content Volume	31
Licensed Content Issue	11
Licensed Content Pages	13
Type of use	Dissertation/Thesis
Requestor type	Author of this Wiley article
Format	Print and electronic
Portion	Full article
Will you be translating?	No
Title of your thesis / dissertation	MRI Investigations of Metabolic and Structural Changes in Alzheimer's Disease and Vitamin D Deprivation
Expected completion date	Sep 2019
Expected size (number of pages)	230
Requestor Location	[REDACTED] [REDACTED] Attn: Dickson Wong
Publisher Tax ID	EU826007151
Total	0.00 CAD
Terms and Conditions	

TERMS AND CONDITIONS

This copyrighted material is owned by or exclusively licensed to John Wiley & Sons, Inc. or one of its group companies (each a "Wiley Company") or handled on behalf of a society with which a Wiley Company has exclusive publishing rights in relation to a particular work (collectively "WILEY"). By clicking "accept" in connection with completing this licensing transaction, you agree that the following terms and conditions apply to this transaction (along with the billing and payment terms and conditions established by the Copyright

Clearance Center Inc., ("CCC's Billing and Payment terms and conditions"), at the time that you opened your RightsLink account (these are available at any time at <http://myaccount.copyright.com>).

Terms and Conditions

- The materials you have requested permission to reproduce or reuse (the "Wiley Materials") are protected by copyright.
- You are hereby granted a personal, non-exclusive, non-sub licensable (on a stand-alone basis), non-transferable, worldwide, limited license to reproduce the Wiley Materials for the purpose specified in the licensing process. This license, **and any CONTENT (PDF or image file) purchased as part of your order**, is for a one-time use only and limited to any maximum distribution number specified in the license. The first instance of republication or reuse granted by this license must be completed within two years of the date of the grant of this license (although copies prepared before the end date may be distributed thereafter). The Wiley Materials shall not be used in any other manner or for any other purpose, beyond what is granted in the license. Permission is granted subject to an appropriate acknowledgement given to the author, title of the material/book/journal and the publisher. You shall also duplicate the copyright notice that appears in the Wiley publication in your use of the Wiley Material. Permission is also granted on the understanding that nowhere in the text is a previously published source acknowledged for all or part of this Wiley Material. Any third party content is expressly excluded from this permission.
- With respect to the Wiley Materials, all rights are reserved. Except as expressly granted by the terms of the license, no part of the Wiley Materials may be copied, modified, adapted (except for minor reformatting required by the new Publication), translated, reproduced, transferred or distributed, in any form or by any means, and no derivative works may be made based on the Wiley Materials without the prior permission of the respective copyright owner. **For STM Signatory Publishers clearing permission under the terms of the [STM Permissions Guidelines](#) only, the terms of the license are extended to include subsequent editions and for editions in other languages, provided such editions are for the work as a whole in situ and does not involve the separate exploitation of the permitted figures or extracts**, You may not alter, remove or suppress in any manner any copyright, trademark or other notices displayed by the Wiley Materials. You may not license, rent, sell, loan, lease, pledge, offer as security, transfer or assign the Wiley Materials on a stand-alone basis, or any of the rights granted to you hereunder to any other person.
- The Wiley Materials and all of the intellectual property rights therein shall at all times remain the exclusive property of John Wiley & Sons Inc, the Wiley Companies, or their respective licensors, and your interest therein is only that of having possession of and the right to reproduce the Wiley Materials pursuant to Section 2 herein during the continuance of this Agreement. You agree that you own no right, title or interest in or to the Wiley Materials or any of the intellectual property rights therein. You shall have no rights hereunder other than the license as provided for above in Section 2. No right, license or interest to any trademark, trade name, service mark or other branding ("Marks") of WILEY or its licensors is granted hereunder, and you agree that you shall not assert any such right, license or interest with respect thereto
- NEITHER WILEY NOR ITS LICENSORS MAKES ANY WARRANTY OR REPRESENTATION OF ANY KIND TO YOU OR ANY THIRD PARTY, EXPRESS, IMPLIED OR STATUTORY, WITH RESPECT TO THE MATERIALS

OR THE ACCURACY OF ANY INFORMATION CONTAINED IN THE MATERIALS, INCLUDING, WITHOUT LIMITATION, ANY IMPLIED WARRANTY OF MERCHANTABILITY, ACCURACY, SATISFACTORY QUALITY, FITNESS FOR A PARTICULAR PURPOSE, USABILITY, INTEGRATION OR NON-INFRINGEMENT AND ALL SUCH WARRANTIES ARE HEREBY EXCLUDED BY WILEY AND ITS LICENSORS AND WAIVED BY YOU.

- WILEY shall have the right to terminate this Agreement immediately upon breach of this Agreement by you.
- You shall indemnify, defend and hold harmless WILEY, its Licensors and their respective directors, officers, agents and employees, from and against any actual or threatened claims, demands, causes of action or proceedings arising from any breach of this Agreement by you.
- IN NO EVENT SHALL WILEY OR ITS LICENSORS BE LIABLE TO YOU OR ANY OTHER PARTY OR ANY OTHER PERSON OR ENTITY FOR ANY SPECIAL, CONSEQUENTIAL, INCIDENTAL, INDIRECT, EXEMPLARY OR PUNITIVE DAMAGES, HOWEVER CAUSED, ARISING OUT OF OR IN CONNECTION WITH THE DOWNLOADING, PROVISIONING, VIEWING OR USE OF THE MATERIALS REGARDLESS OF THE FORM OF ACTION, WHETHER FOR BREACH OF CONTRACT, BREACH OF WARRANTY, TORT, NEGLIGENCE, INFRINGEMENT OR OTHERWISE (INCLUDING, WITHOUT LIMITATION, DAMAGES BASED ON LOSS OF PROFITS, DATA, FILES, USE, BUSINESS OPPORTUNITY OR CLAIMS OF THIRD PARTIES), AND WHETHER OR NOT THE PARTY HAS BEEN ADVISED OF THE POSSIBILITY OF SUCH DAMAGES. THIS LIMITATION SHALL APPLY NOTWITHSTANDING ANY FAILURE OF ESSENTIAL PURPOSE OF ANY LIMITED REMEDY PROVIDED HEREIN.
- Should any provision of this Agreement be held by a court of competent jurisdiction to be illegal, invalid, or unenforceable, that provision shall be deemed amended to achieve as nearly as possible the same economic effect as the original provision, and the legality, validity and enforceability of the remaining provisions of this Agreement shall not be affected or impaired thereby.
- The failure of either party to enforce any term or condition of this Agreement shall not constitute a waiver of either party's right to enforce each and every term and condition of this Agreement. No breach under this agreement shall be deemed waived or excused by either party unless such waiver or consent is in writing signed by the party granting such waiver or consent. The waiver by or consent of a party to a breach of any provision of this Agreement shall not operate or be construed as a waiver of or consent to any other or subsequent breach by such other party.
- This Agreement may not be assigned (including by operation of law or otherwise) by you without WILEY's prior written consent.
- Any fee required for this permission shall be non-refundable after thirty (30) days from receipt by the CCC.
- These terms and conditions together with CCC's Billing and Payment terms and conditions (which are incorporated herein) form the entire agreement between you and WILEY concerning this licensing transaction and (in the absence of fraud) supersedes

all prior agreements and representations of the parties, oral or written. This Agreement may not be amended except in writing signed by both parties. This Agreement shall be binding upon and inure to the benefit of the parties' successors, legal representatives, and authorized assigns.

- In the event of any conflict between your obligations established by these terms and conditions and those established by CCC's Billing and Payment terms and conditions, these terms and conditions shall prevail.
- WILEY expressly reserves all rights not specifically granted in the combination of (i) the license details provided by you and accepted in the course of this licensing transaction, (ii) these terms and conditions and (iii) CCC's Billing and Payment terms and conditions.
- This Agreement will be void if the Type of Use, Format, Circulation, or Requestor Type was misrepresented during the licensing process.
- This Agreement shall be governed by and construed in accordance with the laws of the State of New York, USA, without regards to such state's conflict of law rules. Any legal action, suit or proceeding arising out of or relating to these Terms and Conditions or the breach thereof shall be instituted in a court of competent jurisdiction in New York County in the State of New York in the United States of America and each party hereby consents and submits to the personal jurisdiction of such court, waives any objection to venue in such court and consents to service of process by registered or certified mail, return receipt requested, at the last known address of such party.

WILEY OPEN ACCESS TERMS AND CONDITIONS

Wiley Publishes Open Access Articles in fully Open Access Journals and in Subscription journals offering Online Open. Although most of the fully Open Access journals publish open access articles under the terms of the Creative Commons Attribution (CC BY) License only, the subscription journals and a few of the Open Access Journals offer a choice of Creative Commons Licenses. The license type is clearly identified on the article.

The Creative Commons Attribution License

The [Creative Commons Attribution License \(CC-BY\)](#) allows users to copy, distribute and transmit an article, adapt the article and make commercial use of the article. The CC-BY license permits commercial and non-

Creative Commons Attribution Non-Commercial License

The [Creative Commons Attribution Non-Commercial \(CC-BY-NC\) License](#) permits use, distribution and reproduction in any medium, provided the original work is properly cited and is not used for commercial purposes.(see below)

Creative Commons Attribution-Non-Commercial-NoDerivs License

The [Creative Commons Attribution Non-Commercial-NoDerivs License](#) (CC-BY-NC-ND) permits use, distribution and reproduction in any medium, provided the original work is properly cited, is not used for commercial purposes and no modifications or adaptations are made. (see below)

Use by commercial "for-profit" organizations

Use of Wiley Open Access articles for commercial, promotional, or marketing purposes requires further explicit permission from Wiley and will be subject to a fee.

Further details can be found on Wiley Online Library

<http://olabout.wiley.com/WileyCDA/Section/id-410895.html>

Other Terms and Conditions:

v1.10 Last updated September 2015

Questions? customercare@copyright.com or +1-855-239-3415 (toll free in the US) or +1-978-646-2777.

Dickson Wong | Curriculum Vitae

MD/PhD CANDIDATE IN MEDICAL BIOPHYSICS

Education

The University of Western Ontario*Doctor of Medicine (M.D.)*

Schulich School of Medicine and Dentistry

London, ON

2018–present

The University of Western Ontario*Doctor of Philosophy (Ph.D.), Medical Biophysics*

Advisor: Dr. Robert Bartha

London, ON

2015–present

McMaster University*Bachelor of Engineering (B.Eng.), GPA – 4.0*

Electrical and Biomedical Engineering

Hamilton, ON

2011–2015

The Royal Conservatory of Music*Performance Associateship Diploma (ARCT), Honours*

Piano

Toronto, ON

2009

Publications

2019 (In Preparation): “Chronic Vitamin D deficiency in adult APP/PS1 mice: Effect on memory performance and brain metabolite levels”. **Dickson Wong**, Miranda Bellyou, Alex Li, Marco Prado, Olivier Beauchet, Cédric Annweiler, Manuel Montero-Odasso, Robert Bartha. *Journal of Neurochemistry*.

2019 (In Preparation): “Observing metabolite changes in short versus long echo time functional magnetic resonance spectroscopy at 7-Tesla”. Peter Jeon, Michael Mackinley, Kara Dempster, **Dickson Wong**, Lena Palaniyappan, Jean Théberge. *Magnetic Resonance in Medicine*.

2019 (Submitted): “Glutamate and Dysconnection in the Salience Network: Neurochemical, Effective-connectivity, and Computational Evidence in Schizophrenia”. Roberto Limongi, Peter Jeon, Michael Mackinley, Tushar Das, Kara Dempster, Jean Théberge, Robert Bartha, **Dickson Wong**, Lena Palaniyappan. *Biological Psychiatry*.

2019 (Accepted with Minor Revisions): “Relating Hippocampal Glutamate to Structural Changes and Cognitive Performance in Alzheimer’s Disease: A 7T MRI Study”. **Dickson Wong**, Samir Atiya, Jennifer Fogarty, Manuel Montero-Odasso, Stephen Pasternak, Chris Brymer, Michael Borrie, Robert Bartha. *Journal of Alzheimer’s Disease*

2019 (Submitted): “7T Magnetic Resonance Spectroscopy of the Hippocampus in Non-Lesional Temporal Lobe Epilepsy”. John Adams, Simona Nikolova, Suzan Brown, **Dickson Wong**, Robert Bartha, Jorge G Burneo. *Epilepsy Research*.

2018: *Optimized in vivo brain glutamate measurement using long-echo-time semi-LASER at 7T*. **Dickson Wong**, Amy L. Schranz, Robert Bartha. *NMR in Biomedicine*: 31:e4002. <https://doi.org/10.1002/nbm.4002>

2018: *BIDS Extension Proposal 22 (BEP022): MRS (Magnetic Resonance Spectroscopy)*. **Dickson Wong**, Maryam Mozaffari, Yiming Xiao, Jenny Chan. *Brain Imaging Data Standard*. <https://docs.google.com/document/d/1pWCb02YNv5W-UZZja24fZrdXLm4X7knXMiZi7E2z7mY/>

2018: *¹H MR spectroscopy of the motor cortex immediately following transcranial direct current stimulation at 7 Tesla*. Kayla Ryan, Krzysztof Wawrzyn, Joseph S. Gati, Blaine A. Chronik, **Dickson Wong**, Neil Duggal, Robert Bartha. *PLOS ONE* 13(8): e0198053. <https://doi.org/10.1371/journal.pone.0198053>

Presentations and Abstracts

2018 (Poster): “Relating Hippocampal Glutamate to Structural Changes and Cognitive Performance in Alzheimer’s Disease: A 7T MRI Study”, **Dickson Wong**, Samir Atiya, Jennifer Fogarty, Manuel Montero-Odasso, Stephen Pasternak, Chris Brymer, Michael Borrie, Robert Bartha, Alzheimer’s Association International Conference, July 22, 2018, McCormick Place, Chicago, IL.

2018 (Presentation): “Relating Hippocampal Glutamate to Structural Changes and Cognitive Performance in Alzheimer’s Disease: A 7T MRI Study”, **Dickson Wong**, Samir Atiya, Jennifer Fogarty, Manuel Montero-Odasso, Stephen Pasternak, Chris Brymer, Michael Borrie, Robert Bartha, Imaging Network Ontario Symposium, March 28, 2018, Chestnut Residence & Conference Centre, Toronto, ON.

2017 (Poster): “Vitamin D Supplementation May Protect Against Oxidative Stress in a Vitamin D Deficient Double-Transgenic Mouse Model of Alzheimer’s Disease”, **Dickson Wong**, Miranda Bellyou, Olivier Beauchet, Manuel Montero-Odasso, Cedric Annweiler, Robert Bartha, Alzheimer’s Association International Conference, July 17, 2017, ExCeL London, London, UK.

2017 (Poster): “Combined Memantine and Vitamin D Treatment Provides the Same Cognitive Benefit As Memantine Alone in a Chronically Vitamin D Deficient Double-Transgenic Mouse Model of Alzheimer’s Disease”, **Dickson Wong**, Miranda Bellyou, Olivier Beauchet, Manuel Montero-Odasso, Cedric Annweiler, Robert Bartha, Alzheimer’s Association International Conference, July 16, 2017, ExCeL London, London, UK.

2017 (Poster): “Vitamin D Supplementation May Protect Against Oxidative Stress in a Vitamin D Deficient Double-Transgenic Mouse Model of Alzheimer’s Disease”, **Dickson Wong**, Miranda Bellyou, Olivier Beauchet, Manuel Montero-Odasso, Cedric Annweiler, Robert Bartha, Alzheimer’s Imaging Consortium, July 15, 2017, ExCeL London, London, UK.

2017 (E-Poster): “Optimal Echo Time for In-Vivo Glutamate Detection at 7T Using semi-LASER 1H-MRS”, **Dickson Wong**, Amy Schranz, Robert Bartha, International Society for Magnetic Resonance in Medicine Annual Meeting, April 22, 2017, Hawai’i Convention Center, Honolulu, HI.

2017 (Poster): “Memantine and Vitamin D Supplementation Improves Cognition in Chronically Vitamin D Deficient APP/PS1 Mice”, **Dickson Wong**, Miranda Bellyou, Olivier Beauchet, Manuel Montero-Odasso, Cedric Annweiler, Robert Bartha, London Health Research Day, March 28, 2017, London Convention Center, London, ON.

2017 (Poster): “Improved Glutamate Detection in the Brain at 7T Using Long Echo-Time 1H-MRS”, **Dickson Wong**, Amy Schranz, Robert Bartha, Imaging Network of Ontario Symposium, March 15, 2017, Double Tree Hilton, London, ON.

2016 (Poster): “Enabling Quantification of Ultra-High Field 1H-MRS of the Brain Using Simulated A Priori Knowledge”, **Dickson Wong**, Robert Bartha, London Health Research Day, March 29, 2016, London Convention Centre, London, ON.

2016 (Presentation): “Towards quantification of ultra-high field 1H-MR spectroscopy of the brain using simulated a priori knowledge”, **Dickson Wong**, Robert Bartha, Medical Biophysics Graduate Seminar, March 3, 2016, The University of Western Ontario, London, ON.

2016 (Presentation): “Magnetic Resonance Imaging in Early Alzheimer’s Disease”, **Dickson Wong**, Clinician-Scientist Trainee Symposium, Jan 4, 2016, The University of Western Ontario, London, ON.

2015 (Poster): “Imito-64: An Electrotactile Computer Interface for the Visually Impaired”, **Dickson Wong**, Dennis Yazhensky, Andrew Mahabal, Electrical and Computer Engineering Expo, April 7, 2015, McMaster University, Hamilton, ON.

2014 (Presentation): “Evaluation of Intra-Fraction Prostate Motion during SBRT Treatment using Robotic Radiosurgery”, Kundan Thind, Raimond Wong, **Dickson Wong**, Carrie Schultz, Tom Chow, RadioSurgery Society SRS/SBRT Scientific Meeting, May 8, 2014, Hilton Minneapolis, Minneapolis, MN.

2013 (Poster): “Applying Motion-Artifact Removal Techniques in an NIRS BCI: Effects on NIRS Signal Quality and BCI Accuracy”, **Dickson Wong**, Sabine Weyand, Tom Chau, 7th Annual Ward Student Research Day, July 23, 2013, Holland Bloorview Kids Rehabilitation Hospital, Toronto, ON.

2013 (Presentation): “Evaluation of PTV Margins for Lung SBRT on CyberKnife and Trilogy”, Lindsay Mathew, **Dickson Wong**, Bill Edwards, Raimond Wong, Anand Swaminath, Marcin Wierzbicki, Tom Chow, RadioSurgery Society SRS/SBRT Scientific Meeting, Feb 22, 2013, La Costa Resort, Carlsbad, CA.

2012 (Presentation): “Intra-fractional Target Motion During CyberKnife Treatment For Brain Lesions”, **Dickson Wong**, William Edwards, Raimond Wong, Tom Chow, RadioSurgery Society SRS/SBRT Scientific Meeting, Feb 22-25, 2012, La Costa Resort, Carlsbad, CA.

Invited Lectures

2018 (Lecture): “Introduction to Reproducibility and Data Sharing”, **Dickson Wong**, Brainhack Western, May 3, 2018, Western University, London, ON.

2017 (Lecture): “Magnetic Resonance Spectroscopy at 7 Tesla”, **Dickson Wong**, Centre for Functional and Metabolic Mapping, March 18, 2017, Robarts Research Institute, London, ON.

2017 (Lecture): “Assessing the Combination of Vitamin D and Memantine for Alzheimer’s Disease Treatment with Ultra-High Field MRI”, **Dickson Wong**, Centre for Functional and Metabolic Mapping Winter School, March 17, 2017, Robarts Research Institute, London, ON.

2015 (Lecture): “Radios, Magnets and Alzheimer’s Disease: How magnetic resonance imaging is being used to look for early signs of Alzheimer’s disease”, **Dickson Wong**, Retiring With Strong Minds, December 17th, 2015, Windermere on the Mount, London, ON.

Academic Awards and Distinctions

J. B. Hargreaves/J. L. F. Hargreaves MD/PhD Award (\$10,000; annually) <i>The University of Western Ontario</i>	London, ON 2018–Present
The Canadian Institutes of Health Research MD/PhD Studentship (\$21,000; annually) <i>The University of Western Ontario</i>	London, ON 2015–Present
Course Award <i>Patient-Centred Clinical Methods</i> Awarded for exemplary performance in Patient-Centred Clinical Methods (Year 1)	London, ON Oct 2019
Oral Presentation Award, 1st Place <i>Imaging Network Ontario Symposium</i> Presentation: Relating Hippocampal Glutamate to Structural Changes and Cognitive Performance in Alzheimer’s Disease: A 7T MRI Study	Toronto, ON March 2018
Oral Presentation Award <i>Robarts Research Retreat</i> Presentation: Memantine and Vitamin D Supplementation Improves Cognition in Chronically Vitamin D Deficient APP/PS1 Mice	London, ON May 2017
Educational Trainee Stipend (\$600) <i>International Society for Magnetic Resonance in Medicine Annual Meeting & Exhibition</i>	Honolulu, HI Apr 2017
Frederick Banting and Charles Best Canada Graduate Scholarship (\$17,500) <i>The University of Western Ontario</i> Project: The Combination of Vitamin D and Memantine for Alzheimer’s Disease Treatment	London, ON May 2016

Western Graduate Scholarships (\$4,500; annually) <i>The University of Western Ontario</i>	London, ON 2015–2019
Alexander Graham Bell Canada Graduate Scholarships (\$17,500), Declined <i>McMaster University</i> Project: Assessing Non-Linear Dynamic Behaviour of the Brain Using Combined EEG/fMRI	Hamilton, ON May 2015
Dean's Excellence Engineering Doctoral Award (\$127,500), Declined <i>McMaster University</i> Awarded to exceptional incoming PhD students	Hamilton, ON 2015
1st Place, Biomedical Engineering Design Project Category (\$500) <i>Electrical and Computer Engineering Expo</i> Project: Imito-64: An Electrotactile Display for the Visually Impaired	Hamilton, ON 2015
McMaster Chancellor's Gold Medal Award <i>For the graduating undergraduate student who ranks highest in scholarship, leadership, and influence</i> McMaster University	Hamilton, ON 2015
Undergraduate Awards for Scholarship <i>McMaster University</i>	Hamilton, ON 2011–2014
2014: The Kudsia Family Scholarship	
2013–2015: The Provost's Honour Roll Medal	
2013: The Herbert A. Ricker Scholarship	
2012: The Dr. Harry Lyman Hooker Scholarship	
2011: The McMaster Honour Award, Level 3	
2011–2015: Dean's Honour Roll	
2009: McMaster Engineering & Science Entrance Prize	

Memberships

2015-present: Clinician Investigator Trainee Association of Canada (CITAC)
2015-present: Alzheimer's Association International Society to Advance Alzheimer's Research and Treatment (ISTAART) Student Member
2011-present: Golden Key International Honour Society Member